

Beyond the Limit: Nuclear Magnetic Resonance Investigations of Supramolecular Assemblies

Dissertation

zur Erlangung des akademischen Grades

doctor rerum naturalium

(Dr. rer. nat.)

im Fach Biophysik eingereicht an der

Mathematisch-Naturwissenschaftlichen Fakultät I
der Humboldt-Universität zu Berlin

von

Andi Mainz, Diplom Biochemiker,

Präsident der Humboldt-Universität zu Berlin

Prof. Dr. Jan-Hendrik Olbertz

Dekan der Mathematisch-Naturwissenschaftlichen Fakultät I

Prof. Dr. Andreas Herrmann

Gutachter/in:

1. Prof. Dr. Bernd Reif

2. Prof. Dr. Harmut Oschkinat

3. Prof. Dr. Holger Dobbek

Tag der mündlichen Prüfung: 27.08.2012

to my family

Zusammenfassung

Eine Vielzahl zellulärer Prozesse wird durch große Proteinkomplexe reguliert. Strukturelle Untersuchungen dieser supramolekularen Maschinen auf atomarer Ebene sind essentiell um mechanistische Einblicke in biologische Vorgänge zu erlangen, sowie bei Fehlfunktion dieser Systeme therapeutische Ansätze zu finden. Die Kernspinresonanz- (NMR) Spektroskopie stellt eine vielseitige Methode dar um die Struktur und Funktion von Proteinen zu untersuchen. Die Strukturanalyse von großen Biomolekülen mittels Lösungs-NMR ist jedoch nur beschränkt möglich. Die Festkörper-NMR Spektroskopie mit Probenrotation im sogenannten magischen Winkel (MAS) stellt dagegen eine molekulargewichtsunabhängige Methode zur Charakterisierung biologischer Komplexe dar. Für die Anwendung der MAS NMR waren jedoch Kristallisationsverfahren für lösliche Proteine bisher unumgänglich.

Im Rahmen dieser Arbeit wurde eine neue Methode entwickelt, die die MAS NMR Spektroskopie an großen Biomolekülen in Lösung erlaubt. Proteinlösungen können demnach durch MAS und dessen Ultrazentrifugationseffekt homogene Proteinsedimente ausbilden, in denen die rotatorische Diffusion großer Proteinkomplexe überwiegend aufgehoben ist. Auf diese Weise können klassische Festkörper-NMR Methoden angewandt werden, ohne dass Präzipitations- oder Kristallisationsverfahren erforderlich sind. In Kombination mit Proteindeuterierung, Protonen-detektierten NMR Experimenten sowie paramagnetischer Relaxationsverstärkung ermöglichte diese neuartige Methode die Detektion und Zuordnung von Rückgrat-Amidresonanzen des 20S Proteasoms mit einem Molekulargewicht von 1.1 MDa. Die experimentellen Daten weisen außerdem daraufhin, dass die Sensitivität und die spektrale Auflösung mit zunehmender Molekülmasse des Zielproteins verbessert werden.

Die Anwendung von MAS NMR auf Proteinlösungen wurde des Weiteren genutzt um das kleine Hitzeschockprotein α B-Crystallin (α B) und dessen Cu(II)-Bindungseigenschaften zu untersuchen. Das Chaperon (600 kDa) spielt eine wesentliche Rolle in der zellulären Proteinhomeostase, ist jedoch aufgrund seiner Polydispersität strukturell biologisch nur schwer zugänglich. Die Anbindung von Cu(II) moduliert die oligomere Architektur und die Chaperonaktivität von α B. Das α B-Oligomer als auch dessen isolierte dimere Untereinheit wurden in Anwesenheit von Cu(II) durch verschiedenste NMR Techniken und andere biophysikalische Methoden charakterisiert. Die Ergebnisse zeigen, dass die konservierte

α -Crystallin-Domäne ein Cu(II)-Ion mit pikomolarer Affinität bindet. Die potentiellen Cu(II)-Liganden sind H83, H104, H111 und D109 in den β 3- β 4- und β 5- β 6+7-Schleifen nahe der Monomer-Monomer Interaktionsfläche. Darüber hinaus konnte eine Cu(II)-induzierte Konformationsänderung in der N-terminalen Domäne beobachtet werden. Letztere vermittelt nicht nur die intermolekulare Anordnung der Untereinheiten im α B-Oligomer, sondern auch die Wechselwirkung mit Substratproteinen. Das sich daraus ergebende Modell beinhaltet die Cu(II)-induzierte Freilegung von Substrat-Interaktionsflächen und Veränderungen in der dynamischen Quartärstruktur sowohl der dimeren Untereinheit als auch des oligomeren Komplexes von α B. Die hohe Bindungsaffinität von α B in Bezug auf redoxaktives Cu(II) hat Implikationen für die zelluläre Proteinhomöostase und die oxidative Stressresistenz. Interessanterweise spielt oxidativer Stress eine wesentliche Rolle im Verlauf der Alzheimer Krankheit (AD). Elektronenmikroskopie und dynamische Lichtstreuungsexperimente deuten darauf hin, dass das Aggregationsverhalten des AD-relevanten Amyloid β -Peptids ($A\beta$) durch die Wirkungsweise von α B verändert wird. Über NMR-Studien konnte die $A\beta$ -Bindungsstelle in der hydrophoben β 4- β 8-Furche der α -Crystallin-Domäne lokalisiert werden. Wie MAS Festkörper-NMR Experimente weiterhin zeigen konnten, führt die Inkubation von $A\beta_{1-40}$ mit substöchiometrischen Mengen von α B zu strukturell definierten $A\beta_{1-40}$ -Aggregaten. Die hier erbrachten Forschungsergebnisse leisten einen wesentlichen Beitrag zu dem mechanistischen Verständnis von kleinen Hitzeschockproteinen und ihrer Wechselwirkung mit leicht aggregierenden Substraten. Insbesondere die neuentwickelte MAS NMR Spektroskopie von sedimentierten Biomolekülen legt den Grundstein für zukünftige Struktur- und Dynamikuntersuchungen an großen molekularen Maschinen.

Summary

Various processes in the living cell are regulated by large machineries with molecular weights in the megadalton regime. Atomic-level investigations of these supramolecular assemblies are therefore fundamental to gain mechanistic insights into life and the ability to rationally intervene in case of malfunctioning of these systems. Nuclear magnetic resonance (NMR) spectroscopy is a versatile method to study the structure and function of proteins. However, structural investigations of large biomolecules by solution-state NMR are challenging in case the molecular weight of the complex exceeds 150 kDa. Magic-angle-spinning (MAS) solid-state NMR is a powerful tool for the characterization of biomolecular systems irrespective of their molecular weight. Crystallization, however, is required if this technique is applied to soluble proteins.

In the scope of this work, a novel approach was developed, which opens new perspectives in the investigation of supramolecular modules by MAS NMR. Using simply protein solutions, the ultracentrifugal forces during MAS yield fairly homogeneous sediments of high density, in which rotational diffusion of large protein complexes is impaired. Typical solid-state NMR techniques can thus be applied without the need of precipitation or crystallization procedures. This novel approach in combination with protein deuteration, proton-detection and paramagnetic relaxation enhancement enabled the observation and the assignment of backbone amide resonances of a 20S proteasome assembly with a molecular weight of 1.1 MDa. The experiments show further that the sensitivity and the resolution improve with increasing molecular weight.

Similarly, this MAS NMR approach was used to characterize the small heat-shock protein α B-crystallin (α B) with respect to its Cu(II)-binding capability. The chaperone (600 kDa) plays an essential role in cellular protein homeostasis. Structural investigations at atomic resolution are hampered due to its polydispersity. Binding of Cu(II) modulates the oligomeric architecture and the chaperone activity of α B. The multimer assembly and its isolated dimeric core domain were studied by various NMR techniques and other biophysical methods to unravel the effects of Cu(II) on the chaperone function. We show that the conserved α -crystallin core domain is the elementary Cu(II)-binding unit specifically coordinating one Cu(II) ion with picomolar binding affinity. Putative Cu(II) ligands are H83, H104, H111 and D109 within the β 3- β 4- and

β 5- β 6+7-loops at the dimer interface. Moreover, the metal ion triggers structural reorganization in the N-terminal domain, which is known to mediate the intermolecular arrangement in α B oligomers as well as the binding of client proteins. We therefore suggest that Cu(II)-binding unblocks potential client binding sites and alters quaternary dynamics of both the dimeric building block as well as the higher-order assemblies of α B. The high-affinity of α B towards redox-active Cu(II) has implications in protein homeostasis and oxidative stress resistance. Intriguingly, oxidative stress is also implicated in the progression of the Alzheimer's disease (AD). Electron microscopy and dynamic light scattering experiments show that α B modulates the aggregation behavior of the AD-related amyloid β -peptide (A β). Our NMR data suggest that the A β -binding site of α B involves the hydrophobic β 4- β 8 groove of the α -crystallin domain. Moreover, co-incubation of A β ₁₋₄₀ and substoichiometric amounts of the chaperone yield well-defined A β ₁₋₄₀ aggregates, which are amenable for structural analysis by MAS solid-state NMR spectroscopy.

The findings of this work contribute to the mechanistic understanding of small heat-shock proteins and their interaction with aggregation-prone clients. In particular, we expect that MAS NMR employed to biomolecules in solution will be a novel tool to explore structural and dynamic properties of large biological machines in the future.

Table of Contents

Zusammenfassung.....	I
Summary	III
Table of Contents	V
Abbreviations.....	IX
1 Introduction and Objectives.....	1
1.1 Protein Homeostasis	1
1.1.1 Protein Folding and Molecular Chaperones	2
1.1.2 Heat-Shock Proteins (HSPs).....	3
1.1.3 Small Heat-Shock Proteins (sHSPs).....	5
1.1.3.1 Structure and Function of α B-crystallin	8
1.1.3.2 Copper Biochemistry	11
1.1.4 Protein Degradation: The Proteasome	15
1.1.5 Amyloid Aggregation and the Alzheimer's Disease	17
1.2 Nuclear Magnetic Resonance Spectroscopy	20
1.2.1 Nuclear Spins.....	20
1.2.2 Relaxation of Excited Spin States	23
1.2.3 NMR Investigations of Large Biomolecules	26
1.2.4 Solid-State NMR	27
1.2.4.1 Magic-Angle-Spinning (MAS).....	27
1.2.4.2 Cross-Polarization.....	29
1.2.4.3 Perdeuteration and Proton-Detection.....	30
2 Materials and Methods	31
2.1 Solutions and Media	31
2.1.1 Buffer Solutions.....	31
2.1.2 Cell Growth Media	31
2.2 Microbiological and Molecular Biological Methods	32
2.2.1 Polymerase Chain-Reaction (PCR)	32
2.2.2 Agarose Gel-Electrophoresis	32
2.2.3 Determination of DNA Concentration	33
2.2.4 DNA Restriction with Endonucleases	33
2.2.5 Ligation of DNA Fragments.....	33
2.2.6 Ligation Independent Cloning (LIC).....	34
2.2.7 Site-Directed Mutagenesis.....	34
2.2.8 Transformation of <i>E. coli</i> Cells	34

Table of Contents

2.2.9	Colony-PCR.....	35
2.2.10	Amplification and Extraction of Plasmid-DNA	35
2.2.11	Recombinant Protein Expression.....	36
2.2.11.1	Unlabeled Protein	36
2.2.11.2	^{13}C and ^{15}N Enrichment in Proteins.....	36
2.2.11.3	$^{13}\text{C}/^{15}\text{N}$ Enrichment and Perdeuteration.....	37
2.2.12	Cell Harvest and Storage	37
2.3	Biochemical Methods and Sample Preparation.....	38
2.3.1	Cell Lysis.....	38
2.3.2	Anion-Exchange Chromatography (AEC)	38
2.3.2.1	Weak AEC	38
2.3.2.2	Strong AEC.....	39
2.3.3	Size-Exclusion Chromatography (SEC).....	39
2.3.4	Analytical SEC for Protein Characterization.....	40
2.3.5	SDS-PAGE	40
2.3.6	Dialysis	40
2.3.7	Concentration of Protein Samples by Ultrafiltration.....	41
2.3.8	Storage of Protein Samples.....	41
2.3.9	Preparation of Monomeric $\text{A}\beta_{1-40}$	41
2.3.10	Alignment of Protein Sequences	42
2.4	Biophysical Methods	42
2.4.1	Determination of Protein Concentration.....	42
2.4.2	Dynamic Light Scattering (DLS)	42
2.4.3	Inductively-Coupled-Plasma Mass Spectrometry (ICP-MS)	44
2.4.4	Isothermal Titration Calorimetry (ITC).....	44
2.4.5	<i>In-vitro</i> Chaperone Activity Assay	45
2.4.6	Electron Microscopy (EM).....	46
2.4.7	Circular Dichroism (CD) Spectroscopy	46
2.4.8	Fluorescence Spectroscopy.....	47
2.4.9	Fluorescence Correlation Spectroscopy (FCS).....	48
2.4.10	Estimation of Rotational Correlation Times.....	49
2.4.11	X-ray Crystallography	50
2.4.12	Modeling of the Cu(II) Coordination Sphere	50
2.5	NMR Spectroscopy	51
2.5.1	Solution-State NMR Spectroscopy.....	51
2.5.1.1	Backbone Resonance Assignment of αB10m	51
2.5.1.2	Titration of αB10m with Divalent Metal Ions	52
2.5.1.3	^{13}C Direct Detected Experiments.....	53
2.5.1.4	^{15}N Relaxation Measurements	54
2.5.1.5	Estimation of Overall Rotational Correlation Times from T_1/T_2	54

2.5.1.6	Resonance Assignment of Monomeric A β ₁₋₄₀	55
2.5.1.7	Titration of α B10m with Monomeric A β ₁₋₄₀	56
2.5.1.8	Perdeuterated α B in Solution	56
2.5.2	Nuclear Magnetic Relaxation Dispersion (NMRD)	56
2.5.3	Magic-Angle-Spinning (MAS) NMR Spectroscopy	58
2.5.3.1	Precipitation of α B for Conventional Solid-state NMR	58
2.5.3.2	Comparison of Soluble and Precipitated α B Multimers	59
2.5.3.3	Titration of α B Multimers with Divalent Metal-Ions	59
2.5.3.4	The 20S Proteasome Assemblies of <i>Thermoplasma acidophilum</i>	60
2.5.3.5	Aggregates of A β ₁₋₄₀ in the Presence of α B	60
2.5.3.6	¹ H-detected FROSTY MAS NMR	61
3	Results.....	63
3.1	Protein Preparation	63
3.1.1	Full-length α B	63
3.1.1.1	α B Constructs with N-terminal Affinity-tag	63
3.1.1.2	Cloning of Tag-free α B	64
3.1.1.3	Overexpression and Purification of α B	65
3.1.2	The Excised α -crystallin Domain: α B10m	66
3.1.2.1	Cloning of Construct	66
3.1.2.2	Overexpression and Purification of α B10m and its Mutants	67
3.2	α B-crystallin and Metal-Binding	68
3.2.1	Effects of Metals on the Morphology of α B Multimers	68
3.2.2	Modulation of α B Chaperone Activity by Cu(II)	70
3.2.3	Stoichiometry of Cu(II)-binding: ICP-MS Experiments	72
3.2.4	Affinity and Stoichiometry of Cu(II)-binding: ITC Studies	72
3.2.5	Fluorescence Quenching: Cu(II)-Affinity of the ACD	73
3.2.6	Secondary Structure and Thermal Stability	74
3.2.7	Effects of Cu(II) on the Quaternary Structure of the ACD	77
3.2.8	Crystallization of the ACD	79
3.2.9	NMR Investigations on Full-length α B Multimers	80
3.2.10	NMR Investigations on the Dimeric α B10m	81
3.2.10.1	Resonance Assignment of apo- α B10m	81
3.2.10.2	NMR Titration Studies	82
3.2.10.3	¹³ C-detected NMR Experiments	86
3.2.10.4	The AP Interface and its Dynamics	89
3.2.10.5	The Cu(II) Coordination Sphere	95
3.3	The Interaction of α B-crystallin with A β ₁₋₄₀	97
3.3.1	Resonance Assignment of Monomeric A β ₁₋₄₀	97
3.3.2	Secondary Structure Propensity of A β ₁₋₄₀	98
3.3.3	A β ₁₋₄₀ -Binding to the Chaperone α B	99

Table of Contents

3.3.4	Inhibition of A β ₁₋₄₀ Fibril Formation.....	100
3.3.5	Structural Investigations of A β ₁₋₄₀ Aggregates.....	102
3.4	MAS NMR on Protein Solutions.....	103
3.4.1	The Multimers of α B and the FROSTY Approach	104
3.4.2	The 20S Proteasome Assemblies of <i>Thermoplasma acidophilum</i>	107
3.4.3	Rotational Diffusion of Large Protein Complexes	110
3.4.3.1	Estimation of Rotational Correlation Times.....	110
3.4.3.2	Nuclear Magnetic Relaxation Dispersion (NMRD)	112
3.4.3.3	Fluorescence Correlation Spectroscopy (FCS).....	113
3.4.4	¹ H-detected FROSTY MAS NMR	115
3.4.4.1	Perdeuterated α B Multimers in Solution	115
3.4.4.2	Perdeuterated 20S Proteasome Assemblies in Solution	119
4	Discussion and Conclusions	129
4.1	Protein Preparation	129
4.2	α B-crystallin and Metal-binding	129
4.3	The Interaction of α B-crystallin with A β ₁₋₄₀	135
4.4	MAS NMR on Protein Solutions.....	138
5	Appendix	143
5.1	DNA and Protein Sequences	143
5.1.1	Vector DNA.....	143
5.1.2	PCR Primer Sequences	144
5.1.3	Primer Sequences for Site-directed Mutagenesis	144
5.1.4	Protein Sequences.....	145
5.1.5	Protein Parameters	146
5.2	NMR Data	147
5.2.1	PDSO Spectra of α B Oligomers in Solution	147
5.2.2	Chemical Shifts of apo- α B10m	148
5.2.3	Chemical Shifts of Cu(II)- α B10m	150
5.2.4	Chemical Shifts of Monomeric A β ₁₋₄₀	151
5.2.5	Chemical Shifts of the α -subunit in $\alpha_7\beta_7\beta_7\alpha_7$ -(11S) ₁₄	152
5.2.6	Pulse Programs for ¹ H-detected Solid-state NMR Experiments	155
	References	162
	Acknowledgements.....	174
	Publications.....	177
	Conferences and Workshops	178
	Eidesstattliche Erklärung.....	179

Abbreviations

2D/3D	two dimensional, three dimensional
α B	α B-crystallin
α B10m	protein construct comprising residues 64-152 of α B and bearing the mutation N146D
A β	amyloid β -peptide
ACD	α -crystallin domain
AD	Alzheimer's disease
ADP	adenosine diphosphate
AEC	anion-exchange chromatography
AP	anti-parallel
APP	amyloid precursor protein
ATP	adenosine triphosphate
BSA	bovine serum albumin
C'	carbonyl atom
CCS	copper chaperone for superoxide dismutase
CD	circular dichroism
CIP	calf-intestinal phosphatase
CP	cross polarization
CS	citrate synthase
CSA	chemical shift anisotropy
CSI	chemical shift index
CSP	chemical shift perturbation
CV	column volume
DLS	dynamic light scattering
DMSO	dimethyl sulfoxide
DNA	desoxyribo-nuclein-acid
<i>E.coli</i>	<i>Escherichia coli</i>
EDTA	ethylenediaminetetraacetic acid
Ek	enterokinase
EM	electron microscopy
EPR	electron paramagnetic resonance
FCS	fluorescence correlation spectroscopy
FID	free induction decay
FROSTY	freezing rotational diffusion of protein solutions at low temperature and high viscosity
fw	forward
GSH	glutathione
HMQC	heteronuclear multiple quantum coherence
HSP	heat-shock protein
HSQC	heteronuclear single quantum coherence
ICP-MS	inductively-coupled-plasma mass spectrometry
IDP	intrinsically disordered protein
INEPT	insensitive nuclei enhanced by polarization transfer
IPAP	in-phase anti-phase
IPOD	insoluble protein inclusion
IPTG	isopropyl β -D-1-thiogalactopyranoside
ITC	isothermal titration calorimetry
JUNQ	juxtannuclear quality control
Da	Dalton
LB	Luria-Bertani
MAS	magic angle spinning
MBP	maltose binding protein
MCR	mean count rate
MISSISSIPPI	multiple intense solvent suppression intended for sensitive spectroscopic investigation of protonated proteins, instantly

Abbreviations

MPD	2-methyl 1,3-propanediol
MS	mass spectrometry
NEF	nucleotide-exchange factor
NMR	nuclear magnetic resonance
NMRD	nuclear magnetic relaxation dispersion
NOE(SY)	nuclear Overhauser enhancement (spectroscopy)
OD	optical density
PAGE	polyacrylamide gelelectrophoresis
PBS	phosphate buffered saline
PCR	polymerase chain reaction
Pd	polydispersity
PDB	protein data bank
PDSF	proton-driven spin diffusion
PEG	polyethylene glycol
ppm	parts per million
PRE	paramagnetic relaxation enhancement
PrP	prion protein
REDOR	rotational echo double resonance
RE	restriction enzyme
rf	radio-frequency
RFDR	radio frequency driven recoupling
ROS	reactive oxygen species
rv	reverse
SAXS	small-angle X-ray scattering
SDS	sodium dodecylsulfate
sHSPs	small heat-shock protein
SEC	size-exclusion chromatography
SOD	superoxide dismutase
SSP	secondary structure propensity
TEV	tobacco etch virus
TOCSY	total correlation spectroscopy
TPPI	time-proportional phase incrementation
TROSY	transverse relaxation-optimized spectroscopy
UPS	ubiquitin-proteasome system
UV	ultraviolet
wt	wildtype

Standard chemical and physical abbreviations are not listed. Nucleotides are abbreviated by the standard one-letter code. Amino acids are abbreviated by the standard one- or three letter code.

1 Introduction and Objectives

1.1 Protein Homeostasis

Proteins are the key players of life and their biological functions are multi-faceted. Mammalian cells typically express more than 10,000 different types of proteins with diverse three-dimensional structures and cellular functions [1]. This multitude of protein species and its temporal flow must be stringently maintained and regulated in the living cell. Protein homeostasis (proteostasis) is therefore crucial for cellular viability. Several control machineries have evolved to fine-tune the balance between i) protein synthesis, ii) protein folding, and iii) protein clearance (**Fig. 1A**). Pathological conditions, environmental influences, metabolic stress, cancer and aging are known to disturb this sensitive balance [2,3]. Cellular strategies to cope with fluctuations of the proteome rely on the coordinated action of the quality control apparatus as well as the systems that regulate protein biogenesis, assembly, trafficking, and translocation [3]. All aspects of protein quality control involve the class of molecular chaperones, which accomplish *de novo* protein folding as well as the stabilization and the refolding of non-native proteins [4]. In futile cases, chaperones also guide misfolded proteins to the autophagy system and the degradation machinery, namely the ubiquitin-proteasome system (UPS) [1]. The sequestration of misfolded proteins in spatially distinct protein inclusions, known as quality control compartments, is a further mechanism to prevent the accumulation of toxic protein waste [5]. Recently, two different compartments have been defined – the JUNQ (juxtannuclear quality control) and the IPOD (insoluble protein inclusion), which fulfill distinct functions within the proteostatic network [6]. Whilst JUNQ sequesters soluble non-native proteins and operates in conjunction with chaperones and proteasomes, the IPOD contains insoluble protein aggregates and is associated with the autophagy-related Atg8.

Hundreds of proteins participate in the regulation of cellular proteostasis [3]. In the following, selected members of molecular chaperones and the UPS are described in more detail. Protein folding in the network of these chaperone and degradation systems is outlined. Amyloidogenic aggregation is highlighted as a special case of protein misfolding and uncontrolled self-association.

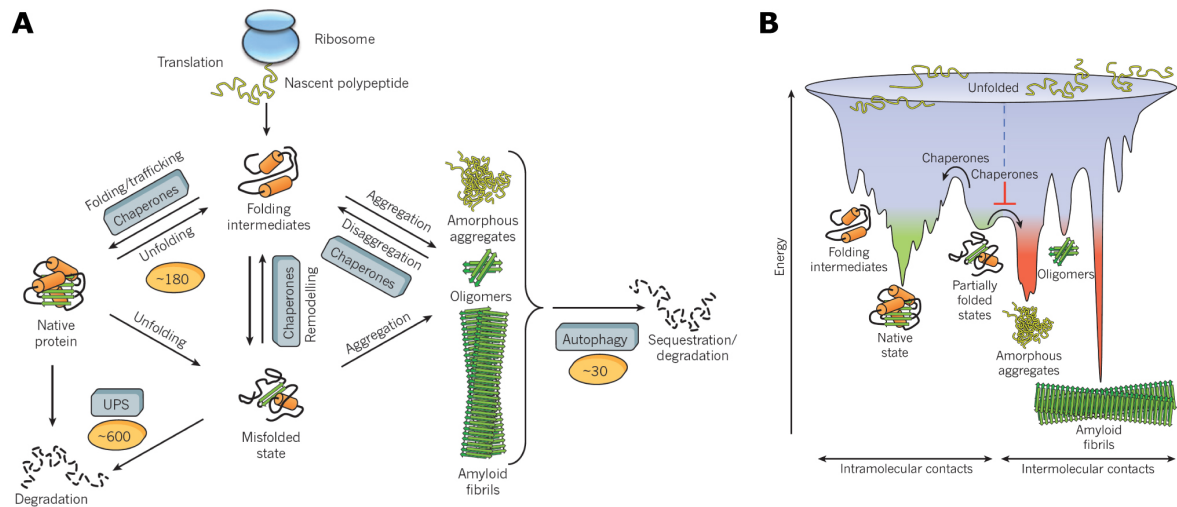


Fig. 1 Protein folding and the role of the chaperone machinery. (A) From the cradle to the grave: protein fates and the cellular proteome maintenance system. In mammalian cells, proteostasis is accomplished by a synchronized network of molecular chaperones, the UPS (ubiquitin-proteasome system) and autophagy system with approximately 180, 600 and 30 components, respectively. Together with the transcription and translation machinery, this network assures protein biogenesis, maintenance and clearance. This proteostatic balance is fundamental for cellular functionality and integrity. **(B)** Schematic illustration of the funnel-shaped free-energy landscape of protein folding, which might overlap with that of intermolecular aggregation. Polypeptide chains need to traverse free-energy barriers to reach downhill-paths towards the native fold (green). Folding intermediates and partially folded states accumulate and are imminent to form amorphous aggregates, pre-fibrillar oligomeric states or amyloid fibrils (red). Molecular chaperones inhibit protein aggregation by stabilizing partially folded states and assist in protein (re-)folding by lowering energetic barriers. Both figures are taken from [1].

1.1.1 Protein Folding and Molecular Chaperones

The amino acid sequence of a protein encodes the three-dimensional structure and consequently the biological function of the respective protein [7]. However, many proteins exhibit very slow folding rates or even fail to adopt their native state [4,8]. The huge conformational space of a polypeptide chain and the diverse combinations of many weak and non-covalent intramolecular interactions render the folding reaction a highly complex process. It is the burial of hydrophobic residues within the protein interior that is one of the major driving forces, inducing an intramolecular chain collapse [9,10]. The conformational space becomes progressively restricted during the folding reaction, however, partially folded states can be transiently populated and kinetically trapped in local energy minima (**Fig. 1B**) [11]. In particular, larger and/or multi-domain proteins have an increased propensity to populate such misfolded states [12]. The incomplete folding reaction entails that hydrophobic residues and segments are partially exposed to the aqueous environment [13]. As in the case of intramolecular folding, hydrophobic forces also promote the intermolecular association and

the formation of amorphous aggregates (**Fig. 1B**). This tendency of unstructured or partially folded proteins to associate in non-native fashions is especially pronounced in the crowded cellular environment with cytosolic protein concentrations in the range of 300–400 g/L [1]. In addition to the heterogeneous amorphous aggregates, amyloid fibrils with high structural order may also form [14]. Intriguingly, such fibrillar aggregates are often accompanied by soluble oligomeric states of rather heterogeneous appearance [14,15]. These less-ordered oligomeric structures might be considered as analogues of the kinetically trapped intermediates in protein folding. A recent model suggests, that aggregates of misfolded proteins provoke cell toxicity by diminishing the capacity of the protein folding machinery [16]. Accordingly, the chaperoning and proteolytic systems are sequestered and blocked by these toxic aggregates. This overstrain impairs the proteostatic capacity of the cell [16]. The up-regulation of protein quality control systems, namely chaperones, the UPS and autophagy, has been shown to reverse the deleterious effects of disease-related protein aggregates [17].

The formation of amorphous and fibrillar aggregates is restricted *in vivo* by the intervention of the cellular chaperone network [1,18]. Molecular chaperones are capable of stabilizing misfolded proteins prior to aggregation and to assist protein folding. Since all members of this protein class are up-regulated in response to cellular stress, e.g. elevated temperatures, they are also known as heat-shock proteins (HSPs) [1]. Commonly, chaperones are classified with respect to their molecular weight, namely HSP100, HSP90, HSP70, HSP60, HSP40 as well as the small HSPs (sHSPs) with molecular weights in the range of 12-43 kDa [19]. Chaperones can be further differentiated by their mode of action, i.e. the utilization of ATP, and are termed foldases (ATP-dependent) and holdases (ATP-independent), respectively [4]. These two types are outlined separately in the next chapters with a focus on the sHSP family.

1.1.2 Heat-Shock Proteins (HSPs)

ATP-dependent chaperones like HSP70s, HSP90s and the chaperonins (HSP60s) are capable of promoting *de novo* protein folding as well as refolding of stress-denatured proteins [19]. This assistance in structural maturation is achieved by repetitive substrate binding and release cycles, which are regulated by the hydrolysis of ATP to ADP and the intervention of several cofactors such as the nucleotide-exchange factors (NEFs) [1]. The recognition and transient binding of hydrophobic patches, typically exposed by non-native proteins, protects against self-aggregation and enables the folding reaction to proceed after ATP-driven substrate

release. The underlying principle is known as kinetic partitioning [20], which requires that the folding rate constant (k_{fold}) is greater than the association constant (k_{on}) for chaperone (re-)binding of partially folded substrates, and that k_{on} exceeds the self-association rate constant k_{agg} of higher-order aggregates ($k_{\text{fold}} > k_{\text{on}} > k_{\text{agg}}$) (**Fig. 2A**). Under cellular stress conditions, k_{agg} may become greater than k_{on} resulting in protein aggregation, unless expression of the chaperone machinery is elevated via the stress-response pathway [21].

The HSP70 system and the chaperonins operate sequentially along the folding path of a protein [22]. Folding of newly synthesized and nascent polypeptide chains is assisted by the integrated action of the HSP40 and HSP70 chaperone systems (upstream chaperones) [23]. However, many proteins, such as actins and tubulins, encounter high energetic barriers en-route to their native and functionally active state [24]. In those cases, the association to the chaperone (k_{on}) may become faster than the folding (k_{fold}). These proteins are stabilized by the chaperone in a non-aggregated state, but require the intervention of the specialized chaperonins (downstream chaperones) [1]. An unique feature of the chaperonin family is the release of substrate proteins into a folding chamber, rather than the cytosolic environment. Prominent members are the eukaryotic HSP60s and the bacterial GroEL, that form large double-ring complexes (800-900 kDa) [23]. The spacious interiors can accommodate substrate proteins up to molecular weights of ~60 kDa [1]. Non-native protein structures are sequestered via their hydrophobic surfaces and bound in the lumen of the chaperonin complex. The corresponding HSP10 proteins (eukaryotes) and GroES (bacteria) function as ATP-regulated lids of the folding cage, thereby completely encapsulating the substrate protein [25]. Closure of the folding chamber induces a highly hydrophilic (net negatively charged) surface of its inner wall, which promotes the folding reaction of the enclosed substrate [25]. The encapsulation of a single polypeptide chain impedes aggregation and the devastating interaction with other cellular components [26]. Furthermore, the steric confinement has been suggested to accelerate the folding rate by entropically destabilizing flexible folding intermediates and favoring more compact, native-like structures [27]. Chaperonins are thus enabled to diminish both enthalpic as well as entropic barriers in the free-energy landscape of protein folding. Mechanistic details of the chaperonin system GroEL-GroES are illustrated in **Fig. 2B**.

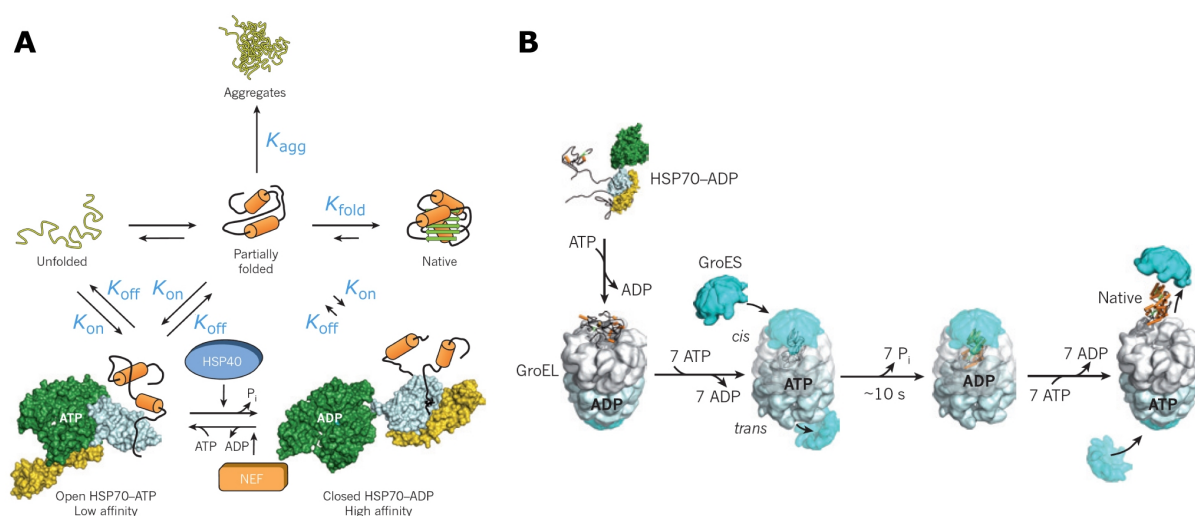


Fig. 2 Chaperone-mediated protein folding. (A) The chaperone cycle of the eukaryotic HSP70 system and the principles of kinetic partitioning (see text) are illustrated. Unfolded and misfolded proteins are sequestered by one of several HSP40 cofactors, that recruit the substrate to the ATP-bound HSP70 (low-affinity, open state). ATP hydrolysis induces closure of the peptide-binding domain (yellow). In this high-affinity (closed) state, the substrate is tightly bound to the chaperone. Several nucleotide-exchange factors (NEFs) catalyze the substitution of ADP by ATP, which finally promotes substrate release. Kinetic partitioning is achieved for $k_{fold} > k_{on} > k_{agg}$, where k_{fold} , k_{on} , k_{agg} denote the folding rate constant, the association constant of substrate binding to the chaperone and the aggregation rate constant of the substrate, respectively. (B) The bacterial chaperonin GroEL-GroES and its folding cage. Aberrantly folded proteins with slow k_{fold} are guided to the chaperonin by the stabilizing HSP70 system. The apical domains of the seven-membered GroEL rings bind the substrate and are structurally rearranged upon ATP binding. Subsequently, the substrate is enclosed in the folding chamber of GroEL by the GroES lid (*cis*-complex), which causes the dissociation of ADP, GroES and substrate from the opposite side of the complex (*trans*-complex) (omitted for clarity). The GroES-induced hydrophilic nature of the inner wall allows the substrate to fold during the hydrolysis of seven ATP molecules (~10 s). The cycle is finished (substrate release) by binding of ATP and GroES to the *trans* complex. Both figures are taken from [1].

Certainly, there are several other chaperone and chaperonin systems known, such as the HSP90 and TRiC proteins, respectively, which are not discussed here [1,23]. The integrated action of all these multi-component molecular machines in cooperation with the sHSP family, the UPS and autophagy ensures the stability of the cellular proteome.

1.1.3 Small Heat-Shock Proteins (sHSPs)

Small heat-shock proteins (sHSPs) represent a diverse class of molecular chaperones that have been found in all six kingdoms of life except some pathogenic bacteria [28]. The number of sHSPs of an organism varies considerably, with the higher eukaryotes raising a broader phalanx of sHSPs for cellular stress response (*Mycobacterium tuberculosis*: 1, *Escherichia coli*: 2, *Drosophila melanogaster*: 4, *Homo sapiens*: 10, *Arabidopsis thaliana*: 19) [28].

The sHSPs play a fundamental role during cellular stress by ‘rescuing’ misfolded or partially unfolded proteins from final proteolytic degradation [29,30]. Therefore, sHSPs constitute the ‘first line of defense’ in terms of cellular stress. The ATP-independent sequestration of client proteins prevents irreversible aggregation and enables subsequent intervention of refolding-competent chaperone systems like HSP40-HSP70 and HSP100 (**Fig. 3**) [31,32]. *In vitro* studies have shown that sequestered client proteins are folding competent, however, the trapped polypeptides need to be reactivated once cellular stress has been overcome [33]. Notably, sHSPs are not competent to spontaneously release bound clients, and thus cooperate with the ATP-dependent chaperones [28,32]. This cellular strategy to buffer aggregation is highly efficient, in particular considering the ATP-independent mechanism of sHSPs and the low-energy state of the cell under stress conditions. The possibility to rescue misfolded proteins from the sHSPs-stabilized reservoir of aggregation-prone polypeptides circumvents *de novo* synthesis of the respective proteins. These economic aspects may illustrate the important role of sHSPs in proteome maintenance.

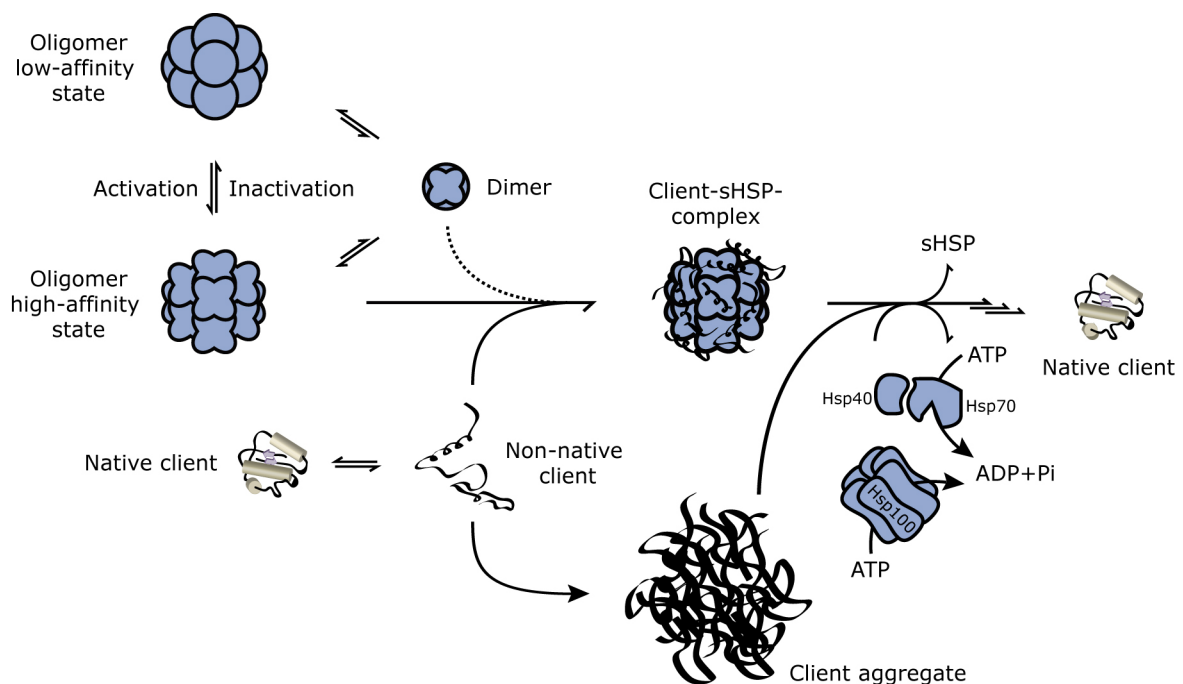


Fig. 3 The anti-aggregation property of sHSPs. The multimeric assemblies of sHSPs are highly dynamic and exchange subunits rapidly (mostly dimeric substructures). Upon cellular stress, the activated state is capable of binding non-native proteins that otherwise undergo irreversible aggregation. The non-native protein is stabilized within the highly soluble client-sHSP-complex and is directed to the ATP-dependent refolding machineries, e.g. HSP40/HSP70 and HSP100. The figure is adapted from [28].

Despite their diversity in sequence and size, sHSPs share common features such as small molecular weights (12-43 kDa), domain architecture, formation of large oligomeric assemblies with dynamic quaternary structure, induction in response to cellular stress and the prevention of protein aggregation (holdase function) [28]. This protective function of sHSPs remained elusive until bovine α -crystallin and murine HSP26 were reported to exhibit chaperone activity *in vitro* [30]. The ability to bind diverse non-native proteins at high client-sHSP stoichiometries (up to one substrate molecule per dimeric subunit) further highlights the efficiency of this cellular strategy to manage irreversible protein aggregation [34].

A characteristic trait of the sHSP family is the conserved α -crystallin domain, which is flanked by variable N- and C-terminal domains [35,36]. Dimerization of the α -crystallin core domain forms the basic building block of higher-order assemblies, which are established by intermolecular linkage via the terminal anchors (further structural details are given in Chapter 1.1.3.1). The sHSPs represent highly dynamic assemblies, which exchange subunits (primarily dimers) in a constant manner [37]. Due to this subunit exchange, hetero-oligomers may form in compartments with different types of sHSPs, as is the case for α A-crystallin (α A) and α B-crystallin (α B) in the mammalian eye lens [38]. This appears as a valid mechanism to modulate the characteristics and the substrate specificity of sHSPs.

Generally, molecular chaperones exist in states of low and high substrate affinity (**Fig. 3**) [28]. In ATP-dependent chaperones, the binding and hydrolysis of ATP triggers the transition between the two functional states [4]. By contrast, ATP has no direct role in the regulation of sHSPs chaperone activity [28]. Many members of the sHSP family are constitutively inactive, e.g. yeast HSP26, but become activated by typical stress factors such as elevated temperatures [39]. The dynamic behavior of sHSPs permits the potential client binding sites, which are hydrophobic in character and mostly buried in the oligomeric assembly, to become exposed upon subunit dissociation [40–42]. Indeed, several sHSPs become more hydrophobic under stress conditions [28,42,43]. Dynamic release and incorporation of subunits may thus reflect an inherent ‘sensing’ mechanism of sHSPs to recognize and sequester non-native proteins in the cellular environment as well as to stabilize the client proteins in the context of a soluble client-sHSP-complex. This hypothesis has been supported by studies on human HSP27, which requires subunit dissociation for client sequestration [41]. However, there are experimental results for yeast HSP26 and human α -crystallin, whereby subunit exchange does not correlate with chaperone activity [44,45]. In these cases, chaperone activation may be promoted by

structural rearrangements within the multimeric assembly. It is tempting to note, that the mechanism of regulation may rely on modulation of quaternary dynamics and alteration of client binding site accessibility. The structural plasticity of thermally-activated pea HSP18.1 has been demonstrated to correlate with its ability to protect firefly luciferase from aggregation [37]. More than 300 different client-chaperone stoichiometries were observed in these studies. It appears that the ability to form polydisperse ensembles, constitutively or in response to stress, is an essential element for the chaperone mechanism of sHSPs.

1.1.3.1 Structure and Function of α B-crystallin

The sHSP α B-crystallin (α B) was originally discovered in the mammalian eye lens as the B-subunit of α -crystallin [30]. Its function is to maintain the transparency and high refractive index of the eye lens, thereby counteracting cataract formation and visual impairment [46]. Besides this specific lenticular function, the biological role of human α B is manifold. Likewise it is localized in several other tissues such as the lung, kidney, brain, cardiac and skeletal muscle [47]. α B was shown to interact with a wide range of substrate proteins that either aggregate amorously or form amyloid fibril structures [30,48–50]. As a consequence α B was found to be involved in multiple sclerosis, cancer, cardiomyopathy and various neurodegenerative diseases like Parkinson's and Alzheimer's disease [31,51,52].

The 20 kDa protein α B assembles into highly dynamic and polydisperse complexes of about 600 kDa (24-32 subunits) [53]. A general feature of sHSPs is the α -crystallin domain (ACD), which is a conserved core domain of about 90 residues adopting a β -sandwich structure (**Fig. 4A,B**) [28]. The ACD is flanked by variable N-terminal (~60 residues) and C-terminal domains (~25 residues) that accomplish the multimeric assembly. The formation of dimeric building blocks via shared β -sheets (strands β 6 and β 7') is a conservative trait of sHSPs (**Fig. 4C**) [35,36]. The dynamic nature of sHSPs, and the α B oligomers in particular, hindered their structural characterization [54]. Crystal structures of sHSPs have been determined only for HSP16.9 from wheat and HSP16.5 from *Methanococcus jannashii*, revealing 12-mer and 24-mer assemblies, respectively (**Fig. 4D,E**) [35,36]. The C-terminal anchors comprise a conserved IXI-motif that packs into hydrophobic grooves (strands β 4- β 8) of neighboring molecules on the surface of the complexes. By contrast, the N-terminal domains are usually involved in intermolecular interactions within the central cavity of sHSPs assemblies.

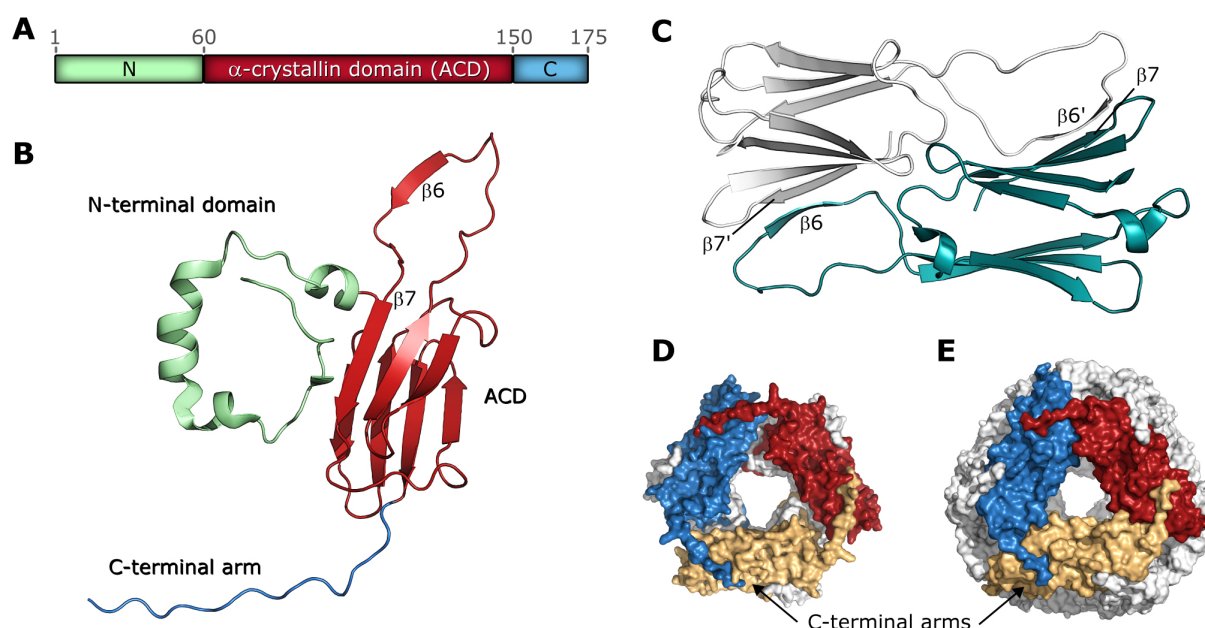


Fig. 4 Subunit assembly of sHSPs. (A) The domain organization of sHSPs is illustrated. The α -crystallin domain (ACD) is flanked by N- and C-terminal sequences. Residue numbers are exemplarily shown for α B. (B) Crystal structure of wheat HSP16.9 illustrating the topology of the monomeric subunit [35]. The conserved ACD (red) adopts an immunoglobulin-like fold with two anti-parallel β -sheets forming a β -sandwich structure. The strands $\beta 6$ and $\beta 7$ that form the dimer interface are indicated. The ACD is flanked by variable N- (green) and C-terminal sequences (blue), which accomplish the higher-order assembly. (C) Dimerization of the α -crystallin domain via the strands $\beta 6$ and $\beta 7'$ forms the building block of oligomeric assemblies. The two monomers of wheat HSP16.9 are colored in cyan and grey, respectively [35]. (D) The 12-mer assembly of wheat HSP16.9 is shown with three dimeric building blocks colored in red, blue and yellow [35]. Two hexameric rings with three-fold symmetry arrange in a double-disk fashion. (E) For comparison, HSP16.5 of *Methanococcus jannashii* is depicted [36]. Three dimeric building blocks are highlighted in red, blue and yellow, respectively. Four of such hexameric rings are arranged with tetrahedral geometry in the 24-mer. The C-terminal anchors interact with neighboring monomers and thereby stabilize the complex.

Only truncated variants of α B, containing the ACD without the terminal anchors, were amenable for X-ray crystallography and solution-state NMR [55–57]. Electron microscopy (EM) of negatively-stained α B revealed the envelope of a 24-mer with tetrahedral symmetry [58,59] (**Fig. 5C**). Recently, solid-state magic-angle-spinning (MAS) NMR enabled structural studies of full-length α B and provided insights into the oligomeric architecture of α B [57,60,61] (**Fig. 5B,D**). In all atomic-level structures of α B variants, the ACD folds into a β -sandwich structure comprising the two sheets $\beta 8$ - $\beta 9$ - $\beta 3$ -($\beta 2$) and $\beta 4$ - $\beta 5$ - $\beta 6$ +7 (**Fig. 5A,B**). The separated $\beta 6$ and $\beta 7$ strands, as observed for HSP16.5 and HSP16.9, have merged into one strand $\beta 6$ +7 in α B. The structurally variable $\beta 2$ strand was refined only for two of five molecules in the asymmetric unit [55]. Two monomers form an anti-parallel β -sheet along the $\beta 6$ +7 strands (bottom sheet). The dimer interface has been termed AP (anti-parallel) interface

[56]. A shared groove is located above the AP interface, which appears to be polymorphic, since three different alignment registers were observed [55,56]. The curvature of the dimeric building block varies significantly. The solid-state NMR structure of α B multimers reveals a highly bended ACD dimer [60]. This curvature is supposed to respond to changes of the pH [60]. An extensive network of ionic interactions spans the interface. This network involves charged residues of the strands β 3, β 4 as well as β 5, β 6+7 and the intervening loops. Notably, the conserved R120 of one monomer is involved in a bidentate ion pair with D109 of the neighboring molecule [55,56,60]. The missense mutation R120G causes an increase of the oligomeric size and a decrease in the *in vitro* chaperone efficiency [62]. Co-precipitates of desmin and α B-R120G are found in cardiac muscle tissue of patients suffering from desmin-related cardiomyopathy [52].

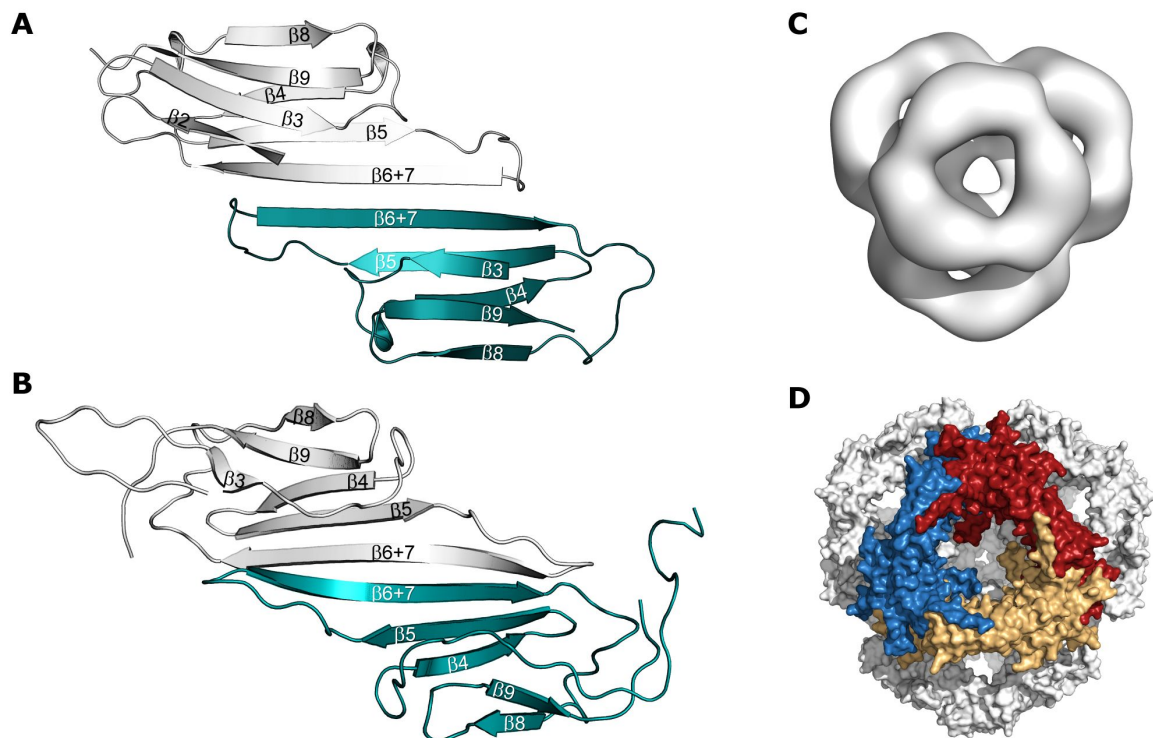


Fig. 5 Structural information for the α B assembly. (A) Crystal structure of the isolated ACD dimer (α B residues 67-157) [55]. The two monomers are colored cyan and grey, respectively. β -strands are labeled. Strands β 6+7 form the anti-parallel (AP) interface and an extended bottom-sheet. The two top-sheets (β 2- β 3- β 9- β 8) form a shared groove above the AP-interface. The variable β 2 strand is disordered in one of the two monomers. (B) Solid-state NMR structure of the ACD dimer as present in full-length α B multimers (residues 64-152 are shown) [60]. The two monomers are colored cyan and grey, respectively. β -strands are labeled. In comparison to the isolated ACD, the dimer is much more curved in the context of α B multimers. Hence, the shared groove becomes more accessible. (C) EM density map of the α B 24-mer [58]. The view along one threefold axis shows the tetrahedral arrangement of four hexameric rings, each formed by three dimeric building blocks. (D) Structural model of the 24-mer of α B as obtained by combined data from solid-state NMR, EM and SAXS (small-angle X-ray scattering) [61]. Three dimeric building blocks are highlighted in red, blue and yellow, respectively. The flexible C-terminal extensions are omitted for clarity.

The dimeric substructure of α B represents the building block of its higher-order assemblies [60,61]. Due to the dynamic subunit-exchange, the resulting α B ensemble is consequently heterogeneous. The intrinsic subunit-exchange and domain dynamics have been shown to be essential for α B chaperone activity [54,63,64]. Intriguingly, divalent metal ions like Cu(II) and Zn(II) can act as modulators of this chaperone property [65–67]. It was shown recently that α B can coordinate Cu(II) with a picomolar affinity, whereas the interaction with other divalent metal ions is significantly weaker [68]. Cu(II) affects the secondary structure and oligomeric size of α B [68,69]. Furthermore, α B is able to reduce Cu(II)-mediated formation of reactive oxygen species (ROS), thereby conferring cytoprotection to cells under conditions of oxidative stress [68]. Moreover, it has been shown, that α B exhibits redox activity, which induces oxidation of residue M35 in the amyloid β -peptide A β_{1-40} [49].

To date, no structural information concerning the Cu(II)-binding property of α B has been obtained, and it is a total mystery, how the metal ion can affect the chaperone mechanism of α B, which itself is far from being understood. This work focuses to a great extent on the metalloprotein α B and its interaction with paramagnetic Cu(II). A comprehensive biophysical characterization was envisaged in order to locate the metal center in α B and thus to understand the effects on the chaperone structure and function. The following chapter outlines the biological role of copper as well as the structural details of copper-binding proteins.

1.1.3.2 Copper Biochemistry

Copper is an essential trace element in biological systems, in which it is mainly found in the cupric state (Cu(II)) [70]. The average diet of adult humans in western countries contains from 0.6 to 1.6 mg copper per day [71]. On entering the blood plasma and interstitial fluid from intestinal cells, copper becomes sequestered by albumin, transcuprein, small peptides and amino acids [70]. However, albumin and transcuprein appear to be the primary components of the exchangeable plasma copper pool [72,73]. Most of the copper is transported to the liver, where it is incorporated into ceruloplasmin during its biosynthesis [74]. The distribution of copper in the organism is mainly achieved by ceruloplasmin [75]. The major role of copper within the living cell is to serve as a cofactor for enzymes and electron transport proteins that are involved in energy and antioxidant metabolism. Copper-dependent enzymes such as cytochrome-c oxidase, superoxide dismutase (SOD) and metallothioneine function to reduce reactive oxygen species or molecular oxygen [70].

However, due to its redox activity, excessive levels of copper can result in adverse oxidative damage of proteins, DNA and lipids, whereby ROS are produced through a Fenton-type reaction (**Fig. 6A**) [76,77]. Therefore, copper homeostasis is carefully regulated through a system of copper transporters, such as Ctr1 (influx) and ATP7A/B (efflux) [78]. Genetic defects of these systems lead to copper deficiencies known as Menke's and Wilson's disease [79]. The intracellular transport of copper has been shown to be accomplished by several copper-binding proteins, that have been termed copper chaperones [80]. Those proteins escort the potentially toxic copper ion to its final destination within the cell (**Fig. 6B**). For instance, CCS (copper chaperone for superoxide dismutase) binds Cu(I) and transfers the metal to apo-SOD [81]. Copper is also escorted into mitochondria by the copper chaperone COX17, and thus plays a crucial role for copper delivery to the respiration-related cytochrome-c oxidase [82]. Other copper chaperones have been reported as well [83]. The majority of yet identified copper chaperones adopts an 'open-faced β -sandwich' fold with a conserved MXCXXC metal-binding motif, which coordinates Cu(I) in a trigonal complex via the three sulfur ligands [84]. Due to the network of copper chaperones and copper-binding proteins, there is basically no free copper within the living cell [85].

The most common endogenous copper ligands in proteins are nitrogen (His, backbone amide), sulfur (Cys, Met) and oxygen (Asp, Glu, Tyr) [86,87]. The metal centers in copper proteins can be classified into three different types according to their spectroscopic properties. Proteins which bind type I copper are known as cupredoxins or blue copper proteins due to their extraordinarily intense absorption near 600 nm (charge transfer in the copper-cysteine bond) [88]. The corresponding EPR spectra of the oxidized state (Cu(II)) are characterized by unusually small hyperfine coupling constants ($A_{\parallel} < 95 \times 10^{-4} \text{ cm}^{-1}$) [88–90]. Type I copper proteins usually bind the metal ion with distorted tetrahedral geometry using two histidines, one cysteine and one methionine [89]. However, different arrangements are possible and led to subgroups of type I copper centers. Azurin and plastocyanin are the most prominent members of this class, and are involved in electron transfer processes [91]. The cupredoxin fold, being a Greek key β -barrel structure with a loop containing three copper ligands and an adjacent β -strand bearing the fourth ligand, is similar to that of the immunoglobulin domain (**Fig. 6C**) [89].

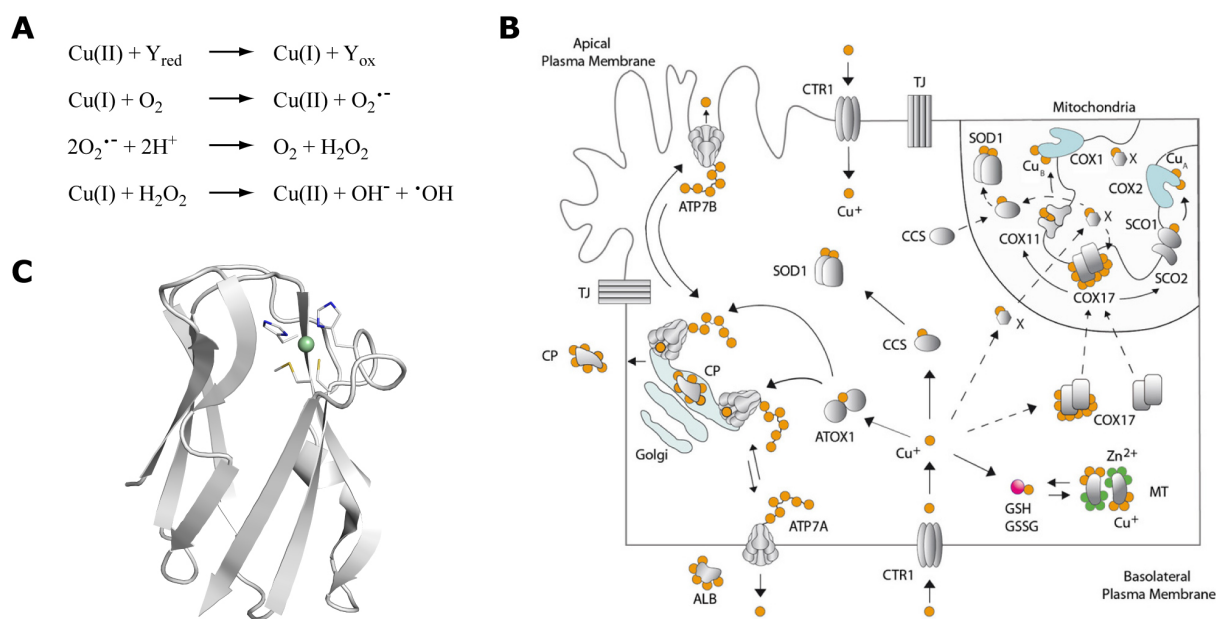


Fig. 6 Fates of copper in the living cell. (A) Production of reactive oxygen species through a copper-mediated Fenton-type reaction. Reductants (Y_{red}), such as ascorbic acid, are able to reduce Cu(II) to Cu(I) , which in turn induces the generation of the cell-toxic superoxide, hydrogen peroxide and hydroxide radicals. (B) Copper trafficking in an epithelial cell. The apical and the basolateral plasma membrane domains are separated by tight junctions (TJ). The transporter Ctr1 controls the influx of Cu(I) (orange), which is either stored in a complex with metallothioneins (MT), most probably mediated by glutathione (GSH), or escorted by specific copper chaperones to its final cellular destination. Accordingly, the chaperone CCS transfers Cu(I) to Cu/Zn-SOD , COX17 conveys Cu(I) to the Cu_A and Cu_B sites of mitochondrial COX (via SCO1/2 and COX11), and Atox1 escorts the metal ion to the P-type ATPases ATP7A/B. The major pool of copper ions is incorporated into ceruloplasmin (CP) in the Golgi apparatus. Ceruloplasmin, albumin (ALB) and transcuprein function to distribute copper within the organism. The figure is taken from [92]. (C) The cupredoxin fold. The X-ray structure of the blue copper protein plastocyanin is shown to illustrate the Greek key β -barrel structure, which is found in all cupredoxins and blue oxidases [93]. A similar arrangement is present in Cu/Zn-SOD . The copper coordination sphere of plastocyanin consists of $1 \times \text{Met}$, $1 \times \text{Cys}$ and $2 \times \text{His}$ residues. The copper ion is illustrated as a green sphere.

Type II copper sites exhibit normal extinction coefficients and large hyperfine couplings constants ($A_{\parallel} > 140 \times 10^{-4} \text{ cm}^{-1}$) in EPR spectra [89,90]. The biological functions of type II copper proteins are diverse, but chemical reactivity is the common trait of these proteins. Prominent examples include SOD, galactose oxidase, lysine oxidase and amine oxidases, such as dopamine β -monooxygenase [94]. The enzyme Cu/Zn-SOD catalyzes the dismutation of superoxide to oxygen and hydrogen peroxide, and is thus part of the oxidative stress response of the cell [95,96]. Cu/Zn-SOD coordinates copper in a tetrahedrally distorted square plane using four histidine residues [97,98]. One of these histidines bridges copper and zinc being 6.3 Å apart. Zinc is tetrahedrally coordinated by three histidines and an aspartic acid [97,98]. A water molecule is positioned 3 Å from the copper ion.

Type III copper centers are characterized by a strong absorption at 330 nm, by the absence of an EPR signal and a pair of copper atoms, which is antiferromagnetically coupled [89]. Such a type III pair of copper atoms can be found in hemocyanins – a class of multimeric proteins which function as oxygen transporters in arthropods and mollusks [99].

Furthermore, several copper proteins have been reported to feature multiple types of copper centers [100]. Such multinuclear copper sites are described for the blue oxidases ascorbate oxidase, nitrite reductase and ceruloplasmin. The copper enzyme ascorbate oxidase contains four copper ions per monomeric subunit and catalyzes the four-electron reduction of molecular oxygen to water [101]. Metal coordination is achieved via a type I copper site and a trinuclear copper cluster, which involves a type III copper pair and a type II copper [102]. Eight histidine residues are involved in the coordination of the trinuclear copper cluster [102]. The corresponding domains of ascorbate oxidase and the other blue oxidases adopt an eight-stranded Greek key β -barrel as in the case of the cupredoxins [103]. This conserved fold has led to the conclusion that the cupredoxins and the blue oxidases evolved from a common ancestor [89,104,105]. A Greek key β -barrel was originally discovered and described for SOD [98,106]. This structural motif, though distinct from that of cupredoxins, seems to be a common trait of most copper proteins.

The coordination spheres of selected copper proteins are illustrated in **Fig. 7A-C**. Besides these well-established copper proteins and enzymes, several other copper-binding proteins have been recently discovered. In particular, polypeptides which are associated with neurodegenerative disorders, such as Parkinson's disease and Alzheimer's disease, have been shown to specifically bind copper ions [107]. Prominent examples are the prion protein [108,109], α -synuclein [110,111], the amyloid precursor protein (APP) [112,113] and its proteolytic products, the amyloid β peptides ($A\beta_{1-40}/A\beta_{1-42}$) [114–116] (see Chapter 1.1.5).

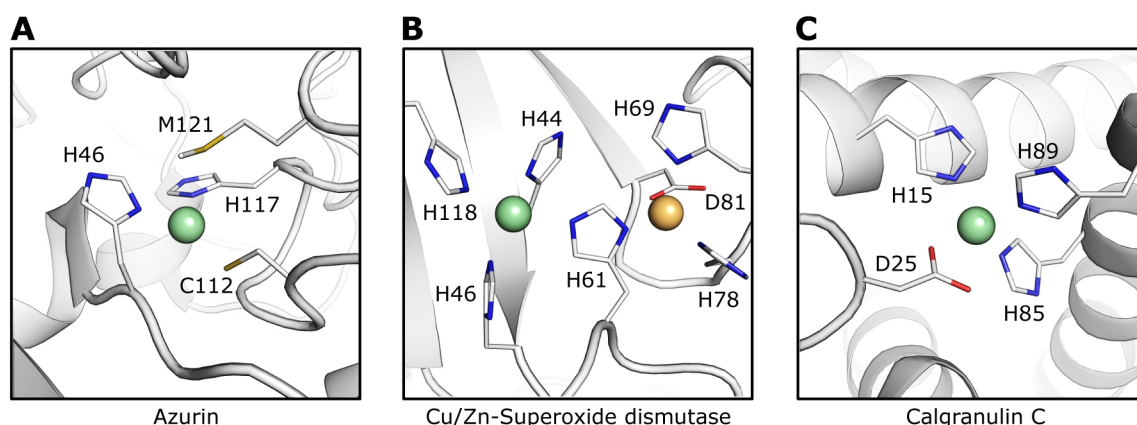


Fig. 7 Coordination spheres of selected copper proteins. Ligating residues are labeled. Copper and zinc ions are depicted as green and orange spheres, respectively. **(A)** Type I copper site of the cupredoxin azurin (PDB 4AZU) [117]. The distorted tetrahedral geometry is accomplished by 1×Cys, 1×Met and 2×His residues. **(B)** Type II copper center of Cu/Zn-SOD (PDB 1SDA) [118]. The copper ion is coordinated by four histidines in a distorted square plane. Zinc is ligated by 1×Asp and 3×His residues, with H61 bridging the two metal ions. **(C)** Type II copper site of calgranulin C (PDB 1ODDB) [119]. The tetrahedral coordination sphere comprises 1×Asp and 3×His residues.

1.1.4 Protein Degradation: The Proteasome

Proteins that fail to be reactivated by the chaperone network need to be cleared from the cell in order to prevent the toxic effects of those misfolded and aggregated protein states [16]. Proteolytic degradation is thus an essential element for protein homeostasis and cellular integrity [120]. The majority of soluble misfolded proteins is degraded via the ubiquitin-proteasome system (UPS) [121,122]. This proteolytic pathway involves the E1/E2/E3 ligase cascade, which stringently controls the polyubiquitination of target proteins [123]. This tagging of misfolded proteins assigns them for proteosomal degradation, which may require additional factors such as the p97/Cdc48-Ufd1-Npl4 complex [124,125]. The proteolytic 20S core particle (670 kDa) represents the enzymatic machinery of the 26S proteasome. Four heptameric rings assemble in an $\alpha_7\beta_7\beta_7\alpha_7$ fashion to form the barrel-shaped structure of the 20S proteasome complex (**Fig. 8**) [126–128]. The outer α_7 rings control the uptake of substrate proteins into the lumen of the complex via its N-terminal gates [129–131].

Furthermore, the α_7 rings interact with the polyubiquitin-recognizing 19S proteasome [132] and the immune-response-related 11S activator (**Fig. 8**) [133]. The catalytic chamber is established by the two inner β_7 rings and encompasses the active sites for proteolytic cleavage in the lumen of the barrel. The N-terminal threonine residues perform the nucleophilic attack for peptide bond hydrolysis [134,135]. The proteasome represents the central degradation

machinery for most proteins in the cell, and it is thus an attractive target for anti-cancer drug development [136,137].

The α -subunit and the β -subunit of the 20S proteasome can be produced separately by recombinant expression, with each of the subunits spontaneously forming a complex of two heptameric rings [138]. The mixture of both components results in the native $\alpha_7\beta_7\beta_7\alpha_7$ assembly. Rational mutant design has also succeeded to generate α_7 single-ring assemblies (180 kDa) as well as monomeric variants accessible for conventional solution-state NMR spectroscopy, focusing on the protein backbone [138]. The modular character is a prerequisite for selective isotopic labeling of subunits and enables NMR spectroscopic investigations with reduced signal overlap. The application of methyl-TROSY (transverse relaxation-optimized spectroscopy) techniques on $^{13}\text{C}^1\text{HD}_2$ -labeled isoleucine- $\delta 1$, leucine and valine methyl groups in otherwise fully-deuterated proteins has shown that large protein complexes such as the 20S proteasome can be investigated by solution-state NMR [131,138,139] (see Chapter 1.2.3). In particular, information on internal dynamics can be obtained by this approach, leading to a better understanding of biological mechanisms in large molecular machines.

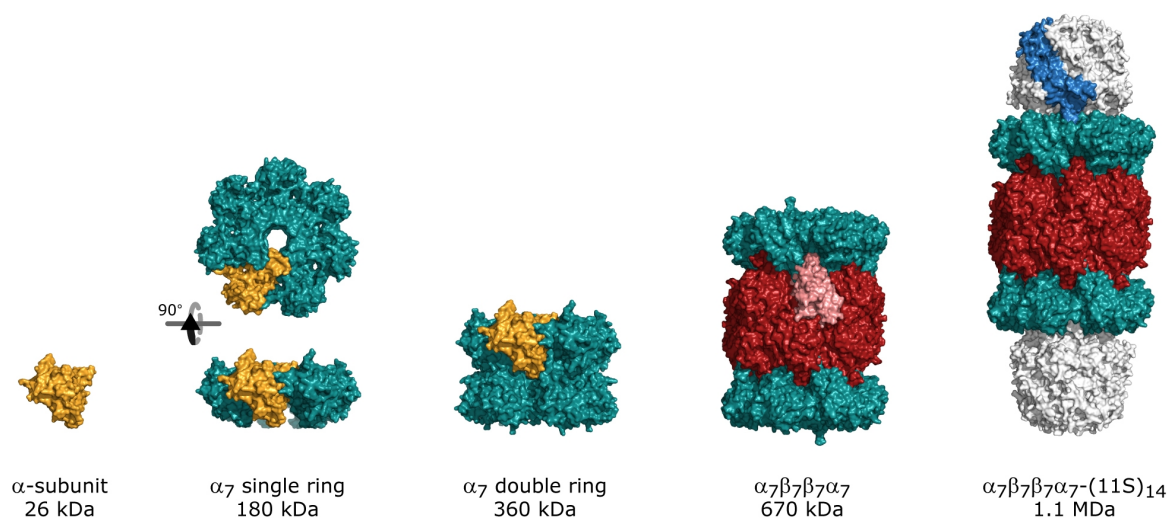


Fig. 8 The modular architecture of the proteasome. Different proteasome assemblies of *Thermoplasma acidophilum* and *Trypanosoma brucei* are illustrated with the molecular weight increasing from left to right (see bottom). The heptameric rings of the α -, β - and 11S-subunits are colored in green, red and white, respectively, whereas the single subunits are highlighted in orange, salmon and blue, respectively. The structures were visualized using PDB entries 1PMA [126] and 1FNT [133], respectively.

1.1.5 Amyloid Aggregation and the Alzheimer's Disease

Alzheimer's disease (AD) is the most common form of dementia resulting in the loss of memory and intellectual abilities [140]. The greatest risk factor for this neurodegenerative disorder is age [140]. Therefore, the incidence and prevalence of AD has increased dramatically in the last century due to the extended life span in modern countries [141].

Pathologically, AD is characterized by extracellular cortical amyloid deposits as well as by intraneuronal helical filaments, which are referred to as senile plaques and neurofibrillary tangles, respectively (**Fig. 9A**) [141]. The primary component of the amyloid plaques has been identified as a 39-42 residue polypeptide [142–144]. This so-called amyloid β peptide ($A\beta$) is a proteolytic fragment of the α -amyloid precursor protein (APP) [145,146] – an ubiquitously expressed 110-130 kDa transmembrane protein, whose biological function is still poorly understood [147–149]. However, there is growing evidence, that APP is involved in metal ion homeostasis of the cell [112,113,150]. According to that, APP possesses a cysteine-rich metal-binding domain within the extracellular N-terminal region (**Fig. 9B**) [150]. The copper binding site of APP, which is structurally similar to that of the copper chaperones Atx1 and CCS, exhibits a strong affinity for Cu(II) ($K_d \approx 10^{-8}$ M) and is capable of reducing the Cu(II) ion *in vitro* [112,113].

Proteolytic processing of APP is primarily accomplished by the endoproteases β - and γ -secretase, which generate the two major cleavage products $A\beta_{1-40}$ and $A\beta_{1-42}$, respectively (**Fig. 9B**) [151]. In a healthy individual, the shorter fragment $A\beta_{1-40}$ is the most abundant species (> 85%) [145], whereas the production of the elongated peptide $A\beta_{1-42}$ increases by a factor of 1.5-1.9 in patients with familial forms of AD [152]. The early-onset familial AD can be ascribed to mutations in the genes for APP (chromosome 21), presenilin-1 (chromosome 14) and presenilin-2 (chromosome 1) [153,154]. Those mutations result either in elevated levels of total $A\beta$ peptides or an increase of $A\beta_{1-42}$ only [155,156]. Moreover, patients with Down's syndrome (trisomy 21) develop features of dementia due to increased AD-like brain depositions of amyloid plaques [157]. The extra copy of chromosome 21 in these individuals is suggested to elevate the intraneuronal accumulation of $A\beta_{1-42}$ [157].

The formation of amyloid plaques is a characteristic hallmark of AD [143]. These deposits mainly consist of amyloid fibrils of self-assembled $A\beta$ peptides (**Fig. 9C**). $A\beta$ belongs to the class of intrinsically disordered proteins (IDPs), meaning that these polypeptides are

inherently devoid of any structural order in solution [158]. AD is thus referred to as a protein misfolding or conformational disease [159]. The hydrophobic nature of the A β peptide causes the self-association into soluble oligomers, protofibrils and finally mature filaments of 10-20 nm diameter [160]. A β fibrils adopt a so-called cross- β structure, in which extended β -sheets run perpendicular, and their interstrand hydrogen bonds parallel, to the fibril axis (**Fig. 9D**) [161]. The cross- β structure is a conserved structural motif of amyloid fibrils and yields a characteristic 4.8 Å reflection in X-ray fiber diffraction [160]. However, amyloid fibrils of A β_{1-40} occur in a wide range of morphologies differing in fibril width and helical twist [160,162,163]. This morphological heterogeneity hampered structural characterization of the fibrillar assemblies. The most detailed information on A β fibril structure has been provided by solid-state NMR spectroscopy. Studies on both A β_{1-40} and A β_{1-42} revealed two stacked parallel in-register β -sheets as the structural basis of the fibrillar assemblies (**Fig. 9D**) [164,165].

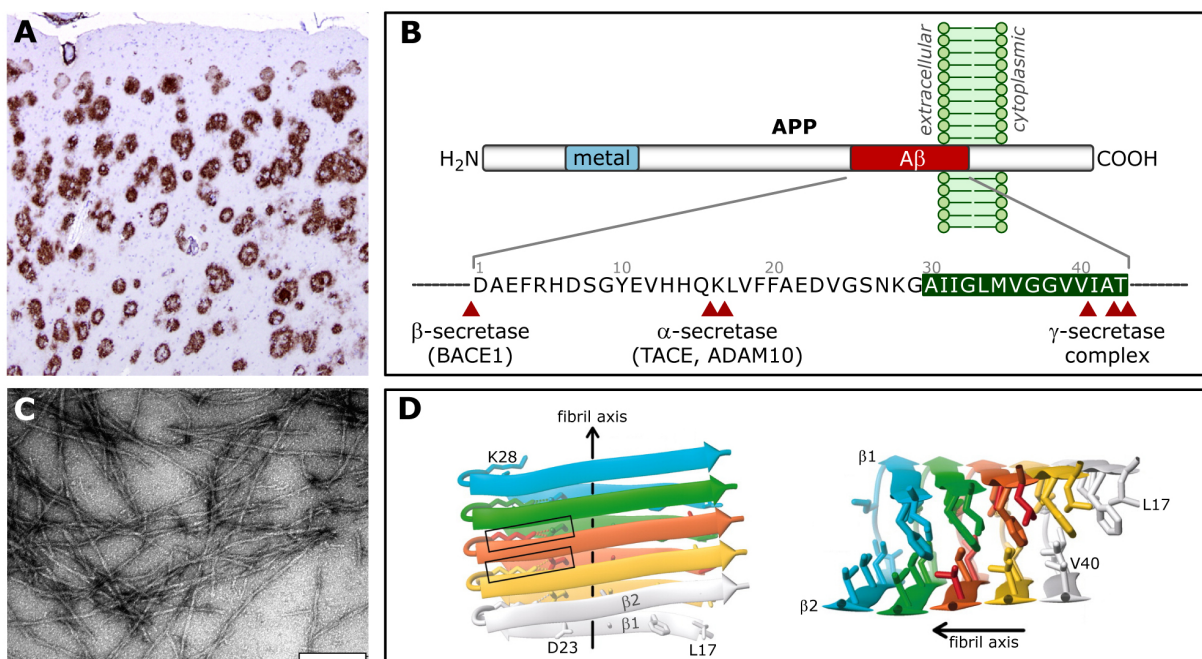


Fig. 9 Production, self-assembly and deposition of A β . (A) Senile amyloid plaques in the cerebral cortex of AD patients. The extracellular spherical lesions are immunostained against A β [166]. (B) Metabolic processing of the transmembrane protein APP by the endoproteases α -, β - and γ -secretase. Proteolytic recognition sites are indicated as red arrows. Processing by the β - and γ -secretases yields the fragment A β (red), which is a 39-42 residue peptide. The sequence of A β is enlarged with the corresponding residue numbers shown on top. The sequence encoding for the hydrophobic transmembrane region of A β is highlighted in green. The metal-binding domain of APP is indicated in blue. (C) Mature amyloid fibrils of A β_{1-40} as seen by electron microscopy (negative stain). The 0.2 μ m scale bar is shown on the lower right. (D) Structural model of A β_{1-42} fibrils illustrating the cross- β motif [165]. The peptide forms two β -strands that stack to each other in a 'steric-zipper' fashion. Intermolecular assembly of these β -strands yields two extended β -sheets. The orientation of the fibril axis (arrow) converges with that of the interstrand hydrogen bonds. The boxes highlight intermolecular salt-bridges between D23 and K28. The figure is adapted from [165].

Fibril formation is controlled by two kinetic parameters: the nucleation rate and the elongation rate [167,168]. The nucleation process is the rate-limiting step in amyloidogenesis [167–169]. Once the amyloid nucleus has formed, fibril elongation proceeds rapidly. Soluble oligomers may be considered as on-pathway aggregation states that drive the nucleation process [170,171]. However, these oligomeric assemblies may also be kinetically trapped similar to misfolded states in protein folding (see Chapter 1.1.1) [1]. It has been shown that oligomeric states of A β , likewise rich in β -strand structure, represent the actual cell-toxic species, rather than the insoluble amyloid deposits [171]. Soluble A β oligomers were found in AD brains, and their abundance correlates well with loss of synapses and cognitive perception [172,173]. The deleterious effects of oligomeric A β species have been potentially ascribed to pore formation in biological membranes, caspase activation and elevated oxidative stress [174–176]. Indeed, A β has been identified as a metalloprotein specifically binding Cu(II) in the N-terminal region [177]. NMR and EPR studies implicated a square planar 3N1O configuration via three histidine residues (H6, H13, H14) and a yet not determined oxygen ligand [177,178]. Cu(II)-A β has been shown to generate ROS *in vitro* [179,180]. Increased levels of lipid peroxidation as well as DNA and protein oxidation products in AD brains point towards a significant role of oxidative stress in AD pathology [76,181]. Furthermore, the production of free radicals most likely provokes oxidation of A β residues M35 and Y10 [76,181]. Dityrosine-bridged A β oligomers were shown to be highly neurotoxic, whereas oligomers of the variant A β -Y10A were devoid of cell-toxic effects [182]. However, the causes of neuronal cell death in AD brains still remain unclear.

Interestingly, expression of the sHSP α B has been shown to be up-regulated in brains of patients suffering from neurodegenerative disorders such as AD [183–185]. Despite its protective role as a member of the protein quality control machinery, α B has been found to be co-aggregated in AD plaques [183,186]. The relation between α B and A β was further established by the observation of frequent equatorial supramolecular cataracts in lenses of AD patients [187]. Experimental data provided evidence, that α B interacts transiently with the hydrophobic sequence L₁₇FFAV₂₁ of monomeric A β ₁₋₄₀, and that α B is capable of oxidizing residue M35 [49]. Moreover, the chaperone was shown to attach to the fibrillar forms of A β ₁₋₄₀ and A β ₁₋₄₂ [188]. The intervention of α B impedes A β fibril formation *in vitro* [189–191], mainly by inhibition of fibril elongation [188], but concomitantly increases the cytotoxicity of the amyloid peptide in isolated rat neurons [190]. Therefore, it has been

suggested that the chaperoning action of α B provokes the accumulation of non-fibrillar aggregation intermediates, which exhibit neurotoxic properties such as pore formation and/or redox reactivity [176,190,192]. However, other results have demonstrated that the α B-mediated inhibition of A β fibril formation is accompanied by a decline of the toxicity towards human brain pericytes [189]. Due to the conflicting results, it is far from being clear, how the elevated expression of α B in response to cellular stress and its co-localization in amyloid deposits affects the progression of AD. So far, atomic resolution details concerning the interaction between α B and A β are rare. Here, NMR spectroscopy was employed to further define the interaction sites of both proteins and to understand the effects of α B on the aggregation properties of A β ₁₋₄₀.

1.2 Nuclear Magnetic Resonance Spectroscopy

This chapter introduces selected concepts of modern nuclear magnetic resonance (NMR) spectroscopy, in particular with respect to relaxation properties and the investigation of biomolecules with high molecular weights. However, for a comprehensive understanding of the physical principles of NMR, the reader is referred to the literature [193–196].

1.2.1 Nuclear Spins

Nuclei may possess an intrinsic angular momentum \vec{I} , known as spin, depending on their spin quantum number I (with $I = 0, 1/2, 1, 3/2, 2, \dots$). Relevant nuclides for biological NMR spectroscopy are ^1H , ^{13}C , ^{15}N , ^{19}F , ^{31}P ('spin- $1/2$ ' nuclei) and ^2H , ^{14}N ('spin-1' nuclei), respectively. The magnitude of the spin angular momentum is quantized according to

$$|\vec{I}| = \hbar \sqrt{I(I+1)}, \quad (1)$$

with $\hbar = h/2\pi$ and h being the Planck constant. The spin angular momentum of a spin- I nucleus has $2I+1$ projections onto an arbitrarily chosen axis. Accordingly, the z-component of \vec{I} , denoted I_z , is quantized:

$$I_z = m\hbar. \quad (2)$$

The magnetic quantum number m has values of $I, I-1, I-2, \dots, -I$. The spin angular momentum of a spin- $1/2$ nucleus (e.g. ^1H , ^{13}C) thus has two permitted orientations, that is

$I_z = \pm 1/2\hbar$. The two states are usually referred to as the α - and β -state, respectively. However, in the absence of an external magnetic field, these states are degenerate, and thus \vec{I} has no preferred directions.

The magnetic moment $\vec{\mu}$ of a nucleus directly arises from its spin angular momentum:

$$\vec{\mu} = \gamma \vec{I}, \quad (3)$$

where γ denotes a nucleus-specific proportionality constant, known as the gyromagnetic ratio. Tab. 1 lists some of the NMR relevant nuclides and their properties. As can be seen, ^1H has the largest gyromagnetic ratio and high natural abundance.

Tab. 1 Selected nuclides and their NMR-relevant properties.

Nuclide	I	γ ($10^7 \text{ T}^{-1} \text{ s}^{-1}$)	Natural abundance (%)
^1H	1/2	26.75	99.985
^2H	1	4.11	0.015
^{13}C	1/2	6.73	1.108
^{14}N	1	1.93	99.63
^{15}N	1/2	-2.71	0.37
^{17}O	5/2	-3.63	0.037
^{19}F	1/2	25.18	100.0
^{29}Si	1/2	-5.32	4.7
^{31}P	1/2	10.84	100.0

In an external magnetic field \vec{B} , which by definition is oriented along the z-axis ($\vec{B} = (0; 0; B_0)$), the degeneracy of the possible orientations of $\vec{\mu}$ is removed. This effect is also known as the Zeeman-splitting. The energy E of the interaction between the magnetic moment μ_z (projection of $\vec{\mu}$ onto \vec{B}) and the magnetic field \vec{B} is given by:

$$E = -\mu_z B_0 = -m \hbar \gamma B_0. \quad (4)$$

Due to the selection rule for NMR ($\Delta m = \pm 1$), the resulting energy difference between the two Zeeman states (for spin- $1/2$ nuclei) amounts to

$$\Delta E = h \nu = \hbar \omega = \hbar \gamma B_0. \quad (5)$$

The Boltzmann distribution is given by:

$$\frac{n_\beta}{n_\alpha} = e^{-\Delta E / kT} = e^{-\hbar \gamma B_0 / kT}, \quad (6)$$

where n_α and n_β are the populations of the ground and the excited state, respectively, k denotes the Boltzmann constant and T is the temperature. It can be deduced, that the population difference between the α - and the β -state for ^1H is on the order of only 10^{-5} ($B_0 = 11.7 \text{ T}$, $T = 300 \text{ K}$). In contrast to spectroscopic techniques that focus on electronic transitions, NMR is thus a rather insensitive method. This sensitivity problem has been faced by the utilization of high magnetic field strengths B_0 and the investigation of high- γ nuclei, in order to maximize the Zeeman-splitting between the ground and excited spin states. The signal-to-noise ratio S/N of NMR experiments relates to (amongst others):

$$S / N \propto n \gamma_e \sqrt{\gamma_d^3 B_0^3 N_s}, \quad (7)$$

where n denotes the number of nuclear spins being observed, γ_e and γ_d are the gyromagnetic ratios of the nuclei being excited and detected, respectively, and N_s represents the number of accumulated spectra. It is evident from Eq. 7, that the excitation and detection of ^1H spins is desirable for optimal S/N in NMR spectra, since ^1H has the largest gyromagnetic ratio. For example, since $\gamma_{^1\text{H}}/\gamma_{^{15}\text{N}} \approx 10$, the detection of ^1H *versus* ^{15}N resonances theoretically yields a sensitivity improvement of ~ 32 , which in turn reduces the required experimental time by a factor of ~ 1000 .

Based on the resonance condition (Eq. 5), transitions between spin states can be achieved by appropriate radio-frequency (rf) pulses according to

$$\omega_{rf} = \omega = \Delta E / \hbar = \gamma B_0, \quad (8)$$

with ω_{rf} and ω representing the pulse radio-frequency and the nuclear resonance (Larmor) frequency, respectively. As derived elsewhere [194], rf pulses are thus capable of changing spin populations as well as generating coherences. This circumstance is extensively used in NMR experiments, in which a well-designed sequence of pulses and delays manipulates spin states in a controlled fashion in order to yield structural or dynamic information.

A characteristic property of nuclear spins is the so-called chemical shift δ (in units ppm), which is defined as the Larmor frequency relative to the resonance frequency of a reference spin according to

$$\delta = \frac{\sigma_{ref} - \sigma}{1 - \sigma_{ref}} \times 10^6 \approx (\sigma_{ref} - \sigma) \times 10^6. \quad (9)$$

The average isotropic shielding constant σ renders the resonance frequency of a nuclear spin dependent on its electronic environment in the molecule:

$$\omega = -\gamma B_0(1 - \sigma). \quad (10)$$

Due to this unique property, NMR has become the most powerful tool for the elucidation of molecular structures in organic chemistry. As an orientation-dependent constant, σ is described by its spatial components σ_{11} , σ_{22} and σ_{33} . The chemical shift anisotropy (CSA) is defined as

$$\Delta\sigma = \sigma_{11} - (\sigma_{22} + \sigma_{33})/2 \quad (11)$$

and the asymmetry is given by

$$\eta = \frac{3(\sigma_{22} - \sigma_{33})}{2\Delta\sigma}. \quad (12)$$

Hence, it can be deduced, that fast rotational diffusion of a molecule in solution averages out the orientation-dependent components, which finally yields exclusively the isotropic chemical shift. This, however, does not apply to rigid solids, in which molecular reorientation is absent (see Chapter 1.2.4).

1.2.2 Relaxation of Excited Spin States

As aforementioned, the application of rf pulses disturbs the equilibrium of a spin system – it may alter populations and/or generate coherences. For example, a π pulse inverts the population distribution, whereas a $\pi/2$ pulse equalizes the populations and creates coherences. Two types of relaxation processes may be differentiated: i) spin-lattice (or longitudinal) relaxation, which concerns the recovery of spin populations according to the Boltzmann distribution, and ii) spin-spin (or transverse) relaxation, which describes the decay of spin coherences. The longitudinal and transverse relaxation rates are termed R_1 and R_2 , respectively. The corresponding time constants are T_1 and T_2 , respectively.

The excited spin states are restored to equilibrium by fluctuations of local magnetic fields. Random molecular motions cause the nuclear spins to experience time-dependent local magnetic fields potentially providing frequency components appropriate to fulfill the resonance condition ($\omega \approx \gamma B_0$) and to stimulate energy emission. Such molecular motions include overall rotational reorientation, vibrations, internal dynamics of atoms or molecular

groups, and motions of paramagnetic centers. The probability of a motional mode to provide a particular frequency is described by the spectral density function $j(\omega)$, for example, for the isotropic rotational reorientation of a molecule in solution:

$$j(\omega) = d_{00} \cdot J(\omega) = d_{00} \cdot \frac{2}{5} \frac{\tau_c}{1 + \omega^2 \tau_c^2}, \quad (13)$$

with d_{00} being a term including all relevant physical constants for the considered interaction (see Eq. 17). The parameter τ_c is termed the correlation time of the respective fluctuation of local fields. In case of overall reorientation, τ_c thus represents the rotational correlation time and is the average time required for a particle to rotate by an angle of about one radian. For a globular protein, τ_c is given by the Stoke's law:

$$\tau_c = \frac{4\pi\eta R_h^3}{3kT} \quad \text{with } R_h \approx \sqrt[3]{\frac{3M_w}{4\pi\rho N_A}} + R_{hyd}, \quad (14)$$

where η is the dynamic viscosity of the solvent at temperature T , ρ is the average density for proteins (1.37 g cm^{-3}), R_{hyd} is the hydration radius (typically $1.6\text{-}3.2 \text{ \AA}$), R_h and M_w are the hydrodynamic radius and the molecular weight of the protein and N_A is the Avogadro's number. The following approximation applies to proteins in water: $\tau_c [\text{ns}] \approx 0.6 M_w [\text{kDa}]$. Thus, typical rotational correlation times of mid-sized proteins in aqueous solution at room temperature are on the order of 5-20 ns.

For nuclear spins with $I > 1/2$, e.g. ^2H , ^{14}N , quadrupolar interactions are the major source of relaxation, whereas relaxation processes of spin- $1/2$ nuclei in large biomolecules are mainly determined by dipole-dipole interactions and chemical shift anisotropy.

Two dipolar-coupled nuclei I and S experience correlated time-dependent magnetic fields and thus relax in a concerted fashion. The contribution of spin S to the relaxation of spin I via dipole-dipole interactions can be described by a longitudinal relaxation rate

$$R_1^{DD} = (d_{00}/4) \{J(\omega_I - \omega_S) + 3J(\omega_I) + 6J(\omega_I + \omega_S)\} \quad (15)$$

and a transverse relaxation rate

$$R_2^{DD} = (d_{00}/8) \{4J(0) + J(\omega_I - \omega_S) + 3J(\omega_I) + 6J(\omega_S) + 6J(\omega_I + \omega_S)\} \quad (16)$$

(given for single quantum coherence I^+). The constant d_{00} is given by

$$d_{00} = \frac{\mu_0^2 \hbar^2 \gamma_I^2 \gamma_S^2}{(4\pi)^2 r_{IS}^6} = b_{IS}^2 \quad \text{with } b_{IS} = -\frac{\mu_0}{4\pi} \frac{\hbar \gamma_I \gamma_S}{r_{IS}^3}, \quad (17)$$

with μ_0 being the magnetic constant, γ_I and γ_S being the gyromagnetic ratios of the dipolar-coupled nuclei I and S, and r_{IS} denoting their internuclear distance. $J(0)$ is the spectral density at zero frequency. The constant b_{IS} is known as the dipole-dipole coupling constant. As can be seen, the dipolar interaction is strongly dependent on the internuclear distance. Moreover, the magnitude of the through-space interaction increases with high gyromagnetic ratios.

Another important source of relaxation is the chemical shift anisotropy, which describes the orientation dependence of chemical shifts with respect to the external magnetic field. The contribution of CSA to the longitudinal and transverse relaxation rates are given by

$$R_{1I}^{CSA} = d_{00} J(\omega_I) \quad (18)$$

$$R_{2I}^{CSA} = (d_{00}/6) \{4J(0) + 3J(\omega_I)\}, \quad (19)$$

with

$$d_{00} = (\Delta\sigma \gamma_I B_0)^2 / 3 = \Delta\sigma^2 \omega_I^2 / 3. \quad (20)$$

$\Delta\sigma$ represents the generalized CSA constant, which is determined by the anisotropy and the asymmetry of the considered chemical bonds. As can be seen, CSA-mediated relaxation scales quadratically with the external magnetic field strength B_0 .

Relaxation of nuclear spins may also be affected by paramagnetic centers, such as Cu(II) and Mn(II) ions in metalloproteins. The effect has been termed paramagnetic relaxation enhancement (PRE) and is induced by the strong magnetic moment of the unpaired electron of the paramagnetic species. The PRE rate Γ is proportional to the square of the gyromagnetic ratio γ_I of the NMR-observed nucleus according to

$$\Gamma_1 = \frac{2}{5} \left(\frac{\mu_0}{4\pi} \right)^2 \gamma_I^2 g^2 \mu_B^2 s(s+1) J_{SB}(\omega_I) \quad (\text{longitudinal relaxation}) \quad (21)$$

and

$$\Gamma_2 = \frac{1}{15} \left(\frac{\mu_0}{4\pi} \right)^2 \gamma_I^2 g^2 \mu_B^2 s(s+1) \{4J_{SB}(0) + 3J_{SB}(\omega_I)\} \quad (\text{transverse relaxation}), \quad (22)$$

where s is the electron spin quantum number, g is the electron g-factor and μ_B denotes the magnetic moment of the unpaired electron. The generalized spectral density function $J_{SB}(\omega_I)$ is given by:

$$J_{SB}(\omega_I) = r^{-6} \frac{\tau_c}{1 + \omega^2 \tau_c^2}, \quad (23)$$

with r being the electron-nucleus distance. For example, efficient relaxation of ^1H resonances occurs in a sphere of approximately 12 Å radius around a Cu(II) center. This sphere contracts to approximately 6 Å employing ^{13}C -detection. Low γ -nuclei are thus less susceptible to PRE and their observation by NMR may be exploited to facilitate the identification of ligating residues in paramagnetic metalloproteins [197,198].

1.2.3 NMR Investigations of Large Biomolecules

One way to access large biomolecules is simply to shift their rotational correlation times to NMR-suitable regimes, which may be achieved by either increasing the temperature [138] or by decreasing the viscosity of the dispersant (see Eq. 14). Encapsulating a protein in a reversed micelle, which itself is dissolved in a low viscosity fluid such as propane, has been shown to yield high-resolution NMR spectra [199,200]. Obviously, the applicability of these approaches is limited. Thermally instable proteins will not endure elevated temperatures. And even high temperatures on the order of 60 °C are not able to compensate the very slow tumbling of common protein complexes.

The transverse relaxation rate R_2^{DD} arising from dipolar interactions scales with the square of the gyromagnetic ratios of the coupled spins (see Eq. 17). Considering the fact that $\gamma_{1\text{H}}/\gamma_{2\text{H}} \approx 6.5$, perdeuteration of proteins drastically weakens the dipolar interactions network, and thus decreases the transverse relaxation of nearby nuclei. Extensive deuteration is routinely employed in solution-state NMR investigations of large protein systems [201,202].

The local fields that are generated by dipolar-coupled spins (dipole-dipole relaxation) and by the surrounding electrons (CSA relaxation) are similarly modulated by the overall molecular tumbling. The two relaxation mechanisms are therefore said to be cross-correlated. The relaxation interference may result in mutual cancellation of dipole-dipole and CSA relaxation. This effect has been exploited in TROSY (Transverse Relaxation Optimized Spectroscopy) techniques in order to select for long-lived coherences giving rise to narrow linewidths [203].

The approach takes advantage of the dipole-dipole/CSA cross-correlated relaxation of heteronuclear, J -coupled two-spin systems, e.g. the ^1H - ^{15}N amide of a protein backbone. The constructive and destructive interference of the two relaxation mechanisms yields multiplet components with different relaxation properties [203]. An appropriate pulse sequence design ensures the predominant use of the slowly decaying coherences. The broadening/narrowing effect can be influenced by the choice of the external magnetic field strength, since CSA relaxation is proportional to the square of B_0 (see Eq. 20).

The development of TROSY-type techniques thus enabled the characterization of supramolecular protein assemblies like GroEL-GroES [204], p53/HSP90 [205], ClpP [206,207], L7/L12 of the ribosome [208], the 13 MDa viral capsid protein [209], and the 20S proteasome [131,138]. However, even at very high magnetic fields, low molecular tumbling rates limit the applicability of solution-state NMR in the investigation of these systems. In particular backbone assignments become increasingly difficult for macromolecular complexes beyond 200 kDa. Typically, methyl-based experiments are performed for these very large systems, as contributions from overall tumbling to the $J(0)$ spectral density are reduced to 1/9 due to the fast three-fold rotation of the methyl group [210]. In those studies, resonance assignments are merely achieved by extensive mutant screening [138].

In summary, solution-state NMR is still constricted in studying supramolecular complexes due to its dependence on rotational diffusion rates. A promising approach to overcome these size-limitations is the application of solid-state NMR, since intrinsic molecular tumbling is absent in rigid solids. As described in the next chapter, solid-state NMR is therefore a powerful tool for the structural investigation of, amongst others, large protein assemblies.

1.2.4 Solid-State NMR

1.2.4.1 Magic-Angle-Spinning (MAS)

The Hamiltonian for the dipolar interaction between two spins I and S is given by

$$\hat{H}_{IS}^{DD} = \frac{\mu_0 \hbar}{4\pi} \frac{\gamma_I \gamma_S}{r_{IS}^3} \left(\hat{I} \cdot \hat{S} - \frac{3(\hat{I} \cdot \vec{r}_{IS})(\hat{S} \cdot \vec{r}_{IS})}{r_{IS}^2} \right). \quad (24)$$

\hat{I} and \hat{S} represent the spin operators for spins I and S, respectively. In high magnetic fields, the secular part of the Hamiltonian for a homonuclear spin system can be expressed as

$$\hat{H}_{IS}^{DD} = (3\cos^2 \theta_{IS} - 1) \cdot \frac{1}{2} b_{IS} (3\hat{I}_z \hat{S}_z - \hat{I} \hat{S}). \quad (25)$$

For heteronuclear spin pairs, this simplifies to:

$$\hat{H}_{IS}^{DD} = (3\cos^2 \theta_{IS} - 1) b_{IS} \hat{I}_z \hat{S}_z. \quad (26)$$

In both equations, θ_{IS} describes the angle between internuclear vector \vec{e}_{IS} (joining the centres of the two nuclei) and the external magnetic field (represented by vector \vec{e}_z) according to:

$$\cos \theta_{IS} = \vec{e}_{IS} \cdot \vec{e}_z. \quad (27)$$

Therefore, the dipole-dipole interaction between two spins is inherently orientation-dependent, since the vector \vec{e}_{IS} changes its direction as the molecule rotates. However, the rapid and stochastic character of molecular tumbling in an isotropic liquid causes anisotropic interactions such as dipole-dipole interactions and CSA to average efficiently, as can be evaluated from:

$$\int_0^\pi d\theta_{IS} \sin \theta_{IS} (3\cos^2 \theta_{IS} - 1) = 0. \quad (28)$$

By contrast, anisotropic interactions do not vanish in rigid solids due to the absence of rotational reorientation. The spatial term $(3\cos^2 \theta_{IS} - 1)$ is equal to zero at the so-called *magic-angle* θ_M :

$$\theta_M = \arctan \sqrt{2} \cong 54.74^\circ. \quad (29)$$

In solid-state NMR, sampling of all possible orientations can be artificially achieved by fast rotation around an axis inclined at θ_M . This approach was thus coined magic-angle-spinning (MAS) [211], and it removes most of the anisotropic interactions in a powder sample, provided that the spinning frequency is fast relative to the respective interaction. Typical spinning frequencies in MAS solid-state NMR are on the order of 10 to 60 kHz, which efficiently average dipole-dipole interactions of low- γ nuclei (^{13}C , ^{15}N , etc.) as well as CSA [212]. Due to the high gyromagnetic ratio, ^1H spins are a source of strong dipolar couplings ($b_{\text{HH}} \approx 130 \text{ kHz}$ at $r_{\text{HH}} = 1 \text{ \AA}$, see Eq. 17), which can not be easily removed by MAS. Conventional MAS solid-state NMR spectroscopy thus relies on the observation of low- γ nuclei, in particular ^{13}C , and strong ^1H decoupling. Such heteronuclear decoupling sequences

are accompanied by substantial sample heating, which may compromise the integrity of biological materials.

1.2.4.2 Cross-Polarization

The effect of MAS is crucial to obtain well-resolved solid-state NMR spectra. However, the removal of anisotropic interactions may be considered as a loss of structural information, and may thus be reversed in a controlled manner. Dipole-dipole interactions, e.g., can be reintroduced by appropriate dipolar recoupling techniques such as Cross-Polarization (CP) [213], Radio Frequency Driven Recoupling (RFDR) [214], Rotational Echo Double Resonance (REDOR) [215] and Rotational Resonance (R^2) [216]. These methods are routinely used in solid-state NMR for the transfer of magnetization among nuclei, which is essential for multidimensional correlation spectroscopy [217]. Hence, magnetization transfers in the solid-state commonly rely on dipolar (through-space) interactions between the respective nuclei of interest, whereas in solution-state NMR, scalar (through-bond) couplings (J -couplings) are mainly used by employing the so-called Insensitive Nuclei Enhanced by Polarization Transfer (INEPT) step [218].

One of the most important elements in solid-state NMR pulse sequences is the CP block, which achieves dipolar recoupling by adequate rf irradiation on two channels according to the MAS-adapted Hartmann-Hahn matching condition [219]:

$$\Delta\omega_{rf} = \omega_I - \omega_S = \gamma_I B_{1,I} - \gamma_S B_{1,S} = n \cdot \omega_R \quad \text{with } n = \dots, -2, -1, +1, +2, \dots \quad (30)$$

where ω_I and ω_S are the effective spin-lock fields on the two channels I and S, respectively, and ω_R equals the spinning frequency. The approach ensures that the energy gap between the respective spin states of spins I and S in the doubly rotating frame are equalized. The heteronuclear dipole-dipole Hamiltonian acts in such a way that the net energy of the spin system is conserved during the contact pulse. Under these circumstances, transitions of spin I are compensated by opposite transitions of spin S. The CP approach is usually employed subsequent to the excitation of abundant high- γ nuclei (^1H) in order to transfer the magnetization to low- γ nuclei (^{13}C , ^{15}N). Besides this sensitivity improvement, the initial ^1H excitation allows for faster data accumulation due to the shorter spin-lattice relaxation times of ^1H compared to heteronuclei such as ^{13}C .

1.2.4.3 Perdeuteration and Proton-Detection

Various homonuclear mixing schemes, like PDS (Proton-Driven Spin Diffusion) [220,221], DARR (Dipolar Assisted Resonance Recoupling) [222], DREAM (Dipolar Recoupling Enhancement through Amplitude Modulation) [223] or PAIN (Proton Assisted Insensitive Nuclei Cross Polarization) [224] have been developed in order to obtain distance restraints for structure determination. However, the use of ^1H chemical shifts, in particular by direct ^1H -detection, is hampered by the strong dipolar interactions. Although high MAS rates have been used for direct ^1H -detection, the achievable ^1H linewidths in fully protonated proteins were still on the order of 400 Hz at 40 kHz MAS [225]. By contrast, reducing the proton density by deuteration and a subsequent back-exchange of all amide protons yielded ^1H linewidths on the order of 150 Hz [226]. This approach enabled triple resonance experiments and protein structure determination at higher spinning frequencies [227]. Moreover, extending the deuteration strategy to the exchangeable sites yielded ^1H linewidths of 15-24 Hz at moderate MAS rates [228]. Further studies provided evidence that protonation levels of ~20-40% at labile sites in otherwise fully deuterated proteins give the best compromise between resolution and sensitivity [229].

An apparent drawback of sparse protonation is the fact that longitudinal relaxation rates R_1 of ^1H are significantly reduced, which requires prolonged recycle delays and typically results in loss of sensitivity. Paramagnetic agents such as Cu(II)-EDTA have been successfully used to mediate PRE and consequently to speed up data acquisition in solid-state NMR [230]. Therefore, the PRE approach enabled multidimensional solution-state-like NMR experiments [231].

Nonetheless, the application of MAS solid-state NMR spectroscopy in all its diversity is limited to rigid and immobilized solids that are devoid of any rotational mobility. Hence, crystallization or precipitation procedures are required for solid-state NMR investigations of biological macromolecules. Sample preparation and homogeneity are thus commonly considered the bottle neck en-route to well-resolved spectra, that are indispensable for structural investigations.

2 Materials and Methods

2.1 Solutions and Media

If not indicated otherwise, chemicals and supplementary materials were purchased from Bruker Biosciences (Karlsruhe, Germany), Fluka (Neu-Ulm, Germany), Merck (Darmstadt, Germany), Roth (Karlsruhe, Germany) and Sigma-Aldrich (Deisenhofen, Germany).

2.1.1 Buffer Solutions

Tab. 2 summarizes the employed buffer solutions and their respective composition.

Tab. 2 Buffer solutions used in this work.

Buffer	Application	Composition
TAE buffer	Agarose gel electrophoresis	40 mM Tris-acetate, pH 8.0, 0.1 mM Na ₂ EDTA
Lysis buffer	Cell lysis	20 mM Tris-HCl, pH 8.5, 2 mM MgCl ₂ , 1x Complete Protease Inhibitor Cocktail (Roche), 3000 units/mL Benzonase [®] Nuclease (Novagen)
Buffer A	Anion exchange chromatography	20 mM Tris-HCl, pH 8.5, 1 mM EDTA
Buffer B	Anion exchange chromatography	20 mM Tris-HCl, pH 8.5, 1 mM EDTA, 1 M NaCl
SEC buffer	Size exclusion chromatography	20 mM Tris-HCl, pH 7.5, 1 mM EDTA, 50 mM NaCl
PBS	Standard sample buffer	50 mM NaH ₂ PO ₄ /Na ₂ HPO ₄ , pH 7.5, 50 mM NaCl
TBS	Sample buffer for EM	50 mM Tris-HCl, pH 7.5, 50 mM NaCl

2.1.2 Cell Growth Media

LB (Luria-Bertani) medium was prepared as described by Sambrook *et al.*. LB agar was prepared using LB agar powder (Merck). LB media and agar were subsequently autoclaved. LB agar plates were prepared by adding the antibiotic Kanamycin (AppliChem) to a final concentration of 25 µg/mL and pouring 25 mL of the mixture onto sterile Petri dishes (VWR). After cooling, the plates were flipped and stored at 4 °C.

Isotopic labeling of proteins was accomplished by growing cells in 2xM9 minimal medium. The composition was as follows (in the order of adding to water): 86 µM EDTA, 16 µM FeSO₄, 1.8 µM ZnCl₂, 0.3 µM CuSO₄, 2 mM MgCl₂, 0.3 mM CaCl₂, 100 mM Na₂HPO₄/KH₂PO₄ (pH 7.2), 20 mM NaCl, 2-4 g/L glucose, 3 mg/L Thiamin-HCl

(AppliChem), 3 mg/L Biotin (AppliChem), 0.5 g/L NH_4Cl , 25 mg/L Kanamycin. All stock solutions were autoclaved, except the vitamins, the antibiotic, the glucose and the NH_4Cl , which were sterile-filtrated. The content of glucose was varied depending on the length of expression and the protease-susceptibility of the construct in order to prevent starving of cells. In case of fully-protonated ^{13}C , ^{15}N -labeled protein, the M9 minimal medium contained ^{13}C -glucose and $^{15}\text{NH}_4\text{Cl}$. Protein deuteration was achieved by providing fully deuterated ^2H , ^{13}C -glucose and 99.9% D_2O . Accordingly, all additives were dissolved in D_2O .

2.2 Microbiological and Molecular Biological Methods

2.2.1 Polymerase Chain-Reaction (PCR)

Amplification of DNA fragments for cloning purposes was achieved using the PCR technique performed on the C1000 ThermalCycler (BioRad). Primer DNA was purchased from Biotex (Berlin-Buch). The polymerase KOD (Novagen) was applied according to the manufacturer's instructions. The vectors pET-30-Ek/LIC- αB (kindly provided by Dr. Katja Fölber) and mod.pET-30- αB served as templates for the reaction. Used primers are summarized in the Appendix (Tab. 5). The PCR program started with an initial denaturation period (5 min, 94 °C) and finished with a final elongation period (7 min, 72 °C). In between, 40 cycles of denaturation (30 s, 94 °C), annealing (30 s, 52/62 °C) and elongation periods (2 min, 72 °C) were run. The annealing temperature in the first 3 cycles was 52 °C and increased thereafter to 62 °C. The PCR product was visualized and purified by agarose gel-electrophoresis.

2.2.2 Agarose Gel-Electrophoresis

Separation of target DNA from various reaction mixtures was accomplished by agarose gel-electrophoresis. Percentage of agarose (0.9-1.5% w/v) was depending on the molecular size of target DNA. 10 μL of sample were mixed with 2 μL of gel loading dye, blue (NEB) and loaded onto the gel. Electrophoresis was performed in an EasyCast[™] gel chamber (OWL Separation Systems) filled with TAE buffer and by applying a voltage of 150 V. Estimation of DNA length was done with the aid of 100 bp and 1 kbp DNA ladders (NEB). Use of 1% v/v

ethidium bromide (Serva) enabled visualization of DNA bands under UV-light. Bands of interests were cut from the gel and subjected to DNA gel extraction (Millipore, Montage).

2.2.3 Determination of DNA Concentration

DNA concentration was assessed by measuring the absorption at a wavelength of 260 nm ($A_{260\text{nm}}$). Drops of 1 μL were measured in triplicate using the NanoDrop 1000 spectrophotometer (Thermo Fisher Scientific). Sample purity was judged from the ratio $A_{260\text{nm}}/A_{280\text{nm}}$ (protein contamination) being optimal in the range of 1.7-2.0 and the ratio $A_{260\text{nm}}/A_{230\text{nm}}$ (contamination from salts, phenols, etc.) being optimal when larger than 1.5.

2.2.4 DNA Restriction with Endonucleases

In order to generate compatible DNA fragments for ligation, PCR products and vector DNA were subject to enzymatic double digestion employing the restriction endonucleases (RE) *NdeI* and *NcoI* in reaction buffer 4 (NEB). The performance of *NdeI* revealed critical for successful cloning. Only fresh enzyme was used. The 5'-overhang sequence upstream of the RE-site, which was introduced into the insert via PCR, was extended from 6 to 9 bp thereby facilitating *NdeI* binding and digestion (see Appendix Tab. 5). Employed amounts of insert and vector DNA were on the order of 1 μg and 4 μg respectively. The reaction mixtures were incubated at 37 °C for 2 h (vector) and 4 h (insert) due to the low efficiency of *NdeI*. Before being purified by agarose gel-electrophoresis, the reaction mixture containing the vector was subject to dephosphorylation by calf intestinal phosphatase (CIP, from NEB) to inhibit self-religation of single-digested vector. CIP was inactivated at 65 °C for 20 min.

2.2.5 Ligation of DNA Fragments

After electrophoretic purification and subsequent extraction from agarose gels, DNA fragments with compatible *NdeI* and *NcoI* sticky-ends, respectively, were fused using T4 ligase (Novagen). Total DNA amounted to 100-400 ng per reaction at which a molar ratio of 1:6 (vector : insert) was provided. Incubation was performed either for 5 h at room temperature (full-length αB) or over night at 16 °C (αB10). T4 ligase was inactivated at 65 °C for 10 min. NovaBlue GigaSingles[™] cells (Novagen) were transformed usually with 1 μL of

the reaction mixture (approximately 2-5 ng of DNA). Higher volumes decreased transformation efficiency considerably.

2.2.6 Ligation Independent Cloning (LIC)

The vector pET-30-Ek/LIC- α B encoded for N-terminally His₆-tagged α B with an enterokinase (Ek) cleavage-site for tag-removal (see Appendix 5.1.1 for vector map). Replacement of the Ek cleavage-site with that specific for Thrombin (Th) and Tobacco Etch Virus protease (TEV), respectively, was accomplished according to the LIC protocol (Novagen). The corresponding primers are listed in the Appendix (Tab. 5). This approach yielded the constructs pET-30-Th- α B and pET-30-TEV- α B.

2.2.7 Site-Directed Mutagenesis

Initially, the point mutation N146D was introduced in the truncated construct α B10 (residues 64-152), which is termed α B10m in the following. α B10m and further mutants were generated using the QuikChange[®] Site-Directed Mutagenesis Kit or the corresponding Lightning Kit (Stratagene). Primers were designed in compliance with the manufacturer's instruction and are specified in the Appendix (Tab. 6). Based on the length of the template vector mod.pET-30- α B10 of 5.6 kbp and the PfuUltra polymerase activity of 1 kb/min at 68 °C, the PCR extension period was set to 5.8 min. XL1-Blue cells (Stratagene) were used for plasmid amplification. The mutagenesis was verified by DNA sequencing (Eurofins MWG Operon).

2.2.8 Transformation of *E. coli* Cells

Transformation of different strains of *E. coli* with plasmid-DNA was accomplished via heat-shock of competent cells. Frozen cells were thawed on ice. Aliquots of 20-50 μ L were gently mixed with 1 μ L of target plasmid-DNA (100-400 ng/ μ L) and incubated on ice for approx. 20 min. The heat-shock was initiated at 42 °C for a period of 30-45 s. After 5 min on ice, 500 μ L of LB medium were added and shaking for 1 h at 37 °C followed. Different volumes of the cell suspensions (50-250 μ L) were dispersed on LB agar plates containing 25 μ g/mL of the antibiotic Kanamycin (Kan) for selection of transformants. Plates were either incubated overnight at 37 °C or for three days at room temperature. Incubation times and volumes

varied slightly depending on the bacterial strain used (BL21-DE3, NovaBlue GigaSingles[™], XL1-Blue). The protocol was adapted according to the respective manufacturer (Novagen/Stratagene).

2.2.9 Colony-PCR

Host cells for cloning were tested after transformation for the desired cloning product. Aliquots of 100 μ L from LB-Kan cell cultures (OD_{600} 0.3-0.6) were centrifuged for 10 min at 12,000 \times g. After addition of 30 μ L deionized water to the cell pellets, the samples were incubated at 95 °C for 10 min and subsequently centrifuged for 10 min at 16,000 \times g. 1 μ L of the supernatant, containing the plasmid-DNA, was employed as template DNA in PCR (see Chapter 2.2.1). Primers were chosen such that either the entire insert and its flanking sequences (within T7 promotor/terminator boundaries) or solely the introduced insert was amplified (see Appendix Tab. 5). Reaction products were analyzed by agarose gel-electrophoresis.

2.2.10 Amplification and Extraction of Plasmid-DNA

The super-competent *E. coli* strain NovaBlue GigaSingles[™] (Novagen) was utilized for cloning purposes. Cell colonies were picked from LB agar plates and used for inoculation of 3 mL pre-cultures (LB-Kan). After constant shaking for 2 h at 37 °C, 50 mL of LB-Kan were inoculated with the pre-cultures and incubation at 37 °C proceeded over night. The amplified plasmid-DNA was purified using a commercially available DNA extraction-kit (Promega). Finally, concentration and purity of plasmid-DNA were determined. Correct mutagenesis was verified by DNA sequencing (Eurofins MWG Operon). The DNA was stored at –20 °C.

2.2.11 Recombinant Protein Expression

The *E. coli* strain BL21-DE3 (Novagen) was used as the expression host for recombinant production of α B, α B10m and its variants. Protein expression always started with freshly-transformed cells. Well-separated colonies were picked from LB agar plates and used for inoculation of 3 mL pre-cultures in LB-Kan. These were grown aerobically at 37 °C for approximately 3 h ($OD_{600nm} \approx 0.6$). LB-Kan medium of 50 mL was then inoculated with the pre-culture and incubated over night at 22 °C with constant shaking. In the following, the expression protocols vary for unlabeled, ^{13}C , ^{15}N - and 2H , ^{13}C , ^{15}N -enriched proteins and are separately described below.

2.2.11.1 Unlabeled Protein

A volume of 25 mL of the over night culture was used to inoculate 1 L of LB-Kan medium giving rise to an OD_{600nm} of approximately 0.1. Cell cultures of 500 mL each were incubated at 37 °C in 2 L baffled shake flasks with constant shaking at 120 rpm. Expression was induced by addition of 1 mM IPTG at an OD_{600nm} of 0.6-0.9. The incubation at 37 °C was proceeded for 4 h.

2.2.11.2 ^{13}C and ^{15}N Enrichment in Proteins

For the expression of ^{13}C , ^{15}N -labeled protein, 25 mL of the LB-Kan over night culture was gently centrifuged for 10 min at 1,500×g and 22 °C. The cell pellet was carefully resuspended in 2xM9 minimal medium and used for inoculation of 1 L 2xM9 culture (starting OD_{600nm} of 0.1). Baffled shake flasks (2 L) with 500 mL of the 2xM9 culture were incubated at 37 °C with constant shaking at 120 rpm for aerobic cell growth. When cell density reached an OD_{600nm} of 0.6-0.9, IPTG was added to a final concentration of 1 mM. Protein expression was performed over night at 22 °C with constant shaking at 120 rpm. For full-length α B, the expression period was on the order of 18 h, whereas α B10m expression and that of its mutants was aborted after 14 h in order to prevent proteolytic degradation.

2.2.11.3 $^{13}\text{C}/^{15}\text{N}$ Enrichment and Perdeuteration

Perdeuteration of αB demanded careful adaptation of the expression host cells to the cell-toxic D_2O . Therefore, the 3 mL LB-Kan pre-culture was transferred to 20 mL of LB-Kan and further incubated at 37 °C until an approximate $\text{OD}_{600\text{nm}}$ of 0.8 was reached. After 10 min centrifugation at 1,500×g, the cell pellet was gently resuspended in D_2O -based 2xM9 minimal medium containing, however, glucose and NH_4Cl with natural abundance of isotopes. 200 mL of this cell culture were grown aerobically for approximately 6 h at 37 °C ($\text{OD}_{600\text{nm}}$ of 0.1-0.2), whereas subsequent over night incubation was performed at 22 °C. Cells were centrifuged at room temperature for 20 min at 1,500×g and finally resuspended in D_2O -based 2xM9 minimal medium containing ^2H , ^{13}C -glucose and $^{15}\text{NH}_4\text{Cl}$. Cultures of 500 mL were incubated in 2 L baffled shake flasks at 37 °C for 5 h ($\text{OD}_{600\text{nm}} \approx 0.5$). The temperature was decreased to 22 °C and expression was induced with 1 mM IPTG at an $\text{OD}_{600\text{nm}}$ of 0.6-0.9. Over night expression (18 h) at 22 °C and with constant shaking at 120 rpm gave rise to a final $\text{OD}_{600\text{nm}}$ of approximately 3.0. It should be noted that all employed solutions and additives were D_2O -based and that contamination by H_2O was rigorously avoided.

2.2.12 Cell Harvest and Storage

Following protein expression, cells were centrifuged in 500 mL buckets (Nalgene) for 30 min at 10,000×g and at a temperature of 4 °C. Since all protein constructs were purified via anion-exchange chromatography as the initial purification step, cell pellets were washed by resuspending in 20 mM Tris-HCl (pH 7.5) on ice. Cells were again centrifuged in 50 mL falcon tubes for 45 min at 6,000×g and 4 °C. Cell pellets were weighted and stored at -80 °C.

2.3 Biochemical Methods and Sample Preparation

Protein sequences are summarized in the Appendix 5.1.4 in Tab. 7. A β ₁₋₄₀ was produced and purified by Uwe Fink (FMP Berlin, Germany). The proteasome α - and β -subunits were prepared and assembled by Tomasz Religa (Group of Lewis E. Kay, University of Toronto, Canada) and the 11S activator by Remco Sprangers (University of Tübingen, Germany).

2.3.1 Cell Lysis

Frozen cell pellets were thawed on ice and subsequently resuspended in lysis buffer (8 mL/g pellet). Cell lysis was accomplished with a French[®] pressure cell press (SLM Amicon). After equilibration with lysis buffer, 25 mL of the cell suspension were pumped into the pre-cooled cylinder. Cells were disrupted by applying a pressure of 1,000 psig. The cell homogenate was collected and cooled on ice, before being reinjected for a second cycle. The lysate was then centrifuged for 30 min at 60,000 \times g and 4 °C. Finally, the supernatant was filtered (0.2 μ m, Whatman) and kept on ice for subsequent protein purification. A continuous work flow was especially important for the degradation-prone α B10m and its variants.

2.3.2 Anion-Exchange Chromatography (AEC)

Anion-exchange chromatography (AEC) was the initial purification step for full-length α B, the truncated variant α B10m and its mutants. The theoretical isoelectric points (pI) are 6.8 and 5.9 for α B and α B10m, respectively, as obtained from the ExPASy ProtParam tool [232]. Both proteins are thus negatively charged at the provided pH of 8.5. Whilst α B10m was first subjected to weak and subsequently to strong AEC, full-length α B was directly applied to strong AEC, since its large M_w ensured efficient separation during the final size-exclusion chromatography (SEC). All buffers contained 1 mM EDTA in order to chelate divalent metal ions.

2.3.2.1 Weak AEC

The weak anion-exchanger DEAE-(diethylaminoethyl)-Sepharose (GE Healthcare) was employed for AEC of α B10m and its mutants. The preparative column with a volume (CV) of

175 mL was washed with 2 CV of buffer B and equilibrated with 3 CV of buffer A. Injection of the cell lysate was performed at a flow rate of 5 mL/min. The subsequent washing step (3 CV of buffer A) was followed by a 6 CV gradient of buffer B from 0% to 15%. Strongly bound protein was eluted thereafter with 2 CV of buffer B. Eluted protein was collected in 6 mL fractions which were analyzed by SDS-PAGE. Respective fractions containing α B10m were pooled and diluted threefold in buffer A for subsequent application to strong AEC.

2.3.2.2 Strong AEC

A preparative column with 100 mL of the anion-exchanger Q-Sepharose (GE Healthcare) was used for strong AEC. The column was washed with 3 CV of buffer B and equilibrated with 3 CV of buffer A. Injection of the α B10m pool (weak AEC) and the α B cell lysate, respectively, was performed at a flow rate of 5 mL/min. The program for α B10m elution was as follows: wash with buffer A (3 CV), wash with 2% of buffer B (3 CV), gradient of buffer B from 2% to 14% (9 CV) and a final wash with buffer B (3 CV). The program for α B elution was as follows: wash with buffer A (6 CV), gradient of buffer B from 0% to 18% (10 CV), gradient of buffer B from 18% to 100% (2 CV) and a final wash with buffer B (1 CV). Eluted protein was collected in 6-8 mL fractions and analyzed by SDS-PAGE. Fractions containing the target protein with reasonable purity were pooled and concentrated for subsequent SEC.

2.3.3 Size-Exclusion Chromatography (SEC)

The final purification step separated the proteins with respect to their molecular size. For full-length α B and α B10m, 500 mL columns (XK26, GE Healthcare) filled with Superose 6 and Superdex 75 media (GE Healthcare) were employed, respectively. The columns were equilibrated with 2 CV of SEC buffer. Injection of the concentrated AEC pool and subsequent elution (1.5 CV) with SEC buffer were performed at a flow rate of 1 mL/min. Elution of protein was tracked by online-observation of $A_{280\text{nm}}$. The eluted volume was collected in 9 mL fractions, which were analyzed by SDS-PAGE. Fractions containing the target protein with low protein background were pooled, and the protein concentration was determined.

2.3.4 Analytical SEC for Protein Characterization

Analytical Superose 6 and Superdex 75 10/300 GL SEC columns (GE Healthcare) were employed in order to assess the molecular weight of α B and α B10m, respectively. The columns were equilibrated with 3 CV of PBS buffer. After filtration (0.2 μ m), samples of 200 μ L were injected and eluted at a flow rate of 0.5 mL/min. Standard proteins (GE Healthcare) and mixtures of those were applied to the columns for calibration. The observed retention volumes were correlated with the known molecular weights of standard proteins (bovine Thyroglobulin 669 kDa, horse Ferritin 440 kDa, rabbit Aldolase 158 kDa, hen Ovalbumin 43 kDa, bovine Chymotrypsinogen 25 kDa, bovine Ribonuclease-A 13.7 kDa).

2.3.5 SDS-PAGE

Polyacrylamide gel-electrophoresis (PAGE) was performed under denaturing conditions employing sodium dodecyl sulfate (SDS). Gels and the running buffer were prepared according to Sambrook *et al.* [233]. Polyacrylamide percentages of 15% and 20% were used for analysis of α B and α B10m samples, respectively. Usually, 20 μ L of protein samples were mixed with the same volume of SDS-loading buffer [234]. Following incubation at 95 °C for 5 min, the samples were chilled at room temperature, and 10 μ L each were loaded onto the stacking-gel. Low-molecular weight and peptide markers were employed according to the manufacturer's instructions (Sigma-Aldrich). Electrophoretic separation of proteins was accomplished in an electrophoresis chamber (Mighty Small II, Hoefer) and by applying a voltage of 180 V. Staining of gels was achieved according to Schaeffer *et al.* [235].

2.3.6 Dialysis

For buffer exchange, protein solutions were usually dialyzed against 5 L of the desired buffer. Typical sample volumes ranged from 200 μ L (Slide-A-Lyzer[®], Pierce) to 100 mL (Spectra/Por[®] 7 dialysis tubings, Roth) depending on the required extent of buffer exchange. The regenerated cellulose membranes were chosen according to the desired molecular weight cut-off (MWCO) and incubated in deionized water for 30 min before use. Dialysis was performed over night at 4 °C under constant stirring.

2.3.7 Concentration of Protein Samples by Ultrafiltration

Protein samples were concentrated by ultrafiltration. Large volumes (> 20 mL), e.g. during protein purification, were concentrated in stirred cells (Millipore, Amicon Models 8050/8200) with ultrafiltration-membranes (Millipore). During application of 2-3 bar pressure, the solution was gently stirred at 4 °C. Small sample volumes were concentrated in centrifugal filter units (Millipore, Amicon Ultra-0.5/4/15) according to the manufacturer's instructions. The MWCO was selected depending on the size of the target protein ($\text{MWCO} < M_w/2$).

2.3.8 Storage of Protein Samples

Aliquots of 500 μL of the truncated construct αB10m in PBS were flash-frozen in liquid nitrogen and directly stored at -80 °C. The same applies to full-length αB , but that the flash-frozen samples were subsequently sealed with meshed caps and subjected to lyophilization (Alpha2-4 LDplus instrument, Christ). Lyophilization was performed at approximately -89 °C and 0.013 mbar for 24 h. The dry protein powder was then tightly sealed and stored at -80 °C.

2.3.9 Preparation of Monomeric $\text{A}\beta_{1-40}$

Lyophilized $\text{A}\beta_{1-40}$, which had been recombinantly expressed in *E. coli* and purified from inclusion bodies (Uwe Fink, FMP Berlin, Germany), was initially solubilized in 10 mM NaOH and sonicated for 15 min. Subsequently, an equivalent volume of 2xPBS was added to ensure a physiological pH of 7.4. After final sonication for 15 min, the solution was filtered (0.2 μm) and its concentration determined. The preparation was done on ice with pre-cooled solutions. The procedure assured that the peptide and possible aggregates were completely dissolved.

2.3.10 Alignment of Protein Sequences

Protein sequences of metazoan and non-metazoan sHSPs were obtained from the UniProt database [236] with the following accession codes: human α B/HSPB5 (P02511), bovine α B (P02510), chicken α B (Q05713), mouse α B (P23927), rat α B (P23928), sheep α B (Q5ENY9), human α A/HSPB4 (P02489), human HSP20/HSPB6 (O14558), human HSP22/HSPB8 (Q9UJY1), human HSP27/HSPB1 (P04792), wheat HSP16.9 (P12810), pea HSP18.1 (P19243), *Methanococcus jannashii* HSP16.5 (Q57733), *Escherichia coli* IbpA (P0C054) and *Mycobacterium tuberculosis* HSP16.3 (P0A5B7). The software Vector-NTI (Invitrogen) was used for sequence handling and alignment.

2.4 Biophysical Methods

2.4.1 Determination of Protein Concentration

The concentration of protein solutions was assessed by measuring the absorption of aromatic residues at a wavelength of 280 nm ($A_{280\text{nm}}$). Drops of 2 μ L were measured in triplicate using the NanoDrop 1000 spectrophotometer (Thermo Fisher Scientific). Sample purity was judged from the ratio $A_{280\text{nm}}/A_{260\text{nm}}$ (DNA contamination). In case of very high $A_{280\text{nm}}$ values, e.g. for FROSTY sample preparation, protein solutions were diluted before the measurement. Relevant parameters, obtained from the ExPASy ProtParam tool [232] and used to calculate the concentration of the respective protein, are summarized in Tab. 8 (see Appendix 5.1.5).

2.4.2 Dynamic Light Scattering (DLS)

DLS measurements were performed on a ZEN3500 Zetasizer NanoZS instrument (Malvern Instruments) equipped with a 50 mW laser operating at 532 nm. The instrument detects back-scattering at an angle of 173°. Temperature control was accomplished with an in-built peltier-element. Data analysis and estimation of molecular weights $M_{w,\text{est}}$, assuming globular protein particles, was done using the software DTS 5.03 (Malvern Instruments). All buffers and additive solutions were filtered through 0.2 μ m and final samples through 0.1 μ m filter

devices (Millipore). Quartz-cuvettes (Hellma) for small volumes (12 μL) were provided. Sample volumes of 20 μL were employed for standard experiments. For kinetic measurements and temperature scans, samples of 80 μL were used, and cuvettes were sealed with parafilm. For size measurements, samples of αB (50 μM) and αB10m (100 μM) in PBS buffer were incubated with CuCl_2 , ZnCl_2 and CaCl_2 at a ten-fold molar excess of the respective metal ion. Aliquots of 20 μL were measured at 25 $^\circ\text{C}$. Additionally, the temperature-dependence of the oligomeric size was examined for αB at 60 $^\circ\text{C}$ and 85 $^\circ\text{C}$. After temperature equilibration, three measurements were performed for each sample. Each measurement consisted of 60 runs with a duration of 5 s each, thereby accumulating scattering data for 300 s. All samples revealed monomodal size distributions at ambient temperature. The scattering intensity I_s is proportional to R_h^6 , with R_h quoting the hydrodynamic radius of a particle. This strong size-dependence results in intense scattering for large particles like dust and aggregates, but also for larger, though less-abundant, multimeric states within a monomodal size distribution. Volume-weighting of such size distributions artificially accounts for the high sensitivity of DLS for large particles and emphasizes the smaller species that are actually more abundant in solution. Hence, hydrodynamic diameters D_h and polydispersity indices $Pd\%$ were extracted from volume-weighted size distributions in order to account for the polydisperse nature of the proteins. Intensity-weighted size distributions were inspected, when protein aggregation was monitored at elevated temperatures, i.e. when the status of the entire sample was of interest. Aggregation curves of αB (10 μM) in the absence and presence of metal ions (20 μM) were measured by varying the temperature from 10 $^\circ\text{C}$ to 90 $^\circ\text{C}$ in steps of 1 $^\circ\text{C}$. After 2 min of equilibration at each temperature interval, light scattering fluctuations were measured five times for 10 s each. The temperature scan was performed three times for apo- αB and was highly reproducible. The holo-samples were measured once. For data analysis, D_h was obtained from intensity-weighted size distributions. Kinetic measurements of $\text{A}\beta_{1-40}$ aggregation were performed at an initial peptide concentration of 125 μM . Co-incubation with αB was done at a chaperone concentration of 2.5 μM . The samples were filtered through 0.1 μm membranes (Millipore). Initial size distributions were acquired at 25 $^\circ\text{C}$. After temperature increase to 37 $^\circ\text{C}$ and an equilibration period of 15 min, the samples were automatically measured in time intervals of 4 h. At each time point, three measurements were performed with data accumulation of 300×4 s each.

2.4.3 Inductively-Coupled-Plasma Mass Spectrometry (ICP-MS)

ICP-MS was performed by Frank Kuppler (Group of Gerd Multhaup, Freie Universität Berlin). Samples of α B and α B10m (80 μ M monomer) in PBS were incubated with CuCl_2 (160 μ M) for 2 h at room temperature. The samples were dialyzed over night against a 2000-fold volume of PBS. The protein concentrations were measured again. Samples of 200 μ L were mixed with 1 mL of HNO_3 (65% v/v) and decomposed in a microwave labstation (Ethos Plus, Milestone Inc.) at 170-210 °C and 6 bar for 30 min. ICP-MS was performed using a Element 2 ShieldTorch system (Thermo-Fischer Scientific) in peak-hopping mode with spacing at 0.01 atomic mass units, three points per peak, three scans per replicate and an integration time of 300 ms per point. The rate of plasma flow was 15 L/min with an auxiliary flow of 0.9 L/min and a blend gas flow rate of 0.1 L/min. The rf power was 1.3 kW. The sample was introduced using a crossflow nebulizer at a flow rate of 1.02 L/min. The apparatus was calibrated with 6.5% HNO_3 solution containing copper and zinc at 1, 5, 10, 25, 50, 100, 200 ppb with ^{103}Rh as internal standard for all isotopes. Samples were measured in triplicate.

2.4.4 Isothermal Titration Calorimetry (ITC)

ITC experiments were performed at 25 °C employing a VP-ITC Micro-Calorimeter (Microcal Inc.). Protein samples were dialyzed against a 500-fold volume of PBS, and protein concentrations were determined in triplicate. The samples were degassed for 10 min before use. To stabilize Cu(II) in buffered solution and to minimize unspecific binding of Cu(II) in the titration experiment, $\text{Cu}(\text{Gly})_2$ was used as a weak chelate [68,108]. The glycine solution was prepared by dissolving glycine in the corresponding buffer after dialysis. CuCl_2 was then dissolved in the glycine solution at a 1:4 molar ratio (Cu(II):glycine) in order to ensure complete chelation of Cu(II). All solutions were prepared freshly. Aliquots of 5 μ L of 2 mM Cu(II) were injected into the reaction cell containing either α B10m (110 μ M) or α B (100 μ M). A spacing time of 300 s was used. In control experiments i) $\text{Cu}(\text{Gly})_2$ was injected into PBS only and ii) glycine was injected into the protein solutions. Both experiments revealed very weak and constant heat changes that were subtracted from the binding isotherms of the protein samples. The curves were then fitted to one-site binding models using Microcal Origin (Microcal Inc.). In case of α B10m, the first three data points were excluded from the analysis, since the binding isotherm revealed initial endothermic contributions. This observation might

arise from Cu(II)-induced dissociation of either dimers or higher oligomers. In order to account for the competition between protein and glycine for Cu(II)-binding, the observed dissociation constant $K_{d,app}$ had to be corrected as described previously [68,108]. The real dissociation constant K_d for the Cu(II)-protein interaction was thus obtained as the product of $K_{d,app}$ and the first dissociation constant of the bis-glycine complex $Cu(Gly)_2$ (2.5×10^{-6} M).

2.4.5 *In-vitro* Chaperone Activity Assay

The Zetasizer NanoZS instrument (Malvern Instruments) was used to follow light scattering during heat-induced β_L aggregation. Final concentrations for the different components were as follows: 2 μ M bovine lens β_L (Sigma-Aldrich); 0.5, 1 and 2 μ M full-length αB ; 1 μ M Cu(II). Higher concentrations of Cu(II) induced augmented aggregation of β_L . Lyophilized proteins and $CuCl_2$ were dissolved in PBS and deionized water, respectively. Each sample of 40 μ L was incubated for 15 min at room temperature before measurement. Three runs (5 s duration each) were performed to measure the mean count rate of scattered light. After measuring the initial intensity at room temperature, the sample was heated to 60 °C. The mean count rate was detected in 2 min intervals for a period of 30 min. Each experiment was performed in triplicate. Notably, αB revealed stable at 60 °C in the absence and presence of Cu(II) giving rise to a constant baseline. The scattering intensities were normalized to the maximum intensity of the β_L sample in the absence of αB .

Heat-induced aggregation of citrate synthase (CS) from porcine heart (Sigma-Aldrich) was monitored in a Safire plate reader (Tecan). Stock solutions were prepared freshly. Final concentrations of the components amounted to 2 μ M CS; 2, 4 and 8 μ M for both Cu(II) and αB . Metal chelators were provided at concentrations of 32 μ M (glycine) and 16 μ M (EDTA), respectively. Samples of 200 μ L were prepared in 96-well plates (Costar) in triplicate and sealed with adhesive sealing films (Excel Scientific). The photometer was set to absorption-mode at a wavelength of 340 nm, thereby detecting the intensity of scattered light due to sample turbidity. After temperature equilibration of the instrument at 42 °C, the sample plate was inserted and the kinetic measurement was initialized. Each well was measured in intervals of 5 min for a period of 120 min with a preceding step of sample shaking.

2.4.6 Electron Microscopy (EM)

Acquisition of EM images was kindly performed by Martina Ringling (FMP Berlin) using the EM 902A transmission electron microscope (Zeiss). Samples of α B oligomers were prepared at a concentration of 50 μ M in TBS. CuCl_2 was added at a two-fold molar excess. Typically, diluted samples with final α B concentrations of 1.0-2.5 μ M were used for further studies. Sample volumes of 3.5 μ L were pipetted onto carbon-coated nickel grids (Quantifoil Micro Tools GmbH) and incubated for 45 s to achieve particle adsorption to the surface. For negative staining, the grids were dried with filter paper and subsequently incubated with 3.5 μ L of 2% uranylacetate for 15 s. Finally, the grid was again dried with filter paper.

After preparation of monomeric $\text{A}\beta_{1-40}$ (Chapter 2.3.9), the peptide was incubated for 4 days at 37 °C without agitation in order to provoke fibril formation. The concentration of $\text{A}\beta_{1-40}$ amounted to 125 μ M. Co-incubation with α B was performed at a chaperone concentration of 2.5 μ M. Amyloid samples had to be sonicated for 2 min in order to disrupt clusters of fibrils. The preparation of grids was similar to the procedure described for the α B samples.

2.4.7 Circular Dichroism (CD) Spectroscopy

Far-UV CD spectra were recorded on a J-720 spectropolarimeter (Jasco). Protein stocks were diluted to final concentrations of 10 μ M (α B10m) and 20 μ M (α B), respectively, by using PBS containing sodium fluoride instead of the chloride salt. The holo-forms of both proteins were prepared by saturating with CuCl_2 at five-fold molar excess. After incubation for 1 h at room temperature, the samples were centrifuged and the supernatants were subject to CD experiments. Samples were measured in quartz cuvettes with 0.1 cm path length (Hellma). The spectra were recorded with five scans for data accumulation, a data pitch of 0.1 nm, band widths of 2 nm and a scanning speed of 100 nm/min. The spectral region ranged from 260 nm to 195 nm (α B10m). For full-length α B, the lower limit was set to 200 nm due to scattering of the large particles. The PBS buffer was measured for baseline evaluation and correction. The mean residue ellipticity $[\theta]_{\text{mrm}}$ was derived according to:

$$[\theta]_{\text{mrm}} = \theta \times \frac{M_w}{10 \times d \times c \times (N-1)}, \quad (31)$$

where θ is the observed ellipticity (degrees), M_w is the molecular weight (g/mol), d corresponds to the path length of the cuvette (cm), c denotes the protein concentration (g/mL) and N equals the number of amino acids in the protein sequence (175 for α B, 90 for α B10m). Thermal unfolding of protein was monitored at wavelengths of 216 nm (α B) and 201 nm (α B10m) indicative of β -strand and random-coil secondary structure, respectively. The temperature gradient for α B10m experiments ranged from 15 to 75 °C, although higher temperatures (up to 90 °C) were also scanned in initial tests revealing no further transitions. Melting curves of α B were recorded in a temperature range of 15 to 90 °C. The temperature scan was performed in increments of 0.1 °C and with a heating rate of 1 °C/min. CD spectra were recorded at the initial and final stages of the temperature scans as well as at the initial temperature after the heating process to test for reversibility. For determination of the melting temperature T_m , the melting curves were fitted to a sigmoid function of the type:

$$[\theta]_{mrm} = A + \frac{B - A}{1 + \left(\frac{T_m}{T}\right)^c}, \quad (32)$$

with the parameters $[\theta]_{mrm}$ and T corresponding to the mean residue ellipticity and the temperature, respectively. The curve fitting analysis was performed with Microsoft Excel.

2.4.8 Fluorescence Spectroscopy

The fluorescent signal of the sole tyrosine of α B10m (Y122) was monitored on a Cary Eclipse fluorescence spectrophotometer (Varian) providing a fluorescence cuvette (Hellma). Samples of 200 μ L were prepared containing α B10m (20 μ M) in PBS and increasing concentrations of Cu(II) (0, 5, 6, 8, 12, 16, 20, 24, 30, 40, 60, 80, 150, 200, 400 μ M). As described for the ITC binding studies, Cu(Gly)₂ was employed to stabilize Cu(II) at physiological pH and to inhibit unspecific binding [108]. Measurements were performed at 20 °C. Tyrosine fluorescence was excited at a wavelength (λ_{ex}) of 275 nm, and emission spectra at wavelengths (λ_{em}) ranging from 290 nm to 390 nm were recorded to monitor quenching of the signal by Cu(II). The bandwidth was set to 5 nm. Ten spectra were accumulated for each sample. For determination of the binding constant, the fluorescence intensities at 304 nm in the absence (F_0) and presence of Cu(II) (F) were extracted, and the extent of fluorescence quenching $((F_0 - F)/F_0)$ was plotted versus the metal concentration. The experimental data was fitted using the

function: $Y = F_{\max}X / (K_{d,app} + X)$, with F_{\max} and $K_{d,app}$ being the maximal extent of fluorescence quenching and the apparent dissociation constant, respectively, and Y and X corresponding to the extent of fluorescence quenching and the Cu(II) concentration, respectively. Curve-fitting analysis was done with Microsoft Excel.

2.4.9 Fluorescence Correlation Spectroscopy (FCS)

To obtain information about the overall rotational correlation time of α B, the protein was labeled with the bi-functional fluorescent dye Cy5 bis-succinimidyl ester (GE Healthcare). The conjugation involves free amino groups of protein lysine side-chains and the two *N*-hydroxysuccinimid (NHS) ester moieties of the reactive dye. Due to the generally high abundance of lysine residues on the surface of proteins, a bi-conjugation can be assumed. This ensures rigid co-rotation of the fluorescent reporter with the biomolecule, which is a prerequisite for this method [237]. For the labeling reaction, α B was dialyzed against 100 mM bicarbonate-HCl buffer resulting in a final pH of 8.5. The employed concentration of monomeric α B amounted to 521 μ M, which corresponds to an oligomer (26-mer) concentration of approximately 20 μ M. The reactive dye was dissolved in DMSO at a concentration of 2 mM. A volume of 10 μ L of bis-Cy5 was mixed with 990 μ L of the α B solution. Accordingly, a theoretical oligomer-to-dye ratio of 1:1 was expected. The reaction mixture was incubated at 24 °C for 2 h under continuous shaking, and subsequently subjected to analytical SEC on a Superose-6 column. The conjugated and non-conjugated α B were thereby efficiently separated from free dye. The eluted protein in PBS was pooled and measured with respect to absorption at the wavelengths of 280 nm (A_{protein}) and 649 nm (A_{dye}), respectively. The oligomer-to-dye ratio R was calculated according to:

$$R = \frac{(A_{\text{protein}} - 0.05 \times A_{\text{dye}}) \times \epsilon_{\text{dye}}}{A_{\text{dye}} \times \epsilon_{\text{protein}} \times N}, \quad (33)$$

with $\epsilon_{\text{protein}}$ and ϵ_{dye} being the molar extinction coefficients of the protein (13,980 $\text{cm}^{-1} \text{M}^{-1}$ for α B) and the fluorescent dye (250,000 $\text{cm}^{-1} \text{M}^{-1}$ for bis-Cy5), respectively, and N denoting the number of subunits in the α B oligomer (a 26-mer was assumed here). The calculations yielded an oligomer-to-dye ratio of approximately 5:1, which assured that only one dye molecule was attached to the protein complex. After addition of glycerol and sodium azide to final concentrations of 20% and 0.03%, respectively, Cy5- α B was concentrated to 87 mg/mL and

finally stored at 4 °C. For FCS experiments, this stock solution of Cy5- α B was diluted with non-conjugated α B (concentrations up to 300 mg/mL) at a ratio of 1:50,000 to ensure that single-molecule processes can be observed.

The FCS experiments and data analysis were kindly performed by Christoph Pieper (Group of Jörg Enderlein, University of Göttingen, Germany). The experimental set-up for the FCS measurements has been described in detail [237]. A commercial confocal microscopy system (MicroTime 200 with dual-focus option, Pico-Quant) was used. A single-photon counting electronics (HydraHarp 400, PicoQuant) recorded the detected photons of all four detectors independently with an absolute temporal resolution of 2 ps. All measurements were performed in Lab-TekII chambered cover-glass systems (Nunc Thermo-Electron LED) coated with BSA to prevent non-specific adsorption of target protein. The sample temperature was controlled with a HH500 digital thermometer (Omega Newport Electronics). The excitation was done in PIE mode (PIE-FCS) with laser pulse durations of approximately 50 ps and an inter-pulse distance of 6.25 ns. The fluorescence decay time of Cy5 is around 1 ns. Hence, the fluorescence generated by one pulse had nearly completely decayed before the subsequent excitation pulse. The asynchronous single-photon data was converted into correlation curves using an algorithm described recently [238].

2.4.10 Estimation of Rotational Correlation Times

Theoretical rotational correlation times $\tau_{c,theo}$ of proteins were calculated via the Stokes-Einstein-Debye equation (see Chapter 1.2.2, Eq. 14). For simplification, a spherical particle was assumed. However, higher assemblies of the 20S proteasome exhibit an elongated shape and therefore potentially deviate from the estimations. R_h values of proteins were estimated from their molecular weights using the DTS 5.03 software (Malvern Instruments). In the case of α B, its R_h value of 7.5 nm represents experimental data from DLS and FCS measurements. Viscosities of glycerol in aqueous solution were taken from [239]. These values are reported only for the temperature range from 0 °C to 100 °C. Hence, the data points were extrapolated to lower temperatures. For this purpose, the data was fitted with a polynomial of 4th degree resulting in coefficients of determination R^2 of >0.99. The obtained viscosities at temperatures below 0 °C were used to calculate the corresponding τ_c values for the different proteins.

2.4.11 X-ray Crystallography

Initial screens were based on the crystallization conditions published for the ACD construct of human α B (residues 67-157) [55]. The fine screen was performed in 24-well plates with the hanging-drop approach. α B10m was employed at a concentration of 20 mg/mL (1.94 mM) in 25 mM Tris-HCl (pH8.5), 200 mM NaCl. The protein solution was saturated with a 1.2- and 2-fold molar excess of CuCl_2 and filtered (0.2 μm). The reservoir solution (750 μL /well) contained 100 mM Bicine at pH values of 8.5, 8.7, 9.0, 9.2 and varying amounts of MPD (51, 53, 55, 57, 59, 61%). 2 μL of the reservoir solution were pipetted onto clean cover slips, and 1 μL of the Cu(II) - α B10m solution was added to the drop without mixing. The cover slip was gently reversed and carefully pressed against the edge of the well which was pre-treated with silicone paste to hermetically seal the well. Plates were stored at 20 °C and 4 °C.

Large scale screening was performed in 96-well plates (Hampton Research) with the sitting-drop method. Therefore, a MPD screen was prepared manually by varying the pH (7.6, 8.0, 8.4, 8.6, 8.8, 9.0, 9.2, 9.4) of 100 mM Bicine buffer *versus* the MPD content (50-61% in 1% steps). Additionally, the MPD suite (Qiagen) was also used for crystallization trials. The Cu(II) - α B10m solution was employed at varying protein concentrations (10 mg/mL, 20 mg/mL) in 25 mM Tris-HCl buffer at different pH (pH 7.5, pH 8.5) and with different NaCl concentrations (100 mM, 200 mM). The preparation of crystallization plates was accomplished with a Hydra eDrop instrument (Thermo Scientific). Reservoir volumes of 75 μL were employed. Volumes of 300 nL protein solution and 300 nL reservoir solution were spotted. Plates were hermetically sealed with adhesive sealing films (Excel Scientific) and stored at 20 °C. Crystallization trials to reproduce and further optimize crystal growth were performed by employing protein concentrations of 10, 13, 16 and 20 mg/mL. Crystals were tested for diffraction by Katja Faelber and Yvette Roske (Group of Oliver Daumke and Udo Heinemann, respectively, MDC Berlin, Germany) at BESSY II beam line (Berlin).

2.4.12 Modeling of the Cu(II) Coordination Sphere

The structural model of the Cu(II) -bound ACD was generated by Benjamin Bardiaux (Group of Hartmut Oschkinat, FMP, Germany). The structural model for the Cu(II) -bound ACD dimer of α B was obtained by molecular dynamics simulation and energy minimization performed with CNS 1.2 [240]. Initial atomic coordinates for residues 66-150 were taken

from PDB entry 2WJ7 [55]. Tetrahedral coordination geometry of Cu(II) with N ϵ 2 of H83, H104, H111 and O δ 1 of D109 (monodentate) was constrained according to Harding [241] and included in the PARALLHDG force field [242]. Correspondingly, the bond distances were constrained to 2.02 Å (Cu(II)-N ϵ 2) and 1.99 Å (Cu(II)-O δ 1), respectively. The bond angles for N ϵ 2-Cu(II)-N ϵ 2 and N ϵ 2-Cu(II)-O δ 1 were constrained to 109.5° (tetrahedral) and for C γ -O δ 1-Cu(II) to 120° (monodentate Asp), respectively. The Cu(II) ion was fixed in the planes of the imidazol rings and the carboxylate moiety. All atoms, except for residues V81 to S85 (β 3- β 4-loop) and K103 to F113 (β 5- β 6+7-loop), were harmonically restrained to their initial coordinates. Hence, the large CSP observed for residues belonging to β 2- β 3, indicating structural changes in this N-terminal region, were not taken into account. Additionally, torsion angle database potential was included for unrestrained regions [243]. The program PyMOL (Delano Scientific LLC) was used to generate figures of molecular structures.

2.5 NMR Spectroscopy

2.5.1 Solution-State NMR Spectroscopy

NMR spectrometers (Bruker Biospin) with magnetic field strengths of 14.1 T and 17.6 T were equipped with cryogenically cooled probe-heads. Data acquisition und processing was done using TopSpin 2.0 (Bruker Biospin). Further data analysis and resonance assignments were performed using the software Sparky [244].

2.5.1.1 Backbone Resonance Assignment of α B10m

Solution-state NMR experiments on ^{13}C , ^{15}N -labeled α B10m and its variants were performed at 22 °C in PBS containing 10% D $_2$ O. Monomer concentrations ranged from 0.5 mM to 3 mM. Tab. 3 summarizes the NMR experiments and relevant acquisition parameters.

Tab. 3 NMR experiments performed for α B10m and Cu(II)- α B10m, respectively. Spectral widths and carrier frequencies are given for the indirect dimensions, whereas that of the direct ^1H dimension was set to 10 ppm and 4.7 ppm, respectively, in all cases. Complex data points are given in the order of acquisition times t_3 , t_2 , t_1 . The recycle delay was set to 1.2 s.

Experiment	Data points	Transients	Spectral widths	Carrier frequencies	Miscellaneous
^1H - ^{15}N HSQC	1024×192	4-8	40 ppm (^{15}N)	125 ppm (^{15}N)	
^1H - ^{15}N HSQC	1024×128	16-32	80 ppm (^{15}N)	80 ppm (^{15}N)	12 °C for Arg side-chains
^1H - ^{15}N HMQC (His side-chain)	1024×128	32	100 ppm (^{15}N)	150 ppm (^{15}N)	1-1-echo water suppression
^1H - ^{13}C HMQC	1024×512	16	70 ppm (^{13}C)	40 ppm (^{13}C)	
HNCA	1024×96×96	8	40 ppm (^{15}N) 30 ppm (^{13}C)	125 ppm (^{15}N) 55 ppm ($^{13}\text{C}\alpha$)	
HN(CO)CA	1024×96×96	16	40 ppm (^{15}N) 30 ppm (^{13}C)	125 ppm (^{15}N) 55 ppm ($^{13}\text{C}\alpha$)	
HNCO	1024×96×96	8	40 ppm (^{15}N) 12 ppm (^{13}C)	125 ppm (^{15}N) 174 ppm ($^{13}\text{C}'$)	
HN(CA)CO	1024×80×80	32	40 ppm (^{15}N) 12 ppm (^{13}C)	125 ppm (^{15}N) 174 ppm ($^{13}\text{C}'$)	
(H)CCH-TOCSY	1024×64×64	32	70 ppm (^{13}C)	40 ppm (^{13}C)	20 ms DIPSI spin lock
NOESY-HSQC	1024×96×96	16	40 ppm (^{15}N) 10 ppm (^1H)	125 ppm (^{15}N) 4.7 ppm (^1H)	150 ms NOESY mixing

The data was usually processed with a square sine-bell apodization in direct and indirect dimensions with SSB (shift of the sine-bell) values of 2.0-3.0, depending on spectral resolution and sensitivity. Zero filling was applied to yield data matrices of 2048×512×512. Linear forward/backward prediction was applied to improve the spectral quality, when required.

2.5.1.2 Titration of α B10m with Divalent Metal Ions

In titration experiments, the metal ion (CuCl_2 , ZnCl_2 , CoCl_2 in de-ionized water) was added stepwise to α B10m and its mutants, respectively. Unless otherwise stated, figures show the obtained spectra at an equimolar ratio. EDTA was likewise added to an equimolar ratio. Freshly prepared ascorbic acid was used at ten-fold molar excess with respect to Cu(II). ^1H - ^{15}N HSQC spectra were recorded as indicated in Tab. 3. Signal intensities and chemical shifts were extracted from ^1H - ^{15}N HSQC spectra in the absence and presence of Cu(II). Chemical shift perturbations (CSP) for ^1H - ^{15}N correlations were calculated as follows [245]:

$$CSP = \sqrt{(0.2 \times \Delta\delta_{^{15}\text{N}})^2 + (\Delta\delta_{^1\text{H}})^2}, \quad (34)$$

with $\Delta\delta_{15N}$ and $\Delta\delta_{1H}$ being the absolute values of the chemical shift differences in ppm for ^{15}N and 1H , respectively.

2.5.1.3 ^{13}C Direct Detected Experiments

All ^{13}C -detected experiments were performed at CERM (University of Florence, Italy) in collaboration with Isabella C. Felli and Roberta Pierattelli. The spectra were recorded at 22 °C on a 16.4 T Bruker AVANCE spectrometer, which was equipped with a cryogenically cooled probe-head optimized for ^{13}C direct detection. For mapping ^{13}C chemical shifts, 2D CACO and CBCACO spectra [246,247] were recorded on apo-, Cu(II)- and Zn(II)- α B10m (1 mM). The employed metal concentrations were also 1 mM. For apo- and Cu(II)- α B10m, also 3D CBCACO and 2D CCCO experiments were performed [248]. The experiments enabled transfer of assignments for all 89 residues. The carrier frequencies were placed at 175.0 ppm and 54.0 ppm for C' and $C\alpha$, respectively, at 120.0 ppm for ^{15}N and at 4.0 ppm for 1H . Composite pulse decoupling was applied during acquisition and during some of the elements of the pulse sequences with an rf field strength of 1.7 kHz for 1H (waltz-16) [249] and 1.0 kHz for ^{15}N (garp-4) [250]. The common parameters were: recycle delay of 1.2 s, spectral widths of 50 ppm for C' , 40 ppm for $C\alpha$, 80 ppm for $C\alpha/C_{ali}$. For the 2D experiments 1024×256 data points in the direct and indirect acquisition dimensions, including the increments necessary for spin-state selection, were acquired. For the 3D experiments 1024×40×256 data points were acquired. The number of scans ranged from 16 to 128, depending on experimental sensitivity. Among the different spin-state selection methods implemented for carbonyl direct detection, the IPAP [246] and the S^3E [247] methods were applied to achieve virtual decoupling in the direct acquisition dimension. For each time increment in the indirect dimension two free induction decays (FIDs) were separately acquired and stored. The two FIDs were then added and subtracted to separate the two multiplet components. These were then shifted to the centre of the original multiplet (by $J_{C'C\alpha}/2$ Hz) and again added to obtain a singlet. The data were acquired and processed with the standard Bruker software TopSpin 1.3. CSP values for the ^{13}C -detected CBCACO spectrum were calculated according to:

$$CSP = |\Delta\delta_{C\alpha}| + |\Delta\delta_{C\beta}| + |\Delta\delta_{C'}|, \quad (35)$$

where $\Delta\delta_{C\alpha}$, $\Delta\delta_{C\beta}$ and $\Delta\delta_{C'}$ denote the chemical shift differences in ppm for C', C α and C β resonances, respectively. ^{13}C chemical shift indices (CSI) [251] and secondary structure prediction were obtained using the CcpNmr Analysis software [252].

2.5.1.4 ^{15}N Relaxation Measurements

^{15}N longitudinal (T_1) and transversal (T_2) relaxation times were determined using standard pulse sequences [253] with the following delays: 10, 50, 100, 150, 200, 300, 400, 600, 900, 2000, 5000 ms (T_1 measurements) and 6, 10, 18, 26, 34, 42, 82, 122, 162, 202, 242 ms (T_2 measurements). Signal intensities in the ^1H - ^{15}N 2D correlation sets were extracted using the program Sparky [244]. Relaxation times for each residue were derived from fitting curves with mono-exponential decays of the form:

$$I = I_0 \times (1 - p) \times \exp(-t/T_1), \quad (36)$$

for T_1 measurements and

$$I = I_0 \times p \times \exp(-t/T_2), \quad (37)$$

for T_2 experiments, respectively, where I is the observed signal intensity, I_0 corresponds to the maximal intensity, t denotes the varied relaxation delay, $T_{1,2}$ are the respective relaxation times and p is a correction factor.

2.5.1.5 Estimation of Overall Rotational Correlation Times from T_1/T_2

Rotational correlation times τ_c for the overall tumbling of the protein core were obtained as described elsewhere [254]. Briefly, residue-specific T_1/T_2 ratios, which deviated more than the standard deviation from the mean T_1/T_2 value, were excluded from further analysis. The trimmed mean T_1/T_2 ratio, which resulted from this data handling and basically reflects the rigid protein core, was used for the estimation of τ_c based on the relation:

$$\tau_c \approx \frac{1}{4\pi\nu_{^{15}\text{N}}} \sqrt{6 \frac{T_1}{T_2} - 7}, \quad (38)$$

with T_1/T_2 corresponding to the trimmed mean value and $\nu_{^{15}\text{N}}$ being the ^{15}N Larmor frequency (Hz). Theoretical rotational correlation times $\tau_{c,\text{theo}}$ were estimated with the program Hydro-

NMR [255] based on the X-ray structure of the ACD of human α B [55]. The calculations were run for a temperature of 22 °C and a viscosity of 1.1 cP.

2.5.1.6 Resonance Assignment of Monomeric A β ₁₋₄₀

The uniformly ^{13}C , ^{15}N -labeled A β ₁₋₄₀ peptide was solubilized as described in Chapter 2.3.9. The final solution contained 10% D₂O. The peptide concentration was determined photometrically, with concentrations usually in the range of 200-300 μM . The samples were measured at a magnetic field strength of 14.1 T (Bruker Biospin) and at a temperature of 4 °C. Higher temperatures led to extensive exchange broadening with the loss of the majority of resonances. Initial characterization was done by recording 2D ^1H - ^{15}N HSQC and ^1H - ^{13}C constant-time (ct-) HSQC spectra. For backbone resonance assignment, the following triple resonance experiments were performed: HNCA, HNCACB, HNCO and HN(CA)NNH [256–258]. Assignment of side-chain resonances was achieved via a 3D HCCH-TOCSY experiment [259]. Tab. 4 summarizes the NMR experiments and relevant acquisition parameters.

Tab. 4 NMR experiments performed with ^{13}C , ^{15}N -A β ₁₋₄₀. Spectral widths and carrier frequencies are given for the indirect dimensions, whereas that of the direct ^1H dimension was set to 10 ppm and 4.7 ppm, respectively, in all cases. Complex data points are given in the order of acquisition times t3, t2, t1. The recycle delay was set to 1.2 s.

Experiment	Data points	Transients	Spectral widths	Carrier Frequencies	Miscellaneous
^1H - ^{15}N HSQC	2048×320	8	24 ppm (^{15}N)	118 ppm (^{15}N)	
^1H - ^{13}C ct-HSQC	2048×512	8	70 ppm (^{13}C)	40 ppm (^{13}C)	
HNCA	2048×96×96	8	24 ppm (^{15}N) 30 ppm (^{13}C)	118 ppm (^{15}N) 55 ppm ($^{13}\text{C}\alpha$)	
HNCO	2048×96×76	8	24 ppm (^{15}N) 12 ppm (^{13}C)	118 ppm (^{15}N) 174 ppm ($^{13}\text{C}'$)	
HNCACB	2048×128×64	32	24 ppm (^{15}N) 60 ppm (^{13}C)	118 ppm (^{15}N) 43 ppm ($^{13}\text{C}'$)	
(H)N(CA)NH	2048×62×60	40	24 ppm (^{15}N)	118 ppm (^{15}N)	
H(C)CH-TOCSY	2048×94×94	8	70 ppm (^{13}C) 10 ppm (^1H)	40 ppm (^{13}C) 4.7 ppm (^1H)	20 ms DIPSI spin lock

The secondary structure propensity (SSP) of A β ₁₋₄₀ in solution was accessed by analyzing the obtained ^{13}C chemical shifts of C α and C β according to the procedure suggested by Forman-Kay [260]. The SSP program, which was used for this analysis, is freely available at <http://pound.med.utoronto.ca/software.html>. Residue-specific SSP scores of +1.0 and –1.0 represent fully formed α -helical and β -strand structure, respectively. By contrast, a score of –0.5 indicates that 50% of the conformers occupy β -strand conformation.

2.5.1.7 Titration of α B10m with Monomeric $A\beta_{1-40}$

For client interaction studies, $^{13}\text{C},^{15}\text{N}$ - α B10m was provided at a concentration of 200 μM in the absence and presence of 200 μM unlabeled $A\beta_{1-40}$. The solution of monomeric $A\beta_{1-40}$ was prepared as described in Chapter 2.3.9. Similarly, α B10m was titrated with the peptide α B₁₅₆₋₁₆₄ (synthesized in the group of Michael Beyermann, FMP) comprising the C-terminal tail of α B. The corresponding sequence is as follows: Acetyl-E₁₅₆RTIPITRE₁₆₄-NH₂. The palindromic sequence contains the conserved IXI-motif of sHSPs. The peptide was dissolved in PBS and added to α B10m. ^1H - ^{15}N HSQC spectra were obtained as described in Tab. 3.

2.5.1.8 Perdeuterated α B in Solution

^1H - ^{15}N HSQC spectra of full-length $^2\text{H},^{13}\text{C},^{15}\text{N}$ - α B were obtained at a concentration of 1.1 mM, at a temperature of 22 °C and at a magnetic field strength of 17.6 T. The resonance assignment was achieved by recording 3D HNCO, HNCA and HN(CO)CA [256,261] experiments (described in Tab. 3) and by comparison with published assignments [262,263].

2.5.2 Nuclear Magnetic Relaxation Dispersion (NMRD)

NMRD experiments [264] were performed and analyzed at CERM (Florence, Italy) by Giacomo Parigi and Claudio Luchinat. Longitudinal water proton relaxation rates R_1 of a 100 mg/mL α B solution in PBS containing 20% glycerol were measured with a Stelar fast field cycling relaxometer. The experiments were performed at temperatures of -10 °C, -3 °C and 25 °C. During the relaxation part of the experiment, different magnetic field strengths according to proton Larmor frequencies in the range of 0.01-40 MHz were applied. Additionally, a series of 16 time intervals was used for each relaxation field strength in order to measure the magnetization decay and to extract the corresponding R_1 value. Data accumulation was achieved with 4 scans. The NMRD profile was obtained by plotting the water proton R_1 *versus* the applied magnetic field strength.

Water protons in protein solutions exchange rapidly between the bulk water and the protein-bound state. In the latter case, protons can either be transiently attached to exchangeable sites, such as NH and OH moieties, or to the protein itself in terms of water molecules. Longitudinal relaxation rates R_1 of water protons in protein solutions are mainly ascribed to these exchange processes [264]. The correlation time τ_i , which modulates the dipole-dipole

interactions of each water proton in the protein-bound state as well as exchangeable protein protons, is dominated by the shortest reorientation time τ_c of the protein and the lifetime τ_{Mi} of the coupled protons according to:

$$\tau_i^{-1} = \tau_c^{-1} + \tau_{Mi}^{-1}. \quad (39)$$

The relaxation rate R_1 of water protons is described by the sum of all contributions that arise from each coupled proton:

$$R_1 = \sum_i f_i \left[\frac{1}{R_{1Mi}} + \tau_{Mi} \right]^{-1} = \sum_i f_i \left[\frac{1}{\beta_i (0.2J(\omega, \tau_i) + 0.8J(2\omega, \tau_i))} + \tau_{Mi} \right]^{-1}, \quad (40)$$

with f_i denoting the molar fraction of interacting protons with correlation time τ_i with respect to the bulk water protons. The constant β_i is related to the dipole-dipole interaction energy. The spectral density $J(\omega, \tau_i)$ is described by a Lorentzian function of the form:

$$J(\omega, \tau_i) = \frac{\tau_i}{1 + \omega^2 \tau_i^2}, \quad (41)$$

with ω being equal to 2π times the proton Larmor frequency. By varying the magnetic field, relaxation dispersion profiles can be obtained that include information about the different fractions of water protons interacting with the target protein on different time scales.

The obtained relaxation profiles were fitted to the sum of three Lorentzian dispersions giving rise to three different τ_i values. It has been shown that the weighted average $\langle \tau_c \rangle$ of these correlations times is a good representative of the overall rotational correlation time τ_c of small-sized proteins [265]. However, $\langle \tau_c \rangle$ does not agree well with τ_c of large protein complexes like apoferritin and αB [265]. Therefore, another approach was employed. Assuming fast exchange for the interacting protons ($\tau_M^{-1} > R_{1M}$), the corresponding τ_M term in Eq. 40 can be neglected, except for the fraction of protons with $\tau_i = \tau_c$ (potentially slow-exchange regime). Thus, the data has been fitted to the following function:

$$R_1 = a + b_{se} \left[\frac{1}{0.2J(\omega, \tau_1) + 0.8J(2\omega, \tau_1)} + k_M \right]^{-1} + b_{fe} [0.2J(\omega, \tau_1) + 0.8J(2\omega, \tau_1)] \\ + b_2 [0.2J(\omega, \tau_2) + 0.8J(2\omega, \tau_2)] + b_3 [0.2J(\omega, \tau_3) + 0.8J(2\omega, \tau_3)] \quad (42)$$

where $b_i = f_i \beta_i$ and $k_M = \beta_1 \tau_M$. The indices *se* and *fe* denote slow exchange and fast exchange, respectively. The a term accounts for contributions from protons with very short residence

times. The corresponding dispersion occurs beyond the highest accessible magnetic field. In order to reduce the covariance among the unknown parameters (a , b_{1se} , b_{1fe} , b_2 , b_3 , τ_1 , τ_2 , τ_3 , k_M), the dispersion profiles of αB at temperatures of 25 °C, −3 °C and −10 °C were fit simultaneously. The ratios $\Delta\tau$ between the τ_i values at −3 °C and 25 °C, as well as −10 °C and 25 °C, respectively, were kept constant and fixed to the ratios of estimated rotational correlation times at the corresponding temperatures, as obtained from the Stokes equation. Such reorientation times τ_c for αB amount to 1.2 μs , 3.2 μs and 4.6 μs at 25 °C, −3 °C and −10 °C, respectively, based on the DLS-derived hydrodynamic radius R_h of 9 nm (intensity-weighted data). The parameters $\Delta\tau_{-3^\circ C}$ and $\Delta\tau_{-10^\circ C}$ were thus fixed to 2.67 and 3.83, respectively, during the minimization. The sum of the b_i parameters ($b_{total} = b_{1se} + b_{1fe} + b_2 + b_3$) was constrained to be the same for the three temperatures. In the absence of protein aggregation, the correlation time τ_1 is expected to report on the reorientation time τ_c of αB , due to long-lived water molecules and exchangeable protein protons, whose dipole-dipole interactions are modulated by the protein reorientation time, i.e. with $\tau_M > \tau_c$.

2.5.3 Magic-Angle-Spinning (MAS) NMR Spectroscopy

Widebore NMR spectrometers (Bruker Biospin) with magnetic field strengths of 14.1 T and 16.4 T were equipped with 4 mm and 3.2 mm triple-resonance MAS probe-heads. Data acquisition und processing was done using TopSpin 2.0 (Bruker Biospin), further data analysis and resonance assignments were performed using the software Sparky [244]. MAS rotors were purchased from Bruker Biospin. The magic angle and the homogeneity of the magnetic field were optimized by using KBr and adamantane samples, respectively.

2.5.3.1 Precipitation of αB for Conventional Solid-state NMR

In order to access αB in the solid state, the protein was precipitated with polyethylene glycole (PEG) [57]. Therefore, a solution of αB (25 mg/mL) in PBS and 0.03% NaN₃ was pipetted into a glass bowl, which was positioned in a larger vessel. The bottom of the vessel was filled with an aqueous solution of 50% w/v PEG 8000. The protein solution was carefully mixed with an equivalent volume of 50% w/v PEG 8000. The vessel was hermetically closed for efficient vapor diffusion and stored at room temperature for 3-4 days. The turbid solution was centrifuged into the MAS rotor. Commonly, 5-15 mg of protein were filled into the rotor.

2.5.3.2 Comparison of Soluble and Precipitated α B Multimers

^{13}C direct excitation spectra were recorded for a static sample and by adjusting the MAS frequency to 12 kHz, respectively, using a 14.1 T widebore spectrometer (Bruker Biospin). The effective sample temperature was adjusted to $-10\text{ }^{\circ}\text{C}$. All subsequent experiments were performed using a 16.4 T Avance spectrometer (Bruker Biospin) equipped with a standard triple resonance probe and setting the MAS frequency to 12 kHz. In all experiments, ^1H decoupling was applied using a ^1H rf field of 80 kHz during acquisition. ^1H - ^{13}C CP build-up curves were measured by incrementing the contact pulse duration from 0.0 to 1.5 ms in steps of 15 μs , yielding a pseudo-2D spectrum. No ramp was employed for the contact pulse. For CP, rf field strengths of 65 kHz and 53 kHz were applied to the ^1H and the ^{13}C channel, respectively. Build-up curves for C' , Ca and CH_3 resonances were extracted at chemical shifts of 172 ppm, 52 ppm and 19 ppm, respectively. PDSD spectra of the highly viscous αB solution were recorded as described in Chapter 2.5.3.3. A PDSD mixing time of 15 ms was chosen in order to compare with the spectrum of PEG-precipitated αB . Temperature-dependent PDSD spectra were recorded and processed in the same manner. For the spectra obtained at different temperatures ($+10$, 0 and $-10\text{ }^{\circ}\text{C}$), the lowest contour level is drawn at 4σ from the noise floor to allow for a proper comparison.

2.5.3.3 Titration of αB Multimers with Divalent Metal-Ions

Sample conditions were as follows: 217 mg/mL of ^{13}C , ^{15}N - αB (monomer concentration of $\sim 10\text{ mM}$) in PBS containing 20% v/v glycerol. For the metal- αB samples, CuCl_2 and ZnCl_2 were added to the αB solutions at a three-fold molar excess. 40 μL of the viscous protein solutions were filled into 4 mm MAS rotors. Samples were measured at a magnetic field strength of 16.4 T (Bruker Biospin) and at an effective temperature of $-5\text{ }^{\circ}\text{C}$. MAS was performed at 12 kHz. CP from ^1H to ^{13}C was performed according to the Hartmann-Hahn condition as well as by considering the effects of MAS and the use of ramped contact pulses:

$$\omega_X = f(\omega_{1\text{H}} \pm n\nu_R), \quad (43)$$

with $\omega_{1\text{H}}$ and ω_X being the rf field strengths for ^1H and heteronuclei (here ^{13}C), respectively and $n\nu_R$ denoting an integer multiple of the rotor spinning frequency. The factor f accounts for the use of ramped CPs and amounts to 0.875 when applying a 75-100% ramp (87.5% at mid point). Ramps were generally employed for the low- γ nucleus. The rf field strengths were

matched according to the $n = -1$ Hartmann-Hahn-condition (78 kHz (^1H), 58 kHz (^{13}C)) with a 75-100 % ramp on the ^{13}C channel. CP durations of 0.8 ms were used. ^1H decoupling during indirect and direct evolution periods was performed with a rf field strength of 78 kHz. The PDSM mixing time was set to 50 ms [221]. A recycle delay of 3 s was used. The acquisition times were 10 ms and 12 ms for the indirect and the direct ^{13}C dimensions, respectively.

2.5.3.4 The 20S Proteasome Assemblies of *Thermoplasma acidophilum*

The proteasome α - and β -subunits were recombinantly expressed, purified and assembled by Tomasz Religa (Group of Lewis Kay, University of Toronto, Canada). Only the α -subunit was ^{13}C - and ^{15}N -enriched, and thus visible for NMR. ^{13}C -detected MAS NMR spectra were obtained for the 360 kDa $\alpha_7\alpha_7$ (3.5 mM) and the 670 kDa $\alpha_7\beta_7\beta_7\alpha_7$ (2.3 mM α -subunit) in PBS containing 30% v/v glycerol. The experiments were performed under identical conditions, i.e. at a temperature of -10°C and at 12 kHz MAS. Acquisition and processing parameters were also identical, except that the 2D PDSM spectrum of $\alpha_7\alpha_7$ was recorded with twice the number of scans. Moreover, different CP durations were used due to differing $T_{1\rho}$ of the two assemblies. Contact pulses of 250 μs ($\alpha_7\alpha_7$) and 800 μs ($\alpha_7\beta_7\beta_7\alpha_7$), respectively, were found to give optimal signal-to-noise for the aliphatic region. However, the short CP duration for $\alpha_7\alpha_7$ led to non-efficient build-up of C' signals. PDSM spectra were recorded similarly as described for αB (see Chapter 2.5.3.3).

2.5.3.5 Aggregates of $\text{A}\beta_{1-40}$ in the Presence of αB

Initially, monomeric ^{13}C , ^{15}N - $\text{A}\beta_{1-40}$ in PBS was prepared as described in Chapter 2.3.9. The peptide solution with a concentration of 50 μM was titrated with unlabeled αB in PBS to a final chaperone concentration of 1 μM . Thus, $\text{A}\beta_{1-40}$ was employed at a 50-molar excess with respect to αB , as was also done in EM and DLS aggregation experiments. The final solution contained approximately 4.2 mg of labeled $\text{A}\beta_{1-40}$. The addition of 0.03% NaN_3 inhibited bacterial growth. The sample was incubated for 3 weeks at 37°C without agitation. After incubation, the turbid solution was centrifuged, and the pellet was packed into a 4 mm MAS rotor. The $\text{A}\beta_{1-40}$ aggregate was measured at a magnetic field strength of 16.4 T, a temperature of 12°C and a spinning frequency of 12 kHz. The experimental setup was similar to that described in Chapter 2.5.3.3, except a CP duration of 1.5 ms.

2.5.3.6 ^1H -detected FROSTY MAS NMR

The proteasome α - and β -subunits were recombinantly expressed, purified and assembled by Tomasz Religa (Group of Lewis Kay, University of Toronto, Canada), whereas the 11S activator from *Trypanosoma brucei* was provided by Remco Sprangers (University of Tübingen, Germany). Fully-deuterated proteasome assemblies as well as αB multimers were employed in PBS containing 20% H_2O and 80% D_2O in order to reduce the proton density at the exchangeable sites, and hence to compromise sensitivity and resolution in amide-based experiments. In the case of αB , the protein was lyophilized and re-dissolved in the respective PBS buffer to achieve the desired protonation-level. For the proteasome subunits this was accomplished by de- and renaturation of the proteins. The 11S activator was buffer-exchanged several times. Deuterated glycerol (Sigma-Aldrich) was added to the protein solutions (20-30% v/v). Paramagnetic relaxation enhancement was accomplished by adding Cu(II)-EDTA to a final concentration of 60 mM. The resulting recycle delays were on the order of 300-400 ms.

^1H -detected spectra were acquired at magnetic field strengths of 14.1 T and 16.4 T, respectively. Spinning frequencies of 18-22 kHz were employed. The effective sample temperature was set to 0-5 °C. Cross polarization was performed according to the Hartmann-Hahn condition (Eq. 43). CP durations were on the order of 0.6 ms ($^1\text{H}_\text{N}$ to ^{15}N), 2 ms ($^1\text{H}_\text{methyl}$ to $^{13}\text{C}_\text{methyl}$, ILV labeling) and 2 ms (long range $^1\text{H}_\text{N}$ to ^{13}C). ^1H and ^{15}N heteronuclear decoupling was done with rf field strengths of 4 kHz and 2 kHz, respectively (Waltz-16) [249]. Water suppression was achieved by implementing the MISSISSIPPI sequence [266]. A pulse train of 4×15 ms with rf field strength of 4-10 kHz was used. All experiments were designed in a constant-time fashion to ensure reproducible dephasing of the water resonance as well as to yield optimal signal-to-noise ratios [231,267]. 2D ^1H - ^{15}N correlation spectra (see Appendix 5.2.6 for pulse program) were usually acquired by accumulating 128-256 spectra. The acquisition times in the ^1H and ^{15}N dimension reached values up to 30 ms and 50 ms, respectively, depending on the protein.

HNCO experiments were similarly set up as the ^1H - ^{15}N correlation experiment, except the ^{15}N - ^{13}C INEPT transfers and the $^{13}\text{C}/^{15}\text{N}$ evolution periods [267] (see Appendix 5.2.6 for pulse program). Soft rectangular pulses were used for selective on-resonance $^{13}\text{C}'$ excitation/inversion (~5 kHz/~10 kHz) to reduce artifacts. Off-resonance $^{13}\text{C}\alpha$ inversion during $^{13}\text{C}'$ and ^{15}N evolution periods was achieved with G3 Gaussian shape pulses. Bloch-

Siebert phase shifts due to the shaped pulse (300-900 μ s) were compensated by an additional G3 pulse after on-resonance inversion of all ^{13}C nuclei (see also Chapter 3.4.4.2 **Fig. 63**). Transmitter offsets of 4.7 ppm (^1H), 125 ppm (^{15}N), 174 ppm ($^{13}\text{C}'$) and 57 ppm ($^{13}\text{C}\alpha$) were used. The 2D ^1H - $^{13}\text{C}'$ plane was recorded with 3072 scans and with acquisition times of 40 ms and 25 ms in the ^1H and ^{13}C dimensions, respectively.

For 3D hCXhNH experiments [268], the long range ^1H - ^{13}C CP field strengths were optimized in order to achieve selective magnetization transfer to either the C' or $\text{C}\alpha/\text{C}\beta$ nuclei (see Appendix 5.2.6 for pulse program). The transmitter offsets were set to 174 ppm (hCOhNH) and 34 ppm (hCAhNH), respectively. The CP conditions were sufficiently selective such that reduced spectral widths without folding artifacts were possible. No J -decoupling of $^{13}\text{C}'$ and $^{13}\text{C}\alpha$ nuclei was implemented during ^{13}C evolution due to significant loss in sensitivity. The acquisition times of the 3D hCOhNH spectrum amounted to 80 ms, 20 ms and 11 ms for ^1H , ^{15}N and ^{13}C , respectively. The corresponding values for the 3D hCAhNH spectrum were 80 ms, 19 ms and 7 ms, respectively. Both spectra were recorded with 96 transients per increment.

The 2D ^1H - ^{13}C correlation spectrum of deuterated $\alpha_7\alpha_7$ with CHD_2 -labeled methyl groups of Ile ($\delta 1$ position only), Leu and Val (ILV) was recorded without Cu(II)-EDTA (recycle delay of 2 s). During the 2 ms CP duration, rf fields of 76 kHz (^1H) and 49 kHz (^{13}C) were applied. Decoupling of ^2H during ^{13}C evolution was achieved with an rf field strength of 4 kHz (Waltz-16) [249]. The spectrum was recorded with 128 scans and with acquisition times of 40 ms and 21 ms in the ^1H and ^{13}C dimensions, respectively.

3 Results

3.1 Protein Preparation

3.1.1 Full-length α B

3.1.1.1 α B Constructs with N-terminal Affinity-tag

Initially, human α B was expressed with an N-terminal affinity-tag to facilitate protein purification. The tag-sequence comprised the segments His₆-tag, Thrombin-site, S-tag and Enterokinase-site, but is abbreviated here with ‘His₆’. Proteolytic cleavage of the N-terminal tag by Enterokinase (Ek) revealed to be non-quantitative and non-specific (**Fig. 10A**). Optimization of reaction conditions (incubation time, temperature, protease and CaCl₂ concentration) did not lead to satisfactory results. Replacement of the Ek cleavage-site with that for Thrombin (Th) and Tobacco Etch Virus protease (TEV), respectively, did not sufficiently improve the tag removal (**Fig. 10B**). Formation of hetero-oligomers between cleaved and non-cleaved α B hampered efforts to separate and further purify the target molecule. Hence, the entire N-terminal tag-sequence was removed from the vector pET-30-Ek- α B. All generated constructs of full-length α B are summarized in **Fig. 10C**.

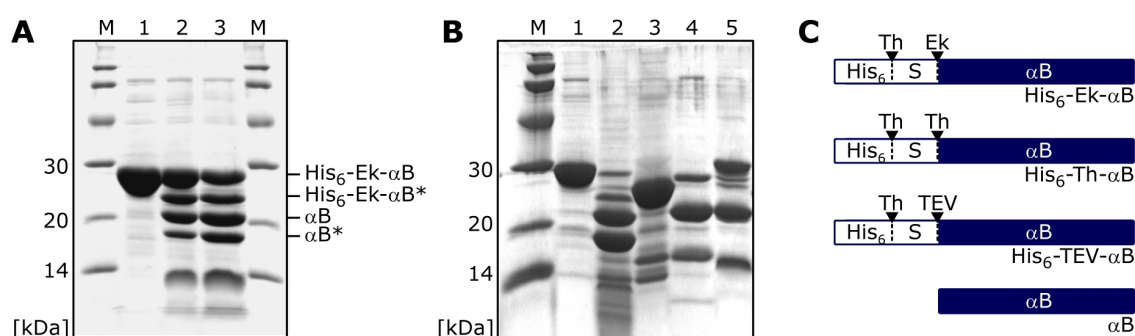


Fig. 10 Proteolytic cleavage of His₆- α B constructs with different protease recognition sites. **(A)** Cleavage of His₆-Ek- α B by Ek: His₆-Ek- α B (25 kDa) before (lane 1), after 15 h (lane 2) and after 40 h (lane 3) incubation with Ek. Molecular weights of marker bands (M) are indicated. The asterisks label the non-specific by-products. **(B)** Cleavage reactions with the proteases Ek, Th and TEV: His₆-Ek- α B (25 kDa) before (lane 1) and after 65 h (lane 2) incubation with Ek, His₆-Ek- α B after incubation with Th (lane 3), His₆-Th- α B incubated with Th for 65 h (lane 4) and His₆-TEV- α B incubated with TEV for 40 h (lane 5). Molecular weights of marker bands (M) are indicated. **(C)** Generated constructs of α B. The primary sequence of α B was preceded by an N-terminal tag comprising the His₆- and S-tag (S). For optimization of tag removal, the protease recognition-site was modified and different proteases (Ek, Th, TEV) were tested. Finally, the entire tag sequence was removed to yield a tag-free α B construct.

3.1.1.2 Cloning of Tag-free α B

For recombinant expression of tag-free α B, the entire N-terminal tag including the His₆-tag, the S-tag and the Ek cleavage-site were removed from the vector pET-30-Ek- α B by conventional cloning. Using PCR, a DNA insert (552 bp) was generated, encoding for human wt- α B with flanking recognition sites for the restriction enzymes *Nde*I and *Nco*I (**Fig. 11A**). The insert and the vector pET-30-Ek- α B were double-digested with *Nde*I and *Nco*I, thereby producing complementary DNA fragments with sticky-ends (**Fig. 11B**). Ligation of the insert and the linearized vector with T4 ligase yielded the modified vector mod.pET-30- α B, which encodes for α B without N-terminal affinity-tag. This was validated by colony-PCR (**Fig. 11C**). DNA sequencing revealed the silent point mutation 213G→A (codon GAG→GAA) resulting in the wild-type residue E71. This mutation originated from the starting construct pET-30-Ek- α B. No further deviations were found. The DNA sequencing results proved that α B is embedded in the vector without any tag sequences and is flanked by the upstream *Nde*I-site, containing the translation start-codon ATG.

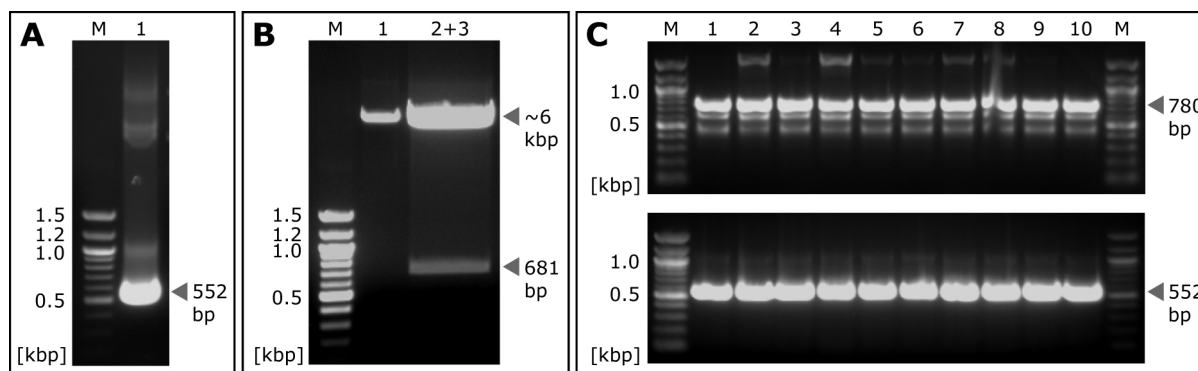


Fig. 11 Cloning of tag-free α B. Results of agarose gel-electrophoresis are shown. Lanes are indicated on top of each panel. Basepair-markers (M) are labeled on the left and target DNA fragments are indicated on the right of each panel. **(A)** α B insert (552 bp) with flanking *Nde*I and *Nco*I restriction sites as amplified by PCR (lane 1). **(B)** Digestion of the vector pET-30-Ek- α B with *Nco*I (lane 1) and with both *Nco*I/*Nde*I (lanes 2+3). The excised fragment encoding for α B with N-terminal affinity-tag is observed at the expected size of 681 bp. **(C)** Ten colonies, transformed with the putative vector mod.pET-30- α B and grown on LB-kanamycin plates, were picked and subject to colony-PCR. The PCR was performed either with T7 promoter/terminator primers (*Top*) or with primers flanking exclusively the α B sequence (*Bottom*). The presence of the 552 bp product indicates that the α B sequence itself was inserted into the vector, whereas the 780 bp fragment ensures the absence of the original tag sequence (approx. 930 bp would correspond to α B with the affinity-tag). All colonies contained the correct vector mod.pET-30- α B.

3.1.1.3 Overexpression and Purification of α B

Overexpression of α B revealed to be highly efficient, presumably due to its pronounced solubility. Ion-exchange chromatography employing the strong anion exchanger Q-Sepharose yielded a well-separated, though broad α B fraction (Fig. 12A,B). Subsequent size-exclusion chromatography of the α B fraction ensured a high purity grade for α B samples (Fig. 12C,D). Protein yields of unlabeled α B were on the order of 100 mg α B/L cell culture. For ^{13}C , ^{15}N - α B and ^2H , ^{13}C , ^{15}N - α B, protein yields decreased to approximately 40-60 mg α B/L cell culture.

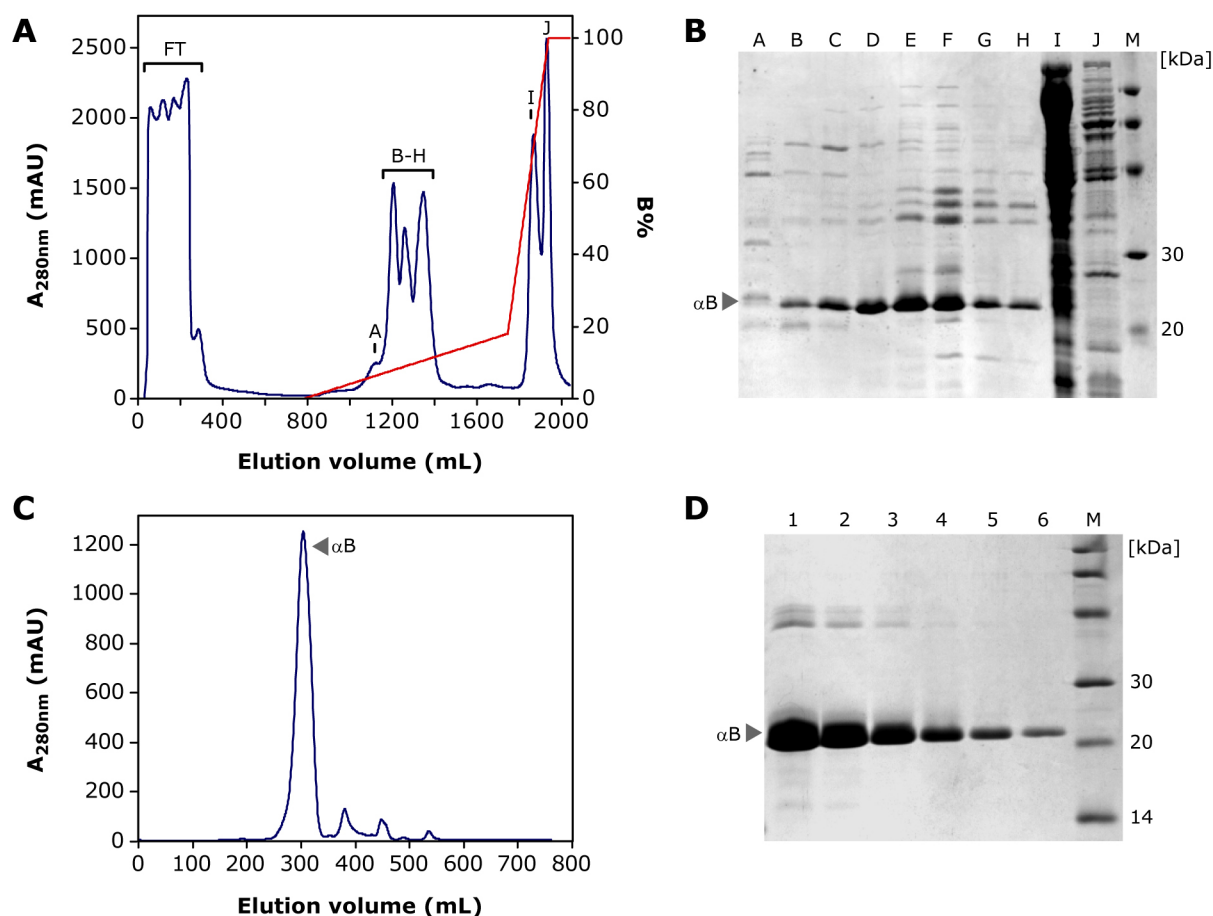


Fig. 12 Representative protein purification of human α B. (A) Anion-exchange chromatogram (Q-Sepharose) of cell-lysate eluted with a stepwise gradient of 1 M NaCl in PBS (buffer B). The absorption at 280 nm ($A_{280\text{nm}}$) and the fraction of buffer B during elution (B%) are shown in blue and red, respectively. The flow-through (FT) contained only small amounts of α B. Labels in the elution profile refer to lanes in (B). (B) SDS-PAGE of the elution profile shown in (A). α B eluted in a fairly broad peak at a NaCl concentration of 80-160 mM (lanes B-H). There were negligible amounts of α B in fractions of high-salt washing steps (lanes I and J). The molecular weight marker (M) is labeled and bands of α B are indicated. (C) Size-exclusion chromatogram (Superose-6) of the AEC pool. The elution profile shows a major peak at approx. 300 mL corresponding to full-length α B. (D) SDS-PAGE of purified α B after anion-exchange and size-exclusion chromatography. Lanes 1 to 6 were loaded with decreasing amounts of α B (8, 4, 2, 1, 0.5 and 0.25 μ g) to evaluate sample purity. The molecular weight marker (M) is labeled and bands of α B are indicated.

3.1.2 The Excised α -crystallin Domain: α B10m

3.1.2.1 Cloning of Construct

The isolated α -crystallin domain (ACD) of α B [57] was obtained similarly to the cloning procedure described for tag-free α B. The DNA sequence encoding for residues G64-V152 (α B10) was amplified by means of PCR (**Fig. 13A**). The resulting insert with appropriate 5'-*Nde*I and 3'-*Nco*I RE sites (297 bp) and the template vector mod.pET-30- α B were digested with the respective RE (**Fig. 13B**). Whereas *Nco*I digestion was quantitative, the performance of *Nde*I appeared to be critical for cloning success. The reaction with *Nde*I revealed challenging in particular for the insert, since a 9 bp overhang was required in order to achieve efficient restriction. Furthermore, the reaction was non-quantitative for the vector (**Fig. 13B**). Treatment with CIP was thus essential to avoid subsequent ligation of non-digested vector. Colony-PCR confirmed successful cloning of the ACD-insert (**Fig. 13C**). The amplified vector mod.pET-30- α B10 and further point mutants, e.g. α B10-N146D (α B10m), were subjected to DNA sequencing for verification.

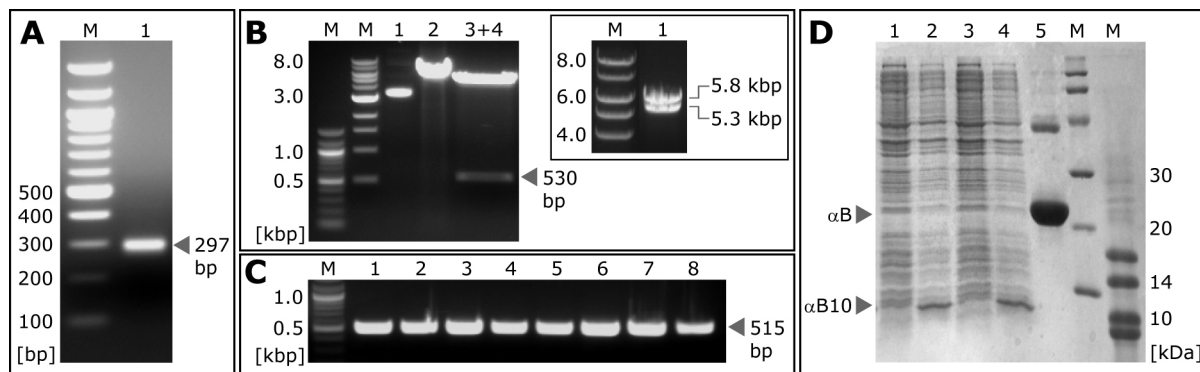


Fig. 13 Cloning of the isolated ACD construct α B10. Results of agarose gel-electrophoresis (**A-C**) and SDS PAGE (**D**) are shown. Relevant bands of marker lanes (M) are labeled. Target DNA and protein is highlighted with an arrow. (**A**) The ACD (α B10) insert (297 bp) with flanking *Nde*I and *Nco*I restriction sites as amplified by PCR (lane 1). (**B**) Digestion of the vector mod.pET-30- α B: super-coiled plasmid-DNA (lane 1), *Nco*I-digested, linearized vector (lane 2) and *Nco*I/*Nde*I-double-digested, linearized vector (lanes 3+4). The excised fragment encoding for full-length α B is observed at the expected size of 530 bp. The inset shows a diluted sample of the vector after double-digestion (lane 1) and illustrates the non-quantitative performance of *Nde*I. (**C**) Colony-PCR was performed with T7 promoter/terminator primers. The presence of the 515 bp product indicates that only the ACD sequence of α B was inserted into the vector (780 bp would correspond to full-length α B, see **Fig. 11C**). All eight colonies contained the correct vector mod.pET-30- α B10. (**D**) SDS-PAGE showing lysates of non-induced (lane 1 and 3) and IPTG-induced (lane 2 and 4) *E. coli* BL21-DE3 cells expressing the truncated construct α B10 (10.3 kDa). Full-length α B (20.2 kDa) is shown as a reference (lane 5).

3.1.2.2 Overexpression and Purification of α B10m and its Mutants

The ACD construct α B10m and its point mutants were expressed in *E. coli* BL21-DE3 cells (**Fig. 14D**). α B10m overexpression was decreased in comparison to full-length α B. More importantly, the truncated construct was highly susceptible to proteolytic degradation during the expression and purification procedure. For isotopically-enriched α B10m, the expression was carried out for 16 h at 22 °C. Increased amounts of ^{13}C -glucose (4 g/L) were necessary to efficiently avoid starvation of cells and thus proteolytic decomposition. Adding protease inhibitors to all buffer solutions impeded degradation during the purification procedure.

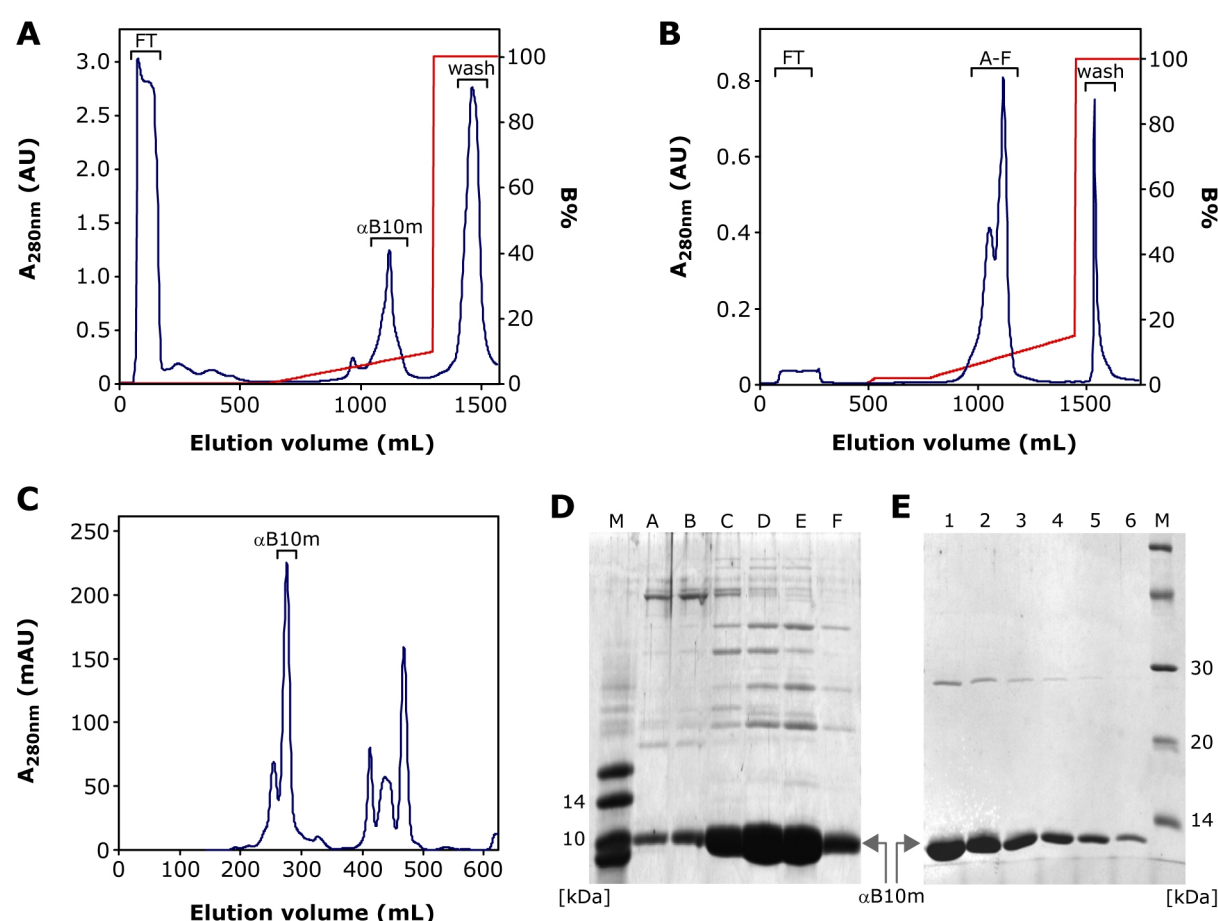


Fig. 14 Representative protein purification of $^{13}\text{C},^{15}\text{N}$ - α B10m. (A) AEC (DEAE-Sepharose) of cell-lysate eluted with a stepwise gradient of 1 M NaCl in PBS (buffer B). The absorption at 280 nm ($A_{280\text{nm}}$) and the fraction of buffer B during elution (B%) are shown in blue and red, respectively. The flow-through (FT) and the high-salt wash fraction (wash) contained negligible amounts of α B10m. The α B10m fraction is indicated and was subject to strong AEC as shown in (B). (B) Same as in (A), but using a Q-Sepharose column. The fractions containing α B10m are labeled (A-F) and analyzed by SDS-PAGE in (D). (C) SEC (Superdex-75) of the AEC-Q pool (lanes C-F in (D)). The elution profile shows a major peak at approx. 280 mL corresponding to α B10m. (D) SDS-PAGE of the fractions (A-F) shown in (B). The molecular weight marker is indicated (M). (E) SDS-PAGE of purified α B10m after AEC and SEC. Lanes 1 to 6 were loaded with decreasing amounts of α B10m (5.2, 2.6, 1.3, 0.6, 0.3 and 0.15 μg) to evaluate sample purity and potential proteolysis. The molecular weight marker is indicated (M) and labeled.

Both, weak and strong anion-exchange chromatography was employed to separate α B10m from the cell-lysate (**Fig. 14A,B**). The protein required both purification steps before being applied to the final size-exclusion chromatography (**Fig. 14C**). To minimize protein impurities, only narrow fractions were pooled (**Fig. 14D**). Finally, the purified α B10m was analyzed by SDS-PAGE, with respect to its purity and degradation status (**Fig. 14E**). Solely intact protein was used for subsequent experiments and further verified by NMR (see below). All mutants of α B10m followed the same protocol. Protein yields amounted to 20 mg/L cell culture for unlabeled α B10m, whereas 40 mg/L cell culture were achieved for ^{13}C , ^{15}N - α B10m. The increase was potentially due to the longer expression periods at 22 °C. The average yield for ^{13}C , ^{15}N -enriched mutants of α B10m was decreased to approximately 10 mg/L cell culture.

3.2 α B-crystallin and Metal-Binding

3.2.1 Effects of Metals on the Morphology of α B Multimers

Initial negative-stain EM images indicated an augmented size of α B particles that were incubated with Cu(II) (**Fig. 15A**). To investigate and to better quantify this effect on the quaternary structure, analytical SEC and DLS experiments were performed. The SEC elution profile of apo- α B yielded a molecular weight of 518 kDa corresponding to a 26-mer as the major species. This is in agreement with earlier studies [53]. In the presence of Cu(II) and Zn(II), the elution peaks were strongly broadened with the original peak slightly shifted towards higher molecular weights. More importantly, the peaks featured distinct shoulders, which revealed molecular weights of approximately 660 kDa (33-mer) and 700 kDa (35-mer) for Cu(II)- and Zn(II)- α B, respectively (**Fig. 15B**). The metal ion Ca(II) basically reproduced the results for apo- α B with only minor changes (498 kDa).

DLS experiments were conducted to yield information about the hydrodynamic size of α B multimers. Upon addition of Cu(II), the hydrodynamic diameter D_h of α B particles increased from 14.7 ± 0.2 nm to 19.0 ± 0.5 nm (**Fig. 15C**). This observation was accompanied by an increase of the polydispersity index $Pd\%$ from 32.9 ± 0.9 % to 36.5 ± 1.8 %. The parameter $Pd\%$ is thereby a measure for the heterogeneity of the oligomeric ensemble. Zn(II) showed an

even more pronounced effect on D_h (21.2 ± 0.3 nm) and $Pd\%$ (40.4 ± 0.9 %). By contrast, Ca(II) did not affect D_h (14.7 ± 0.1 nm) and $Pd\%$ (31.7 ± 0.7 %). Results from SEC and DLS measurements and the resultant oligomer stoichiometries are compared in **Fig. 15D**. The discrepancies between the two methods most likely arise from the R_H^6 dependence of the scattering intensity in DLS experiments. The exact hydrodynamic size of a heterogeneous distribution is thus difficult to access. In summary, the data suggests metal-induced augmentation of αB oligomers. This is consistent with published results [68]. Moreover, the data suggests increased heterogeneity of αB assemblies upon addition of the metal ions Cu(II) and Zn(II), but not Ca(II).

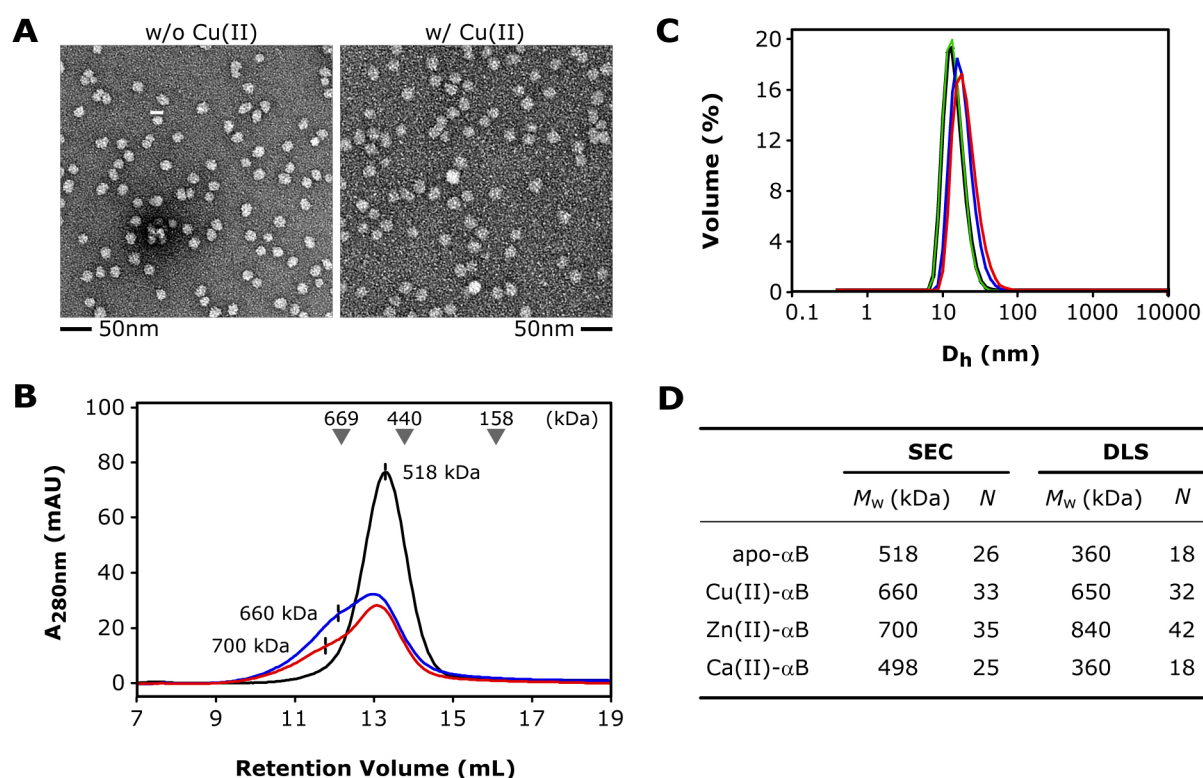


Fig. 15 Effects of metal-binding on the assembly of αB . (A) EM images of negatively-stained αB particles in the absence (Left) and presence of Cu(II) (Right). Scale bars are shown at the bottom. The images were kindly recorded by Martina Ringling (FMP, Germany). (B) Analytical SEC on a Superose 6 column. The absorption at 280 nm (A_{280nm}) versus the retention volume is plotted. Elution profiles of αB in the absence (black) and in the presence of Cu(II) (blue) or Zn(II) (red), respectively, are shown. Molecular weights and retention volumes of standard proteins are indicated (Top) and were used for calibration ($R^2 = 0.998$). (C) DLS experiments on αB multimers in the absence of metal ions (black) and in the presence of Cu(II) (blue), Zn(II) (red) or Ca(II) (green), respectively. Volume-weighted size distributions are shown. (D) Comparison of the SEC- and DLS-derived molecular weights (M_w) and the corresponding number of monomeric subunits (N) for the respective αB species in the absence and presence of metal ions.

3.2.2 Modulation of α B Chaperone Activity by Cu(II)

The increase of light-scattering during heat-induced aggregation of the lens-specific client protein β_L -crystallin (β_L) was used to monitor the chaperone ability of α B. The amorphous aggregation of β_L at 60 °C gave rise to a steep scattering profile, which reached a plateau after approximately 25 minutes (**Fig. 16A**). Addition of the chaperone reduced protein precipitation in a concentration dependent manner. At an equimolar ratio of α B and β_L , the light-scattering intensity after 30 minutes decreased to approximately 35% with respect to the reference experiment. In the presence of Cu(II), this level of protection was already reached at a 4-fold excess of β_L , implying that the chaperone efficiency of α B is elevated by the divalent metal ion (**Fig. 16B**). Higher concentrations of α B reduced β_L aggregation to about 20%. Notably, incubation of α B at 60 °C yielded a constant baseline illustrating that α B itself does not precipitate under the experimental conditions (**Fig. 16A**). Increased amounts of Cu(II) destabilized β_L and induced severe aggregation of the client protein.

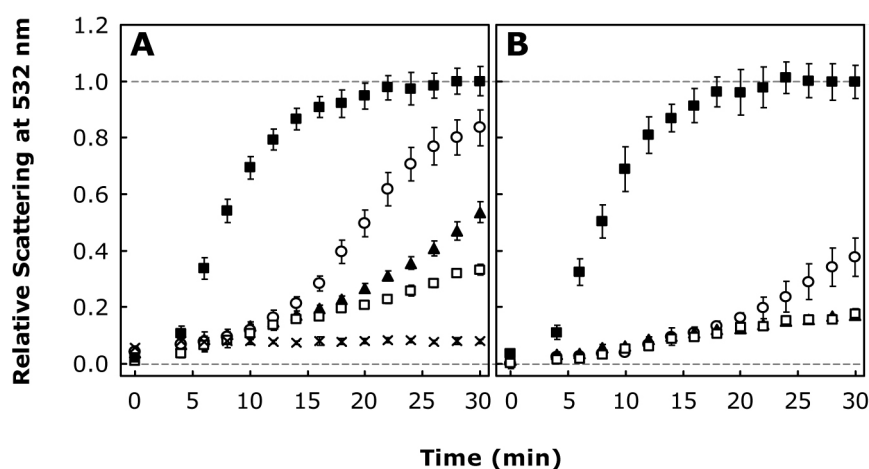


Fig. 16 Chaperone activity of α B with respect to the heat-induced aggregation of lens-specific β_L -crystallin. The chaperone property was monitored in the absence (**A**) and presence of Cu(II) (**B**). The client protein β_L (2 μ M) was heated to 60 °C in the absence (■) and presence of 0.5 μ M (○), 1 μ M (▲) and 2 μ M (□) α B. (×) denotes the scattering profile for 2 μ M α B alone. Experiments were performed in triplicate.

The enzyme citrate synthase (CS) was used as another client system to examine the effects of Cu(II) on the chaperone abilities of α B. As in the case of β L, Cu(II) dramatically increased the susceptibility of CS to aggregation (**Fig. 17A**). In the absence of Cu(II), α B clearly attenuated CS aggregation in a concentration-dependent manner (**Fig. 17B**). However, considering the high chaperone concentrations employed, the efficiency of protection was less pronounced for the client protein CS compared to that for β L. At an equimolar ratio of CS and α B, client aggregation was slightly decreased in the initial phase, but caused the same extent of light scattering after 120 min. Upon addition of Cu(II), the level of protection by the chaperone was increased predominantly at the beginning of CS aggregation (**Fig. 17D-F**). The weak Cu(II)-chelator glycine did not affect the strong aggregation of Cu(II)-CS, whereas EDTA restored the primary behavior of CS (**Fig. 17C**). Hence, CS is capable to specifically bind Cu(II), and its metal-dependent aggregation behavior complicates the analysis of aggregation profiles.

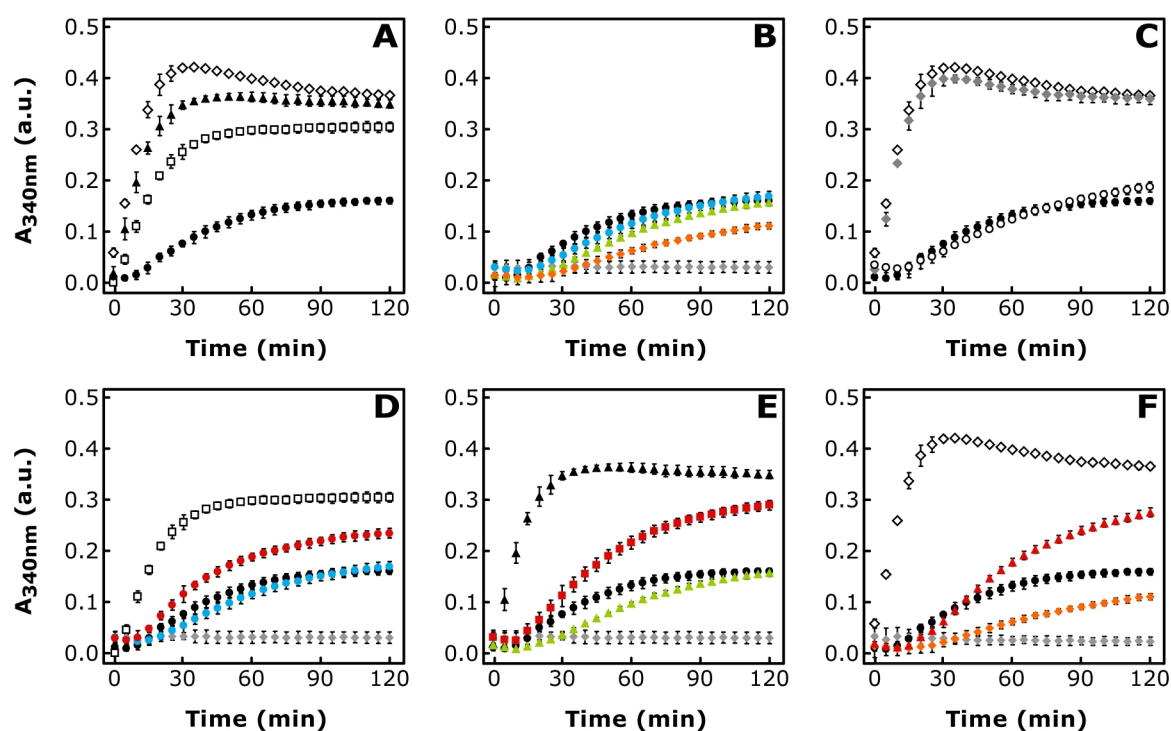


Fig. 17 Chaperone activity of α B with respect to the heat-induced aggregation of citrate synthase (CS). Light scattering due to the aggregation of CS (2 μ M) at 42 $^{\circ}$ C was monitored by measuring the absorbance at 340 nm ($A_{340\text{nm}}$). Aggregation kinetics were measured in triplicate. **(A)** Cu(II)-dependence of CS aggregation: CS in the absence (●) and presence of 2 μ M (□), 4 μ M (▲) and 8 μ M (◇) Cu(II). **(B)** Inhibition of CS aggregation by α B: CS in the absence (●) and presence of 2 μ M (◆), 4 μ M (▲) and 8 μ M (●) α B. (●) denotes 8 μ M α B alone. **(C)** Effect of Cu(II)-chelators. CS in the absence (●) and presence of: 8 μ M Cu(II) (◇); 8 μ M Cu(II), 32 μ M Gly (◆); 8 μ M Cu(II), 16 μ M EDTA (○). **(D)** Chaperone activity of α B in the presence of Cu(II): CS in the absence (●) and presence of: 2 μ M Cu(II) (□); 2 μ M Cu(II), 2 μ M α B (●); 2 μ M α B (◆). (●) denotes 8 μ M α B alone. **(E)** CS in the absence (●) and presence of: 4 μ M Cu(II) (▲); 4 μ M Cu(II), 4 μ M α B (■); 4 μ M α B (▲). (●) denotes 8 μ M α B alone. **(F)** CS in the absence (●) and presence of: 8 μ M Cu(II) (◇); 8 μ M Cu(II), 8 μ M α B (▲); 4 μ M α B (●). (●) denotes 8 μ M α B in the presence of 8 μ M Cu(II).

3.2.3 Stoichiometry of Cu(II)-binding: ICP-MS Experiments

ICP-MS experiments on full-length α B and the core domain α B10m were performed in order to assess the stoichiometry of the interaction between α B and Cu(II) as well as to investigate the binding capabilities of the isolated ACD (α B10m). The experiments revealed comparable Cu(II):protein stoichiometries of 1.18 ± 0.12 and 1.13 ± 0.12 for α B and α B10m, respectively. Similarly, Zn(II) yielded stoichiometries of 1.03 ± 0.10 (α B) and 0.79 ± 0.08 (α B10m), respectively. Both proteins thus bind one metal ion per monomeric subunit.

3.2.4 Affinity and Stoichiometry of Cu(II)-binding: ITC Studies

ITC investigations of oligomeric α B and dimeric α B10m were performed employing the chelate Cu(Gly)₂ (see Chapter 2.4.4). The latter was shown to facilitate the investigation of specific Cu(II)-binding to proteins in ITC studies and to stabilize Cu(II) at physiological pH [108]. In ITC experiments, α B10m and full-length α B revealed strong exothermic heat changes upon injection of Cu(II) with extensive enthalpic contributions to the binding reaction (**Fig. 18A,B**). The ITC curves were fitted assuming an one-site binding model, and the extracted binding parameters are given in the caption of **Fig. 18**. Considering the competition between the target protein and the weak chelator glycine, the real dissociation constant (K_d) can be estimated (see Chapter 2.4.4). The respective K_d values are on the order of 170×10^{-12} M for full-length α B and 31×10^{-12} M for α B10m. The ITC-derived stoichiometries N amount to 1.63 ± 0.03 (α B) and 1.03 ± 0.01 (α B10m), respectively. Picomolar-range affinity was already reported for full-length α B with a K_d of 11×10^{-12} M and a stoichiometry N of 1.30 ± 0.02 [68], which is in agreement with the results presented here. The ITC-derived stoichiometry of 1.63 ± 0.03 for α B deviates from the ICP-MS value (1.18 ± 0.12) and from the published stoichiometry (1.30 ± 0.02) [68]. Conformational and morphological changes of the α B oligomer were observed upon addition of Cu(II) (see Chapter 3.2.1). Such secondary processes induced by Cu(II)-binding also contribute to the observed isotherm, complicate the fitting-analysis and potentially distort the ITC-derived binding parameters for full-length α B. Apart from that, binding affinities and stoichiometries for full-length α B and α B10m with respect to Cu(II) are fairly consistent. The isolated ACD is therefore sufficient to coordinate Cu(II), and involvement of the terminal domains can be excluded.

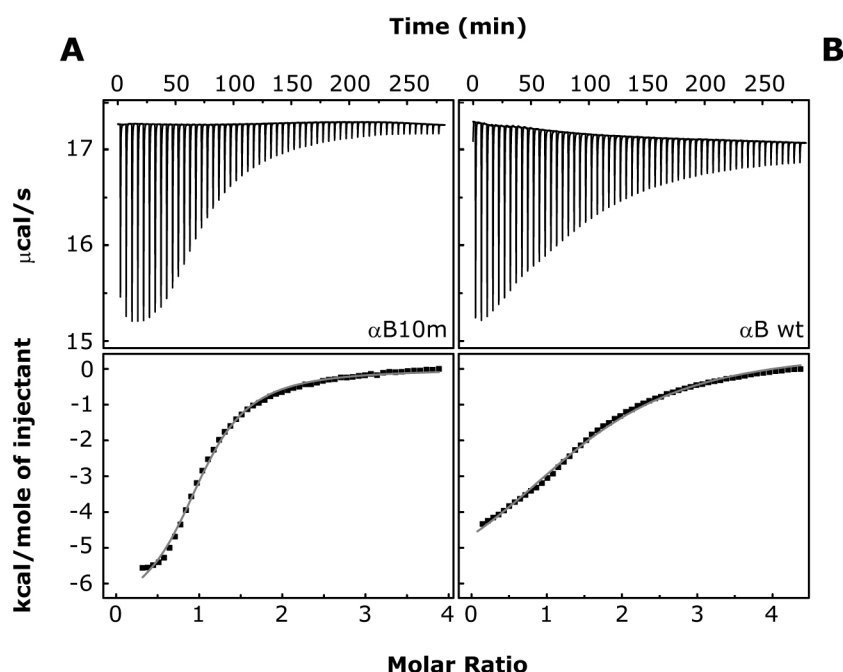


Fig. 18 Specific Cu(II)-binding to α B10m (A) and α B (B) as studied by ITC. Typical ITC raw data is shown in the top panels. Curve-fitting analysis of the binding isotherm (Bottom) gave the following parameters: apparent association constants ($K_{a,app}$, in M^{-1}), enthalpic changes (ΔH , in cal mol^{-1}), entropic changes (ΔS , in $\text{cal mol}^{-1} \text{K}^{-1}$) and binding stoichiometries (N). The derived thermodynamic parameters for Cu(II)-binding to α B10m and α B, respectively, are as follows: $K_{a,app} = 8.02 (\pm 0.41) \times 10^4$, $\Delta H = -6987 \pm 107$, $\Delta S = -0.998$ and $N = 1.03 \pm 0.01$ for the truncated α B10m; $K_{a,app} = 1.53 (\pm 0.07) \times 10^4$, $\Delta H = -7293 \pm 164$, $\Delta S = -5.31$ and $N = 1.63 \pm 0.03$ for full-length α B.

3.2.5 Fluorescence Quenching: Cu(II)-Affinity of the ACD

As reported in an earlier study, binding of Cu(II) to full-length α B induces quenching of tyrosine fluorescence [68]. The corresponding titration experiments yielded a dissociation constant K_d of $9.75 \times 10^{-12} \text{ M}$ for α B multimers [68]. Here, this approach was employed to further characterize the binding-interaction between Cu(II) and the isolated ACD construct α B10m. The excised core domain features only one tyrosine residue in its sequence. Y122 is located at the dimer interface. The fluorescence of the sole tyrosine and its quenching can be monitored during titration of Cu(II) (**Fig. 19A**). Plotting the extent of fluorescence quenching versus the ligand concentration gives the binding curve (**Fig. 19B**). As shown for the ITC binding studies, Cu(II) was employed in its bis-glycine complex $\text{Cu}(\text{Gly})_2$, and the apparent binding constant was corrected for competition. Thereby, a K_d of $42 \times 10^{-12} \text{ M}$ for Cu(II)- α B10m was obtained, which is in agreement with the published K_d for full-length α B [68]. The result is also consistent with the ITC-derived K_d for α B10m ($31 \times 10^{-12} \text{ M}$), confirming the picomolar binding-affinity of the isolated ACD towards Cu(II).

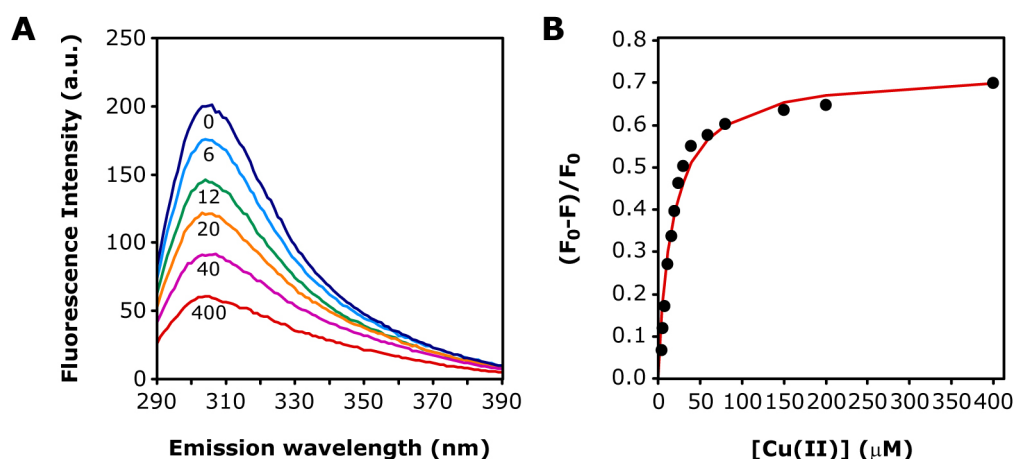


Fig. 19 Fluorescence quenching of the sole tyrosine Y122 at the dimer interface of α B10m. (A) Representative fluorescence spectra of α B10m (20 μ M) obtained in the absence and presence of different concentrations of Cu(II) (in μ M). The excitation wavelength λ_{ex} was set to 275 nm. (B) Extent of fluorescence quenching $(F_0-F)/F_0$ plotted versus the Cu(II) concentration. F_0 and F represent the fluorescence intensities ($\lambda_{\text{em}} = 304$ nm) in the absence and presence of Cu(II), respectively. The derived apparent $K_{\text{d,app}}$ of 17×10^{-6} M corresponds to a real K_{d} of 42×10^{-12} M.

3.2.6 Secondary Structure and Thermal Stability

Far-UV CD spectra of α B10m clearly displayed high content of β -strand secondary structure as expected for the known β -sandwich-fold of the ACD (**Fig. 20A**). The corresponding minimum of the spectrum at a wavelength of 216 nm was even more pronounced in the presence of Cu(II) (**Fig. 20B**). Increased β -strand proportion was also observed for the ACD by NMR spectroscopy (see below). Elevated temperature (75 $^{\circ}\text{C}$) induced random-coil conformation (minimum at 201 nm) for both the apo- and holo-form of α B10m, while still retaining the β -strand portion. Apparently, α B10m and its Cu(II)-bound state unfolded partially upon heating, and this process was reversed at ambient temperature (**Fig. 20A,B**). Monitoring the random-coil fraction during temperature scans yielded sigmoidal melting curves, which revealed similar melting temperatures T_{m} of 43.2 $^{\circ}\text{C}$ and 42.6 $^{\circ}\text{C}$ for Cu(II)-free and Cu(II)-bound α B10m, respectively (**Fig. 20C**). The CD investigations thus show that Cu(II), although raising the fraction of β -strand conformation, apparently does not affect the thermal stability of the isolated ACD. This, however, exclusively applies to the partial unfolding process that was monitored at about 43 $^{\circ}\text{C}$, presumably occurring in a specific region within the protein structure.

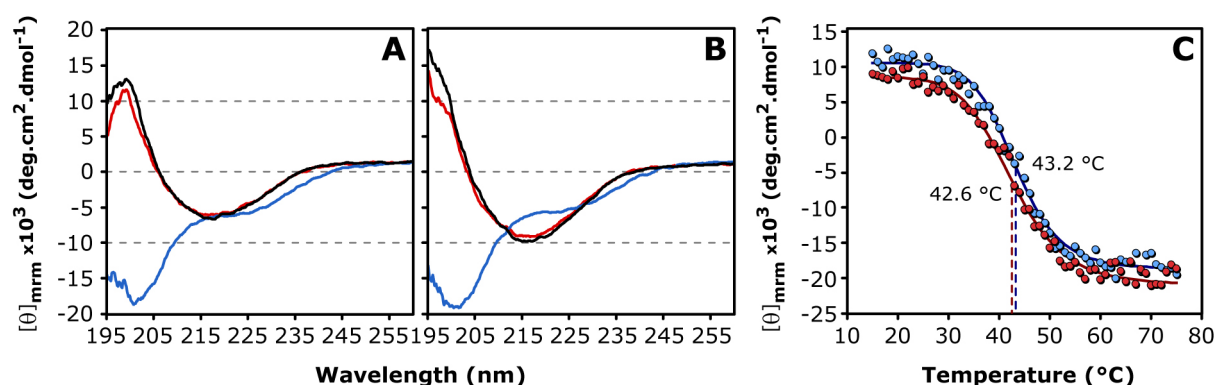


Fig. 20 Secondary structure and thermal unfolding of apo-αB10m and Cu(II)-αB10m. Far-UV CD spectra are shown for αB10m in the absence (A) and presence of Cu(II) (B). Spectra were recorded at temperatures of 15 °C (black), 75 °C (blue) and 15 °C after heating (red). (C) Thermal unfolding of apo-αB10m (blue) and Cu(II)-αB10m (red) monitored by measuring the mean residue ellipticity $[\theta]_{\text{mrm}}$ at a wavelength of 201 nm (random-coil structure). Data points (filled circles) are shown for temperature increments of 1 °C. Curve-fitting (continuous lines) yielded melting temperatures T_m of 43.2 °C and 42.6 °C for apo-αB10m and Cu(II)-αB10m, respectively (indicated by dashed lines).

The far-UV CD spectra of full-length αB were characterized mainly by contributions from β-strand secondary structure (Fig. 21A). As in the case of αB10m, the addition of Cu(II) to αB multimers caused the β-strand fraction to increase (Fig. 21B). Heating of the samples induced the formation of protein aggregates, which revealed high structural order (Fig. 21A,B). Moreover, the initial spectra of Cu(II)-free and Cu(II)-bound αB were not restored by cooling, indicative of irreversible aggregation processes upon heating. The analysis of CD melting curves, obtained by monitoring the mean residue ellipticity $[\theta]_{\text{mrm}}$ at 216 nm, was highly complicated by this irreversible aggregation behavior (Fig. 21C). The high-temperature-plateaus of the melting curves were insufficiently defined or distorted due to aggregation events. Therefore, the derived T_m values of 69.8 °C (apo-αB) and 51.1 °C (Cu(II)-αB) may not properly reflect the actual thermodynamic stabilities of the proteins. DLS experiments performed at elevated temperatures illustrated that neither the apo- nor the holo-state of αB forms protein aggregates at 60 °C (Fig. 22A). At a temperature of 85 °C, formation of large protein aggregates occurred in both cases. Interestingly, the aggregates of Cu(II)-αB were not observable visually, in contrast to those of the apo-state. In conclusion, the binding of Cu(II) induces a structural transition, which is accompanied by the pronounced tendency to form higher oligomers at 60 °C (Fig. 22A).

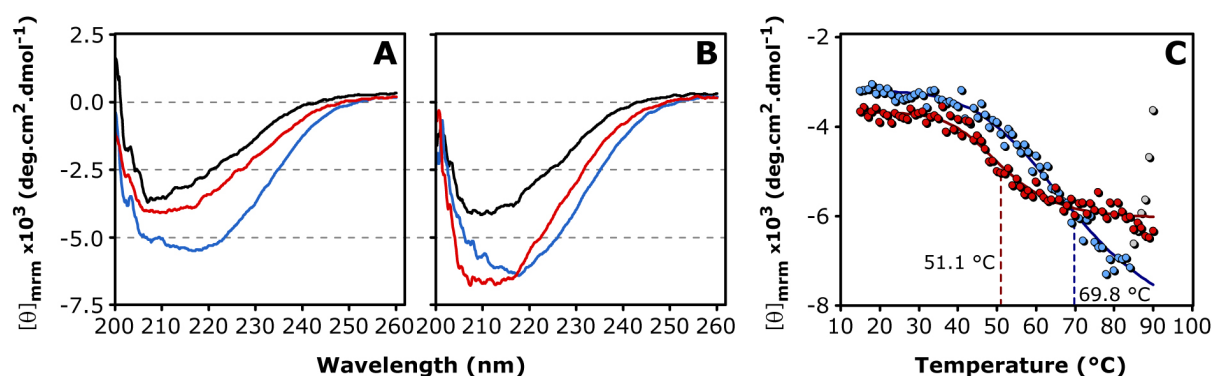


Fig. 21 Secondary structure and thermal unfolding of apo- α B and Cu(II)- α B. Far-UV CD spectra are shown for full-length α B in the absence (**A**) and presence of Cu(II) (**B**). Spectra were recorded at temperatures of 15 °C (black), 85 °C (blue) and 15 °C after heating (red). (**C**) Thermal unfolding and aggregation of apo- α B (blue) and Cu(II)- α B (red) were monitored by measuring the mean residue ellipticity $[\theta]_{\text{mm}}$ at a wavelength of 216 nm (β -strand structure). Data points (filled circles) are shown for temperature increments of 1 °C. Curve-fitting (continuous lines) yielded melting temperatures T_m of 69.8 °C and 51.1 °C for apo- α B and Cu(II)- α B, respectively (indicated by dashed lines). Apo- α B showed extensive aggregation above 84 °C (grey circles). The corresponding data points were excluded from the curve-fitting.

Temperature-dependent aggregation curves revealed the presence of two processes between 60 °C and 75 °C, with the first transition representing the augmentation of α B multimers and with the second transition being tantamount to irreversible protein aggregation (**Fig. 22B**). The aggregation experiments further showed that Cu(II) only marginally affected this behavior, whereas the intervention of Zn(II) considerably increased the aggregation propensity of α B (**Fig. 22B**). The experiments shown here illustrate that i) the thermal stability of the ACD is strengthened in the context of the higher-order assembly of α B, ii) Cu(II) induces pronounced β -strand conformation in terms of α B multimers as well as within the ACD itself, and iii) Cu(II) increases the tendency of α B to form larger oligomers up to temperatures of approximately 65 °C with marginal effects on the aggregation events thereafter.

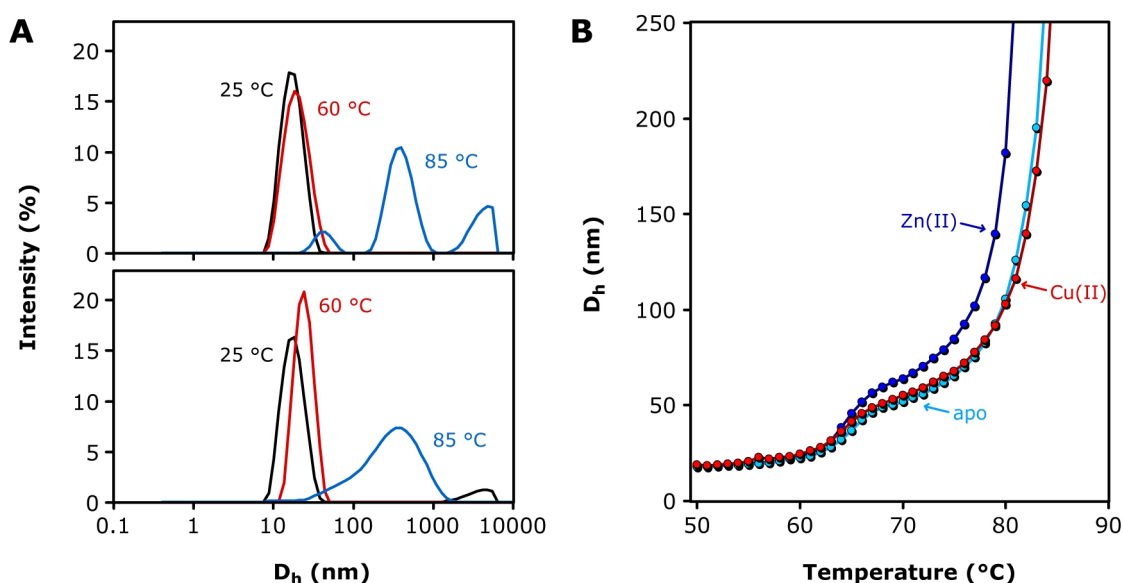


Fig. 22 Aggregation of α B multimers at elevated temperatures. (A) DLS size distributions of α B in the absence (Top) and presence of Cu(II) (Bottom) measured at 25 °C (black), 60 °C (red) and 85 °C (blue). (B) Temperature-dependence of α B particle size (D_h). Unless otherwise stated, the samples were measured at pH 7.5. Aggregation curves are shown for apo- α B (●), Cu(II)- α B (●) and Zn(II)- α B (●). Data points are connected by lines for clarity. Solely, the temperature range from 50 °C to approximately 80 °C is depicted to better visualize the size transitions.

3.2.7 Effects of Cu(II) on the Quaternary Structure of the ACD

As illustrated in **Fig. 23A**, the SEC elution profile of apo- α B10m pointed towards a trimeric state of the ACD construct with a molecular weight M_w of 33.3 kDa. Upon addition of Cu(II), the retention volume slightly increased with a corresponding M_w of 31.8 kDa. Moreover, the elution peak of Cu(II)- α B10m was broadened with the low-molecular-weight shoulder extending towards dimeric and monomeric states. DLS experiments likewise revealed Cu(II)-dependent dissociation of α B10m oligomeric states. The intensity-weighted size distributions showed a decrease in the hydrodynamic diameter D_h from 6.15 ± 0.25 nm to 5.68 ± 0.08 nm for apo- α B10m and Cu(II)- α B10m, respectively (**Fig. 23B**, bottom). Assuming globular particles, these values correspond to molecular weights of 49.3 kDa (apo- α B10m) and 38.7 kDa (Cu(II)- α B10m), respectively. By contrast, the mass distributions (volume-weighted size distributions) gave hydrodynamic diameters of 4.39 ± 0.09 nm and 4.14 ± 0.05 nm in the absence and presence of Cu(II), respectively (**Fig. 23B**, top). The estimation of M_w yielded values of 20.8 kDa (apo- α B10m) and 18.5 kDa (Cu(II)- α B10m), respectively. It should be noted that the large discrepancy between the two weightings arises from the broad size distribution of α B10m ($Pd\%$ of 37.8).

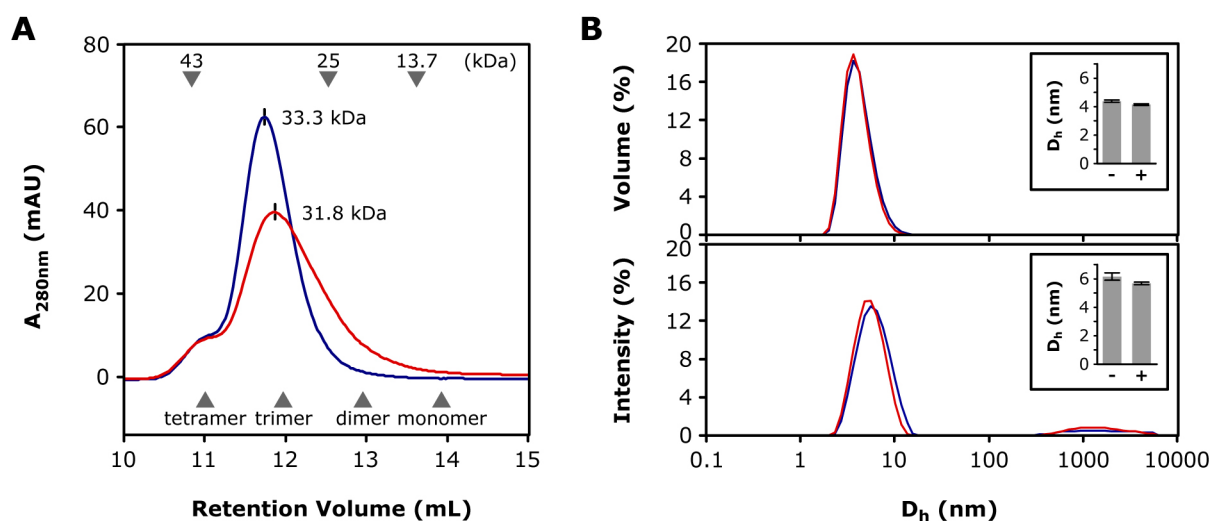


Fig. 23 The oligomeric state of α B10m and the effects of Cu(II). (A) Analytical size-exclusion chromatography of apo- α B10m (blue) and Cu(II)- α B10m (red). Calibration of the column yielded molecular weights of 33.3 kDa and 31.8 kDa for the apo- and holo-form, respectively. The molecular weights of standard proteins are indicated by an arrow at their respective retention volume (Top) and were used for calibration ($R^2 = 0.999$). Theoretical peak positions for different oligomeric states of α B10m (10.3 kDa monomer) are indicated by arrows (Bottom). (B) DLS experiments employing α B10m in the absence (blue) and presence of Cu(II) (red). Size distributions are intensity-weighted (bottom panel) and volume-weighted (top panel). In each case, the obtained hydrodynamic diameters D_h are illustrated in the insets.

Apparently, α B10m populates higher oligomeric states, which accordingly produce higher scattering intensities and thereby cause a shift in the hydrodynamic size towards larger particles. Volume-weighted size distributions are thus the more representative measure of the abundant species in solution, which is the dimeric state for α B10m. However, binding of Cu(II) to the ACD shifts the equilibrium towards the dimeric or even monomeric state. Cu(II)-induced dissociation of α B10m oligomeric forms is also supported by the initial endothermic process in the ITC experiments (Fig. 18A).

NMR ^{15}N T_1/T_2 ratios obtained for apo- α B10m at different protein concentrations and for Cu(II)- α B10m yielded information on the rotational correlation time τ_c and thus on the multimeric state of the proteins [253,254]. The theoretical tumbling correlation time $\tau_{c,\text{theo}}$ at 22 °C is on the order of 8 ns and 15 ns for the monomeric and the dimeric state, respectively (see Chapter 2.5.1.5). At a monomer concentration of 1 mM, τ_c amounted to 18.9 ns. The correlation time at a monomer concentration of 4 mM increased to 22.6 ns, confirming the tendency to form higher oligomers. By contrast, the rotational diffusion of 1 mM α B10m was accelerated significantly in the presence of Cu(II) yielding a τ_c of 13.9 ns. This decrease relative to the apo-form indicates that Cu(II) provokes dissociation of α B10m dimers and higher oligomers.

3.2.8 Crystallization of the ACD

Based on the fact that various ACD constructs of α B and other sHSPs had been successfully crystallized [55,56,269], attempts were made to investigate the Cu(II)-bound state of α B10m by X-ray crystallography. Initial fine-screenings were based on the published crystallization condition of the α B ACD, i.e. at high pH and with MPD as the precipitant [55]. These initial trials were not successful for Cu(II)-bound α B10m. By contrast, two crystals were obtained using a commercially available MPD screen. The **Fig. 24A,B** shows images of the protein crystals and the corresponding crystallization conditions. Crystal growth was very slow (60 days of incubation at 20 °C) due to the reduced concentration of the protein (10 mg/mL) and the precipitant (30-40% MPD). The obtained crystals were tested for diffraction and confirmed to be protein crystals. Due to the low resolution, no dataset was acquired. Attempts to reproduce the crystallization failed.

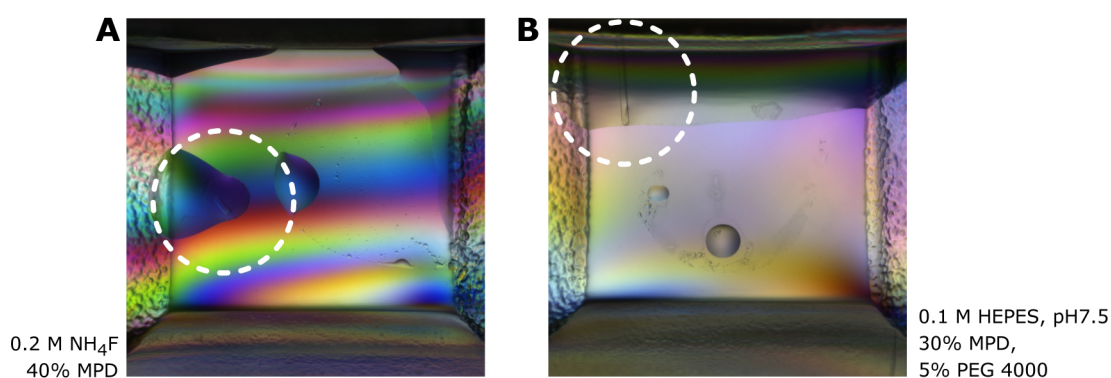


Fig. 24 Crystallization trials with Cu(II)- α B10m. Protein crystals obtained for Cu(II)- α B10m (10 mg/mL) and the corresponding crystallization conditions are shown in (A) and (B), respectively. Positions of protein crystals are highlighted by white circles for clarity. The protein crystals were kindly tested for diffraction at BESSY II beam line by Katja Faelber and Yvette Roske (Group of Oliver Daumke and Udo Heinemann, respectively, MDC, Berlin).

3.2.9 NMR Investigations on Full-length α B Multimers

To monitor the effects of Cu(II) on the structure of α B multimers, we performed MAS NMR experiments employing the FROSTY (Freezing Rotational diffusion Of protein Solutions at low Temperature and high viscosity) approach. In contrast to conventional solid-state MAS NMR, the protein was not precipitated, but investigated in solution (see Chapter 3.4.1). PDSD spectra of apo- and Cu(II)- α B were recorded (for full spectra see Appendix **Fig. 71**). Resolved correlations of residues D109, G112 and I114 disappeared in the presence of paramagnetic Cu(II) (**Fig. 25A-C**). These residues are located at the AP interface of the ACD dimer. The resonances of M68 (β 2- β 3-loop) revealed distinct chemical shift perturbations (CSP) for Cu(II)- α B (**Fig. 25D**). Binding of Cu(II) also affected the resonances of L89 (β 3- β 4-loop) and A57 (N-terminal domain) (**Fig. 25E-F**). Similar effects were observed in the presence of diamagnetic Zn(II), i.e. comparable CSP for M68 and broadening of the A57 and G112 resonances (**Fig. 25b,d,f**). The perturbations involving A57 and M68 indicate structural changes at the N-terminal domain upon metal-binding.

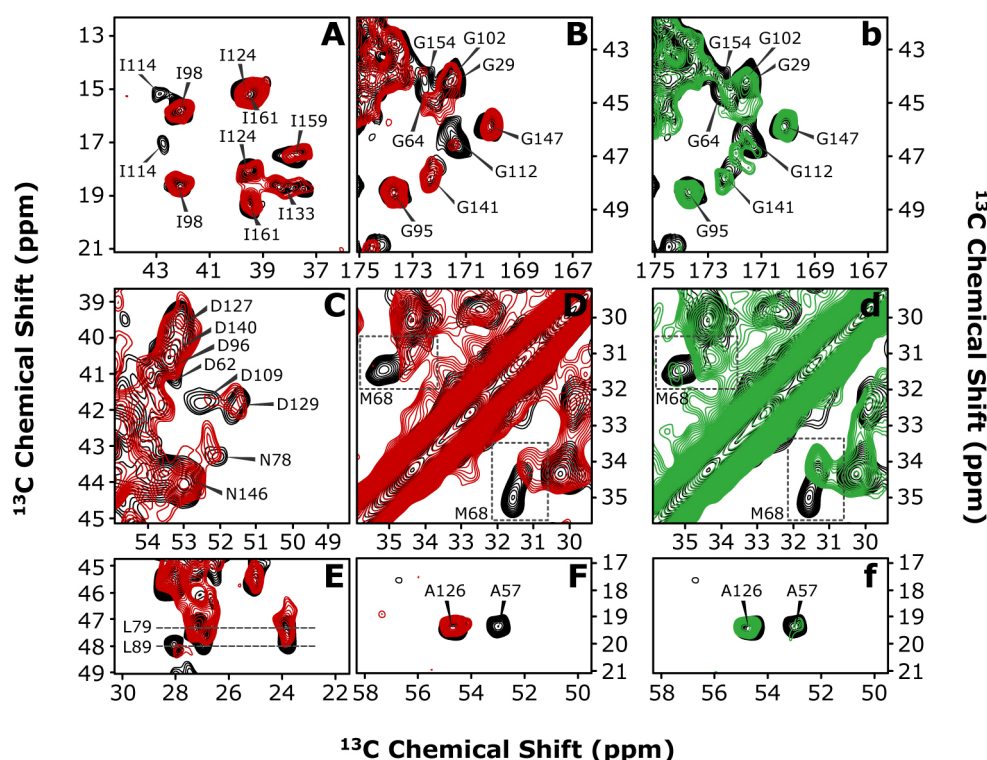


Fig. 25 Monitoring the effects of metal-binding to α B multimers by MAS NMR. Selected regions of PDSD spectra of full-length α B in the absence (black) and presence of Cu(II) (red) or Zn(II) (green), respectively. Correlations of (A) Ile (C β -C δ / γ), (B, b) Gly (C α -C'), (C) Asp/Asn (C α -C β), (D, d) Met (C β -C γ), (E) Leu (C β -C γ /C δ , connected by dashed lines) and (F, f) Ala (C α -C β) are shown. Assignments are taken from [57].

3.2.10 NMR Investigations on the Dimeric α B10m

The ICP-MS and ITC results demonstrated that the ACD is sufficient to coordinate Cu(II). Furthermore, the MAS NMR investigations on the large α B assemblies pointed towards an involvement of interfacial residues in Cu(II)-coordination. The protein construct α B10m represents the excised ACD of human α B and is accessible to solution-state NMR spectroscopy [57]. α B10m was therefore employed to refine the Cu(II)-binding site.

3.2.10.1 Resonance Assignment of apo- α B10m

Assignment of protein backbone resonances was accomplished by acquisition of the standard triple-resonance experiments HNCA, HN(CO)CA, HNCOC, and HN(CA)CO. Despite the expected molecular weight of 20.6 kDa for the ACD dimer, more sophisticated experiments, such as HNCACB or HN(CO)CACB involving the C β chemical shift, were not feasible. However, all the expected amide resonances of apo- α B10m (85 non-proline residues) were unambiguously assigned except that of S139, which is missing in the spectrum (for chemical shift list see Appendix Tab. 9). ^1H - ^{13}C methyl correlations were assigned by combining chemical shift information from (H)CCH-TOCSY and CCCO 3D spectra. Substantial signal overlap was observed for the leucine region.

As demonstrated below, the Cu(II)-bound form of α B10m had to be reassigned due to the large CSP, induced by the metal ion upon binding. **Fig. 26** shows exemplarily the sequential walk along the backbone of residues L131-S138 using the pair of 3D spectra HNCA and HN(CO)CA. These residues constitute the β 8 strand and parts of the preceding loop. It should be noted, that strand β 8 is located at the outer edge of the ACD β -sandwich. Backbone assignment was obtained for 43 residues of Cu(II)- α B10m (for chemical shift list see Appendix Tab. 10).

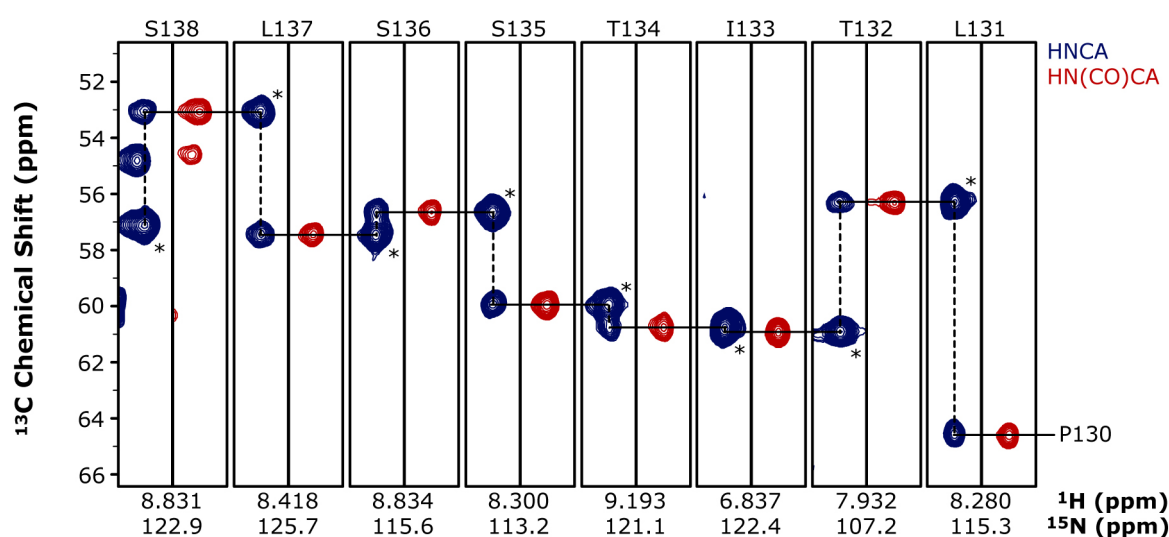


Fig. 26 Assignment of backbone resonances of Cu(II)- α B10m. Depicted is the strip plot for residues L131 to S138, which constitute the β 8 strand and parts of the preceding loop. Strips were extracted pairwise from the 3D spectra HNCA (blue) and HN(CO)CA (red) at ^1H - ^{15}N peak positions (residue i) shown at the bottom. The sequential walk along the protein backbone is illustrated by solid lines representing the interresidual connections to the Ca_{i-1} of the preceding residue. Dashed lines complete the trace by connecting the two HNCA correlations for the Ca_i (asterisk) and the Ca_{i-1} atoms. The HN(CO)CA spectrum exclusively shows the Ca_{i-1} correlation thereby unambiguously identifying the Ca of the preceding residue.

3.2.10.2 NMR Titration Studies

The ^1H - ^{15}N HSQC (heteronuclear single-quantum coherence) spectrum of apo- α B10m is well dispersed implicating a structured and folded α B core domain (**Fig. 27A**). Addition of paramagnetic Cu(II) to α B10m caused severe changes in the ^1H - ^{15}N HSQC spectrum (**Fig. 27A**). Large CSP of up to 1.2 ppm were observed for the holo-form of α B10m. Consistent with the picomolar binding affinity as derived from the ITC and fluorescence measurements, the system is in the slow-exchange regime. New resonances were fully populated at an equimolar ratio of monomer and Cu(II), confirming that the monomeric ACD itself is the basic Cu(II)-binding unit.

The top panel of **Fig. 28A** illustrates the variations in the ^1H - ^{15}N HSQC spectrum induced by Cu(II). The most prominent CSP were observed in the N-terminal loop involving strands $\beta 2$ and $\beta 3$ (residues E71-F75) and at the C-terminus around P148 (residues G147 and R149). Only marginal differences occurred for residues located in strands $\beta 4$, $\beta 8$ and $\beta 9$ at the outer edges of the ACD dimer. By contrast, about 50 % of the resonances were broadened beyond detection due to their spatial vicinity to paramagnetic Cu(II). Signals affected by paramagnetic quenching comprised the N-terminal strand $\beta 2$ (G64-L70), parts of strand $\beta 3$ and the adjacent loop (S76-S85), as well as strands $\beta 5$, $\beta 6+7$ and the intervening loop (E99-R123) (**Fig. 28A**). It is noteworthy, that these regions constitute the AP interface and the adjacent shared groove. The same result was obtained when methyl groups as side-chain

Results

reporters were monitored (**Fig. 27B**). Extinction of resonances was unambiguously identified for the methyl groups of V77 and V81 (strand $\beta 3$ and adjacent loop), V100 (strand $\beta 5$) and I114 (strand $\beta 6+7$). By contrast, the methyl correlations of I124, A126, L131, T132, I133 and T134 (strand $\beta 8$ and preceding loop) were not vanished in the presence of Cu(II).

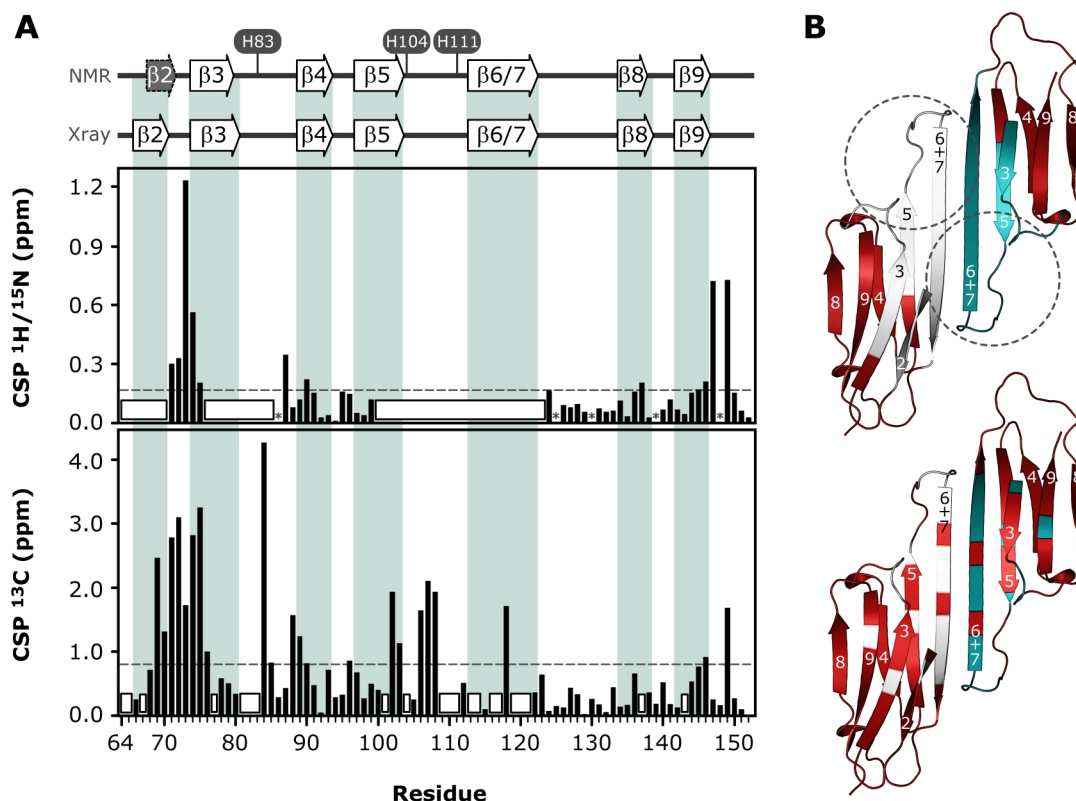


Fig. 28 Summary of the effects induced by Cu(II). (A) Chemical shift perturbations (CSP) and paramagnetic bleaching observed in ^1H - ^{15}N HSQC (Top) and CBCACO spectra (Bottom) of $\alpha\text{B}10\text{m}$ upon addition of Cu(II). CSP (black bars) are plotted versus the protein sequence. Non-observable residues due to PRE are indicated by horizontal bars (white). Prolines and non-assigned residues (S139) are marked with an asterisk. Dashed lines indicate the average CSP. On top of the two panels, secondary structure elements derived from NMR secondary-chemical-shift-analysis and as observed in the X-ray structure of the $\alpha\text{B ACD}$ [55] are shown. The short $\beta 2$ strand (grey-shaded) is observed by NMR only in the presence of Cu(II). Potential Cu(II)-binding histidines are highlighted. (B) Observable residues (red) of Cu(II)- $\alpha\text{B}10\text{m}$ employing ^1H detection (Top) or ^{13}C detection (Bottom) are mapped onto the X-ray structure of the $\alpha\text{B ACD}$ [55]. The two monomers are colored grey and cyan, respectively. β -strands are labeled. The dashed circles indicate the potential Cu(II)-binding region containing the histidines highlighted in (A).

The NMR data pointed towards a Cu(II)-binding region at the AP interface. $\alpha\text{B}10\text{m}$ features five histidines as potential Cu(II) ligands, all of which are distributed near to the AP interface. Residues H83, H104 and H111 are part of the shared groove above the AP interface, whereas residues H101 and H119 are located on the opposite side of the extended β -sheet. Theoretical considerations were made in order to clarify which of the two histidine clusters might be involved in metal ligation. A clash between the theoretical blind zone of 12 Å radius, expected

for ^1H -detected NMR [198], and the experimental data occurs, when positioning the theoretical sphere around H101 (**Fig. 29**). In this case, strand $\beta 4$ and parts of strand $\beta 5$ are observable in ^1H - ^{15}N HSQC spectra of Cu(II)- αB10m , though expected to be quenched. When the theoretical sphere is centered at H104 on the other side of the β -sandwich, as an approximate position of the metal ion, there is complete agreement with the experimental observations except for the loop residue E88 (**Fig. 29**). This might be explained by Cu(II)-induced rearrangements of the $\beta 3$ - $\beta 4$ - and $\beta 5$ - $\beta 6$ +7-loop.

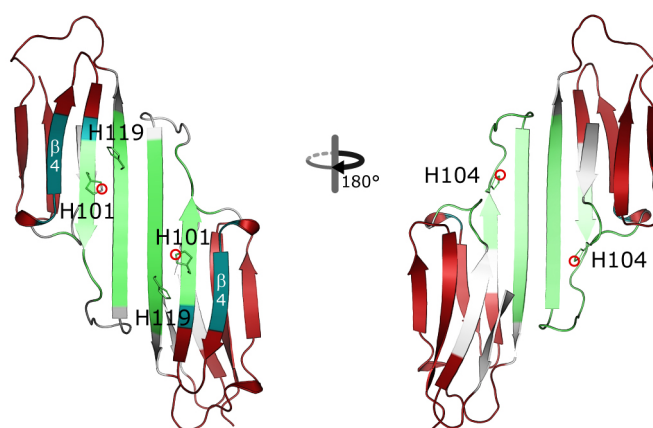


Fig. 29 Comparison of theoretical considerations and experimental data. Theoretical blind regions expected for ^1H -detected NMR experiments (sphere of 12 Å radius [198]) are mapped in green onto the X-ray structure of the ACD [55]. These spheres are centered at H101 on one side of the extended β -sheet (*Left*) and at H104 on the other side within the shared groove (*Right*) as approximate positions of the metal ion. The centers of the spheres are indicated by red circles. Both monomers are colored grey. Observable residues in the presence of Cu(II) (^1H - ^{15}N HSQC) are depicted in red. Clashes between the theoretical spheres and the experimental observations are colored in cyan. Strand $\beta 4$ is labeled.

Ascorbic acid is able to reduce the paramagnetic Cu(II) ion to diamagnetic Cu(I). The addition of an excess of ascorbic acid to Cu(II)-bound αB10m yielded spectra that do not superimpose with the spectra of apo- αB10m (**Fig. 30A**). It can thus be concluded that αB10m is also capable of binding diamagnetic Cu(I), which results in spectra with partial recovery of PRE effects as well as CSP for certain resonances. The Cu(I)-bound state of αB10m was not assigned, and thus explicit specification of perturbed resonances is not possible. However, it is apparent that mainly residues at the AP interface were exchange-broadened by Cu(I)-binding. This was also observed upon addition of the chelator EDTA to Cu(II)- αB10m (**Fig. 30B**). Due to its attomolar affinity towards Cu(II), EDTA should be able to recover the bleached resonances of αB10m .

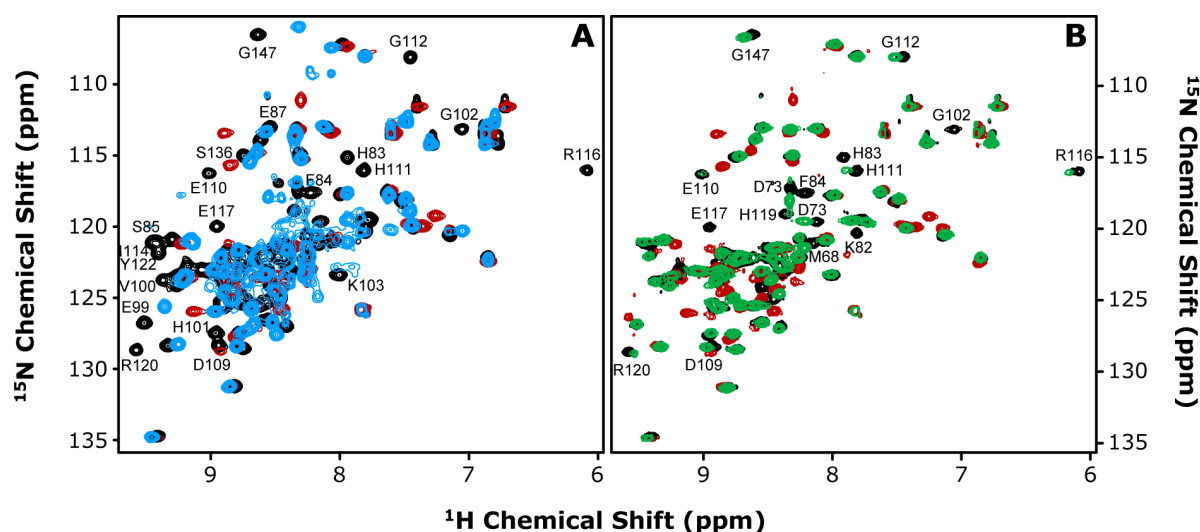


Fig. 30 Effects of ascorbic acid and EDTA on Cu(II)- α B10m. ^1H - ^{15}N HSQC spectra of 1 mM α B10m in the absence (black) and presence of 1 mM Cu(II) (red) are shown in both figures. Cu(II)-bound α B10m was titrated with (A) 10 mM ascorbic acid (blue) thereby producing diamagnetic Cu(I), and with (B) 1 mM EDTA (green). Resonances that lack recovery to the apo-state are labeled. The corresponding residues are located at or near to the AP interface. Spectra were recorded at 22 °C and at a magnetic field strength of 14.1 T.

3.2.10.3 ^{13}C -detected NMR Experiments

^1H nuclei are highly sensitive to PRE (see Chapter 1.2.2). In order to reduce the susceptibility to PRE and thus to further restrict the potential binding region of Cu(II), NMR experiments with ^{13}C excitation and detection were performed. **Fig. 31** shows the CBCACO spectrum of apo- α B10m. The existing assignment for $\text{C}\alpha$ and C' was easily transferred to the spectrum and expanded by the $\text{C}\beta$ chemical shifts. All expected correlations were observed and assigned including proline residues and the side-chain carbonyl correlations of Asn, Asp, Gln and Glu. Furthermore, the CCCO experiment yielded partial assignment of $\text{C}\gamma$ resonances (for chemical shift lists see Appendix Tab. 9 and Tab. 10).

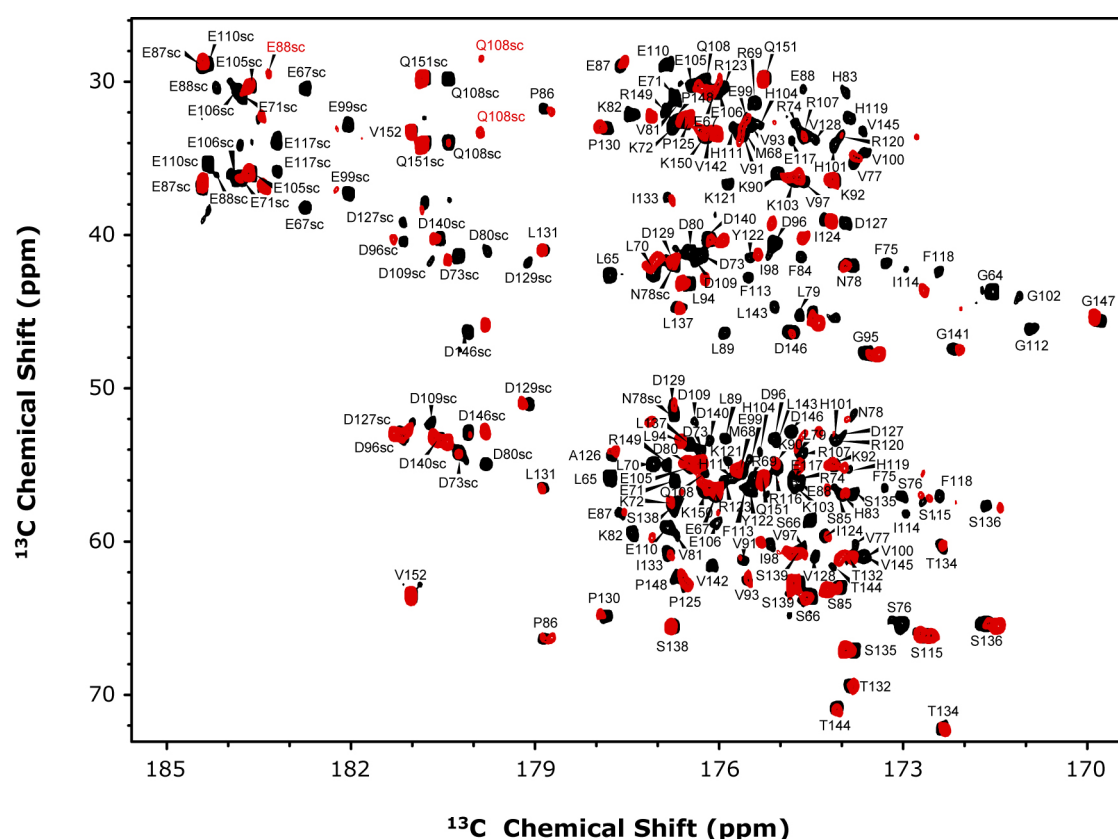


Fig. 31 CBCACO spectra of apo- α B10m and Cu(II)- α B. The spectra were recorded on 1 mM samples of α B10m in the absence (black) and presence of 1 mM Cu(II) (red). Assignments for the apo-form are indicated in black. The C'/C β correlation of A126 is outside of the spectral window shown here. The spectra include the down-field shifted side-chain carbonyl correlations (index sc) of Asp/Asn (C α /C β) and Glu/Gln (C β /C γ). Assignments for the side-chain resonances of E88 and Q108 of the holo-form are indicated in red. Spectra were recorded at 22 °C and at a magnetic field strength of 16.4 T at CERM (Florence, Italy) in collaboration with Isabella C. Felli and Roberta Pierattelli.

The addition of Cu(II) induced the disappearance of resonances as well as significant CSP (**Fig. 31**). As expected, paramagnetic quenching of ^{13}C resonances was less pronounced and 75% of all residues were still detectable. The locus of Cu(II)-binding was thereby restricted to the interconnecting loop between strands $\beta 5$ and $\beta 6+7$ at the AP interface. This loop also contains the residue D109, which is involved in the ion-pair to the disease-related R120 of the neighboring monomer. Resonances belonging to strand $\beta 6+7$ (F113, I114, R116, E117, H119-K121) and the preceding $\beta 5$ - $\beta 6+7$ -loop (H104, D109-H111) disappeared in the presence of Cu(II) (**Fig. 31** and **Fig. 28A**). The results for αB10m are thus in agreement with our findings for the full-length protein. The $\beta 3$ - $\beta 4$ -loop (V81-H83) and the very N-terminal residues (G64, L65) were also affected by paramagnetic broadening. These flexible regions extend into the shared groove and are in proximity to the $\beta 5$ - $\beta 6+7$ -loop. Potential Cu(II) ligands in this region are H83 ($\beta 3$ - $\beta 4$ -loop), H104, E105, E106, D109, E110 and H111 ($\beta 5$ - $\beta 6+7$ -loop).

The CSP for $C\alpha$, $C\beta$ and C' atoms are plotted for each residue in the bottom panel of **Fig. 28A**. The most intense CSP occurred at the N-terminal $\beta 2$ - $\beta 3$ -region of $\alpha B10m$ including residues R69-S76. Several residues at the end of strand $\beta 5$ (G102-K103) and within the $\beta 5$ - $\beta 6+7$ -loop (E106-Q108) were perturbed in the presence of Cu(II) as well. The strongest effect though was observed for the loop residue F84 ($\beta 3$ - $\beta 4$ -loop). Careful examination of the side-chain carbonyl correlations in the CBCACO spectrum revealed explicit CSP for residues E88 and Q108 as parts of the $\beta 3$ - $\beta 4$ -loop and $\beta 5$ - $\beta 6+7$ -loop, respectively (**Fig. 31**). The data suggests structural reorganization of these loops during incorporation of Cu(II).

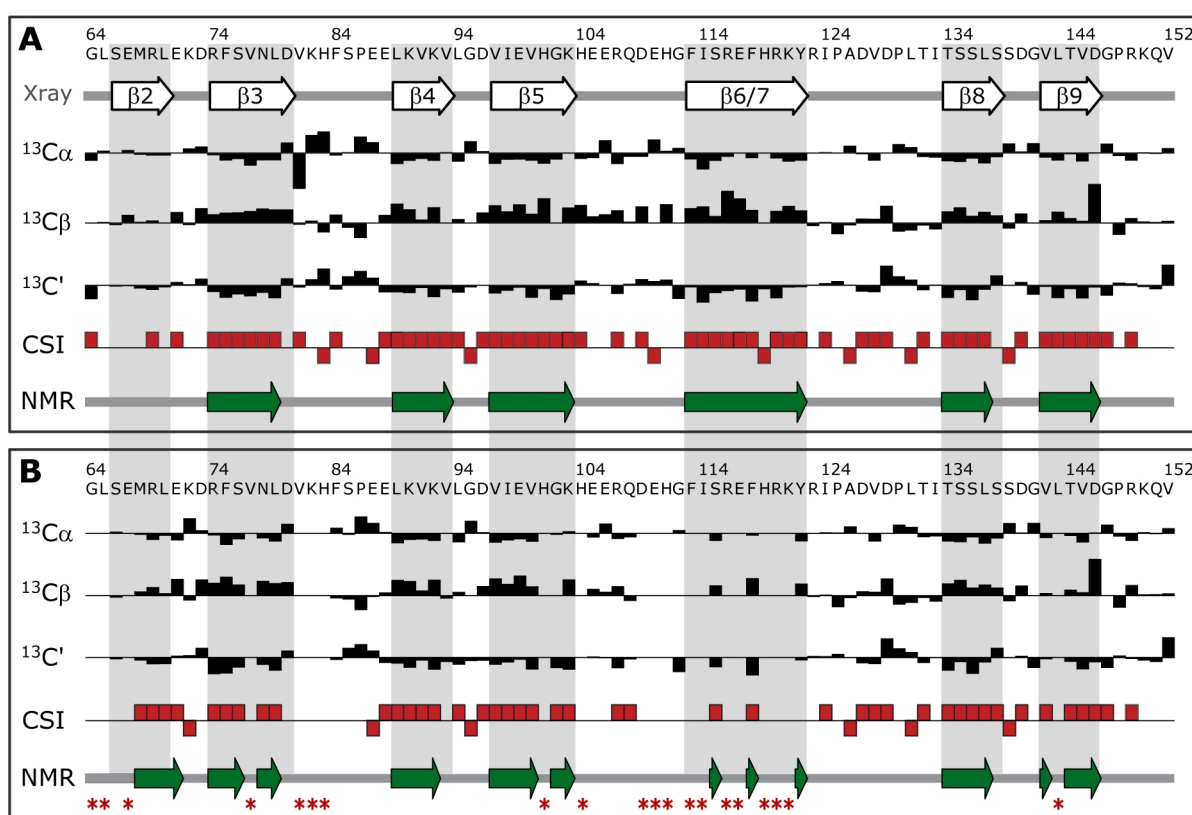


Fig. 32 Carbon chemical shift analysis and secondary structure prediction for apo- $\alpha B10m$ and Cu(II)- $\alpha B10m$. Chemical shift indices (CSI, [251]) and secondary structure elements derived from CBCACO spectra of (A) apo- $\alpha B10m$ and (B) Cu(II)- $\alpha B10m$. CSI (red bars) are based on $C\alpha$, $C\beta$ and C' chemical shift deviations (black bars) from random-coil values and were obtained by using the software CcpNmr [252]. CSI are either positive (β -strand conformation), negative (α -helical conformation) or zero (random-coil conformation). The protein sequence is shown at the top of each panel. Secondary structure elements as observed in the X-ray structure of the αB ACD (white) are depicted at the top of panel (A) and are highlighted in both panels (grey) [55]. Secondary structure elements shown at the bottom of each panel (green) represent the results of the NMR-based approach. Bleached residues in Cu(II)- $\alpha B10m$ are indicated by red asterisks.

^{13}C chemical shifts provide information on protein secondary structure [251]. The secondary structure prediction for apo- αB10m based on chemical shift indices (CSI, [251]) is in good agreement with the ACD crystal structure of αB [55] except for the short $\beta 2$ strand, which is disordered for three of five monomers in the asymmetric unit (**Fig. 32A**). Accordingly, NMR predicts random-coil conformation for this region. Observable changes in secondary structure upon addition of Cu(II) were restricted to the N-terminal stretch M68-E71 (**Fig. 32B**). These residues adopt a β -strand conformation in the holo-form and partially reflect the $\beta 2$ strand observed in the X-ray structure [55]. An elevated extent of β -strand structure was also found in the CD spectra of $\text{Cu(II)-}\alpha\text{B}$ and $\text{Cu(II)-}\alpha\text{B10m}$.

3.2.10.4 The AP Interface and its Dynamics

The titration of αB10m with diamagnetic Zn(II) revealed decreased signal intensities or extinction of resonances in both ^1H - and ^{13}C -detected experiments (**Fig. 33A,C**). The majority of affected residues are located at the AP interface (V100-I124), or in vicinity of the latter, at $\beta 3$ strand and the flanking loop regions (M68-F84).

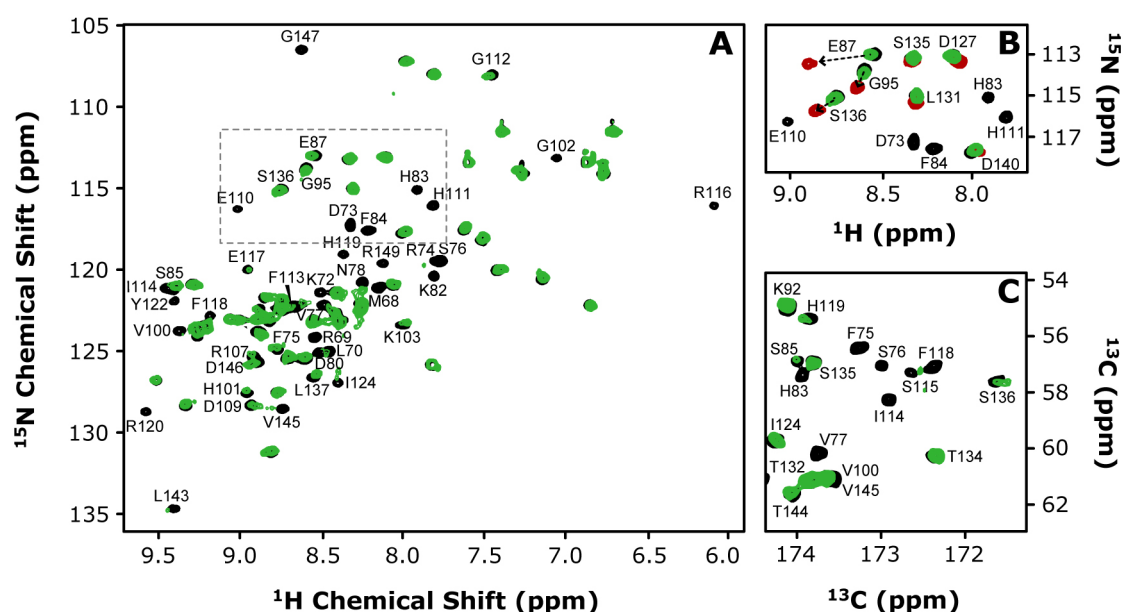


Fig. 33 Chemical exchange induced by Zn(II) -binding. Spectra of 1 mM αB10m in the absence (black) and presence of 1 mM Zn(II) (green) are shown. Spectra were recorded at 22 °C and at a magnetic field strength of 14.1 T. (**A**) ^1H - ^{15}N HSQC spectrum illustrating the disappearance of resonances upon addition of diamagnetic Zn(II) . The affected signals are labeled. The corresponding residues are located at or near to the AP interface. The region surrounded by a box is depicted in (**B**) together with the spectrum obtained from $\text{Cu(II)-}\alpha\text{B10m}$ (red). The figure shows that the effects of Cu(II) - and Zn(II) -binding to αB10m are similar, even though the interaction with Zn(II) is much weaker. (**C**) Section of the CACO spectrum.

Zn(II)-induced CSP were much less intense than those of Cu(II), however, the trend of chemical shift changes was comparable with the typical CSP pattern of Cu(II)- α B10m (**Fig. 33B**). This suggests that the binding-mode of Zn(II) might be the same as compared to Cu(II), but that the interaction of α B10m and Zn(II) is in the fast-exchange regime, implying low binding-affinity (μ M-mM range).

Similarly, binding studies with paramagnetic Co(II) yielded a ^1H - ^{15}N HSQC spectrum that was devoid of resonances arising from interfacial residues (**Fig. 34**). However, no CSP were observed in the presence of Co(II). Based on the titrations with Zn(II) and Co(II), it can be concluded that the disappearance of signals in the spectra of Cu(II)- α B10m is due to both paramagnetic broadening as well as chemical exchange at the AP interface.

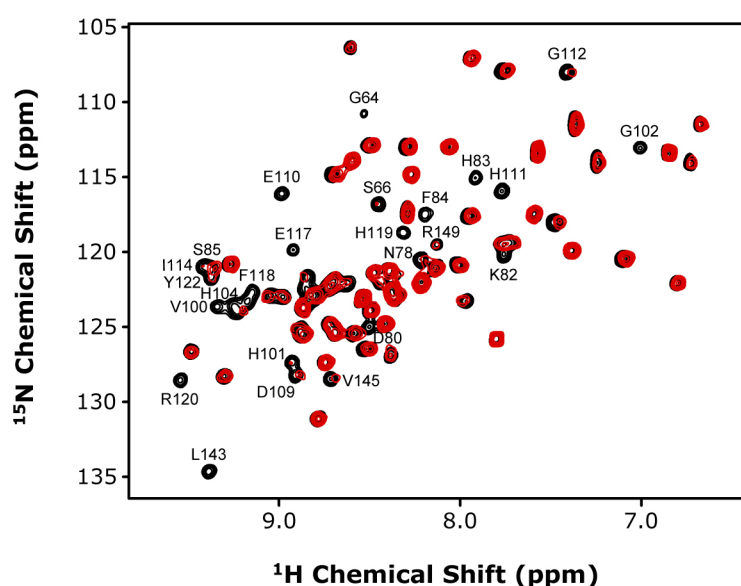


Fig. 34 Chemical exchange induced by Co(II)-binding. ^1H - ^{15}N HSQC spectra of 1 mM α B10m in the absence (black) and presence of 1 mM Co(II) (red) are shown. Resonances vanishing upon addition of paramagnetic Co(II) are labeled. The corresponding residues are located at or near to the AP interface. The signal of R116 is omitted. Spectra were recorded at 22 °C and at a magnetic field strength of 14.1 T.

In order to follow monomer-dimer exchange processes at the AP interface, the signal intensities of the ^1H - ^{15}N HSQC spectrum and ^{15}N T_1/T_2 ratios of apo- α B10m were analyzed (**Fig. 35**). A decrease in signal intensities along with an increase of ^{15}N T_1/T_2 was observed in particular for the AP interface, including strands $\beta 5$ and $\beta 6+7$, but also for $\beta 3$ and the subsequent loop. These results are in agreement with a chemical exchange process at the AP interface involving association-dissociation between monomers in potentially different AP registers.

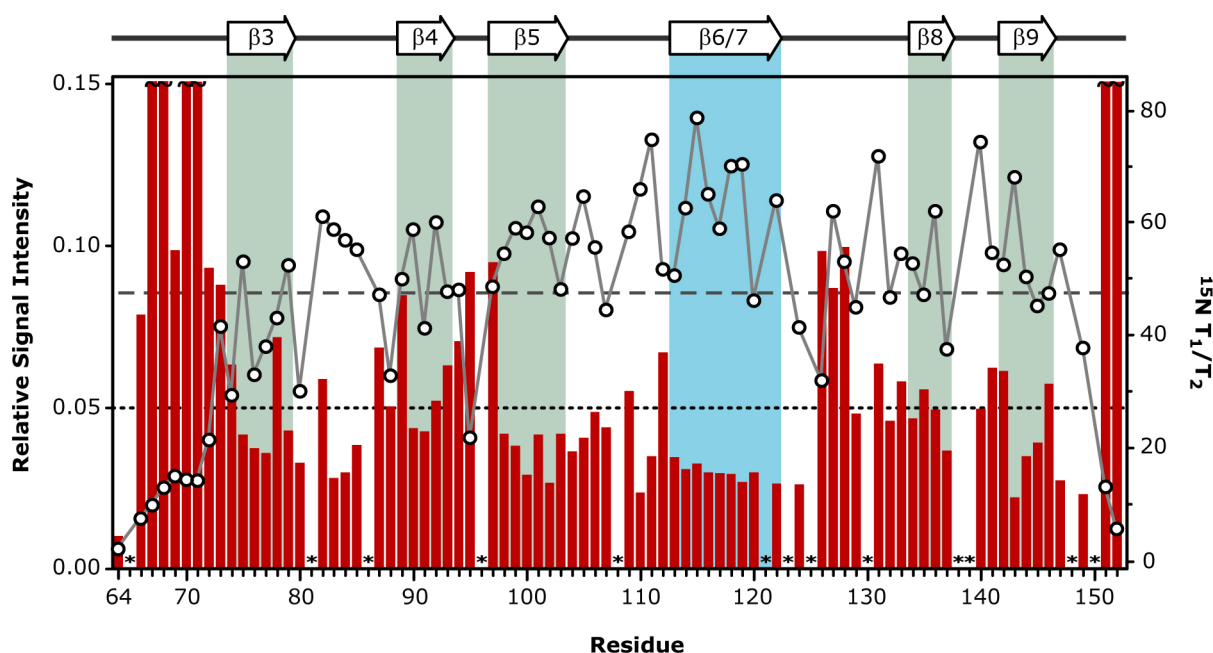


Fig. 35 Dynamics at the AP interface of αB10m . Relative signal intensities of the ^1H - ^{15}N HSQC spectrum (red bars) and $^{15}\text{N } T_1/T_2$ ratios (open circles) for apo- αB10m . Signal intensities were normalized to the signal intensity of V152. Prolines, non-assigned residues and residues revealing extensive signal overlap are marked with asterisks and were excluded from the analysis. Horizontal lines indicate average values for relative signal intensities (dotted line) and $^{15}\text{N } T_1/T_2$ ratios (dashed line) (Q151 and V152 were excluded). Secondary structure elements as observed by NMR are illustrated on top. Strand $\beta 6+7$ forming the dimer interface is highlighted in blue.

Intermolecular contacts of the register arrangement at the AP interface were characterized by ^{15}N -edited 3D NOESY experiments. Besides sequential NOE contacts, an AP2 register [56] with E117 near to the point-symmetric axis was observed (**Fig. 36A**). The spectrum confirmed the intersubunit contacts S115-H119 and F113-K121 as expected for the AP2 state (**Fig. 36C**). The AP1 register [56] with F118 close to the twofold axis would give rise to the NOE contacts E117-H119, S115-K121 and F113-R123 (**Fig. 36B**). Indeed, spatial vicinity was observed between residues E117 and H119, though this correlation might also originate from the AP2 register, in which the respective NH-pairs are 5.6 Å apart from each other. This would also explain the weak signal intensity of this correlation peak. The potential contacts S115-K121 and F113-R123 of the AP1 register were not confirmed due to spectral overlap. Hence, the NOESY approach did not unambiguously detect multiple interface arrangements, which might be transiently populated in solution besides the AP2 state.

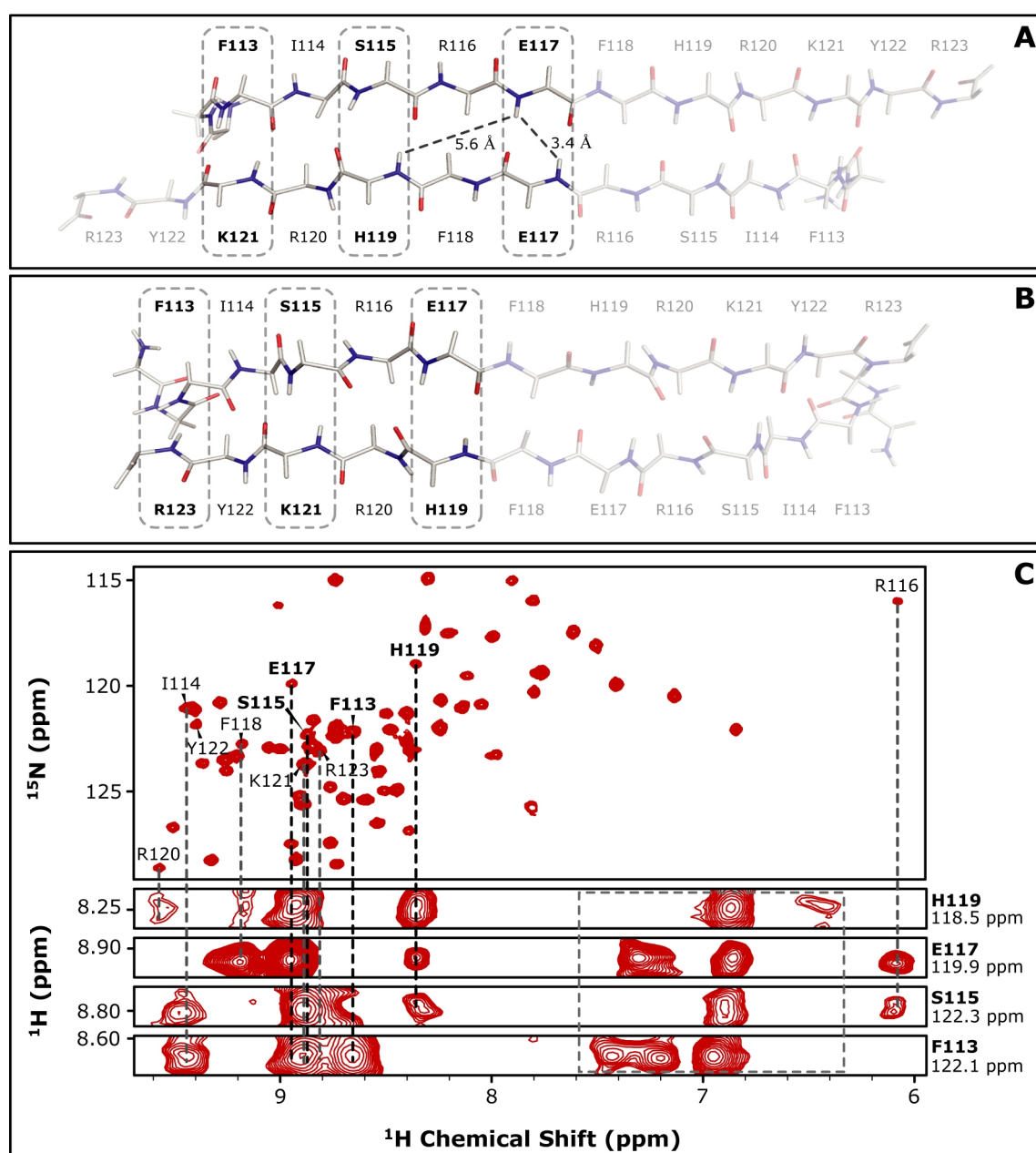


Fig. 36 The AP interface and its register in solution. (A) The AP2 register as observed in the X-ray structure of the α B ACD (residues 67-157) [55]. In this case, E117 is close to the twofold axis. (B) The AP1 state as observed in the X-ray structure of the α B ACD (residues 68-162) [56]. Residue F118 is close to the twofold axis. In both panels, only the backbone atoms of strands β 6+7 (residues F113-R123) are shown. Expected intermolecular contacts (3.4 Å) are highlighted by boxes. Redundant residues due to the point symmetry are depicted with transparency. (C) ^1H - ^{15}N HSQC spectrum (Top) and strips of the ^1H - ^{15}N HSQC-NOESY 3D spectrum (Bottom) recorded on α B10m. The ^{15}N spectral window is reduced to focus on the interfacial residues (F113-R123), which are labeled. Residues for which 3D strips are depicted (at the corresponding ^{15}N chemical shifts of H119, E117, S115, F113) are labeled in bold. Dashed lines facilitate the assignment of resonances in the strips or illustrate problematic spectral overlap, respectively. The dashed box represents spatial contacts to aromatic and amide side-chains. Spectra were recorded at 22 °C and at a magnetic field strength of 14.1 T.

D109 is involved in the intermolecular salt-bridge with R120 and is thus expected to contribute significantly to dimer stability (two salt-bridges per AP interface) [55,56,60]. Given the important role of D109, the point mutant D109A was investigated by NMR spectroscopy. α B10m-D109A completely lost the capability to bind Cu(II), reflected in the absence of paramagnetic quenching and CSP during Cu(II) titration (**Fig. 37A**). Secondly, the mutation D109A caused structural heterogeneity, which was manifested by increased linewidths and multiple sets of resonances, e.g. for the side-chain amide of Q108 (β 5- β 6+7-loop) (**Fig. 37B**). This observation indicates diverse conformational states for Q108 and the β 5- β 6+7-loop. By contrast, when R120 as the salt-bridge partner of D109 was replaced by glycine, as is the case in desmin-related cardiomyopathy [62], Cu(II)-binding competence was not impaired. The ACD variant α B10m-R120G revealed the characteristic wildtype CSP pattern upon addition of Cu(II) (**Fig. 37C,D**). Both mutations induced chemical exchange broadening of resonances originating from interfacial residues. Therefore, it can be concluded that residues D109 and R120 and the ionic interaction between them are essential for the monomer-dimer equilibrium of the ACD.

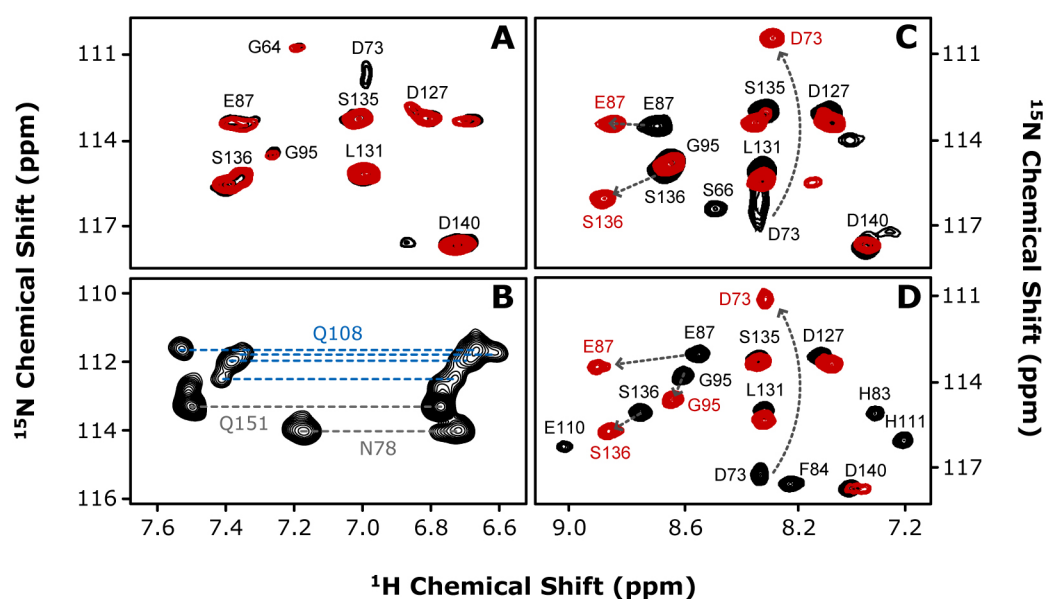


Fig. 37 The role of D109 and R120 in Cu(II)-binding. Sections of ^1H - ^{15}N HSQC spectra of α B10m and its point mutants are shown. The spectra were recorded in the absence (black) and presence of Cu(II) (red) at an equimolar ratio. **(A)** α B10m-D109A. **(B)** Side-chain amide region of apo- α B10m-D109A illustrating the multiple set of resonances for the loop-residue Q108 (blue). **(C)** α B10m-R120G showing the characteristic CSP pattern of α B10m. Assignments of the most perturbed amide resonances are indicated in red. **(D)** The titration of α B10m is shown for comparison. Characteristic CSP are indicated by arrows. Spectra were recorded at 22 °C and at a magnetic field strength of 14.1 T. Assignments for mutant ACDs were transferred from α B10m in unambiguous cases.

Observation of arginine side-chain resonances yielded seven ϵ -NH correlations for the seven arginine residues in α B10m (R69, R74, R107, R116, R120, R123, R149) (**Fig. 38A**). The η -NH₂ region was poorly resolved, except signals revealing a downfield shift in the nitrogen dimension at 76 ppm and proton chemical shifts at approximately 6 ppm and 9.5 ppm (**Fig. 38A**). Such a pattern is known for guanidine moieties of arginines involved in hydrogen-bonds [270]. It might therefore originate from R120 at the AP interface. However, the heterogeneity and the weak signal intensities of these resonances hindered unambiguous assignment.

Labile protons of histidine imidazol-rings usually exchange very rapidly with the aqueous solvent (1500 s^{-1}) [271] and thus escape NMR detection due to the relatively long magnetization transfers in 2D experiments. Nevertheless, the ^1H - ^{15}N HMQC spectrum of α B10m revealed such a correlation at approximately 11.7 ppm (^1H) and 170 ppm (^{15}N) (**Fig. 38B**). The corresponding spectrum of α B10m-H104A was devoid of this signal and thus it most likely arises from residue H104. This implies, that H104, as part of the β 5 strand, is buried in the shared groove and is thereby protected from extensive exchange with the solvent.

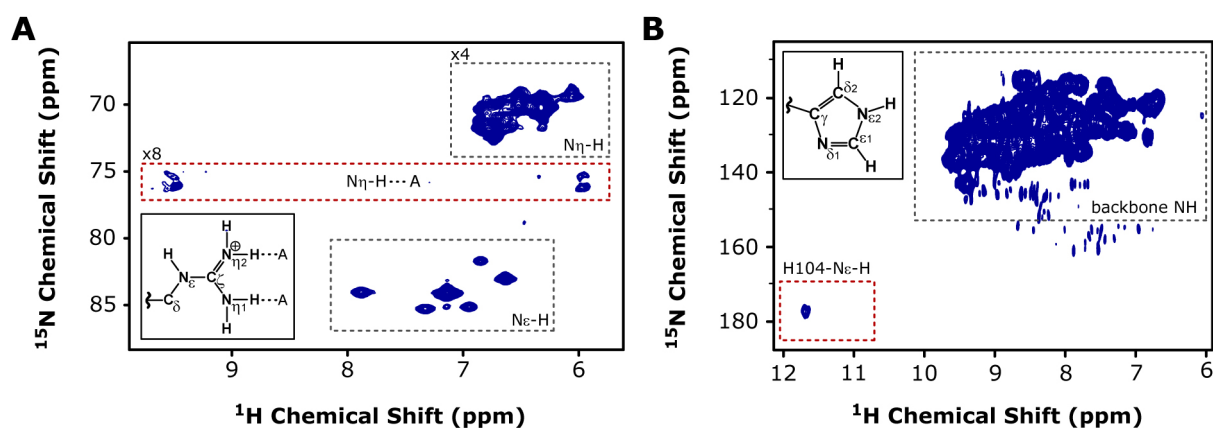


Fig. 38 Observation of histidine and arginine side-chains at the AP interface. (**A**) ^1H - ^{15}N HSQC spectrum of α B10m showing the ϵ - and η -NH correlations of the arginine side-chain. Also shown are downfield-shifted η -NH correlations, that indicate involvement in hydrogen-bonds. The respective regions are surrounded by boxes. The inset illustrates the chemical structure of a protonated guanidino tautomer. 'A' represents an H-bond acceptor. The spectrum was recorded at 12 °C. (**B**) ^1H - ^{15}N HMQC spectrum of α B10m revealing the downfield-shifted NH-moiety of the H104-imidazol-ring at an approximate ^{15}N chemical shift of 178 ppm. The inset depicts the chemical structure of the $\text{N}_{\epsilon 2}$ -tautomeric state of the imidazol-ring. The spectrum was recorded at 22 °C.

3.2.10.5 The Cu(II) Coordination Sphere

The NMR results for the truncated α B10m as well as for full-length α B suggest that two Cu(II) ions bind to the ACD dimer at the opposite ends of the AP interface. Potential Cu(II) ligands in this region are H83 (β 3- β 4-loop), H104, D109 and H111 (β 5- β 6+7-loop) (**Fig. 39A**). Molecular dynamics simulation and energy minimization show that these loop residues can accommodate a Cu(II) ion with metal-ligand distances of about 2 Å and with tetrahedral geometry (**Fig. 39B**). The distances to be covered by the ligands upon binding are 8.4 Å (H111), 5.2 Å (H83), 2.6 Å (H104) and 4.9 Å (D109) with respect to the ligating atoms (His-N ϵ , Asp-O δ), whereas the motions of the backbone C α atoms amount to 3.9 Å (H111), 3.8 Å (H83), 2.3 Å (H104) and 4.0 Å (D109). The large CSP observed for residues within the β 3- β 4- and β 5- β 6+7-loop reflect these structural rearrangements upon coordination of Cu(II). Apparently, the proposed Cu(II)-binding mode implies that the intermolecular salt-bridge between D109 and the disease-related R120 is impaired by the intervention of Cu(II).

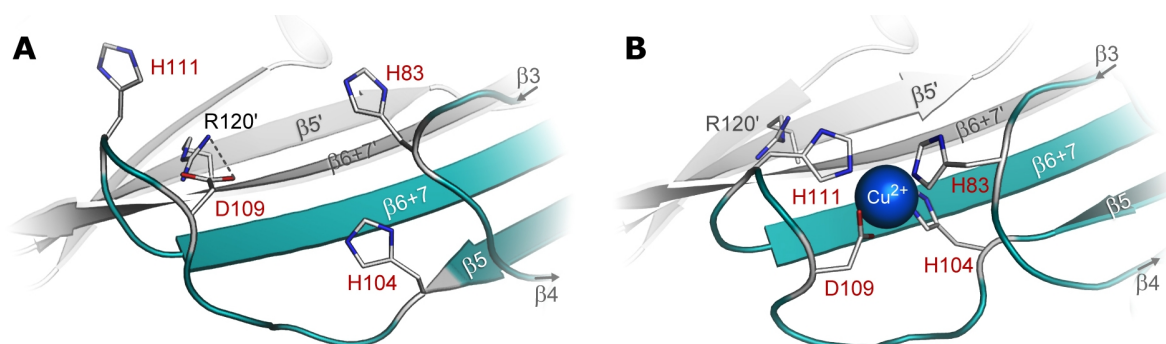


Fig. 39 The putative Cu(II) coordination sphere in human α B. (**A**) The Cu(II)-binding region with the loops connecting strands β 3 and β 4 as well as β 5 and β 6+7 is illustrated for one molecule in the ACD dimer of α B [55]. The two monomers are colored cyan and grey, respectively. Potential Cu(II) ligands are labeled in red. Also shown is the conserved R120' of the opposing molecule forming the ion-pair with D109 across the AP interface. (**B**) Structural model of the potential Cu(II) coordination sphere based on the structure shown in (**A**). The tetrahedral coordination sphere comprises residues H83, H104, H111 and D109 (monodentate mode). The intermolecular salt-bridge between D109 and R120' is thereby disrupted. The structural model was kindly generated by Benjamin Bardiaux (Group of Hartmut Oschkinat, FMP, Germany).

Results

The residues H83, H104, H111 and D109 are integral parts of the shared groove and its ionic network within the ACD of α B [55,56]. A sequence alignment of the ACD of various sHSPs reveals that these residues are conserved in α B among different metazoans (Fig. 40). Moreover, the suggested coordinating ligands are also preserved in human α A, HSP20 and HSP27, whereas HSP22 has diverged. There is only poor conservation in the ACD of non-metazoan sHSPs.

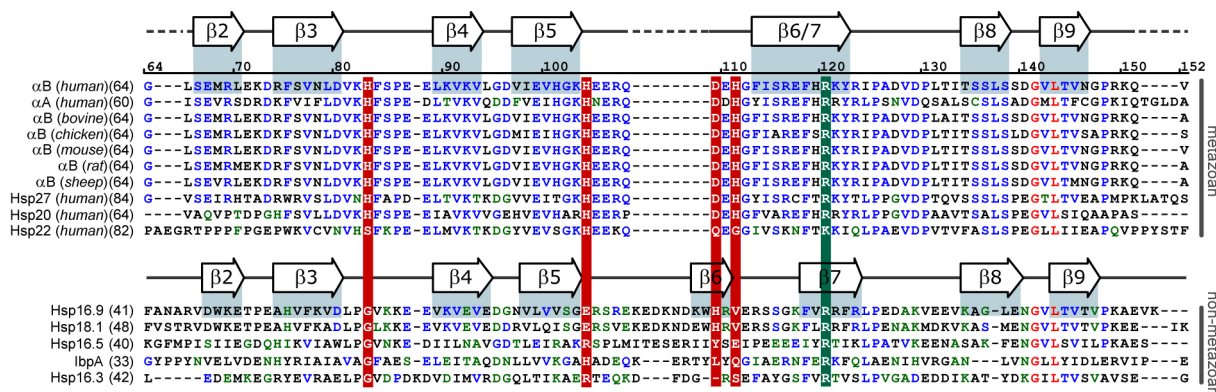


Fig. 40 Conservation of metal-ligating residues in metazoan sHSPs. Sequence alignment of the ACD (residues 64-152 in human α B) for different metazoan and non-metazoan members of the sHSP family. The non-metazoan sHSPs originate from the following organisms: wheat (HSP16.9), pea (HSP18.1), *Methanococcus jannashii* (HSP16.5), *Escherichia coli* (IbpA) and *Mycobacterium tuberculosis* (HSP16.3). Color coding of alignment: identical (red), conservative (blue), weakly similar (green) and non-similar (black). The putative Cu(II)-binding residues H83, H104, D109 and H111 are highlighted in white with a red box. The interfacial residue R120 is highlighted in white with a green box. β -strands as observed in the X-ray structures of the human α B ACD [55] and wheat HSP16.9 [35] are illustrated on top of the respective sequences. The residue numbers on top of the alignment refer to human α B.

3.3 The Interaction of α B-crystallin with $A\beta_{1-40}$

There is growing evidence that the Alzheimer's disease amyloid peptide $A\beta_{1-40}$ and its fibrillar form are clients of the chaperone α B *in vivo* [49,67,188–190]. Biophysical approaches were employed in order to shed light on this interaction.

3.3.1 Resonance Assignment of Monomeric $A\beta_{1-40}$

In the course of this work, the monomeric $A\beta_{1-40}$ peptide was investigated by solution-state NMR. The analysis yielded unambiguous assignment of 37 out of 40 amide resonances (**Fig. 41A**). The amide correlations of residues D1, H6 and H14 were not observed in ^1H - ^{15}N HSQC spectra, though the resonance of F4 revealed some very weak correlations in the 3D spectra indicating another aromatic residue. Thus, there is resonance overlap for F4 and one of the two missing histidines. A slight change of the buffer pH might be a possibility to circumvent this overlap and to access the corresponding histidine signal in the future. Carbon chemical shifts of the peptide backbone were also assigned including $\text{C}\alpha$, $\text{C}\beta$ and C' nuclei (for chemical shift list see Appendix Tab. 11). The $\text{H}\alpha$ - $\text{C}\alpha$ correlations are shown in **Fig. 41B**.

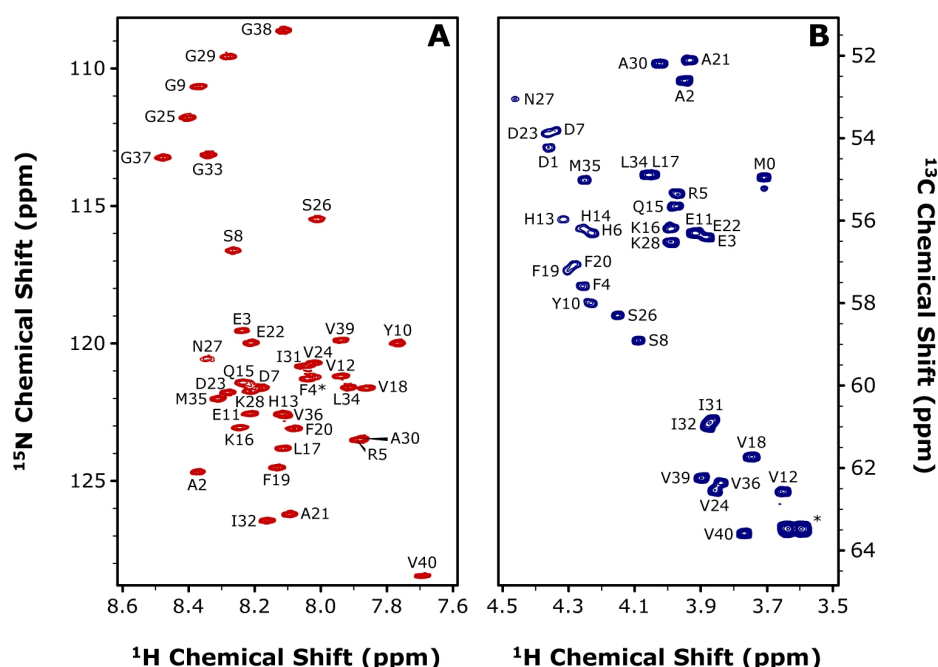


Fig. 41 Resonance assignment of monomeric $A\beta_{1-40}$. (**A**) ^1H - ^{15}N HSQC spectrum obtained for ^{13}C , ^{15}N - $A\beta_{1-40}$ at 4 °C. The asterisk indicates the Phe4 signal overlapping with a histidine resonance. (**B**) $\text{H}\alpha$ - $\text{C}\alpha$ region of the corresponding ^1H - ^{13}C HMQC spectrum. High-field glycine correlations are omitted. The asterisk indicates $\text{C}\beta$ correlations of serine residues. The $A\beta_{1-40}$ peptide was produced by Uwe Fink (Group of Bernd Reif, FMP, Germany).

3.3.2 Secondary Structure Propensity of A β ₁₋₄₀

Analysis of the ^{13}C chemical shifts yielded information on the secondary structure of the monomeric peptide in solution. The conventional method described by Wishart *et al.* [251] revealed random-coil conformation for the entire sequence. However, a tendency towards β -strand conformation in certain regions was apparent. Thus, the secondary structure propensity (SSP) was elucidated by detailed analysis of the ^{13}C chemical shifts according to the approach suggested by Forman-Kay *et al.* [260]. The results confirmed the β -strand propensity of A β ₁₋₄₀ under the employed experimental conditions. SSP scores in the range of -0.1 and $+0.1$ were found for the majority of residues corresponding to random-coil conformation (**Fig. 42A**). However, SSP scores of up to -0.3 clearly indicate β -strand propensity for the sequences E3-D7 and Q15-A21. Intriguingly, the region Q15-A21 includes the hydrophobic core LVFFA and is also found in β -strand conformation in structural models of A β ₁₋₄₀ and A β ₁₋₄₂ fibrils [164,165] (**Fig. 42B**). Thus it seems that the monomeric state of A β ₁₋₄₀ already adopts structural motifs, which are similar to those present in amyloid assemblies.

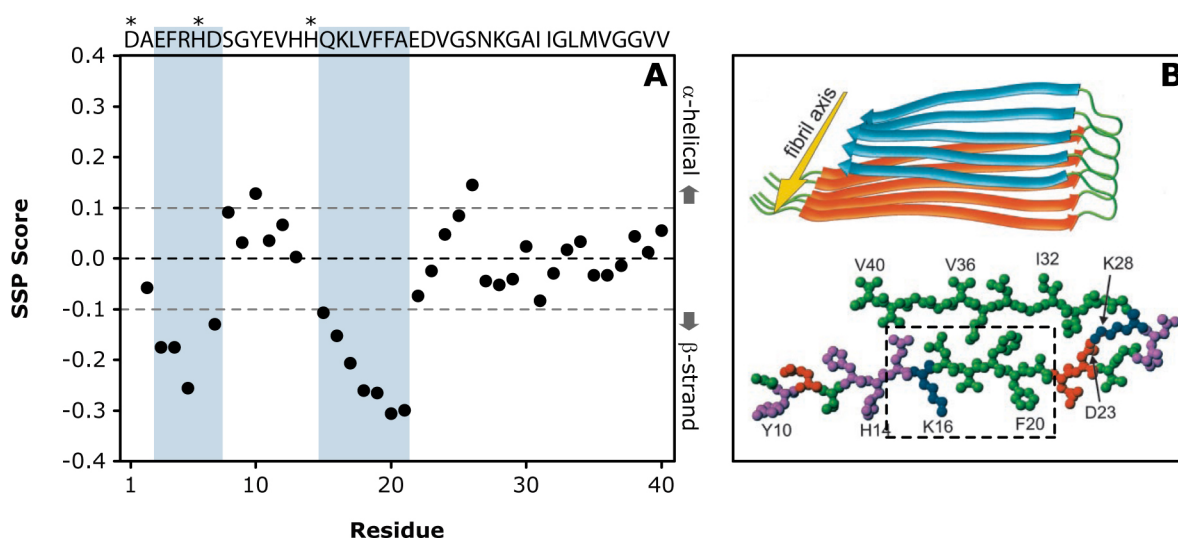


Fig. 42 NMR-derived secondary structure propensity of A β ₁₋₄₀ in solution. (**A**) Secondary structure propensity (SSP) as observed for A β ₁₋₄₀ by solution-state NMR. The SSP score was calculated from C α and C β chemical shifts [260]. The asterisks denote non-assigned residues. Propensities for α -helical (SSP > +0.1) and β -strand conformation (SSP < -0.1) are indicated on the right. The regions with significant deviation from random-coil values are highlighted in blue. (**B**) Structural model for A β ₁₋₄₀ fibrils as obtained from solid-state MAS NMR is shown for comparison (figure adapted from [164]). The cross- β structure alignment is shown on top with the two β -strands colored in orange and blue, respectively. The intramolecular arrangement of the two β -strands is depicted on the bottom. The dashed box highlights the region, which revealed β -strand propensity for monomeric A β ₁₋₄₀ in solution, as shown in (**A**).

3.3.3 A β_{1-40} -Binding to the Chaperone α B

The truncated protein construct α B10m was employed to monitor binding of the potential client A β_{1-40} and to localize the interaction site within the ACD. Upon addition of monomeric A β_{1-40} , the ^1H - ^{15}N HSQC spectrum of α B10m revealed very weak CSP on the order of only 0.02 ppm (**Fig. 43A**). The very small effects indicate binding affinity in the millimolar range. However, mapping the perturbations onto the ACD sequence, it is apparent that the majority of affected residues cluster at strands β 4 and β 8 (**Fig. 43B**). CSP were observed for residues V91-V93, G95, D96 (β 4 region), I124, T134-L137 (β 8 region), E117, H119, R120 (β 6+7) and G147. The β 4 and β 8 strands form the edge of the β -sandwich of the ACD (**Fig. 43B**). This hydrophobic groove is reported to be the interaction site with the C-terminal IPI-motif of a neighboring molecule in the α B multimer as well as a candidate binding site for client proteins [60,272]. Validation of the β 4- β 8 groove as a binding site for the C-terminal extension was done by titrating α B10m with a short peptide, which comprised the α B residues E156-E164 (α B₁₅₆₋₁₆₄). The palindromic sequence contains the conserved IPI-motif. In contrast to the titration experiment with A β_{1-40} , the C-terminal peptide caused extensive exchange-broadening of many amide resonances (**Fig. 44A**). The ^1H - ^{15}N HSQC spectrum of α B10m in the presence of α B₁₅₆₋₁₆₄ clearly showed the perturbation of residues located in strands β 4, β 5 and β 8 (**Fig. 44B**). Hence, the hydrophobic groove β 4- β 8 is indeed the interaction site for both the C-terminal extension of α B as well as the client A β_{1-40} .

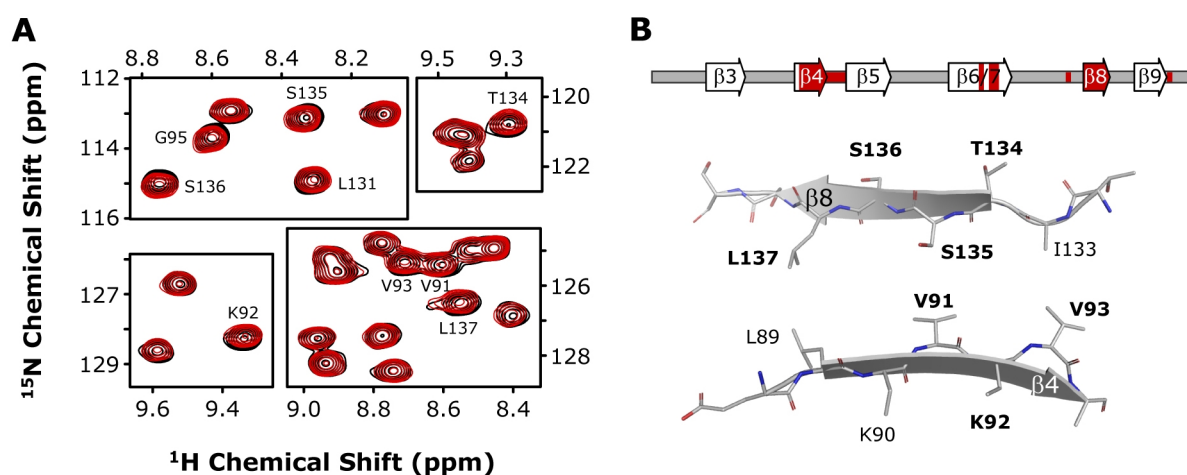


Fig. 43 The A β_{1-40} interaction site of α B10m. (A) Regions of ^1H - ^{15}N HSQC spectra of α B10m in the absence (black) and presence of A β_{1-40} at an equimolar ratio (red). Perturbed resonances are labeled. (B) Secondary structure elements of the ACD are shown (Top). Residues affected by A β_{1-40} binding are highlighted in red and cluster at the strands β 4 and β 8, which form the hydrophobic groove on the edge of the ACD β -sandwich [55] (Bottom). The corresponding residues are labeled. The residues which showed CSP upon addition of A β_{1-40} are highlighted in bold.

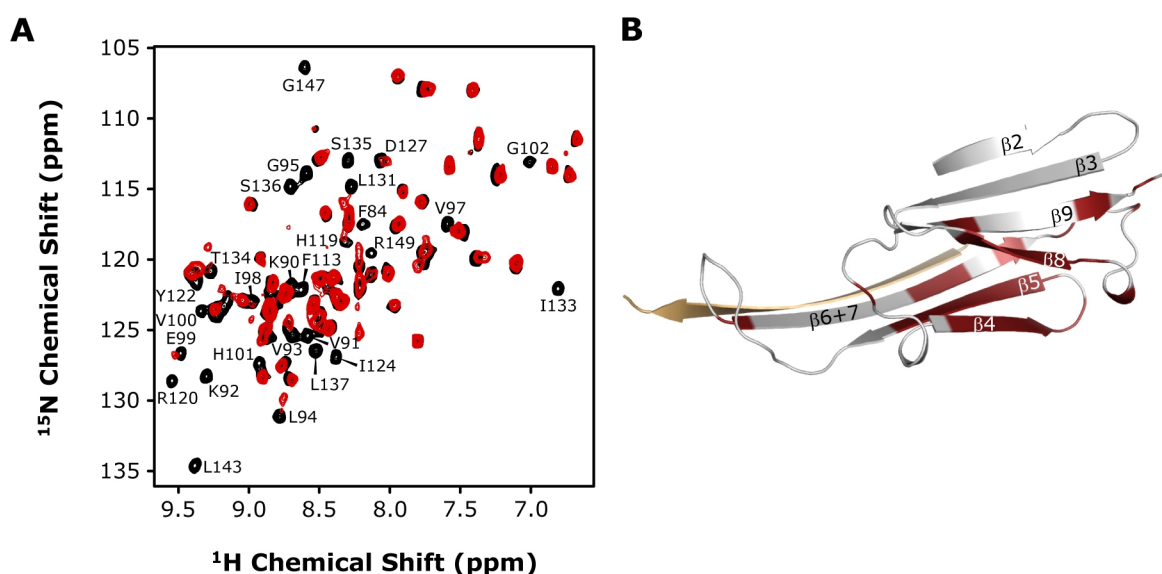


Fig. 44 The role of the $\beta 4$ - $\beta 8$ groove in the ACD of αB . (A) 1H - ^{15}N HSQC spectra of αB_{10m} in the absence (black) and presence of the IPI-motif-containing C-terminal peptide $\alpha B_{156-164}$ (red). Resonances which show exchange broadening are labeled and mapped in red onto the X-ray structure of the αB ACD [55] in (B). The β -strands are labeled. The $\beta 6+7$ strand of the opposing monomer is colored in yellow to indicate the AP interface.

3.3.4 Inhibition of $A\beta_{1-40}$ Fibril Formation

It has been reported that αB is found co-aggregated with $A\beta$ in amyloid plaques of AD patients [186], and that αB is able to inhibit fibril formation of $A\beta$ *in vitro* [188–190]. As can be seen in EM images, incubation of $A\beta_{1-40}$ at 37 °C for 4 days usually results in mature fibrillar structures (Fig. 45A). Despite a 50-molar excess of the client $A\beta_{1-40}$, the chaperone αB efficiently inhibits the fibril formation (Fig. 45A). However, smaller aggregation products were observed. To follow the aggregation process of $A\beta_{1-40}$ in more detail, DLS measurements were performed. Freshly-solubilized $A\beta_{1-40}$ (125 μM) showed a trimodal size-distribution with peaks at hydrodynamic diameters of 3.6 nm (monomer/dimer), 21 nm (oligomer A) and approximately 200 nm (oligomer B) (Fig. 45B). The species with the smallest D_h value agrees well with a monomeric or dimeric state of $A\beta_{1-40}$, whereas the larger particles correspond to higher oligomeric states of the peptide. A comparable trimodal pattern was observed in the presence of αB (2.5 μM). It should be noted that the αB particles with a D_h of ~18 nm also contribute to the oligomer A peak. Incubation of both samples at 37 °C for 105 h yielded different size-distributions. The monomeric/dimeric species was detectable only in the presence of αB . In the absence of αB , the size-distribution contained only one peak at an increased D_h of approximately 100 nm. By contrast, the αB -containing sample showed

increased stability with respect to the initially observed species. **Fig. 45C** shows the different parameters that were monitored during the kinetic measurement. The mean count rate (MCR) reflects the overall scattering intensity produced by the sample. The MCR increased continuously for the $A\beta_{1-40}$ sample in agreement with an ongoing aggregation process. When monitoring the scattering intensity of the individual species, the $A\beta_{1-40}$ monomer/dimer was no longer observable after approximately 35 h, whereas the oligomer A species propagated rapidly (**Fig. 45C**). The corresponding hydrodynamic diameter of oligomer A increased by a factor of five (**Fig. 45C**). By contrast, the monomeric species revealed no shift of its hydrodynamic size, suggesting that monomeric/dimeric building blocks are accumulated into the augmenting oligomer A (**Fig. 45C**). The chaperone αB inhibited the aggregation of $A\beta_{1-40}$, which can be assessed by the constant MCR values during the experiment (**Fig. 45C**).

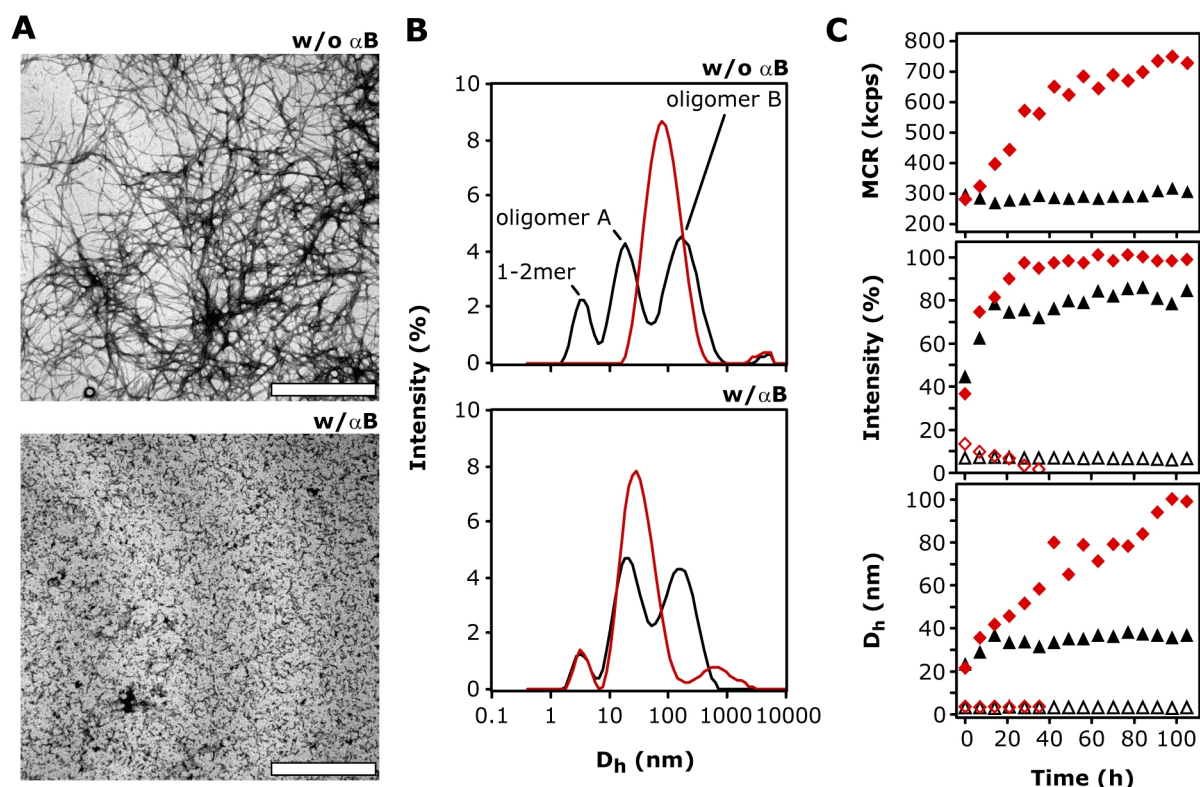


Fig. 45 αB -mediated inhibition of $A\beta_{1-40}$ fibril formation. (A) Negative-stained EM images of $A\beta_{1-40}$ samples incubated for 4 days at 37 °C in the absence (Top) and presence of αB (Bottom). The following concentrations were employed: 125 μM solubilized $A\beta_{1-40}$ and 2.5 μM αB . Scale bars of 1 μm are shown (white). The images were kindly recorded by Martina Ringling (FMP, Germany). (B) Size distributions from DLS measurements are depicted. Solubilized $A\beta_{1-40}$ (125 μM) was incubated in the absence (Top) and presence of 2.5 μM αB (Bottom). The incubation was performed for 105 h at 37 °C. The size distributions are shown for time points $t = 0$ h (black) and $t = 105$ h (red), respectively. The three species observed at the initial stage are labeled (Top). (C) DLS aggregation kinetics of $A\beta_{1-40}$ as described in (B). The mean count rate (MCR), the scattering intensity and the hydrodynamic diameter D_h are plotted versus the incubation time. The MCR is shown for the $A\beta_{1-40}$ sample in the absence (red symbols) and presence of αB (black symbols). The plots showing the scattering intensity and D_h focus on the monomer-dimer peak (open symbols) and the oligomer A peak (closed symbols), respectively.

This inhibitory effect of α B also stabilized the monomeric/dimeric species of $A\beta_{1-40}$, which was detectable at all time points with a constant D_h (**Fig. 45C**). Accordingly, the augmentation of oligomer A was less pronounced with a factor of only 1.7, and its abundance in solution was decreased to 80% with respect to the control experiment without α B. In conclusion, the data show that α B intervenes in the fibril formation process of $A\beta_{1-40}$, which finally results in an accumulation of $A\beta_{1-40}$ molecules in oligomeric or pre-fibrillar states.

3.3.5 Structural Investigations of $A\beta_{1-40}$ Aggregates

The EM images of monomeric $A\beta_{1-40}$ in the presence of α B revealed formation of large aggregates instead of mature fibrils (**Fig. 45A**). Structural characterization of these aggregates was attempted. Similar to the EM sample preparation, a 50-molar excess of isotopically-enriched ^{13}C , ^{15}N - $A\beta_{1-40}$ was co-incubated with unlabeled α B at 37 °C for 3 weeks. The pellet, which was obtained after centrifugation of the turbid solution, was subjected to solid-state MAS NMR spectroscopy. The 2D ^{13}C - ^{13}C correlation spectrum showed reasonable resolution indicating a fairly homogenous sample (**Fig. 46**). The comparison with the spectrum obtained for seeded $A\beta_{1-40}$ fibrils (Juan-Miguel Lopez del Amo, FMP) shows that $A\beta_{1-40}$ within the aggregates is structurally different from its fibrillar state (**Fig. 46**). Two sets of resonances, according to two different conformers, were observed in solid-state NMR spectra of seeded $A\beta_{1-40}$ fibrils. Residue S26 has been found to be located in a turn-region between two flanking β -strands. The S26 resonances of conformer I (tentatively assigned here) are further split into two signals in the case of $A\beta_{1-40}$, which was co-incubated with the chaperone (**Fig. 46**). The heterogeneous appearance of S26 reflects different structural arrangements within the aggregates. The insufficient amount of material hindered resonance assignment, which is required to further describe the structural state of these α B-induced $A\beta_{1-40}$ aggregates.

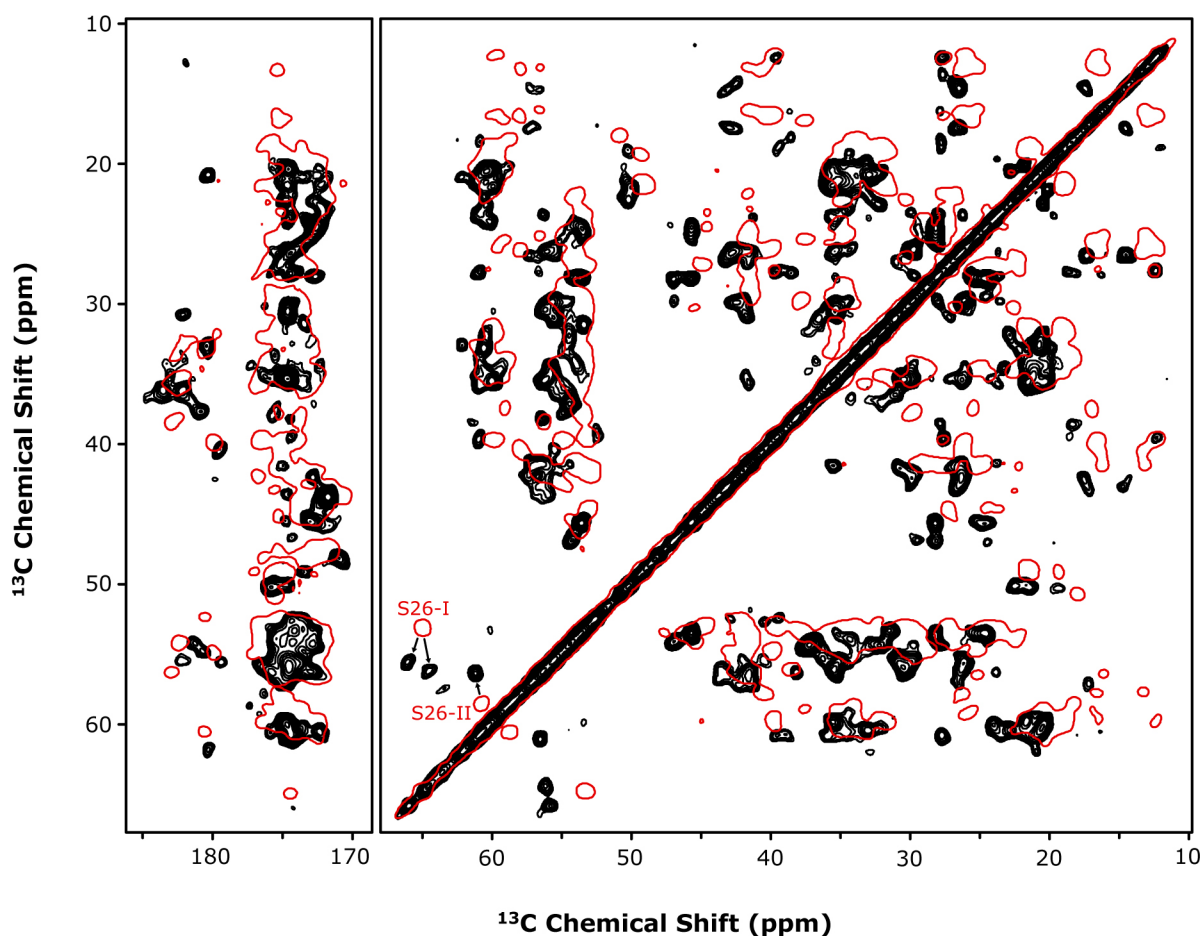


Fig. 46 Aggregates of $A\beta_{1-40}$ investigated by solid-state MAS NMR. 2D PDSD spectrum obtained for $^{13}\text{C}, ^{15}\text{N}$ - $A\beta_{1-40}$, which was co-incubated with unlabeled αB at 37 °C for 21 days (black). The concentrations used were 50 μM and 1 μM for $A\beta_{1-40}$ and αB , respectively. The spectrum was recorded at 12 °C with a spinning frequency of 12 kHz. The PDSD mixing time was set to 50 ms. The carbonyl (*Left*) and aliphatic regions (*Right*) are shown. The spectrum obtained for fibrillar $A\beta_{1-40}$ is superimposed as a reference (red), and the S26 $\text{Ca-C}\beta$ correlations are labeled for the two conformers (Juan-Miguel Lopez del Amo, FMP). Possible CSP of S26 are illustrated as arrows.

3.4 MAS NMR on Protein Solutions

As outlined in the introductory part, MAS solid-state NMR requires rotationally immobilized biomolecules, as in the case of microcrystalline or precipitated protein samples. The preparation of homogeneous samples is thus the essential step to yield high-quality spectra, but often fails. In this study, the applicability of MAS NMR spectroscopy on solutions of large protein complexes was investigated.

3.4.1 The Multimers of α B and the FROSTY Approach

As an initial model system, the large homo-oligomers of α B (~600 kDa) were employed at high concentrations (5-10 mM). MAS NMR spectroscopy yielded high-quality ^{13}C - ^{13}C correlation spectra for the viscous protein solution at $-10\text{ }^{\circ}\text{C}$ and 12 kHz spinning speed (**Fig. 47**). The 2D spectrum was obtained within one day. Linewidths for ^{13}C were on the order of 70-140 Hz, which is reasonable for fully protonated proteins, especially for a heterogeneous system such as α B. Notably, the comparison of spectra obtained for α B in solution and conventionally precipitated α B [57] revealed only marginal differences (**Fig. 48A-D**). Hence, there is no structural discrepancy for α B between the two sample preparations.

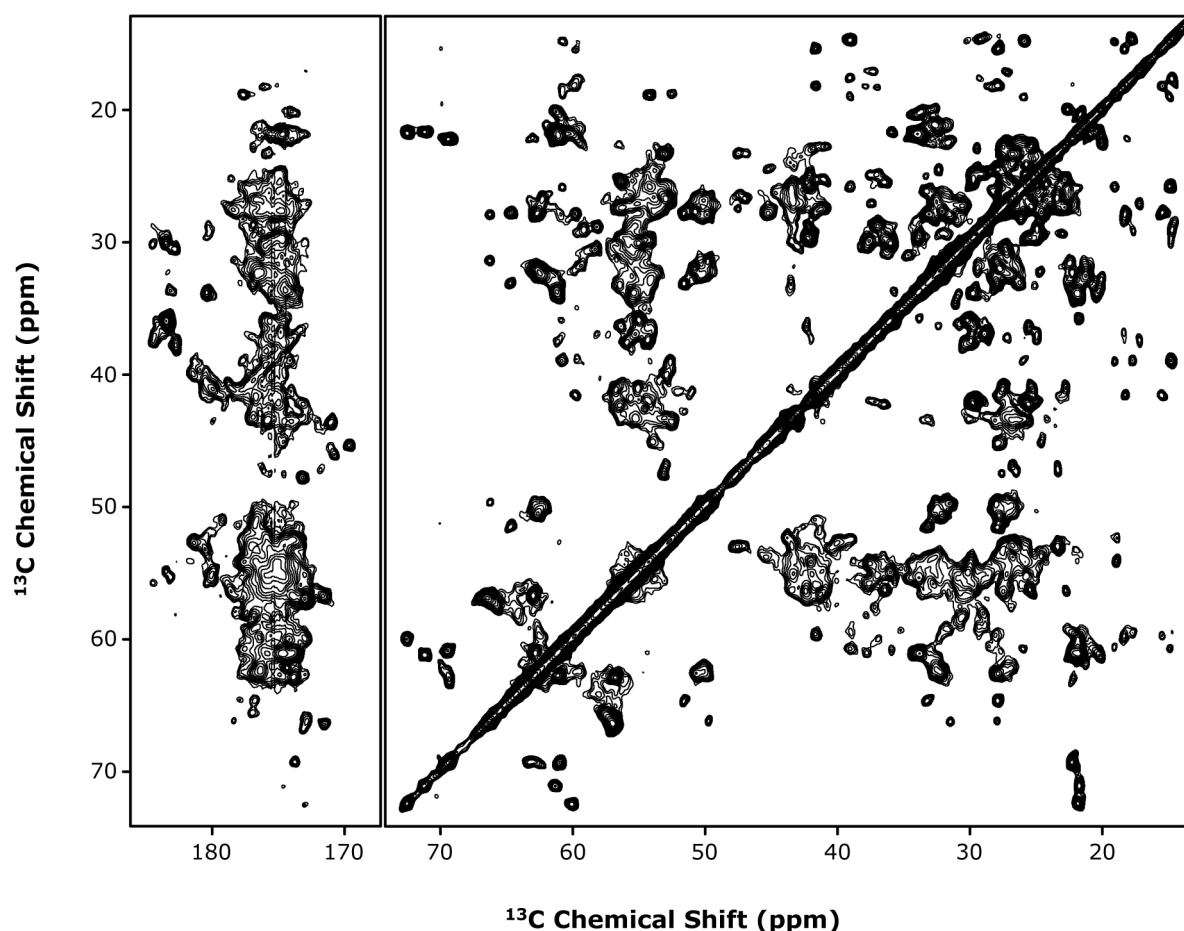


Fig. 47 MAS NMR on α B oligomers in solution. 2D PDSD spectrum obtained for full-length α B at a concentration of 217 mg/mL (~10 mM) in PBS buffer containing 20% glycerol. The spectrum was recorded at $-10\text{ }^{\circ}\text{C}$ with a spinning frequency of 12 kHz. The PDSD mixing time was set to 50 ms. The carbonyl (*Left*) and aliphatic regions (*Right*) are shown.

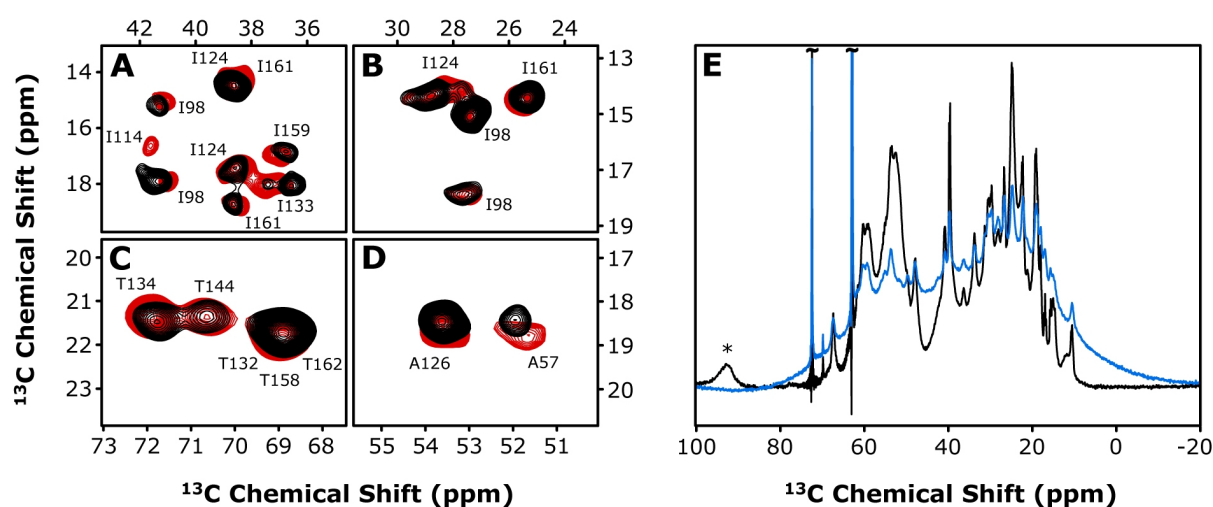


Fig. 48 Solution versus precipitate and the effect of MAS on spectral resolution. (A–D) Selected regions of 2D PDSD spectra recorded for PEG-precipitated αB [57] (red) and αB employed in solution (black). Panels correspond to correlations of (A) Ile (C β -C δ / γ), (B) Ile (C δ -C γ), (C) Thr (C β -C γ), and (D) Ala (C α -C β). Assignments refer to precipitated αB [57]. (E) ^{13}C direct excitation spectra of a solution of ^{13}C , ^{15}N - αB recorded with 12 kHz MAS (black) and under static conditions (blue). The aliphatic region of the spectrum is shown. A carbonyl spinning sideband is marked with an asterisk. Truncated resonances originate from glycerol.

^{13}C direct excitation spectra recorded on the αB solution demonstrate the effect of MAS on the spectral resolution. Under static conditions, the protein signals were largely broadened, whereas sample spinning at 12 kHz efficiently averaged anisotropic interactions, resulting in narrow resonance lines (Fig. 48E). Such a behavior is expected for rigid solids and demonstrates that αB must exhibit extremely slow molecular tumbling under the employed experimental conditions.

To further investigate αB dynamics, CP build-up experiments were performed by incrementing the contact time of the ^1H - ^{13}C Hartmann-Hahn transfer. Fig. 49A shows complete ^{13}C signal build-up for CP durations of 75 to 90 μs for both the soluble and the precipitated αB sample. The magnetization transfer to the carbonyl resonances is significantly slower (~ 500 μs), as carbonyl nuclei are not directly bound to protons. Similar build-up rates for the two sample preparations were also observed with respect to ^{15}N - ^{13}C cross polarization (Fig. 49B). The transferred magnetization from the amide nitrogen to its neighboring carbon atoms reached a maximum at approximately 1.0 ms and 1.2 ms for carbonyl and C α resonances, respectively. The results yielded further evidence that the overall dynamic behavior of soluble αB is comparable with that of its precipitate. This indicates that the large multimer of αB behaves as a solid during the MAS experiment.

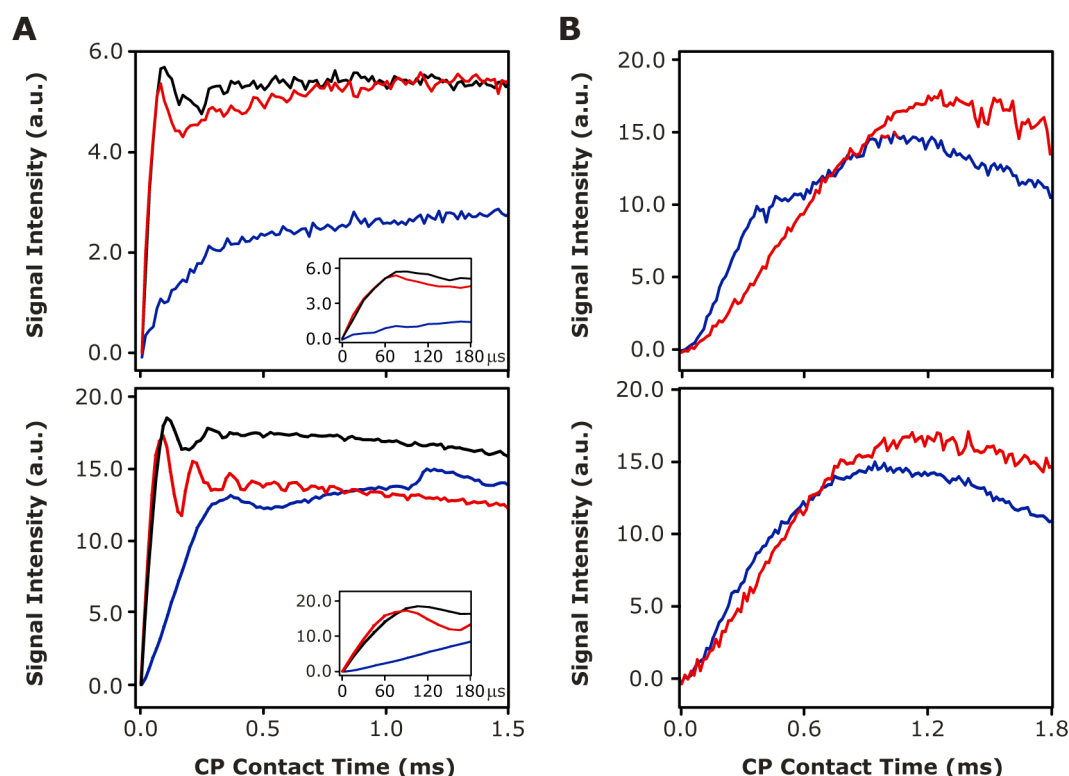


Fig. 49 Cross polarization (CP) build-up curves. Transfer efficiencies are compared for α B in solution (Top) and PEG-precipitated α B (Bottom). Signal intensities are plotted versus the Hartmann-Hahn contact time for Ca (red), C_{methyl} (black) and C' resonances (blue). Efficiencies are shown for the magnetization transfer (A) from ^1H to ^{13}C and (B) from ^{15}N to ^{13}C . The insets in (A) illustrate the initial 180 μs of the ^1H - ^{13}C CP build-ups.

Temperature-dependent 2D PDSD spectra further showed that low temperatures are beneficial for the sensitivity of the experiment (Fig. 50). Due to the presence of glycerol, effective temperatures below 0°C were achieved without freezing the sample. The retardation of protein dynamics yielded increased CP efficiencies and signal intensities. Therefore, suppression of rotational diffusion of proteins in solution is suggested as an approach to study large protein complexes by MAS NMR. Accordingly, the scheme is coined FROSTY (Freezing Rotational diffusion Of protein Solutions at low Temperature and high viscosity) MAS NMR spectroscopy [273].

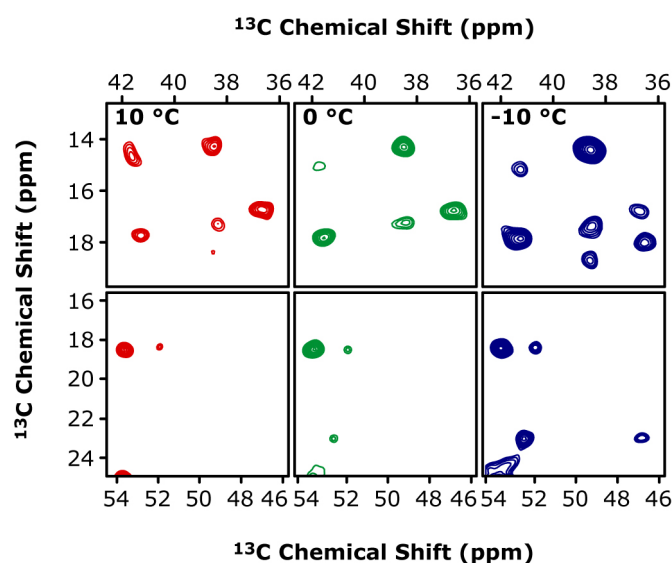


Fig. 50 Temperature-dependence of 2D PDSD spectra. ^{13}C , ^{15}N - αB in solution (100 mg/mL) was measured at effective temperatures of 10 °C (red), 0 °C (green) and -10 °C (blue) as indicated. Spectral changes are shown for Ile(C β -C δ / γ) (Top) and Ala(C α -C β)/Leu(C α / β -C δ) correlations (Bottom). A PDSD mixing time τ_{mix} of 15 ms was used. Spectra were acquired and processed in the same manner. Identical contour levels at 4σ were used in all plots to allow for comparison.

3.4.2 The 20S Proteasome Assemblies of *Thermoplasma acidophilum*

In order to test the FROSTY approach for its general applicability to large protein complexes, another model system was investigated. In the course of this work, different 20S proteasome assemblies of *Thermoplasma acidophilum* were employed to MAS NMR spectroscopy. While focusing exclusively on the NMR-active α -subunit, the assembly with NMR-inactive components, in particular the β -subunit and the 11S-activator, allows to vary the size of the complex under investigation. The PDSD spectrum of the full proteasome assembly $\alpha_7\beta_7\beta_7\alpha_7$ with a molecular weight of 670 kDa yielded ^{13}C linewidths on the order of 80 Hz (**Fig. 51**). A direct transfer of the assignments for the monomeric α -subunit from solution-state NMR [131,138] was not possible due to the different experimental conditions employed ($\Delta T = 60$ °C). However, an unambiguous identification of a few resonances was possible in well-resolved spectral regions. This indicates that FROSTY MAS NMR yields comparable structural information as observed by solution-state NMR.

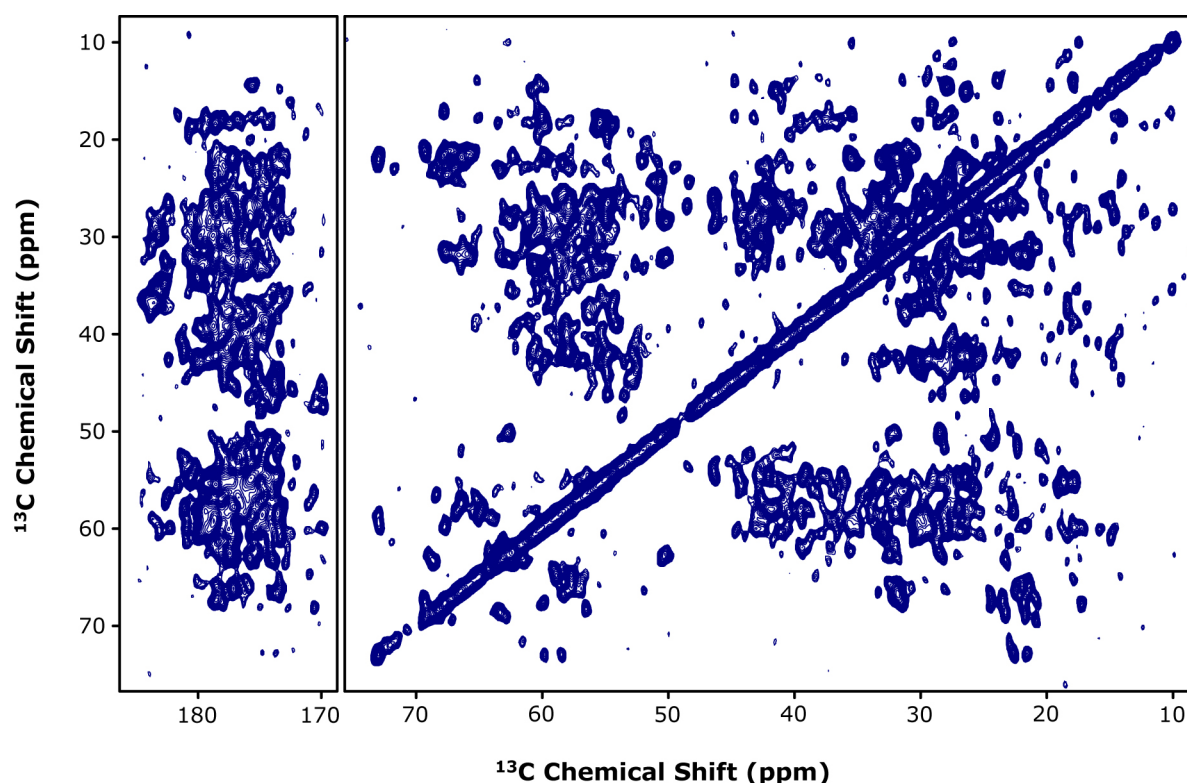


Fig. 51 FROSTY MAS NMR on the 20S proteasome assembly $\alpha_7\beta_7\beta_7\alpha_7$. The 2D PDS spectrum was obtained for $\alpha_7\beta_7\beta_7\alpha_7$ (670 kDa) at a concentration of 110 mg/mL (2.3 mM α -subunit) in PBS containing 30% glycerol. Only the α -subunit (26 kDa) was ^{13}C -enriched. The spectrum was recorded at an effective temperature of -10°C setting the spinning frequency to 12 kHz. A PDS mixing time of 50 ms was used. The carbonyl (*Left*) and aliphatic regions (*Right*) are shown. The proteasome α - and β -subunits were kindly prepared and assembled by Tomasz Religa (Group of Lewis Kay, University of Toronto, Canada).

Employing the 360 kDa $\alpha_7\alpha_7$ double-ring produced similar ^{13}C - ^{13}C correlation spectra, but with reduced resolution and sensitivity (**Fig. 52**). Similarly, the $\alpha_7\alpha_7$ complex showed reduced resolution in 1D CP spectra in comparison to the larger $\alpha_7\beta_7\beta_7\alpha_7$ particle under the same experimental conditions (**Fig. 53A**). Moreover, 1D CP spectra with varying Hartmann-Hahn contact times indicated increased dynamics and $T_{1\rho}$ relaxation rates for $\alpha_7\alpha_7$. The signal intensity for the aliphatic region of $\alpha_7\alpha_7$ and $\alpha_7\beta_7\beta_7\alpha_7$ reached its maximum at CP durations of approximately 200 μs (**Fig. 53B**). The signal intensity for $\alpha_7\alpha_7$ decreased rapidly to 65% at a contact pulse of 800 μs length, whereas $\alpha_7\beta_7\beta_7\alpha_7$ appeared less dynamic with a moderate decrease of the corresponding signal intensity to 85%. The longer CP durations for $\alpha_7\beta_7\beta_7\alpha_7$ consequently allowed for a more efficient polarization of the carbonyl nuclei (**Fig. 53A**). In conclusion, the molecular size of protein complexes plays a crucial role with respect to the performance of FROSTY MAS. Large molecular weights thus yield improved spectral resolution and sensitivity.

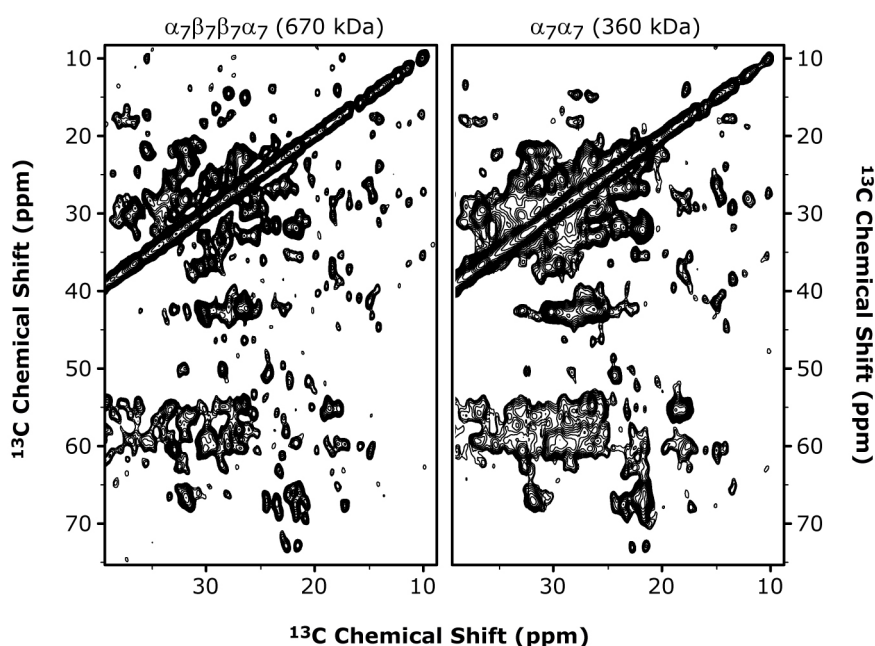


Fig. 52 Effects of molecular weight on spectral resolution for $\alpha_7\alpha_7$ (360 kDa) and $\alpha_7\beta_7\beta_7\alpha_7$ (670 kDa). Aliphatic region of 2D PDSD spectra (mixing time 50 ms). The concentration of the α -subunit amounted to 3.5 mM ($\alpha_7\alpha_7$) and 2.3 mM ($\alpha_7\beta_7\beta_7\alpha_7$), respectively. The spectra were recorded at -10°C and at a spinning frequency of 12 kHz. CP durations were optimized individually to account for the differential dynamics ($\alpha_7\alpha_7$: 250 μs ; $\alpha_7\beta_7\beta_7\alpha_7$: 800 μs). The spectrum of $\alpha_7\alpha_7$ was recorded with twice the number of scans. Apart from that, acquisition and processing parameters were identical.

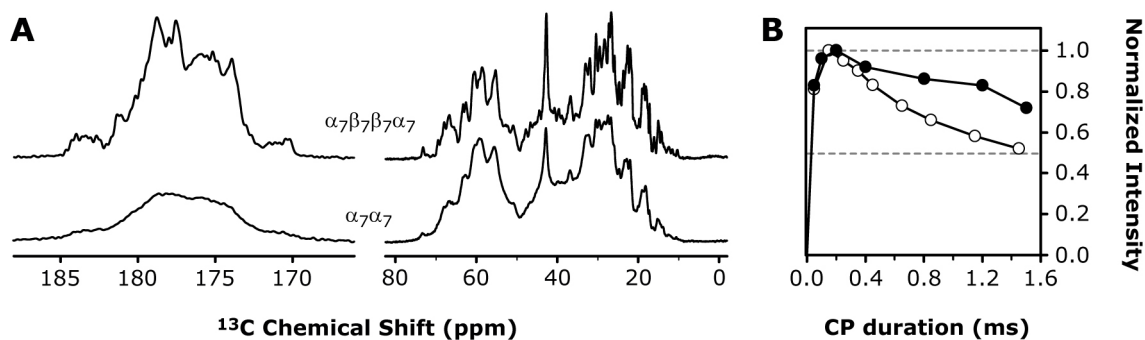


Fig. 53 Differential dynamics and resolution for $\alpha_7\alpha_7$ (360 kDa) and $\alpha_7\beta_7\beta_7\alpha_7$ (670 kDa). (A) 1D ^{13}C spectra using CP contact pulses of 250 μs ($\alpha_7\alpha_7$) and 800 μs ($\alpha_7\beta_7\beta_7\alpha_7$), respectively. The carbonyl (Left) and aliphatic regions (Right) are shown. The concentration of the α -subunit amounted to 3.5 mM ($\alpha_7\alpha_7$) and 2.3 mM ($\alpha_7\beta_7\beta_7\alpha_7$), respectively. The spectra were recorded at -10°C and at a spinning frequency of 12 kHz. Acquisition and processing parameters were identical, except the different CP durations. (B) CP build-up curves of the aliphatic region are shown for $\alpha_7\alpha_7$ (\circ) and $\alpha_7\beta_7\beta_7\alpha_7$ (\bullet).

3.4.3 Rotational Diffusion of Large Protein Complexes

3.4.3.1 Estimation of Rotational Correlation Times

Efficient averaging of anisotropic interactions by MAS usually requires solid materials devoid of any rotational reorientation (see Chapter 1.2.4). The minimum requirement is therefore the absence of molecular tumbling during one rotor period τ_R , which is defined as the inverse of the rotor spinning frequency ν_R . MAS at frequencies ν_R of 12 kHz (4 mm rotor) or 20 kHz (3.2 mm rotor) are thus equal to a rotor period τ_R of 83 μ s and 50 μ s, respectively. For a protein in solution this implies that, in order to fulfill the requirements of MAS, its rotational correlation time τ_c needs to be at least on the order of or larger than these values. Typical correlation times of small proteins in aqueous solution are on the low nanosecond time-scale at ambient temperature, whereas these values can increase to several hundreds of nanoseconds for large protein complexes (see Chapter 1.2.2, Eq. 14).

In order to explain the beneficial effects of MAS when employing solutions of large protein complexes, rotational correlation times of several protein assemblies were estimated from known molecular weights and/or hydrodynamic sizes. The Stokes-Einstein-Debye equation relates the rotational correlation time τ_c of a particle with its hydrodynamic radius R_h at different temperatures and viscosities (**Fig. 54A**, *inset*). Rotational correlation times of α B in different glycerol-water mixtures are plotted versus the temperature in **Fig. 54A**. The curves are based on known viscosities glycerol solutions [239] and were extrapolated to temperatures below 0 °C (see Chapter 2.4.10). The estimations assume R_h of α B to be 7.5 nm as an average value obtained from DLS and FCS experiments. As can be seen, the τ_c values strongly increase at low temperatures and high viscosities. However, the calculations indicate that rotational diffusion of α B as well as the proteasome assemblies occurs on the low microsecond time-scale under typical FROSTY conditions, i.e. -10 °C and in the presence of glycerol (**Fig. 54B**).

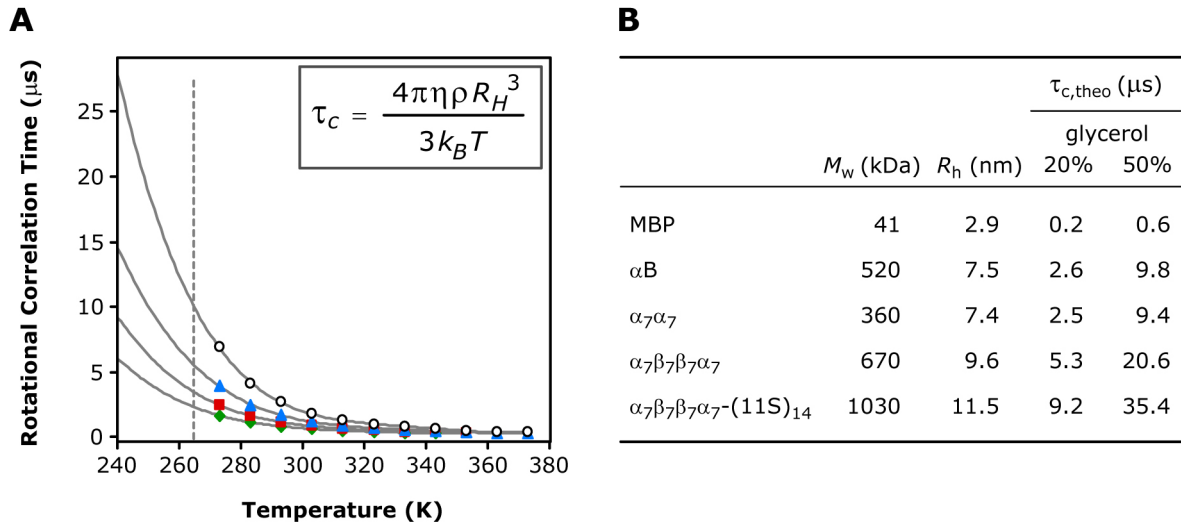


Fig. 54 Estimation of rotational correlation times. (A) Temperature-dependence of rotational diffusion. Calculated rotational correlation times τ_c of α B are plotted versus the temperature for different concentrations (v/v) of glycerol in water (20% (\blacklozenge), 30% (\blacksquare), 40% (\blacktriangle) and 50% (\circ)) according to the Stokes-Einstein-Debye equation (inset). The parameters refer to the viscosity (η), the shape factor (ρ), the hydrodynamic radius (R_h), the Boltzmann constant (k_B) and the temperature (T). The curves were calculated for known viscosities of glycerol in aqueous solution (data points, [239]) and for estimated viscosities from extrapolation to lower temperatures (grey lines). The particles of α B are assumed to have a hydrodynamic radius of approximately 7.5 nm (average value from volume-weighted DLS size-distributions and FCS experiments) and to adopt a spherical shape ($\rho = 1$) as observed in EM. (B) Theoretical correlation times $\tau_{c,theo}$ for the maltose-binding protein (MBP), α B and different proteasome assemblies at a temperature of -10°C . Values of R_h for MBP and the proteasome assemblies were estimated from molecular weights (M_w) assuming spherical particles. R_h of α B represents the average value from volume-weighted DLS size-distributions (7.3 nm) and FCS experiments (7.7 nm). Correlation times are listed for 20% and 50% v/v glycerol in water.

The 1.1 MDa proteasome complex $\alpha_7\beta_7\beta_7\alpha_7-(11S)_{14}$ reveals a τ_c value of approximately 35 μ s in the presence of 50% glycerol. By contrast, τ_c of the 41 kDa maltose binding protein (MBP) amounts only to several hundreds of nanoseconds. The estimations show that the low temperatures and high viscosities employed cannot explain the efficient performance of MAS. The high protein concentrations might be the key aspect to elucidate the observations in FROSTY experiments. Molecular crowding and unspecific protein interactions at the employed concentrations might cause non-linear effects from the Stokes relation. Another possibility is that the effective protein concentration is higher than initially provided due to protein sedimentation during MAS. To answer these questions, NMRD and FCS experiments were performed to experimentally determine the rotational mobility of α B multimers in solution.

3.4.3.2 Nuclear Magnetic Relaxation Dispersion (NMRD)

Water protons and their interaction with protein molecules can be utilized as probes for the rotational reorientation of the proteins [264,265]. This is accomplished by measuring longitudinal relaxation rates (R_1) of the water protons at variable magnetic fields. R_1 rates are mainly influenced by the exchange rates (τ_M^{-1}) between bulk water protons and protons transiently attached to the protein. Relaxation dispersion profiles for α B solutions were recorded under typical FROSTY conditions, i.e. highly concentrated α B (100 mg/mL) in PBS containing 20% glycerol. Earlier studies have shown that NMRD profiles can be described by the sum of three Lorentzian dispersions giving rise to three different correlation times τ_i [265]. The dispersion profiles obtained at 25 °C, -3 °C and -10 °C were fit simultaneously in order to reduce the covariance among the unknown parameters (**Fig. 55A**, see also Chapter 2.5.2). In the case of small proteins, the weighted average $\langle\tau_c\rangle$ of the three τ_i values is in good agreement with rotational correlation times derived from the Stokes-Einstein-Debye equation [265]. However, this does not hold for large protein complexes as has been shown for apoferritin [265]. Accordingly, the obtained $\langle\tau_c\rangle$ value for α B at 25 °C is on the order of 90 ns, which deviates substantially from the Stokes estimation (1.2 μ s). The two major components (82.9% and 10.9%) with correlation times τ_3 of 5.5 ns and τ_2 of 63 ns cause this discrepancy (**Fig. 55A**). These components are likely to originate from water protons that are in the fast exchange regime ($\tau_M^{-1} > \tau_c^{-1}$) with short residence times on the protein. Only the minor component (6.2%) with the correlation time τ_1 of 1.3 μ s corresponds to water protons, that are bound to the protein long enough to report on the protein tumbling rate ($R_{1M} < \tau_M^{-1} < \tau_c^{-1}$). This small fraction of water protons most likely contains the information about the actual rotational correlation time of α B. The obtained τ_1 value of 1.3 μ s at 25 °C is in agreement with Stoke and thus suggests that there are no species with correlation times in the high microsecond range. The small fraction of water protons in the appropriate exchange regime is expected to decrease with increasing M_w and increasing τ_c of the protein (**Fig. 55B**). High viscosities and low temperatures further decrease this fraction of water protons. In conclusion, the NMRD approach can be used to access rotational diffusion rates of proteins, but the method is limited by the time scales of water proton exchange between bulk water and the protein, especially in the case of large protein systems. Hence, FCS was performed to directly monitor very slow tumbling α B particles in solution (see Chapter 3.4.3.3).

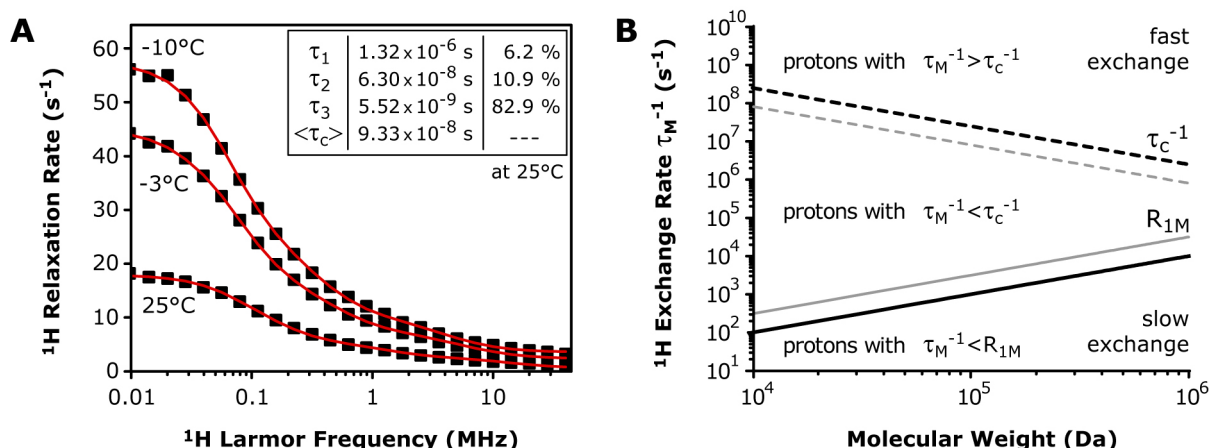


Fig. 55 Water proton relaxation in a concentrated α B solution. (A) Relaxation dispersion profiles of an aqueous solution of α B (100 mg/mL) in PBS containing 20% glycerol. Relaxation rates (■) were measured at temperatures of -10 , -3 and 25 °C as indicated. Red lines represent the fitting curves obtained from a simultaneous fit of all three dispersion profiles. Each profile was fit with three Lorentzians resulting in three components with correlation times τ_i and their respective weights. The obtained parameters for the sample at 25 °C are shown in the inset together with the weighted correlation time $\langle \tau_c \rangle$. (B) Effects of the proteins molecular weight M_w on its tumbling rate τ_c^{-1} (dashed line) and the relaxation rate of water protons, which are dipole-dipole coupled to protons of the protein (R_{1M} , continuous line). This is compared to the water proton exchange rate τ_M^{-1} . The dependencies are illustrated for temperatures of 25 °C (black lines) and -10 °C (grey lines). The diagram is reproduced from the collaboration partners Giacomo Parigi (Group of Claudio Luchinat, University of Florence, Italy), who also performed the NMRD experiments.

3.4.3.3 Fluorescence Correlation Spectroscopy (FCS)

In order to follow diffusion processes of α B in solution, the protein was covalently linked via its lysine side-chains to the fluorescent dye bis-Cy5. The labeling reaction was performed such that, at the most, one molecule of the dye was attached to the α B oligomer. Rigid co-rotation with the protein can be assumed for the bi-functional dye [237]. The measurement of absorption at wavelengths of 280 nm and 649 nm, corresponding to the content of protein and dye, respectively, confirmed the desired protein-to-dye ratio.

FCS was performed on a highly concentrated sample of α B (105 mg/mL) containing 0.002 % of Cy5- α B. According to the MAS NMR experiments, the protein was dissolved in PBS containing 20% glycerol. Data analysis yielded rotational correlation times τ_c of 1.3 μ s and 2.4 μ s at temperatures of 20 °C and -1 °C, respectively (Fig. 56A,B). Theoretical values $\tau_{c,theo}$ were estimated to be on the order of 0.7 μ s and 1.5 μ s, respectively, assuming a spherical particle of $R_h = 7.3$ nm, as observed in volume-weighted DLS size-distributions. FCS measurements employing a diluted α B sample in PBS yielded a reorientation time of 0.47 μ s, which relates to R_h of 7.7 nm. The volume-based hydrodynamic radius from DLS studies is thus fairly consistent with the FCS-derived radius. These results suggest that there is a

deviation from the Stokes-Einstein-Debye relation for α B at a concentration of 105 mg/mL by a factor of approximately 1.6 to 1.8.

Subsequently, a concentration series of α B was measured in order to follow possible crowding effects at higher protein concentrations. Translational and rotational diffusion FCS measurements were performed at a temperature of 20 °C and with varying concentrations of α B in PBS without glycerol. As can be seen, diffusion is slowed down at higher protein concentrations. Translational diffusion was strongly impaired with diffusion coefficients of $362 \times 10^{-9} \text{ cm}^2/\text{s}$ and $5 \times 10^{-9} \text{ cm}^2/\text{s}$ at protein concentrations of 0.1 $\mu\text{g/mL}$ and 300 mg/mL, respectively (**Fig. 57A**). By contrast, the rotational correlation time τ_c of α B at a concentration of 256 mg/mL was only three times larger (1.42 μs) than the corresponding value for the dilute sample (0.47 μs) (**Fig. 57B**). A sample with a concentration of 300 mg/mL did not yield satisfactory results, presumably due to cis-trans isomerization of the fluorescent dye on a time-scale similar to the tumbling rate of the protein complex. Calculated viscosities from the obtained translational and rotational diffusion rates illustrate that, as expected, molecular crowding at high protein concentration affects translational diffusion to a much greater extent than the rotational mobility of α B oligomers (**Fig. 57C**). This is valid in the concentration range investigated, but non-linear behavior might occur at protein concentrations $>300 \text{ mg/mL}$.

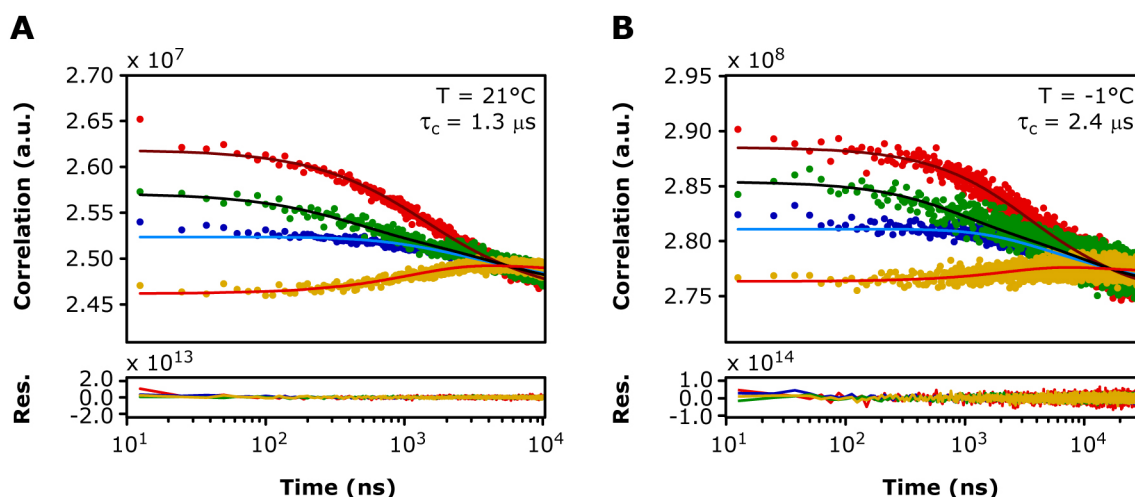


Fig. 56 Rotational correlation times of α B as obtained by FCS at different temperatures. (A) 21 °C, (B) -1°C . The sample contained 100 mg/mL of α B in PBS in the presence of 20% glycerol. The single-photon data of all four detectors (red, green, blue and yellow) are shown (see Chapter 2.4.9). The FCS spectra were kindly acquired and analyzed by Christoph Pieper (Group of Jörg Enderlein, University of Göttingen, Germany).

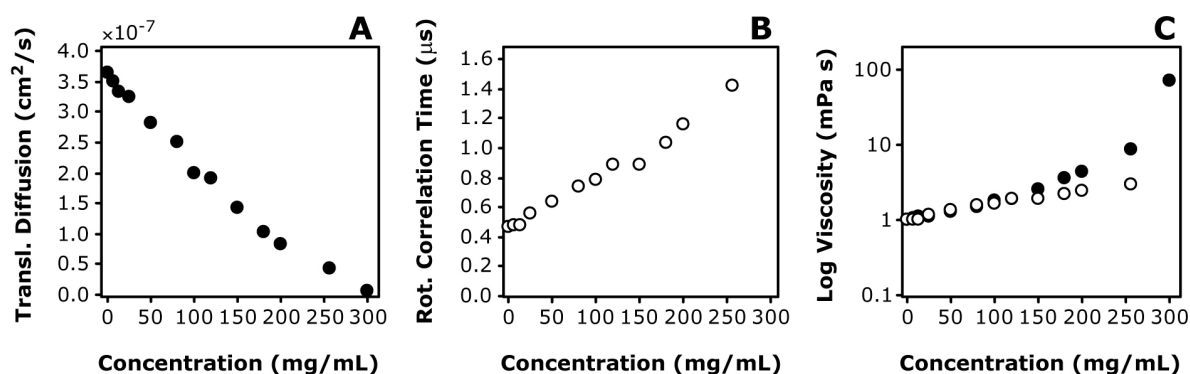


Fig. 57 Translational (A) and rotational diffusion (B) of αB multimers at different concentrations from FCS experiments. (C) Apparent viscosities calculated from the experimentally derived translational (\bullet) and rotational diffusion rates (\circ). Note the logarithmic scale. The experiments were performed with bis-Cy5- αB in PBS without glycerol and at a temperature of 20 °C.

The NMRD and FCS studies revealed that the rotational mobility of the αB particle is in the low-microsecond range under the employed experimental conditions. This regime is expected from theoretical considerations. High viscosity, low temperature and high protein concentration cannot solely account for the suppression of molecular tumbling in MAS NMR experiments. Hence, protein sedimentation during MAS must cause an increased protein concentration at the inner wall of the MAS rotor. Rotational diffusion of protein molecules is suppressed by this dense packing and thus much slower than the MAS rate. Recent results from our co-workers have confirmed this concept [274].

3.4.4 ^1H -detected FROSTY MAS NMR

3.4.4.1 Perdeuterated αB Multimers in Solution

The application of the FROSTY approach is limited by the amount of protein in the MAS rotor and thus by the solubility of the respective protein system. Detection of the high- γ nucleus ^1H is a possibility to increase the sensitivity of FROSTY experiments. Proton-detection in the solid state is hampered due to the presence of a strong ^1H - ^1H dipolar coupling network, which limits the achievable resolution for protonated samples [225]. Consequently, αB was expressed fully-deuterated at non-exchangeable sites, whereas water-exchangeable moieties such as NH- and OH-groups were back-substituted in PBS containing 20% H_2O and 80% D_2O . This proton density has been reported to provide the optimal compromise between sensitivity and resolution [229]. Several cycles of buffer-exchange at elevated temperatures

and subsequent lyophilization ensured that the proton concentration in fact matches the theoretical values, in particular for slow-exchanging residues in the β -sandwich of the ACD. CP-based ^1H - ^{15}N correlation spectra of full-length αB are reminiscent of solution-state HSQC spectra obtained from the ACD construct αB10m (**Fig. 58**). The typical chemical shift pattern of the αB core domain enabled partial transfer of resonance assignments for well-resolved spectral regions, e.g. for L89, G112, R116, R120, D127, V128, T132, G141, L143 and G147. Peak picking yielded approximately 80 backbone resonances, which represents less than half of the expected number of peaks (175 residues). This reduced number of correlation peaks might arise from the dynamic behavior of the N-terminal domain (residues 1-60). In addition, highly-flexible residues at the C-terminus (residues 165-175) are expected to be filtered out during CP. Resonances potentially belonging to residues at the dimer interface, e.g. G112, R116 and R120, showed chemical exchange broadening, resulting in weak signal intensities or multiple sets of resonances. Presumably due to this heterogeneity, the observed linewidths for ^1H and ^{15}N were rather broad with values on the order of 100 Hz and 50 Hz, respectively. These values are comparable to reported linewidths for the β -barrel membrane protein OmpG and for fibrils of the amyloid peptide $\text{A}\beta_{1-40}$ [231]. Experimental transversal relaxation times T_2 for bulk ^1H and ^{15}N amide nuclei of αB were determined to be on the order of 4.1 ms and 8.9 ms, respectively. The corresponding theoretical linewidths for ^1H and ^{15}N thus amount to 80 Hz and 35 Hz, respectively. The discrepancy between the observed and T_2 -derived linewidths indicates static conformational heterogeneity for the αB . The limited sensitivity was compensated by the addition of Cu(II)-EDTA resulting in short ^1H T_1 values of approximately 150-200 ms. The longitudinal relaxation time T_1 in the absence of Cu(II)-EDTA was determined to 2.1 s. The addition of 60 mM Cu(II)-EDTA thereby enabled fast data accumulation and a reduction in measurement time by a factor of ten. Accordingly, ^1H - ^{15}N correlation spectra with reasonable signal-to-noise were obtained within 1.5 hours.

The ^1H - ^{15}N correlation of full-length αB contains histidine side-chain resonances (**Fig. 58, inset**). A similar signal was observed in solution-state ^1H - ^{15}N HSQC spectra of αB10m and assigned to the imidazol-NH group of H104 at the AP interface (**Fig. 38B**). In the case of the full-length protein, the multiple sets of resonances imply either a heterogeneous environment for H104 in the polydisperse multimers of αB , or the presence of several histidine residues that are protected from exchange with water. Short CP durations of less than 1 ms enable fast magnetization transfers and consequently the detection of those fast exchanging NH-groups.

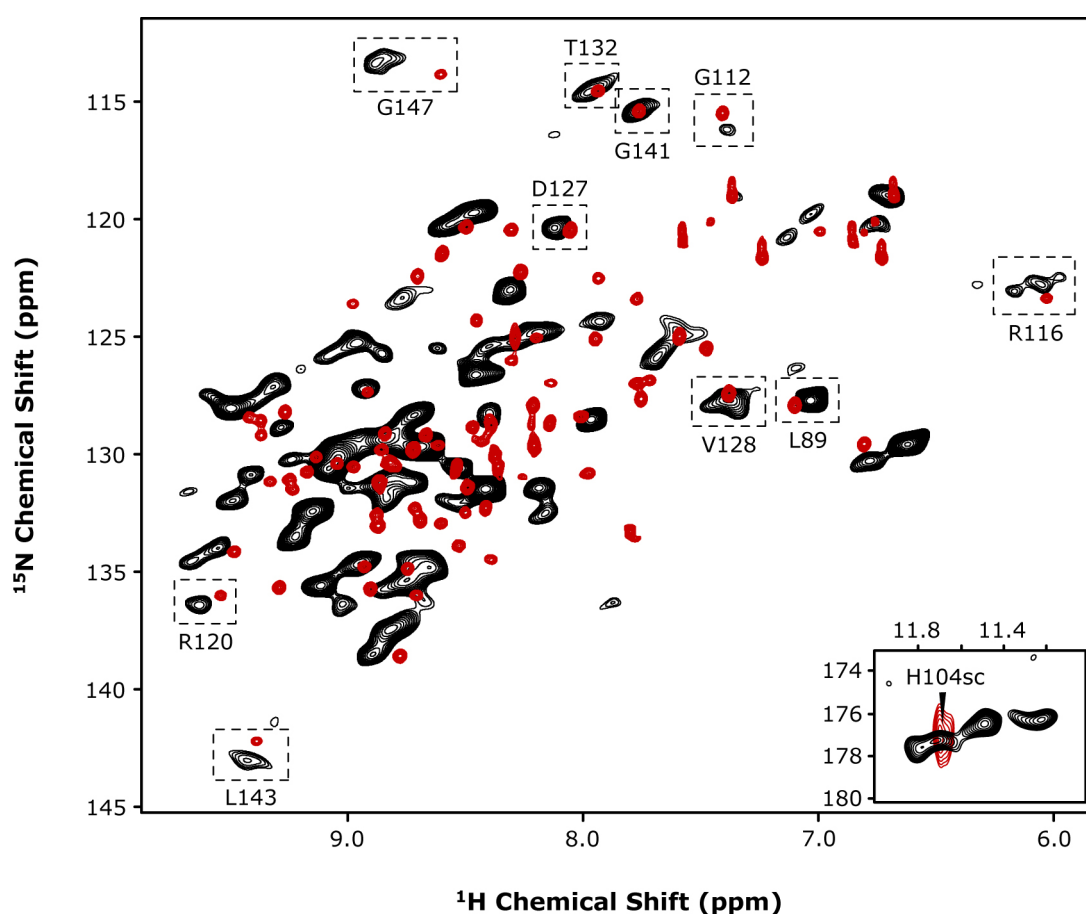


Fig. 58 Proton-detected MAS NMR on perdeuterated α B oligomers in solution. The CP-based ^1H - ^{15}N correlation spectrum of full-length α B (black) was obtained at a concentration of approximately 120 mg/mL (~ 6 mM). The solution-state ^1H - ^{15}N HSQC spectrum of the ACD construct α B10m is shown as a reference (red). The overlay demonstrates the conservation of the chemical shift pattern of the ACD. Transfer of assignments is unambiguous for certain resonances in resolved regions (dashed boxes). The inset shows histidine side-chain resonances as also observed for H104 of α B10m in a solution-state ^1H - ^{15}N HMQC spectrum (red). The FROSTY sample was prepared as follows: ^2H , ^{13}C , ^{15}N - α B back-exchanged in PBS containing 20% H_2O , 80% D_2O , 20% deuterated glycerol and 60 mM Cu(II)-EDTA . The spectrum was recorded at an effective temperature of 0°C and with 18 kHz MAS. The recycle delay was set to 400 ms.

Substitution of CP transfer steps with INEPT elements in the pulse sequence can reveal flexible parts of immobilized biomolecules in MAS NMR spectroscopy. For α B, these through-bond correlation experiments yielded spectra with a reduced set of resonances (30 peaks) in comparison to the dipolar coupling-based experiment (Fig. 59A). *De-novo* resonance assignment is required to unambiguously identify the respective residues. Tentative assignment was possible for the loop residues E87-L89, D127 and G141 due to the conserved chemical shifts in the full-length protein and α B10m. Several signals in the INEPT-based spectrum were not detected in the CP-based experiment, but perfectly superimposed with the solution-state ^1H - ^{15}N HSQC spectrum of full-length α B. The corresponding resonances were

unambiguously assigned to residues A168-K175 in the unstructured C-terminal tail of α B (**Fig. 59B**). It has been reported that the C-terminal region of α B is highly flexible and tumbles independently of the oligomer [262]. The low dispersion in the ^1H dimension clearly underlines the absence of secondary structure. Conventional solution-state NMR thus exclusively detects the very terminal residues of the protein. By contrast, the INEPT-based FROSTY MAS spectrum shows additional residues, that are part of the core domain of α B.

Protein sedimentation prior to the MAS experiment might be an alternative to increase the amount of sample in the MAS rotor. Ultracentrifugation of α B at $180.000\times g$ yielded a transparent and sticky sediment. According to the employed amount of protein, the α B concentration in the sediment can be estimated to be approximately 400-500 mg/mL. The sediment was transferred to a 3.2 mm MAS rotor (~ 16 mg of protein). The experimental resonance lines of this sample were severely broadened, with ^1H and ^{15}N linewidths on the order of 180 Hz and 120 Hz, respectively. The relatively low gain in signal-to-noise by only a factor of 1.5 (expected: 4x) reflects this substantial broadening of resonance lines for the α B sediment. Fast dehydration of the sedimented protein might explain the increased linewidths.

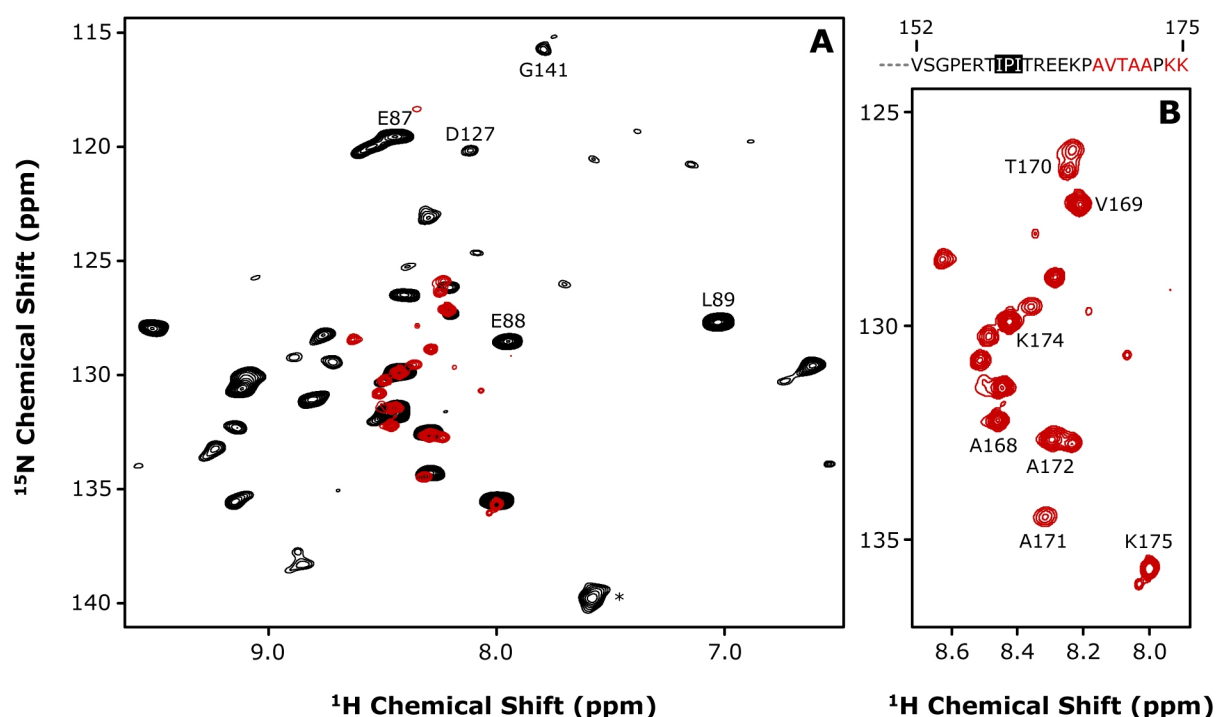


Fig. 59 Flexible regions in α B. (A) ^1H - ^{15}N INEPT correlation spectrum obtained for full-length α B (black) at a concentration of approximately 120 mg/mL (~ 6 mM). The solution-state ^1H - ^{15}N HSQC spectrum of perdeuterated α B is shown as a reference (red). Tentative assignments are shown. A folded arginine side-chain signal is marked with an asterisk. (B) The solution-state ^1H - ^{15}N HSQC spectrum of perdeuterated α B focusing on resonances, that were unambiguously assigned. These resonances originate from the highly flexible and unstructured C-terminus as shown on top (red). The conserved IXI-motif of sHSPs is highlighted.

3.4.4.2 Perdeuterated 20S Proteasome Assemblies in Solution

The different 20S proteasome assemblies of *Thermoplasma acidophilum* are structurally more homogeneous compared to the polydisperse α B system [126]. Moreover, the modular assembly of these protein complexes allows carrying out molecular weight-dependent NMR studies. Whilst observing exclusively the NMR-active α -subunit, the molecular weight of the assembly can be successively increased by adding the NMR-invisible subunits. Proton-detected FROSTY experiments were performed to test whether these supramolecular complexes can be accessed by typical solution-state NMR methods.

Initially, ^1H - ^{13}C correlation experiments were performed using the half-proteasome $\alpha_7\alpha_7$ with a molecular weight of 360 kDa. For this purpose, highly-deuterated $\alpha_7\alpha_7$ was prepared with CHD_2 -labeled methyl groups of isoleucines ($\delta 1$ position only), leucines and valines (ILV) [210]. The FROSTY experiments were performed at an effective temperature of 0 °C. The chemical shift pattern of the CP-based ^1H - ^{13}C correlation spectrum obtained at 20 kHz MAS demonstrates high resemblance to the solution-state spectrum [138] recorded at 50 °C (**Fig. 60A,B**). Transfer of assignments was partially feasible. Line-widths for ^1H and ^{13}C were on the order of 40 Hz and 45 Hz, respectively (**Fig. 60C**). Notably, the methyl resonances of valines and leucines showed reduced signal intensities (approximately 30%) in comparison to isoleucine- $\delta 1$ signals (**Fig. 60C**). The increased proton density of the two methyl moieties in valine and leucine residues is presumably the origin of this decrease. Therefore, it might be beneficial to reduce the degree of protonation by complete perdeuteration of one of the two methyl groups in valines and leucines.

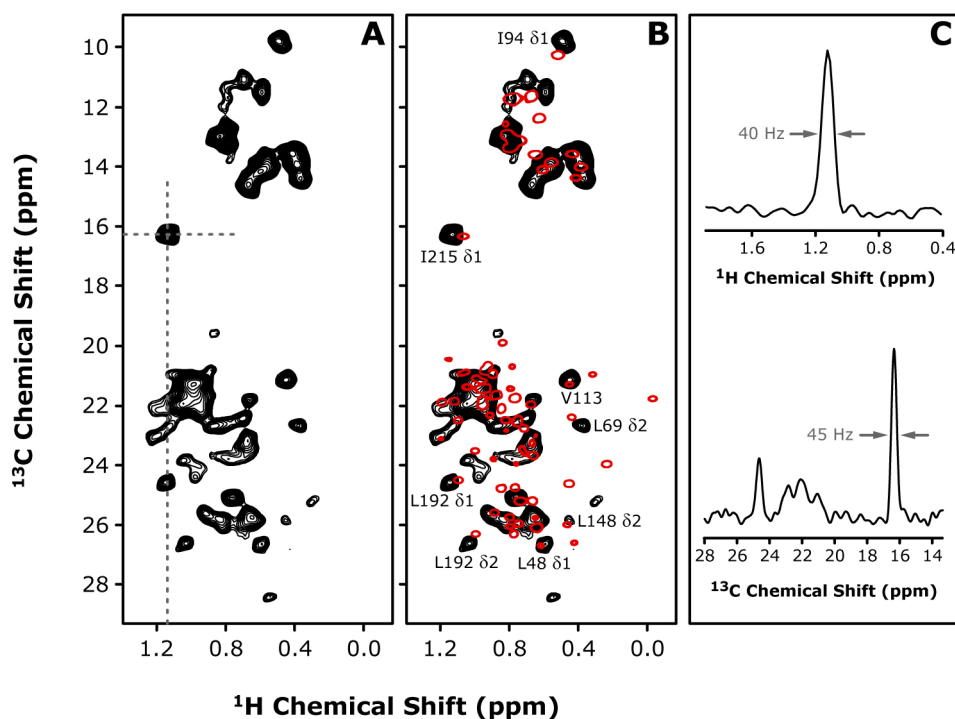


Fig. 60 Detection of methyl moieties in the 360 kDa half-proteasome $\alpha_7\alpha_7$ in FROSTY experiments. (A) 2D ^1H - ^{13}C CP spectrum of the ILV-labeled $\alpha_7\alpha_7$ double ring (black), showing methyl resonances of isoleucines, leucines and valines. The spectrum is superimposed with the solution-state HMQC spectrum of $\alpha_7\alpha_7$ (red, [138]) in (B). Resonances which can clearly be identified from solution-state NMR assignments are labeled. (C) 1D projections at ^1H and ^{13}C chemical shifts of the I215- δ_1 resonance in the ^1H - ^{13}C CP spectrum. The corresponding line-widths at half-height are indicated. For the FROSTY sample, perdeuterated ILV- $\alpha_7\alpha_7$ was employed at a concentration of 92 mg/mL (~ 3.5 mM) in PBS containing 20% H_2O , 80% D_2O and 40% deuterated glycerol. The spectrum was recorded at an effective temperature of 0 $^\circ\text{C}$ and with 20 kHz MAS, whereas the solution-state HMQC spectrum was acquired at 50 $^\circ\text{C}$. The proteasome α - and β -subunits were kindly prepared and assembled by Tomasz Religa (Group of Lewis Kay, University of Toronto, Canada).

Subsequently, we focused on the protein backbone amides by recording ^1H - ^{15}N correlation spectra. Such experiments are routinely performed in solution-state NMR of small-sized proteins, but are difficult to access for protein complexes with a molecular weight of more than 200 kDa. Observation of protein backbone resonances is hampered by the very slow overall tumbling of these large systems in solution (see Chapter 1.2.3). Amide moieties are, however, indispensable for sequential assignment of a protein [256,261,275]. Given that rotational diffusion is absent under typical FROSTY conditions, MAS can efficiently average chemical shift anisotropies and dipolar interactions. As in the case of perdeuterated αB , the α - and β -subunits of the 20S proteasome were recombinantly expressed in fully-deuterated growth medium. The proton density at the exchangeable sites was restricted by back-substitution with PBS containing 20% H_2O and 80% D_2O . Again, only the 26 kDa α -subunit

was enriched with the NMR-observable isotopes ^{13}C and ^{15}N . This allows increasing the molecular weight of the proteasome assembly while restricting the number of resonances.

Fig. 61 shows the obtained ^1H - ^{15}N CP correlation spectra for the 360 kDa $\alpha_7\alpha_7$ double ring (3.3 mM α -subunit) and the 670 kDa $\alpha_7\beta_7\beta_7\alpha_7$ full proteasome (1.9 mM α -subunit). The experiments were performed under identical experimental conditions. The quality of the spectra improves with increasing molecular weight. Despite the lower protein concentration (factor of 1.7), the $\alpha_7\beta_7\beta_7\alpha_7$ sample yields a better sensitivity than $\alpha_7\alpha_7$. Consistent with the results obtained from ^{13}C -detected experiments, the ^1H - ^{15}N correlation spectra for $\alpha_7\alpha_7$ and $\alpha_7\beta_7\beta_7\alpha_7$ illustrate that high molecular weight is a key for a good performance of the FROSTY approach.

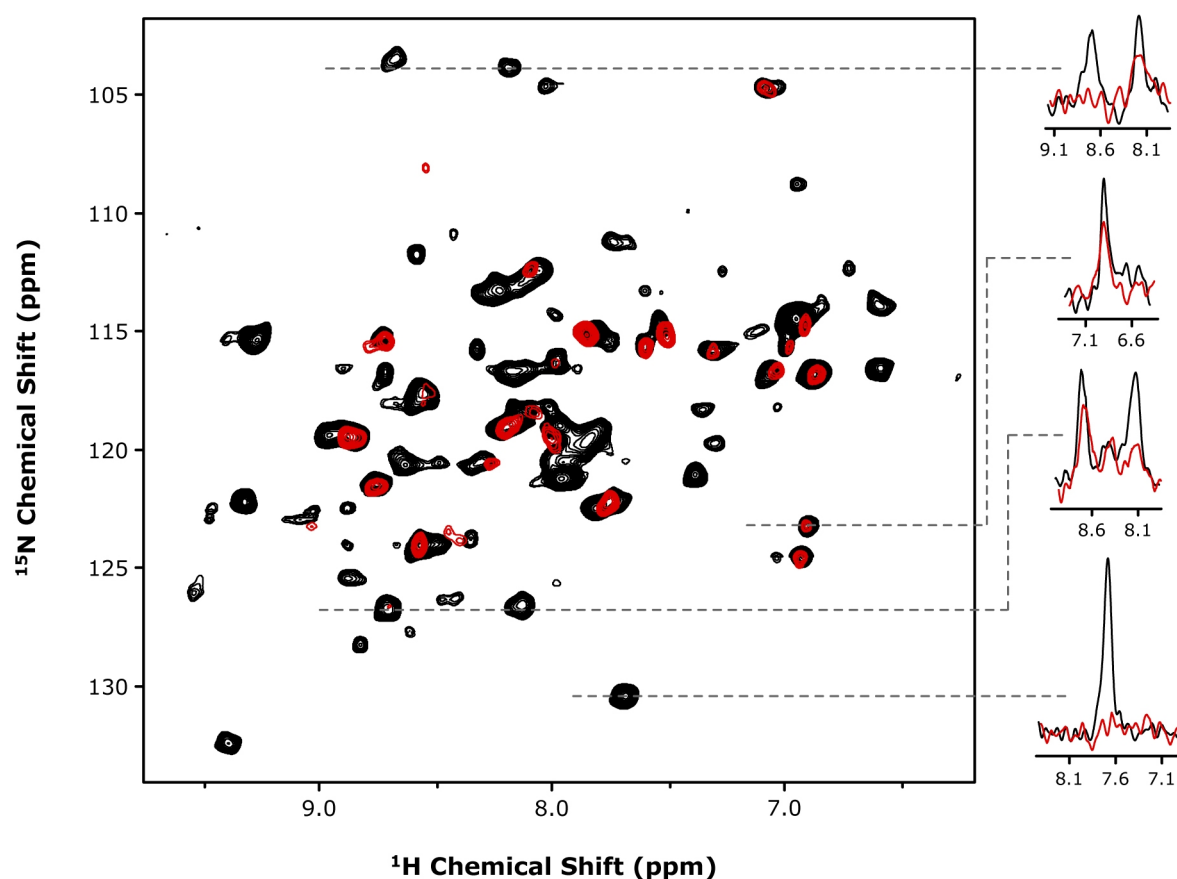


Fig. 61 Proton-detected FROSTY experiments and the impact of molecular weight. CP-based ^1H - ^{15}N correlation spectra obtained for the 360 kDa half-proteasome $\alpha_7\alpha_7$ (red) and the 670 kDa full proteasome assembly $\alpha_7\beta_7\beta_7\alpha_7$ (black). Only the α -subunit was labeled with ^{13}C and ^{15}N . Selected 1D projections at different ^{15}N chemical shifts (dashed lines) are shown at the right. The employed amounts of the α -subunit in the MAS rotor were 2 mg ($\alpha_7\alpha_7$) and 1.2 mg ($\alpha_7\beta_7\beta_7\alpha_7$), respectively. Deuterated glycerol (30% v/v) was added to both samples. The spectra were acquired and processed in the same manner and are depicted at identical contour levels to allow for direct comparison.

The molecular weight of the 20S proteasome was further increased by titration of $\alpha_7\beta_7\beta_7\alpha_7$ with the perdeuterated 11S-activator from *Trypanosoma brucei*. The resulting protein assembly $\alpha_7\beta_7\beta_7\alpha_7-(11S)_{14}$ has a molecular weight of more than 1 MDa [133]. In order to speed up data acquisition, Cu(II)-EDTA (60 mM) was added to the sample giving rise to ^1H T_1 values on the order of 130 ms.

The full proteasome $\alpha_7\beta_7\beta_7\alpha_7$ in complex with the 11S-activator yielded well-resolved ^1H - ^{15}N correlation spectra with narrow line-widths on the order of 40 Hz (^1H) and 20 Hz (^{15}N), respectively (**Fig. 62A**). An overlay with the solution-state ^1H - ^{15}N TROSY spectrum of the heptameric assembly α_7 (180 kDa, [138]) illustrates the high degree of similarity between the two sample preparations (**Fig. 62A**). Considering the presence of the β -subunit and 11S-activator on both surfaces of the heptameric α_7 ring and the difference in experimental temperature of approximately 50 °C, the observed chemical shift changes between the two spectra are reasonable. Peak picking yielded approximately 110 cross-peaks. The published resonance assignment for the heptameric α_7 ring contains 165 assigned amide signals for the 233-residue α -subunit [138]. Chemical exchange line broadening is a plausible cause for the incomplete set of signals. Apparently, this holds true also for the $\alpha_7\beta_7\beta_7\alpha_7-(11S)_{14}$ complex. Several assignments were tentatively transferred from the solution-state spectrum. However, *de-novo* resonance assignment was required for unambiguous identification of residues.

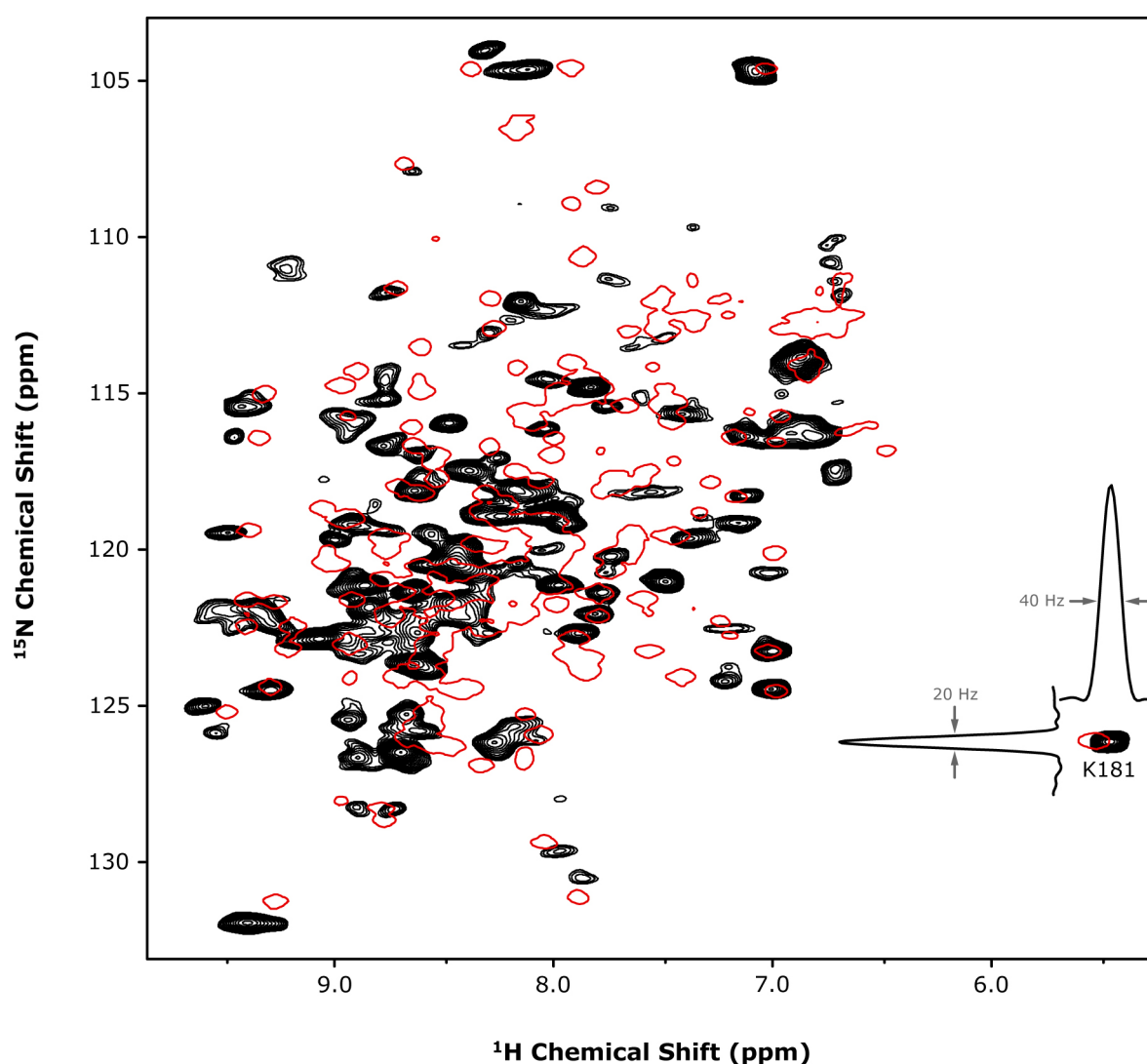


Fig. 62 Protein backbone resonances of a 1MDa proteasome complex observed by FROSTY MAS. (A) CP-based ^1H - ^{15}N correlation spectrum of the full proteasome in complex with the 11S-activator ($\alpha_7\beta_7\beta_7\alpha_7$ - $(11\text{S})_{14}$) (black). The spectrum is superimposed with the solution-state TROSY spectrum of the heptameric α_7 construct (red contours) with a molecular weight of 180 kDa [138]. Tentative assignments are indicated. 1D projections and the corresponding line-widths at half-height for ^1H and ^{15}N are illustrated for K181. For the FROSTY sample, the ^2H , ^{13}C , ^{15}N -labeled α -subunit was assembled with the perdeuterated β -subunit and finally complexed with a 1.5-fold molar excess of perdeuterated 11S-activator. The final protein concentration amounted to 280 mg/mL (~ 3 mM α -subunit) in PBS containing 20% H_2O , 80% D_2O , 20% deuterated glycerol and 60 mM Cu(II)-EDTA . The spectrum was recorded at a MAS frequency of 22 kHz and at an effective temperature of 5 $^\circ\text{C}$, whereas the solution-state TROSY spectrum of α_7 was acquired at 50 $^\circ\text{C}$ [138]. The proteasome α - and β -subunits were kindly prepared and assembled by Tomasz Religa (Group of Lewis Kay, University of Toronto, Canada), whereas the 11S-activator was kindly provided by Remco Sprangers (University of Tübingen, Germany).

To assign the amide resonances, 3D HNCO-type experiments were performed using CP (^1H - ^{15}N) and INEPT elements (^{15}N - ^{13}C) for magnetization transfer [267] (Fig. 63A). However, the HNCO experiment turned out to be highly insensitive giving rise to less than 7% signal intensity compared to the ^1H - ^{15}N correlation experiment (Fig. 63B,C). For comparison, an

intensity of approximately 15% with respect to the ^1H - ^{15}N correlation experiment was reported for chicken α -SH3 [267]. The substantial loss most likely occurs during the INEPT transfer steps from ^{15}N to ^{13}C , and vice versa, in which magnetization is transversal during a period of 60 ms. Experimentally derived transversal relaxation times T_2 for ^{15}N were on the order of 12 ms. These short life-times might explain the inefficiency of the HNCO experiment, but are contradictory to the observed ^{15}N linewidths of 20 Hz and the corresponding theoretical T_2 of 16 ms. In conclusion, the results indicate considerable dynamics of the sedimented proteins. The 2D ^1H - ^{13}C plane of the HNCO experiment required data accumulation of 3 k scans in order to achieve adequate signal-to-noise ratio (**Fig. 63D**).

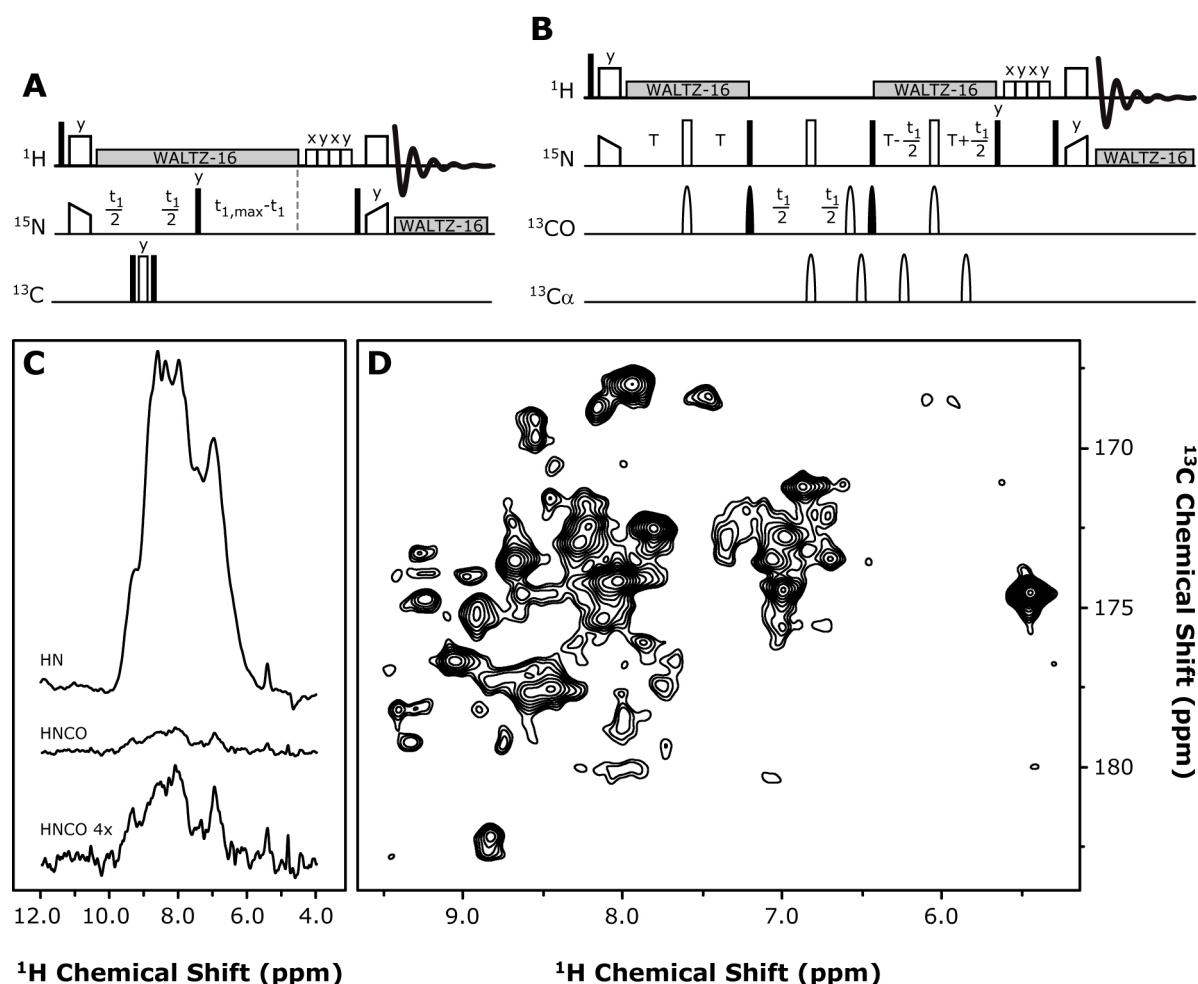


Fig. 63 Triple-resonance experiments on $\alpha_7\beta_7\beta_7\alpha_7$ -(11S) $_{14}$: the HNCO experiment. (**A**) Pulse sequence of the CP-based ^1H - ^{15}N correlation experiment [228,267] (see Appendix 5.2.6 for pulse program). (**B**) Pulse sequence of the HNCO experiment using CP transfer steps (^1H - ^{15}N) and INEPT transfer steps (^{15}N - ^{13}C) [267] (see Appendix 5.2.6 for pulse program). The duration T was set to 12 ms. (**C**) 1D versions of the ^1H - ^{15}N correlation experiment (1 k scans) and the HNCO experiment (4 k scans) are shown with indices HN and HNCO, respectively. The 1D HNCO spectrum is enlarged on the bottom. The additional transfer and refocusing steps in the HNCO experiment led to a signal loss of 93%. The spectra were processed by exponential apodization with a line-broadening of 50 Hz. (**D**) The 2D ^1H - ^{13}C plane of the HNCO experiment was recorded with 3 k scans.

Due to the short T_2 values, INEPT elements were substituted by dipolar-based transfer steps, i.e. long-range CP, in order to generate magnetization on ^{13}C spins [268]. The employed pulse sequence is shown in **Fig. 64A**. Initial ^1H magnetization is transferred directly to nearby ^{13}C nuclei, namely C_α and C' , via long-range CP steps. Usually, these long-range magnetization transfers require durations of 3.5 ms for efficient polarization between the nuclei [268]. Due to the pronounced dynamics of the sample, CP durations with optimal transfer efficiencies were found to be on the order of only 2 ms. Additional magnetization is gained by the COPORADE approach, which uses a combined excitation of ^1H and ^{13}C [268]. After ^{13}C evolution and back-transfer to the amide protons, the magnetization follows a similar path as in the case of the ^1H - ^{15}N correlation. The experiment was designed in a constant-time fashion to ensure reproducible dephasing of the water resonance and thus efficient water suppression. This was crucial because of the high content of water in the FROSTY sample. By setting the ^{13}C carrier frequency on resonance to the aliphatic or carbonyl region, and by providing appropriate CP conditions, the hCXhNH experiment can be converted to a hCAhNH or hCOhNH experiment, respectively. The two experiments give complementary information as illustrated in **Fig. 64B**.

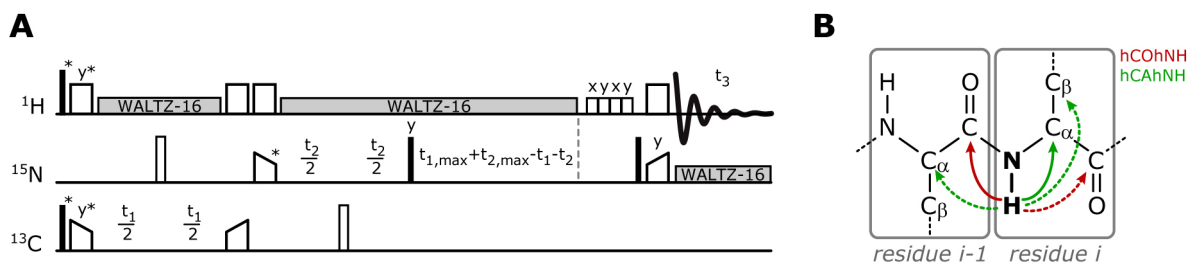


Fig. 64 The 3D hCXhNH experiment [268]. **(A)** Pulse sequence of the hCXhNH experiment (see Appendix 5.2.6 for pulse program). After excitation of both ^1H and ^{13}C nuclei, magnetization is transferred from amide protons to dipolar-coupled carbon atoms by the use of long-range CP steps with durations of 2 ms. Asterisks denote pulses, which were used for TPPI incrementation. The experiment was designed in a constant-time fashion in order to optimize water suppression. **(B)** Illustration of observed correlations in hCXhNH experiments. Each amide proton is dipolar-coupled to carbon atoms of its own residue *i* (intra-residual) and to carbon nuclei of the preceding residue *i*-1 (inter-residual). Thereby, sequential information can be obtained. The long-range CP from ^1H to ^{13}C can be optimized such that magnetization transfer is achieved only to carbonyl (hCOhNH, red arrows) or to aliphatic nuclei (hCAhNH, green arrows). Strong couplings are illustrated with continuous lines, whereas weaker couplings are depicted with dashed lines. Given that the signal-to-noise ratio is sufficient, the hCAhNH experiment can also yield correlations to side-chain nuclei such as C_β and C_γ [268].

Results

Data acquisition amounted approximately to three and five days for the 3D hCOhNH and hCAhNH experiment, respectively. Data analysis yielded backbone resonance assignments for 74 out of 227 non-proline residues (**Fig. 65** and Appendix Tab. 12). These were accessed by comparing the observed chemical shifts of H_N , N_H , $C\alpha$ and C' with the solution-state assignment of the α_7 ring [138]. In some cases, the observation of intra-residual $C\beta$ correlations additionally confirmed the identity of the respective residues. Sequential information further facilitated the assignment procedure. Inter-residual contacts were mainly observed in the hCAhNH spectrum and allowed for a sequential walk along the protein backbone (**Fig. 65**). Approximately 35 observed amide correlations were not assigned, due to missing correlations in the ^{13}C dimension, missing sequential information and/or due to large deviations from the solution-state chemical shifts.

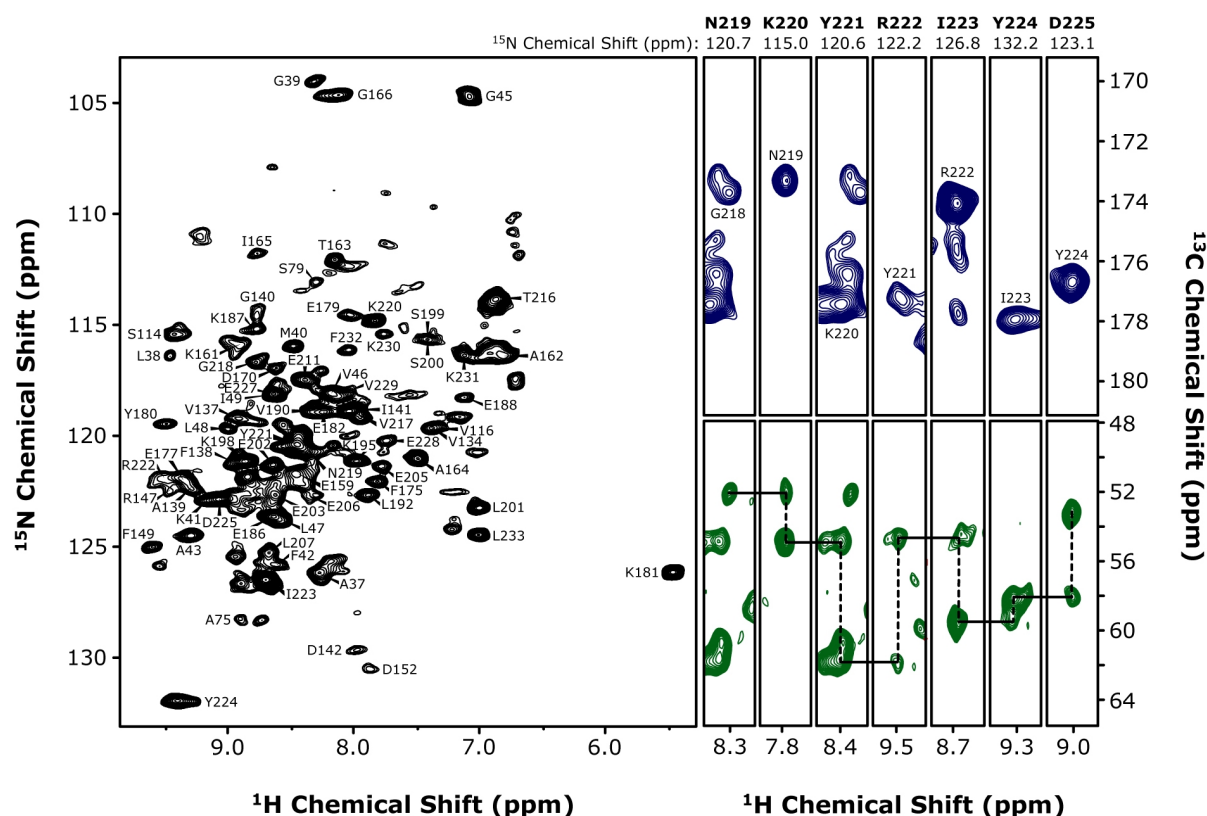


Fig. 65 Backbone resonance assignment of $\alpha_7\beta_7\beta_7\alpha_7$ -(11S)₁₄: the hCOhNH and hCAhNH experiments. The 1H - ^{15}N correlation spectrum of $\alpha_7\beta_7\beta_7\alpha_7$ -(11S)₁₄ and the obtained assignments are shown on the left. A strip plot for residues N219-D225 is illustrated on the right with correlations to carbonyl atoms (blue) and to $C\alpha$ atoms (green). In this case, sequential information was provided only by the $C\alpha$ correlations (lines).

Solution-state NMR yielded backbone resonance assignments for 165 residues of the α_7 ring [138]. In that case, the majority of non-observable residues can be found in the regions M1-S35, D51-I67, A96-102 and A117-R130 (**Fig. 66A**). Similar regions of the $\alpha_7\beta_7\beta_7\alpha_7$ -(11S)₁₄ complex were invisible in FROSTY experiments (**Fig. 66A**). These regions were even more extended. Mapping the non-observable residues onto the X-ray structure of the α -subunit reveals that the corresponding regions are involved in the intermolecular assembly of the different proteasome subunits [126,133] (**Fig. 66B-D**). By contrast, the assigned residues are located at the outer surface of the heptameric α_7 ring and are not involved in intermolecular interactions, neither with the α -subunit itself, nor with the 11S activator and the β -subunit (**Fig. 66D**). Hence, it seems that exchange dynamics between the proteasome subunits hinder the observation of residues, which are located at these intermolecular junctions.

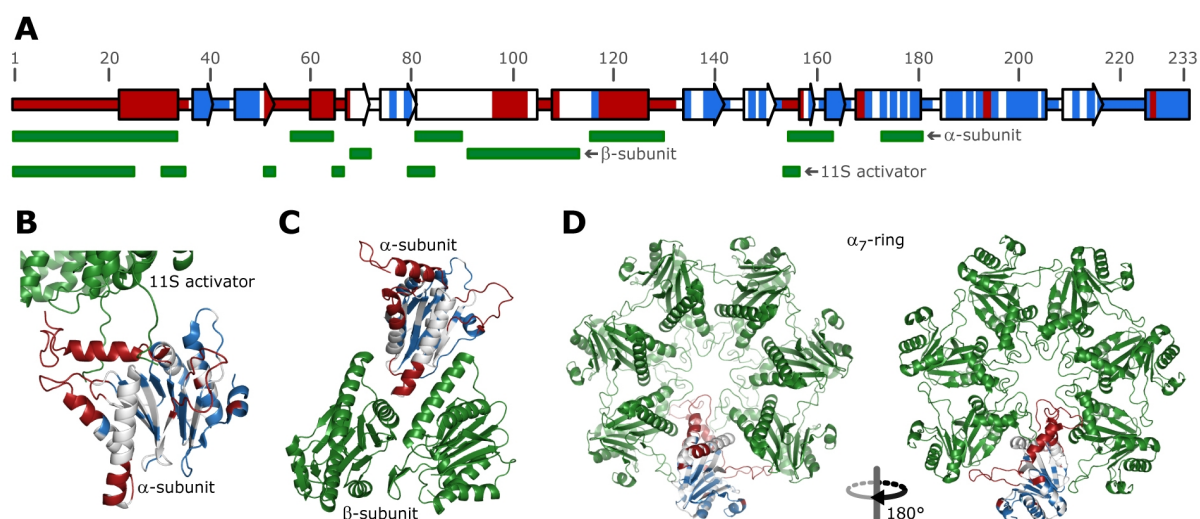


Fig. 66 Intermolecular contacts and exchange dynamics in the 20S proteasome assembly. (A) Primary and secondary structure of the proteasome α -subunit. Secondary structure elements are depicted as arrows (β -strand) and rectangles (α -helix). Residue numbers are shown on top. Residues which were assigned for the $\alpha_7\beta_7\beta_7\alpha_7$ -(11S)₁₄ complex by FROSTY are shown in blue. Red regions were not assigned or not observed for the heptameric α_7 construct by solution-state NMR. Regions within the α -subunit that are involved in intermolecular interactions with the α -subunit itself, the β -subunit and the 11S-activator are depicted below the sequence (green rectangles). All this information is mapped onto the X-ray structure of the α -subunit [126,133] in (B-D). The color-coding is the same as in (A). The respective interaction partners within the proteasome assembly are labeled and shown in green.

4 Discussion and Conclusions

4.1 Protein Preparation

Initial attempts to purify full-length α B with an N-terminal His₆-tag failed due to non-specific and non-quantitative protease cleavage. The yields of correctly cleaved α B were on the order of 50%, indicating that half of the N-termini are most likely buried inside of the oligomeric assembly. Such an arrangement is also observed in the X-ray structure of wheat HSP16.9, in which six N-terminal arms are buried in the inner cavity of the 12-mer assembly, whereas the other six N-terminal domains are disordered, making them potentially accessible to protease cleavage [35]. However, the preparation of tag-free α B was straightforward and resulted in high protein yields of 100 mg of unlabeled α B per liter cell culture. It should be noted that the purified α B, which was used in the scope of this work, was biologically active as demonstrated by the chaperone activity assay. Cloning, expression and purification of the construct α B10m was also successful and yielded a properly folded ACD in agreement with the reported structure. This was the basis for a comprehensive biophysical characterization.

4.2 α B-crystallin and Metal-binding

Recent investigations have shown that α B is able to coordinate Cu(II) with high affinity, thereby suppressing the redox-chemistry and the cytotoxic effects of the transition metal [68]. In addition, the chaperone activity of α B was shown to be modulated by metal ions [65]. These aspects suggest a role of α B in copper homeostasis and imply Cu(II) as a co-factor triggering α B chaperone function. No structural details concerning this interaction were available to date. In this work, NMR spectroscopy and various other biophysical methods were applied to investigate the Cu(II)-binding property of full-length α B and the truncated ACD-construct α B10m.

Fluorescence quenching and ITC experiments revealed a picomolar-range affinity (10^{-12} M) for the core fragment α B10m towards Cu(II). Picomolar affinity has also been reported, and was likewise found in this work, for full-length α B [68]. Binding stoichiometries obtained from ITC- and ICP-MS experiments are consistent and show that one Cu(II) ion is bound per

monomeric subunit. Recently, it was proposed that α B can bind up to five Cu(II) ions per subunit and that the binding sites are distributed over the entire sequence of α B [69]. These results were obtained in an indirect way. The results presented in this work show that the ACD is the basic unit specifically coordinating Cu(II). There is no indication that the terminal sequences contribute to specific binding in any respect. This finding was the basis for the NMR investigations on the isolated ACD. Triple-resonance experiments yielded complete assignment of the α B10m backbone amides except for residue S139. The combination of ^{13}C -detected solution-state NMR experiments and the development of the FROSTY MAS NMR approach enabled the structural elucidation of the Cu(II)-binding property of α B. The NMR experiments show that Cu(II) coordination occurs at the AP interface in the loop region between strands β 5 and β 6+7. This is valid for both the isolated ACD and full-length α B. Potential Cu(II) ligands are H104, D109, H111 (β 5- β 6+7-loop) as well as H83 (β 3- β 4-loop). These residues are conserved among different metazoans, but also for human α A, HSP20 and HSP27. Electron paramagnetic resonance (EPR) experiments employing full-length α B pointed towards a coordination involving three nitrogen donor atoms [65]. This is in agreement with our model, in which the vicinity of H83, H104, H111 and D109 allows for concerted Cu(II)-binding. A tetrahedral Cu(II)-binding motif involving the imidazole rings of three histidines and the carboxylate moiety of an aspartic acid is observed in other protein structures as well, e.g. in Cu,Zn-SOD or calgranulin C [97,119]. However, it cannot be excluded that other ligands such as water or the nearby residues E105, E106 and E110 participate in binding of Cu(II). Hence, coordination geometries other than tetrahedral might be adopted, e.g. tetragonal or bipyramidal arrangements [87]. Whilst the exact geometry of the metal site needs to be experimentally determined, the present data allows for conclusions about the role of Cu(II) in the chaperone function of α B as discussed below. It should also be noted that the proposed model of the Cu(II) coordination sphere does not account for observed structural changes in the N-terminal region (β 2- β 3), but that it focuses exclusively on the β 3- β 4- and β 5- β 6+7-loop. Former molecular modeling studies predicted H101 and H119 (AP interface) as well as H18 (N-terminal domain) as possible residues participating in Cu(II)-binding [65]. Our findings show that neither residues from the N-terminal domain nor the interfacial residues H101 and H119 on the opposing face of the extended bottom-sheet contribute to Cu(II)-binding of α B.

The crystal structure of truncated α A (residues 59-163) revealed an intermolecular Zn(II)-binding motif involving three monomers and the residues H100, E102 (monomer A), H107 (monomer B) and H154 (monomer C) [56]. The sequence alignment between α A and α B yields H104, E106, H111 and G154 as the corresponding residues in α B. Interestingly, the involvement of H104 and H111 is in agreement with our findings. However, our ^{15}N relaxation data clearly excludes an intermolecular Cu(II)-binding motif for α B. Furthermore, a glycine is found in position 154 in α B, and the C-terminal sequence of α B does not contain additional histidine residues.

D109 plays an essential role for Cu(II)-binding as the mutant α B10m-D109A is completely deprived of Cu(II)-binding competence. By contrast, α B10m-R120G retains its Cu(II)-binding capability. This finding suggests that Cu(II) competes with the disease-related R120 of the neighboring monomer for interactions with D109. It is worth emphasizing that there are two Cu(II)-binding sites at the AP interface. The violation of salt-bridges on both edges of the interface consequently affects stability of the dimeric subunit. The crystal structure of the ACD mutant R120G shows the collapse of the bidentate ion-pairs between R120 and D109 [269]. In the mutant, a novel intermolecular salt-bridge is formed between residues D80 and H83 (β 3 strand), thereby inducing closure of the shared groove. The involvement of residues D109 and H83 in Cu(II) coordination might impede formation of both intermolecular ion-pairs. As a consequence, Cu(II) potentially weakens the monomer-monomer interaction and opens the shared groove, thereby entailing that client binding sites become more accessible. The destabilization of the AP interface may also result in an altered register other than the AP2 state. The variability of the AP interface was suggested to contribute to α B polydispersity [55,56]. Increased dynamics at the AP interface might explain the difficulties to crystallize Cu(II)- α B10m. Indeed, dynamic exchange broadening in NMR spectra was observed for the entire set of interfacial residues in case of apo- α B10m, and even more so for Cu(I)- α B10m, Zn(II)- α B10m as well as the mutants α B10m-D109A and α B10m-R120G, respectively. Moreover, Cu(II) substantially decreased the rotational correlation time of α B10m. Likewise, SEC and DLS experiments indicated partial dissociation of α B10m upon addition of Cu(II). The observations suggest that Cu(II) has an impact on quaternary dynamics of the dimeric substructure. Previous studies revealed the monomer-dimer equilibrium of α B as an essential element for chaperone function [276,277].

Upon addition of Cu(II), we found severe CSP for resonances of N-terminal residues located proximal to the AP interface. This was observed for both full-length α B and α B10m. The β 2- β 3 region forms the edges of the shared groove and is of functional and structural relevance. Residues F75-K82 (β 3 strand) and F113-R120 (β 6+7 strand) of α B are crucial for chaperone activity [272]. Protein constructs comprising residues D73-K92 (β 3- β 4) are known as mini-chaperones, which are able to bind and stabilize client proteins. Modification of residues D80 and H83 abolishes the anti-aggregation property of this mini-chaperone [278]. Further studies highlighted the importance of residues N78, K82 and H83 as well as F84 and P86 for the chaperone function of α B [279,280]. The dual role of strand β 3 and the subsequent loop for client and metal ion sequestration is supported by the fact that α B loaded with the client γ -crystallin is impaired in Cu(II)- and Zn(II)-binding [281]. Intriguingly, residues F75-K82 (β 3 strand) were also found to be involved in intermolecular interactions between subunits and thus to maintain the oligomeric network [282]. A recent structural model of α B multimers proposes a 24-mer as the fundamental, though transient, oligomeric state (**Fig. 67A**) [58,60,61]. According to this model, strand β 2 (W60-T63) is either unoccupied (β 2_{free}) or hydrogen-bonded to strand β 3 of its own ACD (β 2_{intra}). Additional dimeric building blocks, which can be accommodated in the 24-mer scaffold, show intermolecular β 2- β 3 contacts in a 28-mer model (β 2_{inter}) [61]. Hence, M68 (β 2- β 3-loop) exists in diverse conformational states and is involved in the intermolecular assembly [57,61]. Our MAS NMR results showed CSP for M68 in Cu(II)- α B. This observation implies Cu(II)-induced structural changes in the N-terminal domain. Residue A57 is located in a loop region between strands β 1 (Y48-P51) and β 2 (W60-T63) [61]. The disappearance of its resonance in PDS spectra of Cu(II)- α B suggests that, in agreement with the oligomer model, A57 is located in close vicinity of paramagnetic Cu(II). The broadening of the A57 resonance in the presence of diamagnetic Zn(II) indicates that metal-binding alters the exchange dynamics in the N-terminal domain. The interfacial strand β 6+7 and the proximal strand β 3 are multifunctional elements in the core of the α B dimer. They represent candidate binding sites for client proteins, maintain the stability of the dimeric building block and contribute to its organisation in multimer assembly. The presented data provide evidence that Cu(II) intervenes in these processes by recruiting its ligands from the β 3- β 4- and the β 5- β 6+7-loop. Here, a model is proposed in which Cu(II) affects dynamics of the dimeric substructure and, in a relayed manner, of the native α B oligomer (**Fig. 67B**) [283].

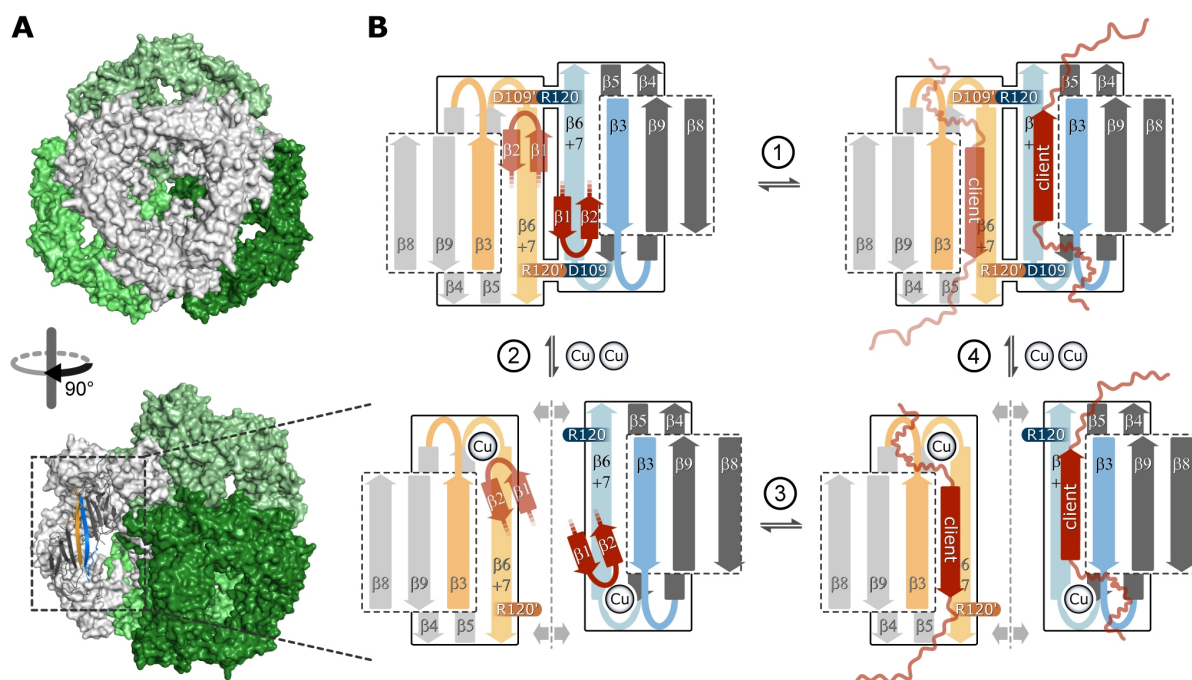


Fig. 67 The role of Cu(II) in the assembly and function of α B. (A) Surface representation of the current 24-mer model of human α B [61]. One hexameric ring containing three dimeric subunits is highlighted in white. The other three hexameric rings of the tetrahedral arrangement are colored in different shades of green. The flexible C-terminal tails (residues 163-175) are excluded for clarity. (Top) View onto a three-fold axis. (Bottom) Side view of the hexameric ring (white) obtained after a clockwise 90° rotation. One ACD dimer (dashed box) shows the shared groove and the AP interface. Strands β 6+7 of the two opposing monomers are colored in orange and blue, respectively. (B) Model for the Cu(II)-induced modulation of α B assembly. The two monomers of the ACD dimer (schematic representation) are colored in light grey and dark grey, respectively. Strands β 3 and β 6+7 defining the AP interface and the shared groove are highlighted for each monomer (orange and blue). For simplicity, only β -strands are depicted (with the exception of the intervening loops between strands β 1 and β 2, β 3 and β 4 as well as β 5 and β 6+7). The intermolecular salt-bridge between D109 and R120 is indicated. The small β 1- β 2 sheet interacting with strand β 3 of its own monomer or of a neighboring molecule is represented in red [61]. Potential client proteins are also represented in red. Cu(II) ions are illustrated as small spheres. (1) Intrinsic dynamics of the N-terminal domain allow release of the β 1- β 2 sheet thereby enhancing subunit exchange and unblocking the client binding site β 3 within the shared groove. (2) Each ACD sequesters one Cu(II) ion. The binding interferes with the intermolecular D109-R120 salt-bridges and induces partial dissociation of the dimer. Residue A57 is part of the β 1- β 2-loop located proximal to the paramagnetic center. (3) Cu(II) affects the intermolecular arrangement between the ACD and the N-terminal anchor. Quaternary structure dynamics and multimer plasticity are thus enhanced. Release of the N-terminal domain leaves the shared groove unoccupied, facilitating the accommodation of destabilized client proteins. (4) Dependent on the client system, Cu(II) coordination might be impaired by the bound client protein as has been shown in the case of γ -crystallin [281].

Consequently, the metal ion modulates α B morphology and plasticity as reflected in the augmented size and increased heterogeneity of Cu(II)- α B oligomers in EM, DLS and SEC experiments. There are indications from temperature-dependent CD experiments that Cu(II) destabilizes the oligomeric assembly, while retaining the integrity of the ACD. Such a destabilization might be tantamount to an elevated exposure of hydrophobic patches and thus of client binding sites. It has been shown by mass spectrometry that the polydispersity of pea

HSP18.1 mainly originates from intrinsic quaternary dynamics and that this plasticity confers the ability to adapt to a diverse range of client proteins [37]. In the case of HSP18.1, quaternary dynamics are temperature-regulated. In addition to post-translational modifications or changes of pH [63,284,285], the divalent metal ion Cu(II) emerges as a further factor regulating α B chaperone function. Indeed, Cu(II)-enhanced chaperone activity was observed for α B with respect to the amorphous aggregation of lens-specific β_L . Attempts to verify this observation with the client protein CS were hindered by its strong Cu(II)-dependent aggregation behavior. It has been reported, that Cu(II) has no effect on the chaperone ability of α B in the case of heat-induced aggregation of CS [68]. On the other hand, Cu(II) yielded an enhancement of α B chaperone efficiency regarding the aggregation of insulin [65]. α B provides variable substrate binding sites [272]. Apparently, chaperone function of α B and the role of Cu(II) therein are substrate-dependent and a function of the accessibility to the respective binding site. The different amounts of α B required to protect the client systems β_L and CS, respectively, from aggregation support this differential behaviour of the chaperone.

α B functions as a molecular chaperone in many human tissues, prevents the harmful aggregation of a diverse range of proteins and thus contributes significantly to stress tolerance of the cell [28,30,48]. Its involvement in various pathologies like Alzheimer's disease, Parkinson's disease, cancer and cataract highlights the essential role of α B as a key player for cellular viability [31,46]. Oxidative stress and free radical damage are typical hallmarks of the above-mentioned pathologies [76,286,287]. Due to its chemistry, the transition metal ion Cu(II) can contribute tremendously to the formation of ROS and hence ultimately to the progression of diseases and aging [77]. Lifelong exposure to high energetic irradiation renders particularly the eye lens susceptible to free radical damage. Augmented expression levels of α B are reported for tissues being subject to high oxidative stress as well as for lens epithelial cells confronted with heavy metal ions like Cu(II) [47,288]. The cytoprotective role of α B might arise not merely from its chaperoning competence, but likewise from its capability to sequester the toxic metal ion Cu(II). Given its high expression levels under stress conditions, α B might compete with other Cu(II)-binding proteins such as the Alzheimer's disease β -amyloid peptide, which has a similar affinity to Cu(II) [115].

Further structural investigations must elucidate the impact of Cu(II) on the chaperone mechanism of α B. The physiological relevance and the consequences of this strong

interaction need to be explored further in order to better understand the role of α B in copper homeostasis and oxidative stress resistance.

4.3 The Interaction of α B-crystallin with $A\beta_{1-40}$

Solution-state NMR and detailed ^{13}C secondary chemical shift analysis demonstrated that the sequence $Q_{15}KLVFFA_{21}$ of monomeric $A\beta_{1-40}$ exhibits considerable propensity for β -strand conformation (**Fig. 68A**). Intriguingly, the region $Q_{15}KLVFFAEDV_{24}$ has been reported to be involved in intermolecular contacts between $A\beta_{1-40}$ molecules in oligomeric assemblies of the peptide (**Fig. 68B**). The $Q_{15}KLVFFA_{21}$ region has also been found in β -strand conformation in a structural model of $A\beta_{1-40}$ fibrils (**Fig. 68C**). Recent solid-state NMR investigations revealed an asymmetric dimer as the basic subunit in $A\beta_{1-40}$ fibrils (Juan-Miguel Lopez del Amo, FMP). In those studies, two equally populated conformers were observed, with the sequence $Q_{15}KLVFFA_{21}$ adopting β -strand conformation in conformer I and being statically disordered in conformer II. It appears that the monomeric $A\beta_{1-40}$ peptide in solution populates to some extent the conformational state, which is a structural element of amyloid assemblies and therefore a prerequisite for the aggregation events.

In addition, the sequence $Q_{15}KLVFFAEDV_{24}$ was also identified as the major interaction site with the molecular chaperone α B [49]. Hence, it was suggested that α B competes with $A\beta_{1-40}$ for interactions with its hydrophobic core $L_{17}VFFA_{21}$ [49]. It is a well-established concept that the sHSP mode of action is to expose hydrophobic patches in order to capture and stabilize misfolded proteins prior to aggregation [28,38]. Former studies have shown that α B does not form a stable complex with monomeric $A\beta_{1-40}$ [188]. Nonetheless, our NMR titration experiments yielded very small CSP upon addition of monomeric $A\beta_{1-40}$ to α B10m. These weak effects occurred in a defined region of the ACD and hence point towards the interaction site with the amyloid peptide. Accordingly, the β 4- β 8 groove of the ACD was unambiguously identified as the binding site for monomeric $A\beta_{1-40}$ (**Fig. 68E**). This region is one of the reported candidate binding sites for client proteins [272]. The C-terminal IPI-motif, corresponding to the conserved IXI-motif of sHSPs, binds and consequently occupies the hydrophobic β 4- β 8 groove [35,56,60] (**Fig. 68D**). This was confirmed in NMR titration studies with α B10m and the C-terminal peptide α B₁₅₆₋₁₆₄ containing the IPI-motif of α B. Cellular stress factors are supposed to induce elevated subunit exchange of the α B assembly

and the dissociation of the C-terminal anchor from a neighboring molecule [37,60]. Thereby, clients such as $A\beta_{1-40}$ are enabled to engage the $\beta 4$ - $\beta 8$ groove. This is presumably a highly dynamic process, which can be judged from the weak interaction between αB_{10m} and $A\beta_{1-40}$. Due to this transient binding, a stable chaperone-client-complex is not observable for the monomeric state of $A\beta_{1-40}$. Such stable complexes have been reported for other client systems [28]. By contrast, full-length αB was shown to bind to $A\beta_{1-42}$ fibrils with a low micromolar affinity and to effectively inhibit the elongation of the fibrils [188]. In this work, EM images revealed that $A\beta_{1-40}$, which is co-incubated with αB , is impaired in generating mature amyloid fibrils. The different species during the aggregation process and the kinetic behavior of this mechanism were examined by DLS experiments. The presence of substoichiometric amounts of αB inhibits the propagation of large $A\beta_{1-40}$ aggregates and mature fibrils (**Fig. 68F**). The chaperone thereby stabilizes the monomeric peptide and oligomeric assemblies in solution. Such a mechanism would allow a more efficient clearance of the amyloid peptide by cellular degradation systems. However, soluble aggregates of $A\beta_{1-40}$ accumulated in the time course of the experiment due to the excess of the peptide. Oligomeric assemblies of $A\beta_{1-40}$ are considered to represent the actual cell-toxic species [175,176]. It has been shown that the intervention of αB and the accompanying inhibition of fibril formation can increase the toxic effects of $A\beta_{1-40}$ in cultured neurons [190]. Extending the incubation time finally leads to the formation of insoluble aggregates and protofibrillar structures (**Fig. 68F**). This observation might reflect the diagnostic finding of co-aggregated αB in amyloid plaques in the brains of AD patients [186]. Here, these ‘ αB -mediated’ aggregates of $A\beta_{1-40}$ were investigated using MAS solid-state NMR spectroscopy. The obtained spectra demonstrate that catalytic amounts of αB force $A\beta_{1-40}$ to follow a different aggregation pathway or to pause at an intermediate stage. The chemical shift pattern is different from that of fibrillar $A\beta_{1-40}$. Furthermore, multiple sets of resonances were observed, e.g. for residue S26. The structural state of $A\beta_{1-40}$ and its higher-order assemblies is thus altered by the chaperoning αB . Further studies are envisaged to characterize the architecture of these assemblies in more detail and to understand the role of αB in their formation. Moreover, the addition of αB to fibril seeds will be a key aspect for solid-state NMR investigations in the future. These experiments will allow to elucidate the chaperone mechanism of αB with respect to the inhibition of $A\beta$ fibril elongation.

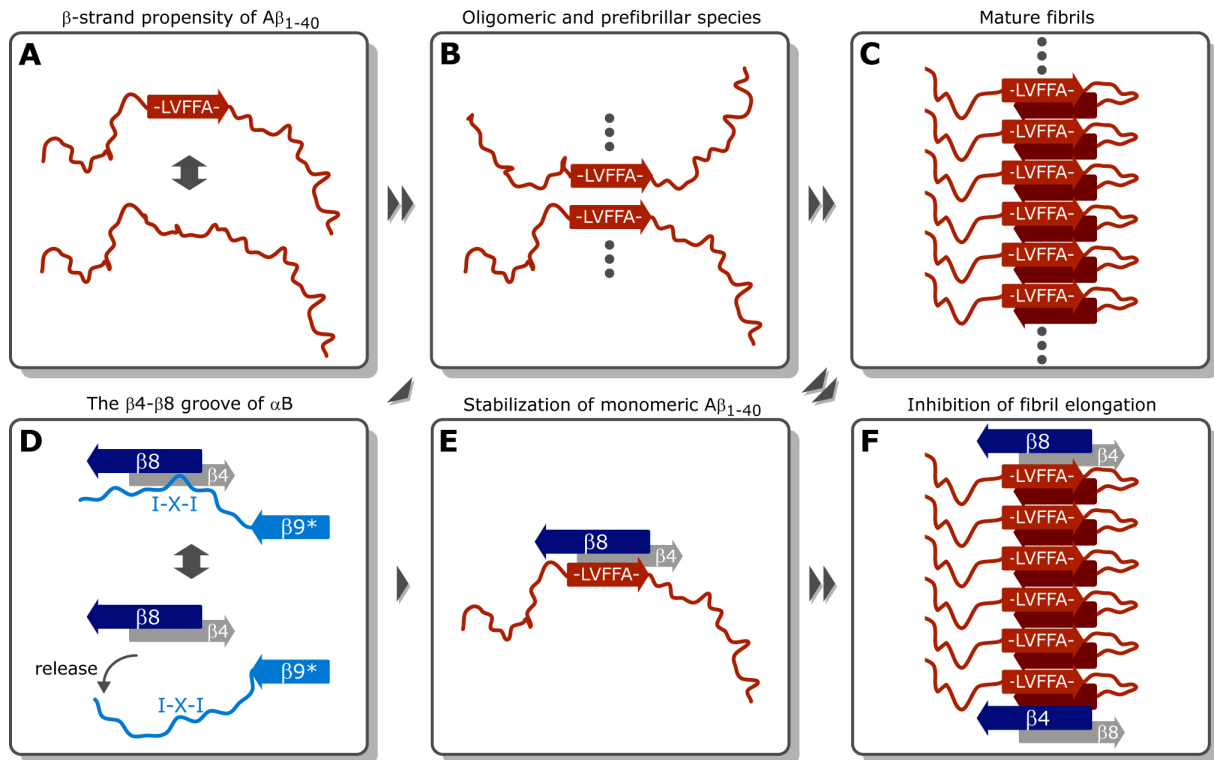


Fig. 68 Simplistic model of $A\beta_{1-40}$ aggregation and the intervention of αB . (A) The region around the hydrophobic core L₁₇VFFFA₂₁ of monomeric $A\beta_{1-40}$ partially adopts β -strand conformation in solution. (B) This β -strand propensity inherently leads to the formation of oligomeric and pre-fibrillar states. The association process induces further structural changes. (C) Subsequently, these nucleation centers proliferate rapidly yielding mature amyloid fibrils. (D) The $\beta 4$ - $\beta 8$ groove of the chaperone αB is blocked by the C-terminal IXI-motif of a neighboring subunit in the oligomeric assembly. Quaternary dynamics allow the release of the intermolecular anchor. (E) αB is enabled to recruit monomeric $A\beta_{1-40}$ via its hydrophobic $\beta 4$ - $\beta 8$ groove. The chaperone thereby competes for $A\beta$ - $A\beta$ interactions and stabilizes the monomeric peptide in solution. (F) The chaperone is also able to cover hydrophobic patches of pre-fibrillar species, thereby impeding the fibril elongation. Smaller aggregates and protofibrils are formed, which can co-precipitate the chaperone. The inhibition of fibril growth can also result in an accumulation of neurotoxic $A\beta_{1-40}$ oligomers.

4.4 MAS NMR on Protein Solutions

Solution-state NMR spectroscopy was very successful in the past in characterizing supramolecular protein assemblies, making use of TROSY-type techniques [139,203,204]. However, even at very high magnetic fields, low molecular tumbling rates limit the applicability of solution-state NMR in the investigation of these systems. This holds true in particular for studying the protein backbone, whose NMR relaxation properties are mainly ascribed to the overall rotational correlation time of the protein. Hence, the rotational mobility is usually enhanced either by observing reporter moieties with fast dynamics such as methyl groups [210], or by lowering the viscosity of the sample. The latter can be achieved by encapsulating a protein in a reversed micelle dissolved in a low viscosity fluid [199,200] or by working at elevated temperatures [138]. These approaches are not generally applicable.

Alternatively, the viscosity of the solution might as well be increased to the static limit to solve the relaxation problem. MAS NMR can then beneficially be employed to average coherent anisotropic interactions, as overall rotational reorientation is absent. MAS solid-state NMR has become a powerful tool for the structural investigation of biomolecules at atomic resolution [161,217]. On the other hand, the requirement to crystallize or precipitate the biological molecule of interest is often a bottleneck. Interaction studies with potential binding partners are often prohibitive, when ligands do not co-precipitate with the target molecule. In addition, crystal-packing artefacts can result in misinterpretation of structural and dynamic data. A protein in solution lacking molecular tumbling is thus ideally suited to circumvent the limitations of the conventional solution- and solid-state NMR approaches.

The results reported here demonstrate the feasibility of MAS NMR applied to biomolecules in solution. The according FROSTY MAS approach utilizes non-frozen protein solutions, in which the molecular tumbling of target proteins is restricted by adding glycerol, employing low temperatures and MAS-induced protein sedimentation. The model system α B revealed well-resolved ^{13}C - ^{13}C correlation spectra, the presence of strong dipolar couplings and MAS-dependent resolution and sensitivity. These characteristics evidenced that α B, supplied in solution and spun at the magic angle, behaves like a rigid solid. In order to fulfill the conditions for efficient averaging of anisotropic interactions by MAS, the target molecule needs to be rotationally immobilized during one rotor evolution. This is tantamount with an extreme long rotational correlation time on the order of 100 μs . The correlation times in the

low microsecond regime, which were measured by NMRD and FCS, indicate that the presence of glycerol and the low temperatures provided can not fully explain the observed protein immobilization. The beneficial effects must therefore originate from MAS and its capability to sediment large protein assemblies due to their high molecular weight. Centrifugal accelerations in typical MAS NMR rotors can be easily calculated (**Fig. 69A**). Spinning frequencies of 12 kHz in a 4 mm rotor (inner diameter of 3.0 mm) and 20 kHz in a 3.2 mm rotor (inner diameter of 2.4 mm) give accelerations of $870.000\times g$ and $1.900.000\times g$, respectively (**Fig. 69B**). These values are in the range of and beyond typical accelerations produced by ultracentrifuges. Very recently, Bertini *et al.* have shown that reversible protein sedimentation of the model system apoferritin (480 kDa) can in fact be achieved by MAS [274]. The ultracentrifugation effect of MAS thus yields a highly concentrated protein layer at the inner wall of the cylindrical rotor (**Fig. 69A**). This dense packing of protein molecules is tantamount to an increased microscopic viscosity, and finally causes the rotational immobilization of the macromolecules. Nonetheless, rotational correlation times of proteins in this phase need to be determined experimentally.

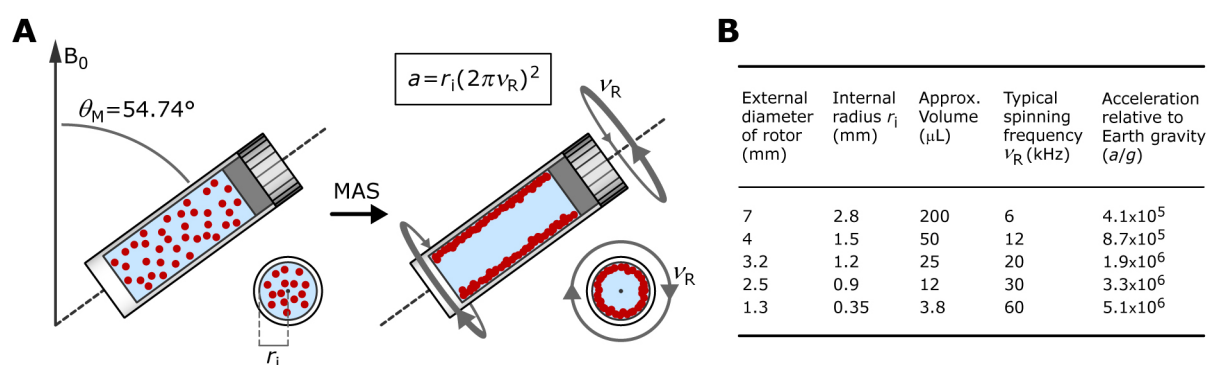


Fig. 69 Ultracentrifugation in MAS rotors. (**A**) The concept of MAS and its potential to sediment macromolecules is illustrated. The cylindrical MAS rotor is flipped by the magic angle θ_M (54.74°) with respect to the external magnetic field B_0 (*Left*). At this point, the macromolecules (red spheres) are stochastically distributed in the solution. Fast spinning of the rotor creates a centrifugal force, which yields a highly concentrated sediment at the inner wall of the rotor (*Right*). The centrifugal acceleration a can be calculated using the equation shown on top, where ν_R and r_i denote the spinning frequency and the internal radius of the rotor, respectively. Views along the rotation axis are illustrated on the lower right in each case. (**B**) Commercially available MAS rotors and their specifications (table adapted from [274]). The volumetric capacity of rotors is dependent on the use of spacers. Centrifugal accelerations are given relative to Earth gravity (in $\times g$) and for spinning frequencies that are routinely used in protein MAS NMR.

It has been suggested that solid-state NMR of MAS-sedimented proteins might be applicable to proteins with molecular weights down to 100 kDa [274]. Solid-state spectra have even been recorded for solutions of bovine serum albumin (67 kDa) and carbonic anhydrase II (29 kDa) [289]. The applicability of the approach is basically dependent on the molecular weight of the protein, the radius and spinning frequency of the rotor, the solvent viscosity and the temperature. These factors finally determine the time required to successfully sediment the target molecule. In the present work, glycerol was used to restrict rotational diffusion of proteins. In terms of sedimentation efficiency, the addition of glycerol to the protein solution can have adverse effects. It was proposed, that the increased viscosity and the reduced dielectric constant of the solution might result in a less efficient sedimentation of proteins and immobilization of molecular tumbling [289]. However, many proteins tend to precipitate at the high concentrations required for FROSTY experiments. Glycerol stabilizes proteins in solution, protects them from aggregation and thus enables increased protein concentrations. Moreover, the use of glycerol permits low temperatures, which in turn further decrease the molecular tumbling. As shown, low temperatures improve the sensitivity of CP-based experiments. Certainly, chemical exchange processes are very sensitive to temperature. Low temperatures can freeze out different conformational states, which finally results in undesirable line-broadening. In conclusion, the addition of glycerol and the choice of temperature are important parameters for FROSTY experiments, that must be adapted individually to the respective biological system.

We could show that the FROSTY approach is not unique for α B, but generally applicable for large protein complexes. The method was verified by employing different proteasome assemblies of *Thermoplasma acidophilum*. The modular architecture enabled molecular weight-dependent MAS experiments, whilst observing only one type of subunit. By selective labeling of the respective components and subsequent subunit assembly, it is basically possible to assign the entire protein complex. ^{13}C -detected spectra revealed that high molecular weights are favorable for spectral resolution and sensitivity, which is contradictory to the size-dependence in conventional solution-state NMR (see Chapter 1.2.2). In addition to the molecular weight, the shape of the target complex may contribute to resolution as well. The $\alpha_7\beta_7\beta_7\alpha_7$ and even more so the $\alpha_7\beta_7\beta_7\alpha_7$ -(11S)₁₄ particles are more elongated than the spherical $\alpha_7\alpha_7$ double disk. Therefore, a preferred orientation within the protein sediment would affect the sample homogeneity and consequently the obtainable spectral resolution.

Besides spectral resolution, the sensitivity is an important criterion for the feasibility of multidimensional NMR experiments. There are several parameters that can be optimized in the future. One major aspect is the amount of protein in the MAS rotor. Thin-walled 3.2 mm rotors provide a similar volumetric capacity as standard 4 mm rotors, whilst allowing the high spinning frequencies needed for ^1H -detection. A factor of two in signal-to-noise can thus be achieved. The amount of protein can be further increased by direct ultracentrifugation into the MAS rotor. Such rotor filling devices have been reported for a variety of biological materials [289]. Theoretically, this procedure may increase the signal-to-noise ratio by a factor of 5-7. We succeeded to enhance the sensitivity of FROSTY experiments by employing protein perdeuteration, PRE and proton-detection. The combination of all these techniques finally enabled us to detect and to assign backbone resonances of the 1.1 MDa proteasome complex $\alpha_7\beta_7\beta_7\alpha_7-(11\text{S})_{14}$. The application of other dipolar-based ^{13}C - ^{13}C and ^{13}C - ^{15}N mixing schemes like REDOR [215] as well as the development of new pulse sequences will help to complete the resonance assignment. CP build-up curves implied relatively short $T_{1\rho}$ values for αB and the proteasome complexes, presumably due to residual rotational mobility. In light of the progress made in NMR hardware performance, the rotational immobilization can be increased by faster MAS frequencies [290]. MAS probe-heads optimized for ^1H -detection will further improve the sensitivity. Efficient water suppression is especially important for FROSTY samples due to the high content of water. Therefore, spectral quality and sensitivity will benefit enormously from gradient-capable MAS probe-heads. Furthermore, it has been shown that deuterons in perdeuterated proteins can be utilized to enhance the sensitivity and to obtain additional structural information [291]. Four-channel MAS probes will thus improve the performance of sophisticated triple-resonance experiments.

It is an inherent feature of MAS solid-state NMR, that this technique is independent of the molecular weight, since intrinsic molecular tumbling is absent. The FROSTY MAS approach applies this concept also to supramolecular assemblies in solution. Interaction studies can be performed as in solution-state NMR titrations. The interaction partners can be quite diverse – from small molecules to protein or DNA molecules. The experiments could even be performed in cellular environment such as cell lysates with potential interaction partners co-sedimenting with the isotopically-labeled target molecule. Membrane proteins sedimented in the membrane fraction might also be accessible with this approach. Furthermore, small proteins or other components can be attached to larger assemblies and function as molecular

probes, that are monitored during various biological processes. Even viral capsid assemblies with molecular weights beyond 10 MDa are well-suited for FROSTY investigations, as long as the repeating subunit is small enough to prevent extensive signal overlap.

Large molecular machineries control and regulate various cellular processes [1,125,292]. Structural investigations at atomic resolution are therefore essential to understand the mechanism and the biological function of these supramolecular modules. FROSTY MAS NMR is a novel tool to overcome protein size limitations of solution-state NMR without the necessity of precipitation procedures required for conventional solid-state NMR spectroscopy.

5 Appendix

5.1 DNA and Protein Sequences

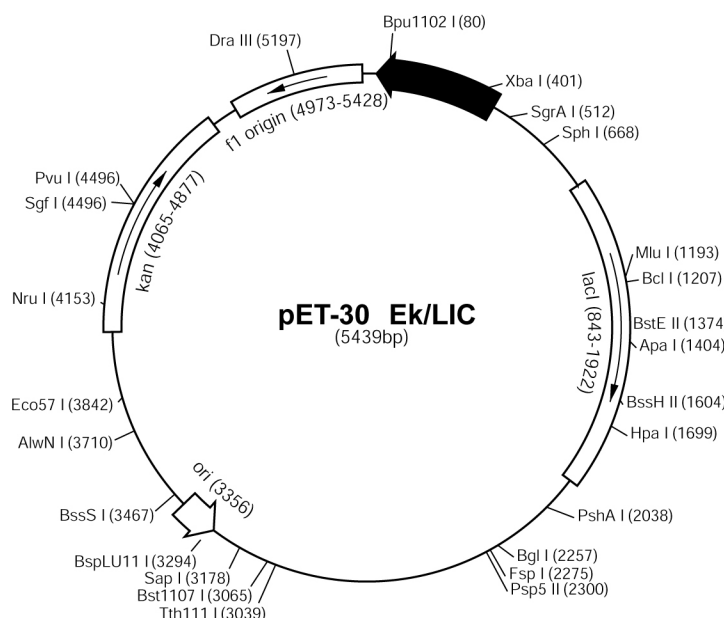
5.1.1 Vector DNA

Fig. 70 shows the vector map and the multiple cloning site of the commercially available vector pET-30 Ek/LIC (Novagen), which was used in the scope of this thesis for expression and cloning purposes.

A

pET-30 Ek/LIC sequence landmarks

T7 promoter	436-452
T7 transcription start	435
His-Tag coding sequence	344-361
S-Tag coding sequence	266-310
Multiple cloning sites (<i>Bse</i> R I - <i>Xho</i> I)	158-224
His-Tag coding sequence	140-157
T7 terminator	26-72
<i>lacI</i> coding sequence	843-1922
pBR322 origin	3356
Kan coding sequence	4065-4877
f1 origin	4973-5428



B

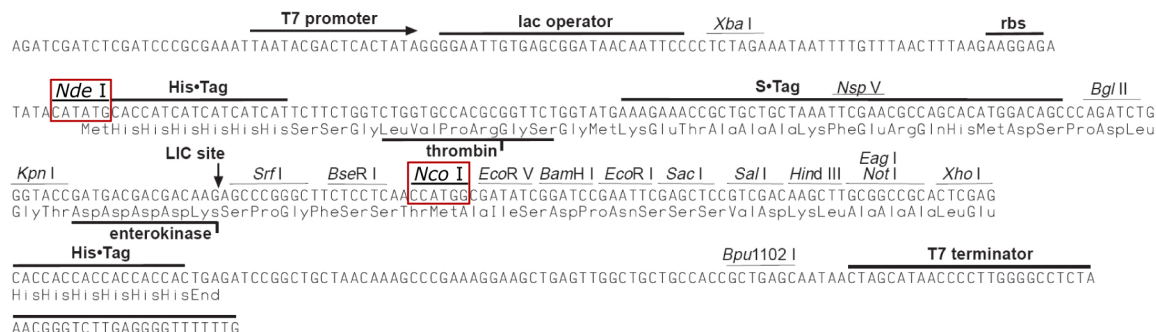


Fig. 70 The vector pET-30 Ek/LIC (figure adapted from Novagen). The vector map (**A**) and the multiple cloning site (**B**) are depicted. The restriction sites for the endonucleases *Nde*I and *Nco*I (highlighted in red) were used for cloning purposes in order to generate tag-free α B and the truncated construct α B10m. Thereby, the complete sequence between these two RE sites was eliminated. The modified vector was termed mod.pET-30.

5.1.2 PCR Primer Sequences

All primers used for cloning of full-length α B and the truncated α B10 are listed in Tab. 5.

Tab. 5 Oligonucleotides used for cloning of α B and α B10 constructs.

Primer for full-length αB		
Primer	Sequence (5'→3')	Cloning purpose
Th-fw	CTGGTGCCACGCGGTTCTATGGACATCGCCATCCACC	N-terminal Thrombin site
TEV-fw	AACCTGTATTTCCAGGGAATGGACATCGCCATCCACC	N-terminal TEV site
Ek-Th-fw	GACGACGACAAGATGCTGGTGCCACGCGGTTTC	Ek/LIC cloning
Ek-TEV-fw	GACGACAAGATGGAAAACCTGTATTTCCAG	Ek/LIC cloning
LIC-rv	GAGGAGAAGCCCGGTCTATTTCTTGGGGGCTGCGG	Ek/LIC cloning
NdeI- α B-fw	GGCCAGCATATGGACATCGCCATCCACCACCCCTGG	Upstream NdeI site
NcoI- α B-rv	CGCCTTCCATGGCTATTTCTTGGGGGCTGCGGTGACAGC	Downstream NcoI site
Primer for the ACD construct αB10 (residues 64-152)		
Primer	Sequence (5'→3')	Cloning purpose
NdeI- α B10- fw	CGTGGCCAGCATATGGGACTCTCAGAGATGCGCCTGG	Upstream NdeI site of α B residue G64
NcoI- α B10- rv	CGCCTT CCATGGCTAGACCTGTTTCCTTGGTCCATTCAC AGT G	Downstream NcoI site of α B residue 152+stop

5.1.3 Primer Sequences for Site-directed Mutagenesis

The primers used for site-directed mutagenesis of α B10 are listed in Tab. 6.

Tab. 6 Oligonucleotides used for insertion of single point mutations in α B10 and α B10m.

Primer	Sequence (5'→3')
α B10-N146D fw	GGGGTCCTCACTGTGGATGGACCAAGGAAACAGG
α B10-N146D rv	CCTGTTTCCTTGGTCCATCCACAGTGAGGACCCC
α B10m-H83A fw	CCTGGATGTGAAGGCCTTCTCCCCAGAGGAACTC
α B10m-H83A rv	GAGTTCCTCTGGGGAGAAGGCCTTCACATCCAGG
α B10m-H104A fw	GAGGTGCATGGAAAAGCTGAAGAGCGCCAGGATGAAC
α B10m-H104A rv	GTTTCATCCTGGCGCTCTTCAGCTTTTCCATGCACCTC
α B10m-H111A fw	GAGCGCCAGGATGAAGCTGGTTTCATCTCCAGGGAG
α B10m-H111A rv	CTCCCTGGAGATGAAACCAGCTTCATCCTGGCGCTC
α B10m-H119A fw	CATCTCCAGGGAGTTCGCCAGGAAATACCGGATCCC
α B10m-H119A rv	GGGATCCGGTATTTCTTGGCGAACTCCCTGGAGATG
α B10m-D109A fw	CATGAAGAGCGCCAGGCTGAACATGGTTTCATCTC
α B10m-D109A rv	GAGATGAAACCATGTTTCAGCCTGGCGCTCTTCATG
α B10m-R120G fw	CATCTCCAGGGAGTTCACGGGAAATACCGGATCCCAGC
α B10m-R120G rv	GCTGGGATCCGGTATTTCCCGTGGAACCTCCCTGGAGATG

5.1.4 Protein Sequences

Amino acid sequences of relevant proteins used in this work are listed in Tab. 7. The accession codes in the Uniprot database [236] are also given.

Tab. 7 Primary structures of proteins used in this work.

Human full-length α B (P02511)

MDIAIHHPWIRPFFPFHSPSRLFDQFFGEHLLESDFPTSTSLSPFYLRPPSFLRAPSWFDTGLSE
MRLEKDRFSVNLVDVKHFSPEELKVKVLGDVIEVHGKHEERQDEHGFISREFHRKYRIPADVDP
LTITSSLSDDGVLTVNGPRKQVSGPERTIPITREEKPAVTAAPKK

α B10-N146D (α B10m) from human α B (P02511), residues 64-152 with N-terminal Met0

MGLSEMRLEKDRFSVNLVDVKHFSPEELKVKVLGDVIEVHGKHEERQDEHGFISREFHRKYRIP
ADVDP LTITSSLSDDGVLTVDGPRKQV

A β ₁₋₄₀ from human APP (P05067) with N-terminal Met0

MDAEFRHDSGYEVHHQKLVFFAEDVGSNKGAIIGLMVGGVV

Proteasome α -subunit from *T. acidophilum* (P25156) with N-term. 4 residue overhang from purification tag

GAMGMQQGQMAYDRAITVFSPDGRLFQVEYAREAVKKGSTALGMKFANGVLLISDKKVRSR
LIEQNSIEKIQLIDYVAAVTSGLVADARVLVDFARISAAQKEKVTYGSLVNIENLVKRVADQMQQ
YTQYGGVPRPYGVSLIFAGIDQIGPRLFDCDPAGTINEYKATAIGSGKDAVVSLEREYKENLPEK
EAVTLGIKALKSSLEEGEELKAPEIASITVGNKYRIYDQEEVKKFL

Proteasome β -subunit from *T. acidophilum* (P28061)

TTTVGITLKDAVIMATERRVTMENFIMHKNGKKLFQIDTYTGMTIAGLVGDAQVLVRYMKAEL
ELYRLQRRVNMPIEAVATLLSNMLNQVKYMPYMVQLLVGGIDTAPHVFSIDAAGGSVEDIYAS
TGSGSPFVYGVLESQYSEKMTVDEGVLDLVIRISAQKQDSASGGMIDVAVITRKDGYVQLPT
DQIESRIRKLGLIL

11S activator from *T. brucei* (Q9U8G2) with N-terminal 4-residue overhang from purification tag

GAMGMPPKRAALIQNLRDSYTETSSFAVIEEWAAGTLQEIEGIAKAAAEAHGTIRNSTYGRAQ
AEKSPEQLLGVLQRYQDLCHNVYCQAETIRTVIAIRIPEHKEEDNLGVAVQHAVLKIIDELEIKT
LGSGEKSGSGGAPTPIGMYALREYLSARSTVEDKLLGSVDAESGKTGGSQSPSLLLELRQIDA
DFMLKVELATTHLSTMVRAVINAYLLNWKKLIQPRTGSDHMVS

5.1.5 Protein Parameters

Molar extinction coefficients and molecular weights [232] of relevant proteins are given in Tab. 8. Molecular weights were calculated in consideration of the different isotopic labeling schemes. These parameters were used for the photometric determination of protein concentration (see Chapter 2.4.1).

Tab. 8 Molar extinction coefficients ϵ and molecular weights M_w of used proteins.

Protein	ϵ (M ⁻¹ cm ⁻¹)	M_w (Da)	Isotopic labeling
α B	13,980	20,159	unlabeled
		21,315	¹³ C, ¹⁵ N
		22,712	² H, ¹³ C, ¹⁵ N
α B10m (and mutants)	1,490	10,313	unlabeled
		10,891	¹³ C, ¹⁵ N
$\alpha_7\alpha_7$	16,390	26,116	unlabeled
		27,575	¹³ C, ¹⁵ N
		29,430	² H, ¹³ C, ¹⁵ N
$\alpha_7\beta_7\beta_7\alpha_7$	29,800	48,388	unlabeled
		49,847	¹³ C, ¹⁵ N (α)
		53,299	² H, ¹³ C, ¹⁵ N (α), ² H (β)
11S activator	21,430	25,229	unlabeled
		27,014	² H
$\alpha_7\beta_7\beta_7\alpha_7$ -(11S) ₁₄	51,230	73,617	unlabeled
		80,313	² H, ¹³ C, ¹⁵ N (α), ² H (β , 11S)
A β ₁₋₄₀	1,490	4,330	unlabeled
		4,574	¹³ C, ¹⁵ N
Citrate synthase	77,800	48,920	unlabeled
β_L -crystallin	53,750	24,390	unlabeled

5.2 NMR Data

5.2.1 PDSD Spectra of α B Oligomers in Solution

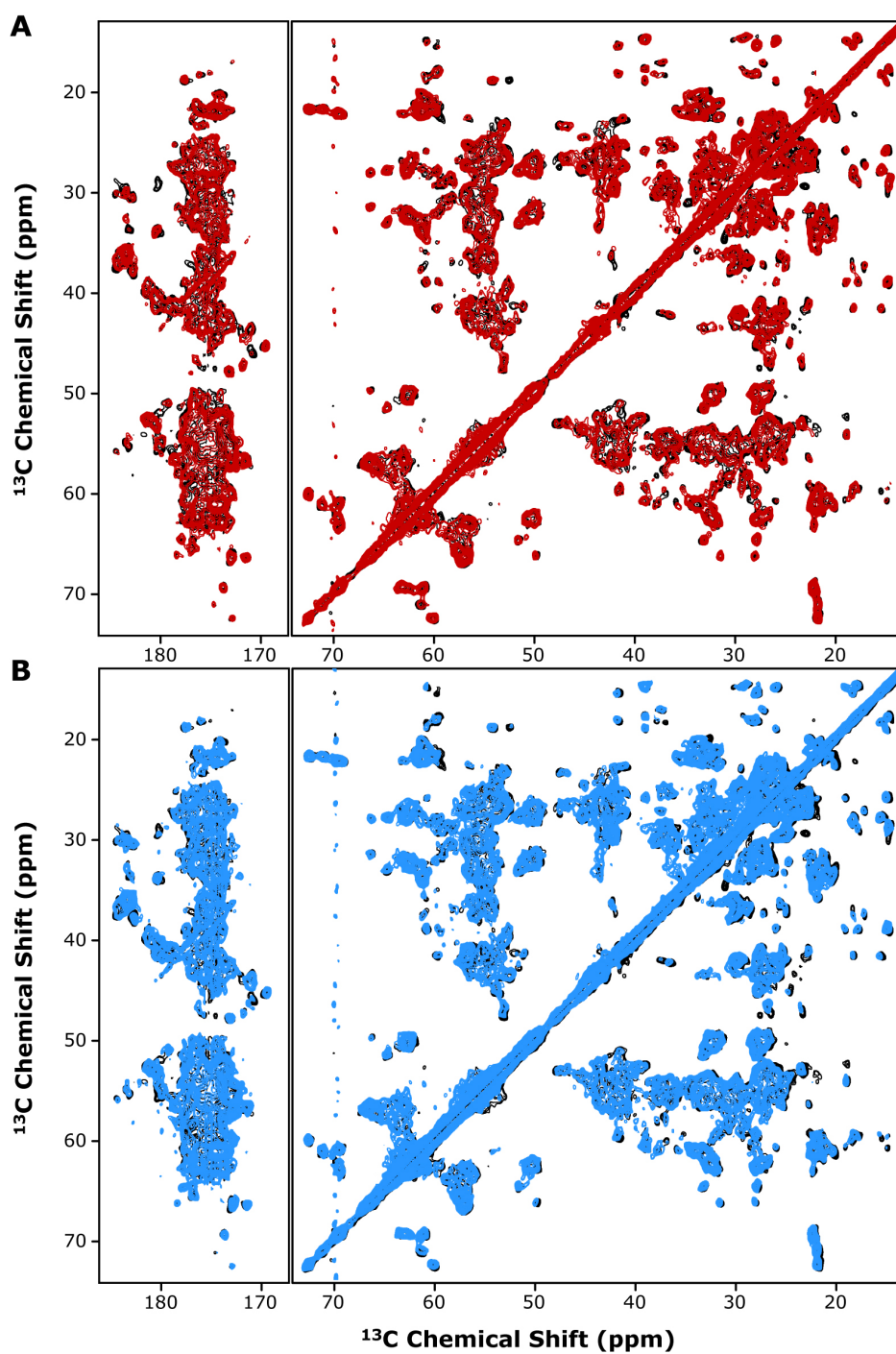


Fig. 71 Metal-binding to α B multimers by MAS NMR. Full 2D PDSD spectra of full-length α B in the absence (black) and (**A**) presence of Cu(II) (red) or (**B**) Zn(II) (blue), respectively. Enlargements are shown in **Fig. 25**.

5.2.2 Chemical Shifts of apo- α B10m

Tab. 9 lists the chemical shifts of unambiguously assigned residues of apo- α B10m.

Tab. 9 Chemical shifts (in ppm) for apo- α B10m in PBS (pH 7.5) at 22 °C.

Residue	H _N	N _H	C'	C α	C β	C γ 1/2	Miscellaneous
G64	8.554	110.68	171.5	43.7			
L65	8.253	121.99	177.8	55.8	42.6	27.0	23.8/24.9 (C δ 1/2), 0.811/0.858 (H δ 1/2)
S66	8.461	116.83	174.5	58.7	63.7		
E67	8.391	123.16	176.0	56.9	30.5	38.3	182.7 (C δ)
M68	8.145	121.03	175.6	55.4	33.2		17.1 (C ϵ), 2.052 (H ϵ)
R69	8.543	124.05	175.4	55.8	31.4	27.2	
L70	8.453	124.93	177.0	54.9	42.5	27.4	25.0/24.1 (C δ 1/2), 0.897/0.845 (H δ 1/2)
E71	8.407	122.65	176.7	56.0	31.1	36.4	183.8 (C δ)
K72	8.506	121.31	176.7	57.7	32.8		
D73	8.322	117.18	176.3	54.1	41.3	180.2	
R74	7.805	119.34	174.7	56.1	32.7	27.2	
F75	8.773	124.80	173.2	56.4	41.8		
S76	7.753	119.35	173.0	57.1	65.5		
V77	8.485	122.06	173.7	60.2	35.2	20.8/19.3	0.256/0.021 (H γ 1/2)
N78	8.247	120.69	173.8	51.7	42.0	176.7	114.0 (N δ), 7.187/6.679 (H δ 1/2)
L79	9.214	123.35	174.7	54.2	45.2	27.2	
D80	8.514	124.96	176.5	54.9	41.1	179.8	
V81	8.745	122.33	176.7	59.6	31.7	22.9/20.6	0.742/0.745 (H γ 1/2)
K82	7.805	120.30	177.4	59.6	32.2		
H83	7.915	115.03	173.9	57.4	30.7		
F84	8.215	117.52	174.7	57.4	41.5		
S85	9.420	121.10	174.0	56.9	63.1		
P86			178.8	66.4	31.7		
E87	8.540	112.93	177.6	58.2	28.9	36.9	184.4 (C δ)
E88	8.057	120.89	174.6	56.1	30.5	36.2	184.2 (C δ)
L89	7.142	120.50	175.9	53.2	46.4		24.4 (C δ), 0.632 (H δ)
K90	8.741	121.82	175.0	55.0	36.0	25.0	
V91	8.604	125.40	175.6	61.3	33.5	20.9	0.468 (H γ)
K92	9.334	128.26	174.1	54.9	36.4	24.9	
V93	8.708	125.36	175.5	62.7	32.7	21.8	
L94	8.811	131.11	176.5	53.7	43.2	27.1	24.5/25.2 (C δ 1/2), 0.821/0.831 (H δ 1/2)
G95	8.595	113.68	173.6	47.8			
D96	8.253	121.99	175.1	53.1	40.5	181.2	
V97	7.621	117.43	174.6	60.5	36.4	21.2	0.906 (H γ)
I98	9.011	122.99	175.1	60.1	41.3	17.9	0.848 (H γ), 15.8 (C δ), 0.828 (H δ)
E99	9.517	126.71	175.5	54.5	32.7	37.3	182.0 (C δ)
V100	9.377	123.67	173.6	61.1	34.7	20.5	0.940 (H γ)
H101	8.958	127.49	174.1	53.2	34.2		
G102	7.055	113.07	171.1	44.0			
K103	7.987	123.27	174.8	56.6	36.4	25.5	
H104	9.267	123.49	175.3	54.1	32.8		
E105	9.062	122.94	176.4	55.1	30.2	36.0	183.6 (C δ)
E106	8.859	121.64	176.0	58.7	30.6	36.5	183.9 (C δ)
R107	8.920	125.32	174.6	54.2	33.5	27.2	
Q108	8.745	122.33	176.2	55.5	29.8	33.9	180.4 (C δ), 111.4 (N δ), 7.310/6.628 (H δ 1/2)

Residue	H _N	N _H	C'	Ca	Cβ	Cγ1/2	Miscellaneous
D109	8.934	128.21	176.4	52.2	41.7	180.7	
E110	9.019	116.19	176.8	59.0	28.9	35.3	184.3 (Cδ)
H111	7.812	115.98	175.7	55.8	33.0		
G112	7.453	107.97	170.9	46.1			
F113	8.668	122.18	175.5	56.7	42.8		
I114	9.461	121.04	172.9	58.3	42.3	16.2	0.889 (Hγ), 14.5 (Hδ), 0.881 (Hδ)
S115	8.888	122.41	172.6	57.3	66.3		
R116	6.086	115.99	175.0	55.7	37.5		
E117	8.955	119.89	174.8	55.8	33.9	35.9	183.2 (Cδ)
F118	9.190	122.76	172.4	57.1	42.4		
H119	8.365	118.97	173.8	55.4	32.3		
R120	9.581	128.61	174.0	53.4	33.6	24.4	
K121	8.892	123.71	175.8	54.8	36.7	25.6	
Y122	9.404	121.82	175.5	56.6	41.5		
R123	8.840	123.10	175.9	56.1	30.3		
I124	8.4	126.85	174.3	59.7	39.1	29.1/17.5	0.651 (Hγ2), 14.4 (Cδ), 0.629 (Hδ)
P125			176.5	62.9	32.5	28.1	
A126	8.41	121.29	177.7	54.3	18.8		1.365 (Hβ)
D127	8.104	113.02	173.9	52.7	39.2	181.1	
V128	7.416	119.94	174.4	61.1	33.7	21.8	0.557 (Hγ)
D129	8.773	127.43	176.7	51.0	41.8	179.1	
P130			177.8	65.0	33.1	28.1	
L131	8.308	114.92	178.8	56.6	41.0		25.2 (Cδ), 0.937 (Hδ)
T132	7.982	107.10	173.8	61.1	69.5	22.1	1.118 (Hγ)
I133	6.849	122.06	176.8	60.8	37.6	28.1/17.9	0.746 (Hγ2), 13.0 (Cδ), 0.730 (Hδ)
T134	9.291	120.80	172.3	60.3	72.4	21.4	1.156 (Hγ)
S135	8.327	113.12	173.8	56.9	67.2		
S136	8.748	114.99	171.6	57.6	65.5		
L137	8.548	126.50	176.6	53.4	44.7		24.1/26.0 (Cδ1/2), 0.716/0.818 (Hδ1/2)
S138	8.855	122.88	176.7	57.8	65.6		
S139			174.7	60.8	62.9		
D140	8.001	117.66	176.1	53.3	40.3	180.5	
G141	7.809	107.91	172.1	47.4			
V142	7.514	118.09	176.1	61.6	33.4	21.4	0.636 (Hγ)
L143	9.410	134.57	175.1	53.8	44.7	27.6	24.4 (Cδ), 0.783 (Hδ)
T144	9.263	124.00	174.1	61.6	71.0	21.6	0.983 (Hγ)
V145	8.741	128.45	173.6	61.1	33.2	19.8	0.607 (Hγ)
D146	8.901	125.58	174.8	52.9	46.3	180.1	
G147	8.624	106.43	169.7	45.6			
P148			176.6	62.3	32.4		
R149	8.122	119.53	176.8	54.8	31.9	28.1	
K150	8.892	123.71	176.2	56.7	33.5	25.1	
Q151	8.553	123.03	175.2	55.9	29.7	34.1	180.8 (Cδ), 113.3 (Nδ), 7.523/6.796 (Hδ1/2)
V152	7.817	125.77	181.0	63.7	33.2	21.7/20.2	0.845/0.823 (Hγ1/2)

5.2.3 Chemical Shifts of Cu(II)- α B10m

Tab. 10 lists the chemical shifts of unambiguously assigned residues of Cu(II)- α B10m.

Tab. 10 Chemical shifts (in ppm) for Cu(II)- α B10m in PBS (pH 7.5) at 22 °C.

Residue	H _N	N _H	C'	C α	C β	C γ 1/2	Miscellaneous
S66			174.5	58.9	63.7		
M68			175.7	55.5	33.7		
R69			175.0	55.0	32.7		
L70			176.2	54.9	42.9		25.0 (C δ 1), 0.897 (H δ 1)
E71	8.440	124.19	176.5	54.6	32.3	36.7	183.5 (C δ)
K72	8.853	121.16	176.6	56.9	32.9		
D73	8.304	110.99	177.0	53.4	41.6	180.4	
R74	7.251	119.14	172.7	56.1	33.5		
F75	8.855	123.86	172.6	55.6	43.6		
S76			172.5	57.3	66.3		
N78			173.9	52.2	42.1	177.1	
L79			174.7	54.0	45.0		
D80			176.6	54.7	41.1		
V81			173.8	54.8	32.1		
F84			175.1	58.9	39.2		
S85			174.2	56.4	63.3		
P86			178.7	66.5	31.9		
E87	8.901	113.38	177.5	58.1	28.6	36.7	184.4 (C δ)
E88	8.043	120.58	175.0	56.3	29.5	37.1	183.3 (C δ)
L89	7.151	119.95	176.2	53.3	45.7		
K90	8.947	121.41	174.6	55.2	36.2		
V91	8.548	124.82	175.6	61.2	33.8	20.9	0.517 (H γ)
K92	9.368	128.19	174.1	55.0	36.4		
V93	8.713	125.52	175.5	62.4	32.3	21.8	
L94	8.848	131.10	176.6	53.6	43.2		
G95	8.634	114.54	173.4	47.9			
D96	8.262	122.74	174.6	52.9	40.3	181.3	
V97	7.604	117.34	174.9	60.7	36.3	21.2	0.906 (H γ)
I98	9.000	123.06	175.3	60.0	41.3	18.0	0.872(H γ), 15.6 (C δ), 0.847 (H δ)
E99	9.579	126.18	175.6	54.6	33.0	37.1	182.2 (C δ)
V100			173.8	60.9	34.7		
G102			172.0	45.0			
K103			174.2	57.0	36.5		
E105			176.3	55.2	30.2	36.0	183.7 (C δ)
E106			176.0	58.0	29.7		
R107			174.2	55.3	32.9		
Q108			175.7	55.4	28.5	33.3	179.9 (C δ), 111.4 (N δ), 7.269/6.592 (H δ 1/2)
G112			170.8	45.7			
S115			172.7	57.1	66.1		
F118			172.1	57.6	43.3		
H119			177.1	59.8	32.2		
Y122			175.3	56.5	41.4		
R123			176.2	56.1	30.7		
I124	8.584	126.93	174.2	59.7	39.1	17.7	0.598 (H γ 2), 14.4 (C δ), 0.608 (H δ)
P125			176.5	62.9	32.5		

Residue	H _N	N _H	C'	C α	C β	C γ 1/2	Miscellaneous
A126	8.346	121.33	177.7	54.2	18.8		1.344 (H β)
D127	8.068	113.29	174.1	52.9	39.2	181.1	
V128	7.351	119.88	174.6	61.0	33.6		
D129	8.806	127.73	176.7	51.0	41.8	179.2	
P130			177.9	64.9	33.0		
L131	8.308	115.27	178.9	56.6	41.0		25.2 (C δ), 0.937 (H δ)
T132	7.956	107.25	173.8	61.1	69.6	22.1	1.118 (H γ)
I133	6.862	122.38	176.8	61.1	37.7	18.1	0.759 (H γ 2), 13.2 (C δ), 0.783 (H δ)
T134	9.222	121.10	172.3	60.3	72.5	21.4	1.156 (H γ)
S135	8.328	113.20	173.9	56.9	67.3		
S136	8.860	115.65	171.4	57.9	65.7		
L137	8.450	125.74	176.6	53.4	44.7		
S138	8.863	122.82	176.8	57.6	65.7		
S139			174.8	60.9	62.9		
D140	7.977	117.67	175.9	53.2	40.4	180.6	
G141			172.0	47.5			
V142	7.475	118.05	176.2	61.6	33.3		
L143	9.397	134.68					
T144	9.171	123.53	174.0	61.3	71.2	21.9	0.999 (H γ)
V145	8.941	128.69	174.0	60.9	33.5		
D146	9.13	125.90	174.3	52.9	45.9	179.8	
G147			169.8	45.4			
P148			176.6	62.3	32.4		
R149	7.469	119.71	176.3	54.8	33.1		
K150	8.820	124.37	176.0	56.8	33.4	25.0	
Q151	8.557	123.33	175.2	55.9	29.8	34.0	180.8 (C δ), 113.3 (N δ), 7.468/6.747 (H δ 1/2)
V152	7.826	125.70	181.0	63.7	33.2	21.7/20.2	0.845/0.823 (H γ 1/2)

5.2.4 Chemical Shifts of Monomeric A β ₁₋₄₀

Tab. 11 lists the chemical shifts of unambiguously assigned residues of monomeric A β ₁₋₄₀.

Tab. 11 Chemical shifts (in ppm) for monomeric A β ₁₋₄₀ in PBS (pH 7.6) at 4 °C.

Residue	H _N	N _H	C'	C α	C β	C γ 1/2	Miscellaneous
M0				54.96	32.58	30.76	3.71 (H α), 1.80 (H β), 2.30 (H γ)
D1			175.64	54.22	41.14		4.36 (H α), 2.49/2.34 (H β 1/2)
A2	8.38	124.59	177.49	52.63	18.85		3.95 (H α), 1.10 (H β)
E3	8.24	119.43	175.92	56.31	30.09		3.88 (H α)
F4	8.05	121.13	175.13	57.54	39.30		4.26 (H α), 2.75 (H β)
R5	7.90	123.40		55.33	31.01	27.10	27.10 (C δ), 3.97 (H α), 1.45/1.35 (H β 1/2), 1.24 (H γ), 2.85 (H δ)
H6			174.98	56.30			4.23 (H α)
D7	8.19	121.49	176.17	53.79	40.90		4.34 (H α), 2.40 (H β)
S8	8.28	116.51	175.00	58.77	63.49		4.09 (H α), 3.64/3.60 (H β 1/2)
G9	8.38	110.56	173.81	45.13			3.66 (H α)
Y10	7.78	119.91	175.56	57.97	38.62		4.23 (H α), 2.75/2.67 (H β 1/2)
E11	8.22	122.45	175.96	56.25	30.09		3.93 (H α)
V12	7.94	121.09	175.97	62.57	32.36	20.56/20.63	3.65 (H α), 1.66 (H β), 0.60/0.50 (H γ 1/2)

Residue	H _N	N _H	C'	C α	C β	C γ 1/2	Miscellaneous
H13	8.12	122.47		55.97	30.52		4.32 (H α)
H14			175.04	56.20	39.84		4.26 (H α), 2.80 (H β)
Q15	8.25	121.31	175.51	55.72	29.26	33.49	3.97 (H α), 1.79/1.70 (H β 1/2), 2.05 (H γ)
K16	8.26	122.99	176.10	56.10	32.82		41.79 (C ϵ), 3.99 (H α), 2.69 (H ϵ)
L17	8.12	123.72	176.62	54.85	42.18	26.75	24.64/23.20 (C δ 1/2), 4.05 (H α), 1.34/1.16 (H β 1/2), 1.29 (H γ), 0.64/0.57 (H δ 1/2)
V18	7.87	121.53	174.97	61.72	33.00	20.39/20.97	3.75 (H α), 1.63 (H β), 0.57/0.47 (H γ 1/2)
F19	8.14	124.42	174.60	57.22	39.99		4.31 (H α), 2.70 (H β)
F20	8.09	122.99	174.53	57.10	39.93		4.28 (H α), 2.80 (H β)
A21	8.10	126.11	177.07	52.17	19.08		3.93 (H α), 1.09 (H β)
E22	8.22	119.86	175.95	56.29	30.19		3.92 (H α)
D23	8.29	121.68	176.37	53.91	40.93		4.37 (H α), 2.48/2.35 (H β 1/2)
V24	8.02	120.58	176.87	62.53	32.19		3.86 (H α), 1.91 (H β)
G25	8.41	111.66	174.30	45.24			3.70 (H α)
S26	8.02	115.36	174.31	58.16	63.65		4.15 (H α), 3.64/3.59 (H β 1/2)
N27	8.35	120.45	175.29	53.04	38.37		4.46 (H α), 2.60/2.53 (H β 1/2)
K28	8.22	121.68	177.02	56.47	32.38		41.85 (C ϵ), 3.98 (H α), 2.72 (H ϵ)
G29	8.28	109.46	173.53	44.86			3.65 (H α)
A30	7.89	123.38	177.45	52.17	18.96		4.02 (H α), 1.10 (H β)
I31	8.06	120.79	176.28	60.84	38.25		3.87 (H α), 1.59 (H β)
I32	8.17	126.32	176.47	60.97	38.31		3.88 (H α), 1.59 (H β)
G33	8.34	113.03	173.52	44.93			3.65 (H α)
L34	7.92	121.48	177.16	54.85	42.37	26.69	24.57/23.38 (C δ 1/2), 4.06 (H α), 1.32 (H β), 1.33 (H γ), 0.65/0.60 (H δ 1/2)
M35	8.32	121.93	175.98	54.98	32.50	31.72	4.25 (H α), 1.77 (H β), 2.31/2.24 (H γ 1/2)
V36	8.12	122.44	176.55	62.40	32.57		3.84 (H α), 1.81 (H β)
G37	8.48	113.11	174.30	45.11			3.71 (H α)
G38	8.12	108.51	173.51	44.86			3.65 (H α)
V39	7.94	119.77	175.43	62.22	32.75		3.90 (H α), 1.82 (H β)
V40	7.69	128.33		63.53	33.25	21.32/20.01	3.77 (H α), 1.78 (H β), 0.64/0.62 (H γ 1/2)

5.2.5 Chemical Shifts of the α -subunit in $\alpha_7\beta_7\beta_7\alpha_7$ -(11S)₁₄

Tab. 12 lists the chemical shifts of unambiguously assigned residues of the α -subunit in the $\alpha_7\beta_7\beta_7\alpha_7$ -(11S)₁₄ proteasome.

Tab. 12 Chemical shifts (in ppm) for the α -subunit in the $\alpha_7\beta_7\beta_7\alpha_7$ -(11S)₁₄ proteasome in PBS containing 20% glycerol and 60 mM Cu(II)-EDTA at an effective temperature of 5 °C.

Residue	H _N	N _H	C'	C α	C β
T36			172.67	63.17	
A37	8.19	126.44	174.57	50.23	
L38	9.38	116.60	173.68	54.03	
G39	8.23	104.25	172.35	45.00	

Residue	H _N	N _H	C'	Ca	Cβ
M40	8.40	116.22	174.53	55.65	
K41	9.10	123.16	176.83	57.49	
F42	8.52	126.06	174.01	56.24	
A43	9.22	124.74		54.29	16.59
N44			174.12	53.31	
G45	7.00	104.88	170.63	46.71	
V46	8.12	118.33	171.11	59.85	
L47	8.47	124.00	174.75		
L48	8.93	119.95	175.00	53.30	
I49	8.57	118.31		59.54	
V74			172.57		
A75	8.82	128.50			
T78			173.47	59.37	
S79	8.23	113.33		58.32	
A96	7.11	124.32			
R115			173.72		
V116	7.31	119.73	177.10	66.13	
V134	7.31	119.94		60.22	
I137			175.33	59.70	
F138	8.85	121.23	175.04	55.91	
A139	9.21	122.65	178.54	49.99	
G140	8.70	114.71	169.64	47.11	
I141	7.91	119.06		58.92	
D142	7.91	129.84			
P146			176.41		
R147	9.38	122.77			
L148			173.20		
F149	9.52	125.28		56.13	
D152	7.80	130.66			
N158			171.69		
E159	8.36	122.00		54.25	
K161	8.84	116.12	175.86	58.08	
A162	6.72	116.64	174.69	51.66	
T163	8.08	112.32	169.85	59.32	
A164	7.42	121.29	174.21	50.92	
I165	8.68	112.01	174.87	60.01	
G166	8.04	104.85		44.09	
K169			176.71		
D170	8.54	117.21		57.71	
V172			177.89	66.27	
V173	8.88	119.74	177.65	67.18	
S174	7.80	115.09	177.22	61.90	
F175	7.74	122.33		61.40	
L176			178.67		
E177	9.27	122.26		59.89	
R178			178.55		
E179	7.95	114.82	177.29	57.05	
Y180	9.41	119.67	174.94	61.56	
K181	5.39	126.38	173.24	53.83	
E182	8.17	119.19		56.05	30.56
P185			177.39	62.17	
E186	8.56	124.00	176.95	60.14	28.58
K187	8.70	115.44	179.50	60.38	
E188	7.05	118.53		58.71	

Residue	H _N	N _H	C'	Ca	Cβ
A189			178.35		
V190	8.26	119.21		66.79	
T191			176.30	67.64	
L192	7.81	122.93		57.83	
I194			178.22	62.46	
K195	7.90	121.38		60.00	32.03
L197			180.99		
K198	8.78	121.40	179.27	60.07	
S199	7.34	115.92	173.90	60.85	
S200	7.34	115.92	173.48	58.17	
L201	6.93	123.44	177.60	54.41	37.32
E202	8.57	121.58	176.87	55.36	29.78
E203	8.56	122.92		58.20	
G204			173.92		
E205	7.71	121.63	175.38	55.52	30.49
E206	8.30	123.00	175.58	54.57	
L207	8.61	125.54		54.52	
P210			175.58	62.47	
E211	8.29	117.73		54.82	
A213			175.35		
S214	9.31	115.59	170.50	56.04	
I215			172.22	59.92	
T216	6.80	114.11	174.58	58.00	72.48
V217	7.96	119.16	177.01	64.99	
G218	8.71	116.94	173.74	44.76	
N219	8.29	120.69	173.30	52.09	
K220	7.77	115.06	177.36	54.88	34.79
Y221	8.40	120.64	177.19	61.71	
R222	9.46	122.18	174.05	54.57	
I223	8.63	126.75	177.84	59.48	
Y224	9.31	132.17	176.74	58.09	37.58
D225	9.01	123.12		53.31	
Q226			178.59		
E227	8.54	118.31	178.81	58.84	28.08
E228	7.67	120.48	179.36	58.84	
K229	8.00	118.22	178.47	66.79	
K230	7.70	115.67	178.47	59.33	
K231	7.00	116.59	177.73	58.11	
F232	7.97	116.39	174.82	58.56	
L233	6.93	124.67		56.45	41.60

5.2.6 Pulse Programs for ^1H -detected Solid-state NMR Experiments

In the following, selected pulse sequences for ^1H -detected solid-state NMR experiments are listed.

The 2D ^1H - ^{15}N correlation (CP-based):

```
;HN 2D correlation via CP
; J-decoupling by waltz16 (1H) & composite pulse (13C)
; constant time type experiment
; with water purge pulse train for water suppression
; phase sensitive (t1)
; f1 (1H)->f3 (15N,t1)->f1 (1H,t2)
;
;p3: 1H p90
;p4: 1H p180
;p5: 15N p90
;p6: 15N p180
;p10: 1H water purge pulses
;p15: CP duration
;p20: 13C p90
;p21: 13C p180
;cpd2: 1H decoupling
;cpd3: 15N decoupling
;
;p12: 15N CP power
;p13: 1H power hard pulses
;p14: 15N power hard pulses
;p16: 13C power hard pulses
;p110: power saturation pulses
;p112: 1H decoupling power
;p115: 1H CP power
;p129: 15N decoupling power
;
;d0: incremented delay (t1 15N)
;d1: relaxation delay
;d2: decremented delay (t1 15N) t1max(ct)
;d11:delay for disk I/O
;d20:delay

#include <Avance.incl>
#include <Delay.incl>

"d11=30m"
"in2=in0"

1 ze
2 d1
  d11 do:f1 do:f3
  20u reset:f1 reset:f2
  5u p12:f3
  5u p13:f1
  5u p16:f2
  p3:f1 ph2
  1u p115:f1

  (p15:spf1 ph3):f3 (p15 ph0):f1
  1u p14:f3
  1u p112:f1
  1u cpd2:f1
```

Appendix

```
d0
(p20 ph0):f2
(p21 ph1):f2
(p20 ph0):f2
d0

p5:f3 ph4
d2
10u do:f1
4u pl10:f1
(p10 ph0):f1
(p10 ph1):f1
(p10 ph0):f1
(p10 ph1):f1
p5:f3 ph7

1u pl2:f3
1u pl15:f1
(p15:spf2 ph6):f3 (p15 ph5):f1

1u pl29:f3
1u cpd1:f3
go=2 ph31
40u do:f1
d11 do:f3 wr #0 if #0 zd
1m ip3
10u id0
10u dd2
lo to 2 times td1
HaltAcqu, 1m
exit

ph0 = 0
ph1 = 1
ph2 = 1 3
ph3 = 0 0 2 2
ph4 = 1 1 3 3 3 3 1 1
ph5 = 0 0 0 0 0 0 0 0 2 2 2 2 2 2 2 2
ph6 = 0 0 0 0 2 2 2 2
ph7 = 3 3 1 1 1 1 3 3
ph31= 1 3 3 1 3 1 1 3 3 1 1 3 1 3 3 1
```

The 3D HNC0 experiment (CP-transfer ^1H - ^{15}N , INEPT ^{15}N - ^{13}C)

```
;3D HNC0 sequence
; via CP (HN) & Inept (NC)
; phase sensitive (t1)
; phase sensitive (t2)
; using constant time in t2
; water suppression using purge pulses
; F1 (H)->F3 (N)->F2 (C=O,t1)->F3 (N,t2)->F1 (H,t3)
;
;p1 : 1H p90
;p2 : 1H p180
;p3 : 13C selective p90 CO
;p4 : 13C selective p180 CO
;p10: water purge pulses
;p14: 13C shaped inversion pulse Gaussian G3 (Ca off-resonance)
;p15: HN CP duration
;p16: NH CP duration
;p21: 15N p90
```



```

;p22: 15N p180
;cpd1: 1H decoupling
;cpd3: 15N decoupling
;p11 : 1H power hard pulse
;p12 : 13C power p180 soft rectang CO
;p13 : 15N power hard pulses
;p14 : 13C power p90 soft rectang CO
;p15: CP power 1H
;p110: 1H power water purge pulse
;p116: 15N decoupling power
;p117: CP power 15N
;p119: 1H decoupling power
;sp5: 13C power shaped inversion pulse (Ca off-resonance)
;spf1: ramp CP
;spf2: ramp CP
;d0 : incremented delay (t1 13C)
;d1 : relaxation delay
;d10: incremented delay (t2 15N)
;d11: delay for disk I/O
;d13: short delay
;d21: 1/(2J(NH)) [5.5 msec]
;d23: 1/(4J(NCO)) [12 msec]
;d26: 1/(4J'(NH)) [2.3 msec]
;d29: incremented delay (t2 15N)
;d30: decremented delay (t2 15N)
;cnst21: CO chemical shift (offset, in ppm)
;cnst22: Calpha chemical shift (offset, in ppm)
;in0: 1/(2 * SW(CO)) = DW(CO)
;nd0: 2
;in10: 1/(4 * SW(N)) = (1/2) DW(N)
;nd10: 4
;in29: = in10
;in30: = in10

```

```

prosol relations=<triple>
#include <Avance.incl>
#include <Delay.incl>

```

```

"in0=inf1/2"
"in10=inf2/4"
"in29=inf2/4"
"in30=inf2/4"

```

```

"d0=3u"
"d10=d23/2-p14/2"
"d11=30m"
"d13=4u"
"d23=12m"
"d29=d23/2-p14/2"
"d30=d23/2-p14/2"
"DELTA=d0*2+larger(p14,p22)-p14"
"DELTA1=d23-10u"

```

```

"spoff2=0"
"spoff3=0"
"spoff8=0"
aqseq 321

```

```

1 d11 ze
2 d1 p11:f1
  d11 do:f3
  20u reset:f1 reset:f3 reset:f2
  3u fq=cnst3:f1
  2u p12:f2
  2u p117:f3
  p1 ph1
  0.4u p15:f1

```

Appendix

```
(p15:spf1 ph3):f3 (p15 ph2):f1
4u pl19:f1
4u cpds1:f1 ph2
2u pl3:f3
DELTA1
(center (p4 ph2):f2 (p22 ph1):f3 )
DELTA1 pl4:f2
(p21 ph1):f3
10u do:f1
(p3 ph4):f2

d0
(center (p14:sp5 ph2):f2 (p22 ph1):f3 )
d0

4u pl2:f2
(p4 ph2):f2
DELTA
(p14:sp5 ph2):f2
4u
4u pl4:f2
(p3 ph1):f2
4u pl19:f1
4u cpds1:f1 ph2

(p21 ph5):f3
d30
(p14:sp5 ph1):f2
d30
4u pl2:f2
(center (p4 ph1):f2 (p22 ph8):f3)
d10
(p14:sp5 ph1):f2
d29

(p21 ph1):f3
10u do:f1
4u pl10:f1
(p10 ph2):f1
(p10 ph1):f1
(p10 ph2):f1
(p10 ph1):f1
4u
(p21 ph6):f3

4u pl17:f3
4u pl5:f1
(p16:spf2 ph2):f3 (p16 ph1):f1
2u pl16:f3
go=2 ph31 cpd3:f3
d11 do:f3 mc #0 to 2
    F1PH(rd10 & rd29 & rd30 & ip4, id0)
    F2PH(ip5, id10 & id29 & dd30)
exit

ph1 =0
ph2 =1
ph3 =1 1 1 1 1 1 1 3 3 3 3 3 3 3
ph4 =0 2
ph5 =1 1 3 3
ph6 =2
ph7 =3
ph8 =0 0 0 0 2 2 2 2
ph31=0 2 2 0 0 2 2 0 2 0 0 2 2 0 0 2
```

The 3D hCXhNH experiment:

```

;hCXhNH 3D sequence with proton detection
; using long range CP between 1H and 13C
; and subsequent CP between 1H and 15N
; using water purge pulses for water suppression
; with constant-time design
; phase sensitive (t1)
; phase sensitive (t2)
; f1(1H)->f2(13C,t1)->f1(1H)->f3(15N,t2)->f1(1H,t3)
;
;p1: 1H p90
;p7: 13C p90
;p8: 13C p180
;p10: 1H water purge pulse
;p15: HN CP duration
;p17: long range HC CP duration
;p21: 15N p90
;p22: 15N p180
;cpd1: 1H decoupling
;cpd3: 15N decoupling
;pl1: 1H power hard pulses
;pl3: 15N power hard pulses
;pl8: 13C power hard pulses
;pl10:1H power water purge pulses
;pl11:1H power HN CP
;pl16:15N decoupling power
;pl17:15N power HN CP
;pl19:1H decoupling power
;pl22: 1H power long range HC CP
;pl23: 13C power long range HC CP
;spf1: ramp HC CP
;spf2: ramp HC CP
;spf3: ramp HN CP
;spf4: ramp HN CP
;d0: incremented delay (t1 13C)
;d1: relaxation delay
;d10:incremented delay (t2 15N)
;d11:delay for disk I/O
;d20:decremented delay (t1 13C)
;d30:decremented delay (t2 15N)

proscl relations=<triple>
#include <Avancesolids.incl>
#include <Delay.incl>

"in0=inf1/2"
"in10=inf2/2"
"in20=in0"
"in30=in10"
"d0=0.3u"
"d10=0.3u"
"d20=30m"
"d30=36.4m"
"d11=30u"

aqseq 321

1 ze
2 1m do:f3
   1m do:f2
   d1
   10u reset:f2 reset:f1
   10u fq=cnst1:f2
   10u pl1:f1

```

Appendix

```
10u pl8:f2
10u pl3:f3

p1:f1 ph4
0.2u pl22:f1
p7:f2 ph4
0.2u pl23:f2
(p17 ph22):f2 (p17:spf1 ph23):f1

d0
(p22 ph8):f3
d0
(p17:spf2 ph3):f1 (p17 ph2):f2

0.2u pl11:f1
0.2u pl17:f3
(p15:spf3 ph5):f3 (p15 ph1):f1
0.5u pl19:f1
0.5u cpds1:f1

d10 pl8:f2
0.2u fq=cnst3:f2
(p8 ph8):f2
d10 pl3:f3
(p21 ph2):f3
d20
d30
0.5u do:f1
0.5u pl10:f1
(p10 ph2):f1
(p10 ph1):f1
(p10 ph2):f1
(p10 ph1):f1
4u
(p21 ph1):f3

0.2u pl11:f1 pl17:f3
(p15:spf4 ph2):f3 (p15 ph1):f1
2u pl16:f3

0.5u cpd3:f3
5u
go=2 ph31
do:f2
1m do:f3
1m mc #0 to 2
    F1PH(rd10 & rd30 & ip4 & ip22 & ip23 , id0 & dd20)
    F2PH( ip5, id10 & dd30)
HaltAcqu, 1m
exit

ph1 =0
ph2 =1
ph3 =0 0 0 0 2 2 2 2
ph4 =0 2
ph5 =0 0 2 2
ph8 =0 0 0 0 0 0 0 2 2 2 2 2 2 2 2
ph22=3 1
ph23=1 3
ph31=2 0 0 2 0 2 2 0 2 0 0 2 0 2 2 0
```


References

- 1 Hartl FU, Bracher A & Hayer-Hartl M (2011) Molecular chaperones in protein folding and proteostasis. *Nature* **475**, 324–332.
- 2 Morimoto RI (2008) Proteotoxic stress and inducible chaperone networks in neurodegenerative disease and aging. *Genes & Development* **22**, 1427–1438.
- 3 Powers ET, Morimoto RI, Dillin A, Kelly JW & Balch WE (2009) Biological and chemical approaches to diseases of proteostasis deficiency. *Annu. Rev. Biochem.* **78**, 959–991.
- 4 Hartl FU (1996) Molecular chaperones in cellular protein folding. *Nature* **381**, 571–580.
- 5 Chen B, Retzlaff M, Roos T & Frydman J (2011) Cellular Strategies of Protein Quality Control. *Cold Spring Harb. Perspect. Biol.* **3**, a004374.
- 6 Kaganovich D, Kopito R & Frydman J (2008) Misfolded proteins partition between two distinct quality control compartments. *Nature* **454**, 1088–1095.
- 7 Anfinsen CB (1973) Principles that govern the folding of protein chains. *Science* **181**, 223–230.
- 8 Herbst R, Schäfer U & Seckler R (1997) Equilibrium intermediates in the reversible unfolding of firefly (*Photinus pyralis*) luciferase. *J. Biol. Chem.* **272**, 7099–7105.
- 9 Tanford C (1978) The hydrophobic effect and the organization of living matter. *Science* **200**, 1012–1018.
- 10 Tanford C (1962) Contribution of Hydrophobic Interactions to the Stability of the Globular Conformation of Proteins. *J. Am. Chem. Soc.* **84**, 4240–4247.
- 11 Bartlett AI & Radford SE (2009) An expanding arsenal of experimental methods yields an explosion of insights into protein folding mechanisms. *Nat. Struct. Mol. Biol.* **16**, 582–588.
- 12 Kerner MJ, Naylor DJ, Ishihama Y, Maier T, Chang H-C, Stines AP, Georgopoulos C, Frishman D, Hayer-Hartl M, Mann M & Hartl FU (2005) Proteome-wide analysis of chaperonin-dependent protein folding in *Escherichia coli*. *Cell* **122**, 209–220.
- 13 Eichner T, Kalverda AP, Thompson GS, Homans SW & Radford SE (2011) Conformational conversion during amyloid formation at atomic resolution. *Mol. Cell* **41**, 161–172.
- 14 Chiti F & Dobson CM (2006) Protein misfolding, functional amyloid, and human disease. *Annu. Rev. Biochem.* **75**, 333–366.
- 15 Bolognesi B, Kumita JR, Barros TP, Esbjorn EK, Luheshi LM, Crowther DC, Wilson MR, Dobson CM, Favrin G & Yerbury JJ (2010) ANS binding reveals common features of cytotoxic amyloid species. *ACS Chem. Biol.* **5**, 735–740.
- 16 Gidalevitz T, Ben-Zvi A, Ho KH, Brignull HR & Morimoto RI (2006) Progressive disruption of cellular protein folding in models of polyglutamine diseases. *Science* **311**, 1471–1474.
- 17 Auluck PK, Chan HYE, Trojanowski JQ, Lee VMY & Bonini NM (2002) Chaperone suppression of alpha-synuclein toxicity in a *Drosophila* model for Parkinson's disease. *Science* **295**, 865–868.
- 18 Hartl FU & Hayer-Hartl M (2009) Converging concepts of protein folding in vitro and in vivo. *Nat. Struct. Mol. Biol.* **16**, 574–581.
- 19 Vabulas RM, Raychaudhuri S, Hayer-Hartl M & Hartl FU (2010) Protein Folding in the Cytoplasm and the Heat Shock Response. *Cold Spring Harb. Perspect. Biol.* **2**, a004390.
- 20 Chiti F, Taddei N, Baroni F, Capanni C, Stefani M, Ramponi G & Dobson CM (2002) Kinetic partitioning of protein folding and aggregation. *Nat. Struct. Biol.* **9**, 137–143.
- 21 Dobson CM (2003) Protein folding and misfolding. *Nature* **426**, 884–890.
- 22 Langer T, Lu C, Echols H, Flanagan J, Hayer MK & Hartl FU (1992) Successive action of DnaK, DnaJ and GroEL along the pathway of chaperone-mediated protein folding. *Nature* **356**, 683–689.
- 23 Mayer MP (2010) Gymnastics of molecular chaperones. *Mol. Cell* **39**, 321–331.
- 24 Frydman J (2001) Folding of newly translated proteins in vivo: the role of molecular chaperones. *Annu. Rev. Biochem.* **70**, 603–647.
- 25 Xu Z, Horwich AL & Sigler PB (1997) The crystal structure of the asymmetric GroEL-GroES-(ADP)7 chaperonin complex. *Nature* **388**, 741–750.
- 26 Horwich AL & Fenton WA (2009) Chaperonin-mediated protein folding: using a central cavity to kinetically assist polypeptide chain folding. *Q. Rev. Biophys.* **42**, 83–116.

- 27 Brinker A, Pfeifer G, Kerner MJ, Naylor DJ, Hartl FU & Hayer-Hartl M (2001) Dual function of protein confinement in chaperonin-assisted protein folding. *Cell* **107**, 223–233.
- 28 Haslbeck M, Franzmann T, Weinfurter D & Buchner J (2005) Some like it hot: the structure and function of small heat-shock proteins. *Nat. Struct. Mol. Biol.* **12**, 842–846.
- 29 Jakob U & Buchner J (1994) Assisting spontaneity: the role of Hsp90 and small Hsps as molecular chaperones. *Trends Biochem. Sci.* **19**, 205–211.
- 30 Horwitz J (1992) Alpha-crystallin can function as a molecular chaperone. *Proc. Natl. Acad. Sci. U.S.A.* **89**, 10449–10453.
- 31 Sun Y & MacRae TH (2005) The small heat shock proteins and their role in human disease. *FEBS J.* **272**, 2613–2627.
- 32 Veinger L, Diamant S, Buchner J & Goloubinoff P (1998) The Small Heat-shock Protein IbpB from *Escherichia coli* Stabilizes Stress-denatured Proteins for Subsequent Refolding by a Multichaperone Network. *J. Biol. Chem.* **273**, 11032–11037.
- 33 Ehrnsperger M, Gräber S, Gaestel M & Buchner J (1997) Binding of non-native protein to Hsp25 during heat shock creates a reservoir of folding intermediates for reactivation. *EMBO J.* **16**, 221–229.
- 34 Lee GJ, Roseman AM, Saibil HR & Vierling E (1997) A small heat shock protein stably binds heat-denatured model substrates and can maintain a substrate in a folding-competent state. *EMBO J.* **16**, 659–671.
- 35 van Montfort RL, Basha E, Friedrich KL, Slingsby C & Vierling E (2001) Crystal structure and assembly of a eukaryotic small heat shock protein. *Nat. Struct. Biol.* **8**, 1025–1030.
- 36 Kim KK, Kim R & Kim SH (1998) Crystal structure of a small heat-shock protein. *Nature* **394**, 595–599.
- 37 Stengel F, Baldwin AJ, Painter AJ, Jaya N, Basha E, Kay LE, Vierling E, Robinson CV & Benesch JLP (2010) Quaternary dynamics and plasticity underlie small heat shock protein chaperone function. *Proc. Natl. Acad. Sci. U.S.A.* **107**, 2007–2012.
- 38 Horwitz J (2003) Alpha-crystallin. *Experimental Eye Research* **76**, 145–153.
- 39 Haslbeck M, Walke S, Stromer T, Ehrnsperger M, White HE, Chen S, Saibil HR & Buchner J (1999) Hsp26: a temperature-regulated chaperone. *EMBO J.* **18**, 6744–6751.
- 40 Giese KC & Vierling E (2002) Changes in oligomerization are essential for the chaperone activity of a small heat shock protein in vivo and in vitro. *J. Biol. Chem.* **277**, 46310–46318.
- 41 Shashidharamurthy R, Koteiche HA, Dong J & McHaourab HS (2005) Mechanism of chaperone function in small heat shock proteins: dissociation of the HSP27 oligomer is required for recognition and binding of destabilized T4 lysozyme. *J. Biol. Chem.* **280**, 5281–5289.
- 42 Lindner RA, Kapur A, Mariani M, Titmuss SJ & Carver JA (1998) Structural alterations of alpha-crystallin during its chaperone action. *Eur. J. Biochem* **258**, 170–183.
- 43 Yang H, Huang S, Dai H, Gong Y, Zheng C & Chang Z (1999) The *Mycobacterium tuberculosis* small heat shock protein Hsp16.3 exposes hydrophobic surfaces at mild conditions: conformational flexibility and molecular chaperone activity. *Protein Sci.* **8**, 174–179.
- 44 Franzmann TM, Wühr M, Richter K, Walter S & Buchner J (2005) The activation mechanism of Hsp26 does not require dissociation of the oligomer. *J. Mol. Biol.* **350**, 1083–1093.
- 45 Aquilina JA, Benesch JLP, Ding LL, Yaron O, Horwitz J & Robinson CV (2005) Subunit exchange of polydisperse proteins: mass spectrometry reveals consequences of alphaA-crystallin truncation. *J. Biol. Chem* **280**, 14485–14491.
- 46 Bloemendal H, de Jong W, Jaenicke R, Lubsen NH, Slingsby C & Tardieu A (2004) Ageing and vision: structure, stability and function of lens crystallins. *Prog. Biophys. Mol. Biol.* **86**, 407–485.
- 47 Iwaki T, Kume-Iwaki A & Goldman JE (1990) Cellular distribution of alpha B-crystallin in non-lenticular tissues. *J. Histochem. Cytochem.* **38**, 31–39.
- 48 Nakamoto H & Vigh L (2007) The small heat shock proteins and their clients. *Cell. Mol. Life Sci.* **64**, 294–306.
- 49 Narayanan S, Kamps B, Boelens WC & Reif B (2006) α B-crystallin competes with Alzheimer's disease β -amyloid peptide for peptide–peptide interactions and induces oxidation of A β -Met35. *FEBS Lett.* **580**, 5941–5946.
- 50 Rekas A, Adda CG, Andrew Aquilina J, Barnham KJ, Sunde M, Galatis D, Williamson NA, Masters CL, Anders RF, Robinson CV, Cappai R & Carver JA (2004) Interaction of the molecular chaperone alphaB-crystallin with alpha-synuclein: effects on amyloid fibril formation and chaperone activity. *J. Mol. Biol.* **340**, 1167–1183.
- 51 Steinman L (2009) A molecular trio in relapse and remission in multiple sclerosis. *Nat. Rev. Immunol.* **9**, 440–447.

References

- 52 Vicart P, Caron A, Guicheney P, Li Z, Prevost M-C, Faure A, Chateau D, Chapon F, Tome F, Dupret J-M, Paulin D & Fardeau M (1998) A missense mutation in the alphaB-crystallin chaperone gene causes a desmin-related myopathy. *Nat. Genet.* **20**, 92–95.
- 53 Aquilina JA, Benesch JLP, Bateman OA, Slingsby C & Robinson CV (2003) Polydispersity of a mammalian chaperone: Mass spectrometry reveals the population of oligomers in α B-crystallin. *Proc. Natl. Acad. Sci. U.S.A.* **100**, 10611–10616.
- 54 Haley DA, Horwitz J & Stewart PL (1998) The small heat-shock protein, [alpha]b-crystallin, has a variable quaternary structure. *J. Mol. Biol.* **277**, 27–35.
- 55 Bagn  ris C, Bateman OA, Naylor CE, Cronin N, Boelens WC, Keep NH & Slingsby C (2009) Crystal structures of alpha-crystallin domain dimers of alphaB-crystallin and Hsp20. *J. Mol. Biol.* **392**, 1242–1252.
- 56 Laganowsky A, Benesch JLP, Landau M, Ding L, Sawaya MR, Cascio D, Huang Q, Robinson CV, Horwitz J & Eisenberg D (2010) Crystal structures of truncated alphaA and alphaB crystallins reveal structural mechanisms of polydispersity important for eye lens function. *Protein Sci.* **19**, 1031–1043.
- 57 Jehle S, van Rossum B, Stout JR, Noguchi SM, Falber K, Rehbein K, Oschkinat H, Klevit RE & Rajagopal P (2009) alphaB-crystallin: a hybrid solid-state/solution-state NMR investigation reveals structural aspects of the heterogeneous oligomer. *J. Mol. Biol.* **385**, 1481–1497.
- 58 Peschek J, Braun N, Franzmann TM, Georgalis Y, Haslbeck M, Weinkauff S & Buchner J (2009) The eye lens chaperone alpha-crystallin forms defined globular assemblies. *Proc. Natl. Acad. Sci. U.S.A.* **106**, 13272–13277.
- 59 Braun N, Zacharias M, Peschek J, Kastenm  ller A, Zou J, Hanzlik M, Haslbeck M, Rappsilber J, Buchner J & Weinkauff S (2011) Multiple molecular architectures of the eye lens chaperone α B-crystallin elucidated by a triple hybrid approach. *Proc. Natl. Acad. Sci. U.S.A.* **108**, 20491–20496.
- 60 Jehle S, Rajagopal P, Bardiaux B, Markovic S, K  hne R, Stout JR, Higman VA, Klevit RE, van Rossum B-J & Oschkinat H (2010) Solid-state NMR and SAXS studies provide a structural basis for the activation of alphaB-crystallin oligomers. *Nat. Struct. Mol. Biol.* **17**, 1037–1042.
- 61 Jehle S, Vollmar BS, Bardiaux B, Dove KK, Rajagopal P, Gonen T, Oschkinat H & Klevit RE (2011) N-terminal domain of {alpha}B-crystallin provides a conformational switch for multimerization and structural heterogeneity. *Proc. Natl. Acad. Sci. U.S.A.* **108**, 6409–6414.
- 62 Bova MP, Yaron O, Huang Q, Ding L, Haley DA, Stewart PL & Horwitz J (1999) Mutation R120G in α B-crystallin, which is linked to a desmin-related myopathy, results in an irregular structure and defective chaperone-like function. *Proc. Natl. Acad. Sci. U.S.A.* **96**, 6137–6142.
- 63 Liu L, Ghosh JG, Clark JI & Jiang S (2006) Studies of alphaB crystallin subunit dynamics by surface plasmon resonance. *Anal. Biochem.* **350**, 186–195.
- 64 Srinivas V, Raman B, Rao KS, Ramakrishna T & Rao CM (2005) Arginine hydrochloride enhances the dynamics of subunit assembly and the chaperone-like activity of alpha-crystallin. *Mol. Vis.* **11**, 249–255.
- 65 Ganadu ML, Aru M, Mura GM, Coi A, Mlynarz P & Kozlowski H (2004) Effects of divalent metal ions on the alphaB-crystallin chaperone-like activity: spectroscopic evidence for a complex between copper(II) and protein. *J. Inorg. Biochem.* **98**, 1103–1109.
- 66 Biswas A & Das KP (2008) Zn²⁺ enhances the molecular chaperone function and stability of alpha-crystallin. *Biochemistry* **47**, 804–816.
- 67 Reif B & Narayanan S (2007) Characterization of Interactions Between Misfolding Proteins and Molecular Chaperones by NMR Spectroscopy. In *Topics in Current Chemistry* (Peters T, ed), pp. 117–167. Springer Berlin Heidelberg.
- 68 Ahmad MF, Singh D, Taiyab A, Ramakrishna T, Raman B & Rao CM (2008) Selective Cu²⁺ binding, redox silencing, and cytoprotective effects of the small heat shock proteins alphaA- and alphaB-crystallin. *J. Mol. Biol.* **382**, 812–824.
- 69 Prabhu S, Srinivas V, Ramakrishna T, Raman B & Rao CM (2011) Inhibition of Cu²⁺-mediated generation of reactive oxygen species by the small heat shock protein [alpha]B-crystallin: The relative contributions of the N- and C-terminal domains. *Free Radical Biol. Med.* **51**, 755–762.
- 70 Linder MC & Haze  gh-Azam M (1996) Copper biochemistry and molecular biology. *Am. J. Clin. Nutr.* **63**, 797S–811S.
- 71 Johnson PE, Milne DB & Lykken GI (1992) Effects of age and sex on copper absorption, biological half-life, and status in humans. *Am. J. Clin. Nutr.* **56**, 917–925.
- 72 Barrow L & Tanner MS (1988) Copper distribution among serum proteins in paediatric liver disorders and malignancies. *Eur. J. Clin. Invest.* **18**, 555–560.

- 73 Wirth PL & Linder MC (1985) Distribution of copper among components of human serum. *J. Natl. Cancer Inst.* **75**, 277–284.
- 74 Weiss KC & Linder MC (1985) Copper transport in rats involving a new plasma protein. *Am. J. Physiol.* **249**, E77–88.
- 75 Healy J & Tipton K (2007) Ceruloplasmin and what it might do. *J. Neural. Transm.* **114**, 777–781.
- 76 Jomova K, Vondrakova D, Lawson M & Valko M (2010) Metals, oxidative stress and neurodegenerative disorders. *Mol. Cell. Biochem.* **345**, 91–104.
- 77 Brewer GJ (2010) Risks of copper and iron toxicity during aging in humans. *Chem. Res. Toxicol.* **23**, 319–326.
- 78 Wang Y, Hodgkinson V, Zhu S, Weisman GA & Petris MJ (2011) Advances in the understanding of Mammalian copper transporters. *Adv. Nutr.* **2**, 129–137.
- 79 Strausak D, Mercer JFB, Dieter HH, Stremmel W & Multhaup G (2001) Copper in disorders with neurological symptoms: Alzheimer's, Menkes, and Wilson diseases. *Brain Research Bulletin* **55**, 175–185.
- 80 Lutsenko S (2010) Human copper homeostasis: a network of interconnected pathways. *Curr. Opin. Chem. Biol.* **14**, 211–217.
- 81 Brown NM, Torres AS, Doan PE & O'Halloran TV (2004) Oxygen and the copper chaperone CCS regulate posttranslational activation of Cu,Zn superoxide dismutase. *Proc. Natl. Acad. Sci. U.S.A.* **101**, 5518–5523.
- 82 Palumaa P, Kangur L, Voronova A & Sillard R (2004) Metal-binding mechanism of Cox17, a copper chaperone for cytochrome c oxidase. *Biochem. J* **382**, 307–314.
- 83 Field LS, Luk E & Culotta VC (2002) Copper chaperones: personal escorts for metal ions. *J. Bioenerg. Biomembr.* **34**, 373–379.
- 84 Harrison MD, Jones CE & Dameron CT (1999) Copper chaperones: function, structure and copper-binding properties. *J. Biol. Inorg. Chem.* **4**, 145–153.
- 85 Rae TD, Schmidt PJ, Pufahl RA, Culotta VC & V. O'Halloran T (1999) Undetectable Intracellular Free Copper: The Requirement of a Copper Chaperone for Superoxide Dismutase. *Science* **284**, 805–808.
- 86 Holm RH, Kennepohl P & Solomon EI (1996) Structural and Functional Aspects of Metal Sites in Biology. *Chem. Rev.* **96**, 2239–2314.
- 87 Bertini I, Cavallaro G & McGreevy KS (2010) Cellular copper management—a draft user's guide. *Coord. Chem. Rev.* **254**, 506–524.
- 88 Choi M & Davidson VL (2011) Cupredoxins—A study of how proteins may evolve to use metals for bioenergetic processes. *Metallomics* **3**, 140–151.
- 89 Elinor T. A (1991) Copper Protein Structures. In *Metalloproteins: Structural Aspects* pp. 145–197. Academic Press.
- 90 Peisach J & Blumberg WE (1974) Structural implications derived from the analysis of electron paramagnetic resonance spectra of natural and artificial copper proteins. *Arch. Biochem. Biophys.* **165**, 691–708.
- 91 Gray HB, Malmström BG & Williams RJ (2000) Copper coordination in blue proteins. *J. Biol. Inorg. Chem.* **5**, 551–559.
- 92 Lalioti V, Muruais G, Tsuchiya Y, Pulido D & Sandoval IV (2009) Molecular mechanisms of copper homeostasis. *Front. Biosci.* **14**, 4878–4903.
- 93 Collyer CA, Guss JM, Sugimura Y, Yoshizaki F & Freeman HC (1990) Crystal structure of plastocyanin from a green alga, *Enteromorpha prolifera*. *J. Mol. Biol.* **211**, 617–632.
- 94 MacPherson IS & Murphy MEP (2007) Type-2 copper-containing enzymes. *Cell. Mol. Life Sci.* **64**, 2887–2899.
- 95 D'Alessandro A & Zolla L (2011) The SODyssey: superoxide dismutases from biochemistry, through proteomics, to oxidative stress, aging and nutraceuticals. *Expert. Rev. Proteomics* **8**, 405–421.
- 96 Maier CM & Chan PH (2002) Role of superoxide dismutases in oxidative damage and neurodegenerative disorders. *Neuroscientist* **8**, 323–334.
- 97 Hough MA & Hasnain SS (1999) Crystallographic structures of bovine copper-zinc superoxide dismutase reveal asymmetry in two subunits: functionally important three and five coordinate copper sites captured in the same crystal. *J. Mol. Biol.* **287**, 579–592.
- 98 Tainer JA, Getzoff ED, Beem KM, Richardson JS & Richardson DC (1982) Determination and analysis of the 2 A-structure of copper, zinc superoxide dismutase. *J. Mol. Biol.* **160**, 181–217.
- 99 van Holde KE, Miller KI & Decker H (2001) Hemocyanins and Invertebrate Evolution. *J. Biol. Chem.* **276**, 15563–15566.
- 100 Kosman DJ (2010) Multicopper oxidases: a workshop on copper coordination chemistry, electron transfer, and metallophysiology. *J. Biol. Inorg. Chem.* **15**, 15–28.

References

- 101 Clark EE, Poillon WN & Dawson CR (1966) Ascorbate oxidase. I. Oxidase activity, copper content and conformational changes. *Biochim. Biophys. Acta* **118**, 72–81.
- 102 Messerschmidt A, Rossi A, Ladenstein R, Huber R, Bolognesi M, Gatti G, Marchesini A, Petruzzelli R & Finazzi-Agró A (1989) X-ray crystal structure of the blue oxidase ascorbate oxidase from zucchini. Analysis of the polypeptide fold and a model of the copper sites and ligands. *J. Mol. Biol.* **206**, 513–529.
- 103 A. M (1993) Blue Copper Oxidases. In *Advances in Inorganic Chemistry* pp. 121–185. Academic Press.
- 104 Messerschmidt A & Huber R (1990) The blue oxidases, ascorbate oxidase, laccase and ceruloplasmin. Modelling and structural relationships. *Eur. J. Biochem.* **187**, 341–352.
- 105 Murphy ME, Lindley PF & Adman ET (1997) Structural comparison of cupredoxin domains: domain recycling to construct proteins with novel functions. *Protein Sci.* **6**, 761–770.
- 106 Getzoff ED, Tainer JA, Stempien MM, Bell GI & Hallewell RA (1989) Evolution of CuZn superoxide dismutase and the Greek key beta-barrel structural motif. *Proteins* **5**, 322–336.
- 107 Hong L & Simon JD (2011) Insights into the thermodynamics of copper association with amyloid- β , α -synuclein and prion proteins. *Metallomics* **3**, 262–266.
- 108 Thompson AR, Abdelraheim SR, Daniels M & Brown DR (2005) High Affinity Binding between Copper and Full-length Prion Protein Identified by Two Different Techniques. *J. Biol. Chem.* **280**, 42750–42758.
- 109 Davies P, McHugh PC, Hammond VJ, Marken F & Brown DR (2011) Contribution of individual histidines to prion protein copper binding. *Biochemistry* **50**, 10781–10791.
- 110 Dudzik CG, Walter ED & Millhauser GL (2011) Coordination features and affinity of the Cu²⁺ site in the α -synuclein protein of Parkinson's disease. *Biochemistry* **50**, 1771–1777.
- 111 Bortolus M, Bisaglia M, Zoleo A, Fittipaldi M, Benfatto M, Bubacco L & Maniero AL (2010) Structural characterization of a high affinity mononuclear site in the copper(II)- α -synuclein complex. *J. Am. Chem. Soc.* **132**, 18057–18066.
- 112 Hesse L, Behr D, Masters CL & Multhaup G (1994) The beta A4 amyloid precursor protein binding to copper. *FEBS Lett.* **349**, 109–116.
- 113 Multhaup G, Schlicksupp A, Hesse L, Behr D, Ruppert T, Masters CL & Beyreuther K (1996) The amyloid precursor protein of Alzheimer's disease in the reduction of copper(II) to copper(I). *Science* **271**, 1406–1409.
- 114 Hong L, Carducci TM, Bush WD, Dudzik CG, Millhauser GL & Simon JD (2010) Quantification of the binding properties of Cu²⁺ to the amyloid beta peptide: coordination spheres for human and rat peptides and implication on Cu²⁺-induced aggregation. *J. Phys. Chem. B* **114**, 11261–11271.
- 115 Sarell CJ, Syme CD, Rigby SEJ & Viles JH (2009) Copper(II) binding to amyloid-beta fibrils of Alzheimer's disease reveals a picomolar affinity: stoichiometry and coordination geometry are independent of A β oligomeric form. *Biochemistry* **48**, 4388–4402.
- 116 Parthasarathy S, Long F, Miller Y, Xiao Y, McElheny D, Thurber K, Ma B, Nussinov R & Ishii Y (2011) Molecular-level examination of Cu²⁺ binding structure for amyloid fibrils of 40-residue Alzheimer's β by solid-state NMR spectroscopy. *J. Am. Chem. Soc.* **133**, 3390–3400.
- 117 Nar H, Messerschmidt A, Huber R, van de Kamp M & Canters GW (1991) Crystal structure analysis of oxidized *Pseudomonas aeruginosa* azurin at pH 5.5 and pH 9.0. A pH-induced conformational transition involves a peptide bond flip. *J. Mol. Biol.* **221**, 765–772.
- 118 Smith CD, Carson M, van der Woerd M, Chen J, Ischiropoulos H & Beckman JS (1992) Crystal structure of peroxynitrite-modified bovine Cu,Zn superoxide dismutase. *Arch. Biochem. Biophys.* **299**, 350–355.
- 119 Moroz OV, Antson AA, Grist SJ, Maitland NJ, Dodson GG, Wilson KS, Lukanidin E & Bronstein IB (2003) Structure of the human S100A12-copper complex: implications for host-parasite defence. *Acta Crystallogr., Sect. D: Biol. Crystallogr.* **59**, 859–867.
- 120 Chondrogianni N & Gonos ES (2010) Proteasome function determines cellular homeostasis and the rate of aging. *Adv. Exp. Med. Biol.* **694**, 38–46.
- 121 Weissman AM, Shabek N & Ciechanover A (2011) The predator becomes the prey: regulating the ubiquitin system by ubiquitylation and degradation. *Nat. Rev. Mol. Cell Biol.* **12**, 605–620.
- 122 Ciechanover A & Iwai K (2004) The ubiquitin system: from basic mechanisms to the patient bed. *IUBMB Life* **56**, 193–201.
- 123 Depraetere V (2001) Getting activated with poly-ubiquitination. *Nat. Cell Biol.* **3**, E181.
- 124 Taylor EB & Rutter J (2011) Mitochondrial quality control by the ubiquitin-proteasome system. *Biochem. Soc. Trans.* **39**, 1509–1513.

- 125 Pickart CM & Cohen RE (2004) Proteasomes and their kin: proteases in the machine age. *Nat. Rev. Mol. Cell Biol.* **5**, 177–187.
- 126 Löwe J, Stock D, Jap B, Zwickl P, Baumeister W & Huber R (1995) Crystal structure of the 20S proteasome from the archaeon *T. acidophilum* at 3.4 Å resolution. *Science* **268**, 533–539.
- 127 Groll M, Ditzel L, Löwe J, Stock D, Bochtler M, Bartunik HD & Huber R (1997) Structure of 20S proteasome from yeast at 2.4 Å resolution. *Nature* **386**, 463–471.
- 128 Unno M, Mizushima T, Morimoto Y, Tomisugi Y, Tanaka K, Yasuoka N & Tsukihara T (2002) The structure of the mammalian 20S proteasome at 2.75 Å resolution. *Structure* **10**, 609–618.
- 129 Groll M, Bajorek M, Köhler A, Moroder L, Rubin DM, Huber R, Glickman MH & Finley D (2000) A gated channel into the proteasome core particle. *Nat. Struct. Biol.* **7**, 1062–1067.
- 130 Bajorek M & Glickman MH (2004) Keepers at the final gates: regulatory complexes and gating of the proteasome channel. *Cell. Mol. Life Sci.* **61**, 1579–1588.
- 131 Religa TL, Sprangers R & Kay LE (2010) Dynamic regulation of archaeal proteasome gate opening as studied by TROSY NMR. *Science* **328**, 98–102.
- 132 Glickman MH, Rubin DM, Coux O, Wefes I, Pfeifer G, Cjeka Z, Baumeister W, Fried VA & Finley D (1998) A subcomplex of the proteasome regulatory particle required for ubiquitin-conjugate degradation and related to the COP9-signalosome and eIF3. *Cell* **94**, 615–623.
- 133 Whitby FG, Masters EI, Kramer L, Knowlton JR, Yao Y, Wang CC & Hill CP (2000) Structural basis for the activation of 20S proteasomes by 11S regulators. *Nature* **408**, 115–120.
- 134 Seemuller E, Lupas A & Baumeister W (1996) Autocatalytic processing of the 20S proteasome. *Nature* **382**, 468–471.
- 135 Stock D, Ditzel L, Baumeister W, Huber R & Löwe J (1995) Catalytic mechanism of the 20S proteasome of *Thermoplasma acidophilum* revealed by X-ray crystallography. *Cold Spring Harb. Symp. Quant. Biol.* **60**, 525–532.
- 136 Adams J (2004) The proteasome: a suitable antineoplastic target. *Nat. Rev. Cancer* **4**, 349–360.
- 137 Adams J (2002) Proteasome inhibitors as new anticancer drugs. *Curr. Opin. Oncol.* **14**, 628–634.
- 138 Sprangers R & Kay LE (2007) Quantitative dynamics and binding studies of the 20S proteasome by NMR. *Nature* **445**, 618–622.
- 139 Sprangers R, Velyvis A & Kay LE (2007) Solution NMR of supramolecular complexes: providing new insights into function. *Nat. Methods* **4**, 697–703.
- 140 Mao P & Reddy PH (2011) Aging and amyloid beta-induced oxidative DNA damage and mitochondrial dysfunction in Alzheimer's disease: implications for early intervention and therapeutics. *Biochim. Biophys. Acta* **1812**, 1359–1370.
- 141 Findeis MA (2007) The role of amyloid beta peptide 42 in Alzheimer's disease. *Pharmacol. Ther.* **116**, 266–286.
- 142 Glenner GG & Wong CW (1984) Alzheimer's disease: initial report of the purification and characterization of a novel cerebrovascular amyloid protein. *Biochem. Biophys. Res. Commun.* **120**, 885–890.
- 143 Glenner GG & Wong CW (1984) Alzheimer's disease and Down's syndrome: sharing of a unique cerebrovascular amyloid fibril protein. *Biochem. Biophys. Res. Commun.* **122**, 1131–1135.
- 144 Masters CL, Simms G, Weinman NA, Multhaup G, McDonald BL & Beyreuther K (1985) Amyloid plaque core protein in Alzheimer disease and Down syndrome. *Proc. Natl. Acad. Sci. U.S.A.* **82**, 4245–4249.
- 145 Younkin SG (1998) The role of A beta 42 in Alzheimer's disease. *J. Physiol. Paris* **92**, 289–292.
- 146 Selkoe DJ (2001) Alzheimer's disease: genes, proteins, and therapy. *Physiol. Rev.* **81**, 741–766.
- 147 Huang H-C & Jiang Z-F (2011) Amyloid-β protein precursor family members: a review from homology to biological function. *J. Alzheimers Dis.* **26**, 607–626.
- 148 Kang J, Lemaire HG, Unterbeck A, Salbaum JM, Masters CL, Grzeschik KH, Multhaup G, Beyreuther K & Müller-Hill B (1987) The precursor of Alzheimer's disease amyloid A4 protein resembles a cell-surface receptor. *Nature* **325**, 733–736.
- 149 Tanzi RE, Gusella JF, Watkins PC, Bruns GA, St George-Hyslop P, Van Keuren ML, Patterson D, Pagan S, Kurnit DM & Neve RL (1987) Amyloid beta protein gene: cDNA, mRNA distribution, and genetic linkage near the Alzheimer locus. *Science* **235**, 880–884.
- 150 Barnham KJ, McKinstry WJ, Multhaup G, Galatis D, Morton CJ, Curtain CC, Williamson NA, White AR, Hinds MG, Norton RS, Beyreuther K, Masters CL, Parker MW & Cappai R (2003) Structure of the Alzheimer's disease amyloid precursor protein copper binding domain. A regulator of neuronal copper homeostasis. *J. Biol. Chem.* **278**, 17401–17407.

References

- 151 Lichtenthaler SF, Haass C & Steiner H (2011) Regulated intramembrane proteolysis—lessons from amyloid precursor protein processing. *J. Neurochem.* **117**, 779–796.
- 152 Suzuki N, Cheung TT, Cai XD, Odaka A, Otvos L Jr, Eckman C, Golde TE & Younkin SG (1994) An increased percentage of long amyloid beta protein secreted by familial amyloid beta protein precursor (beta APP717) mutants. *Science* **264**, 1336–1340.
- 153 Hardy J (1997) The Alzheimer family of diseases: many etiologies, one pathogenesis? *Proc. Natl. Acad. Sci. U.S.A.* **94**, 2095–2097.
- 154 Tilley L, Morgan K & Kalsheker N (1998) Genetic risk factors in Alzheimer's disease. *MP, Mol. Pathol.* **51**, 293–304.
- 155 Jankowsky JL, Fadale DJ, Anderson J, Xu GM, Gonzales V, Jenkins NA, Copeland NG, Lee MK, Younkin LH, Wagner SL, Younkin SG & Borchelt DR (2004) Mutant presenilins specifically elevate the levels of the 42 residue beta-amyloid peptide in vivo: evidence for augmentation of a 42-specific gamma secretase. *Hum. Mol. Genet.* **13**, 159–170.
- 156 Tomita T, Maruyama K, Saido TC, Kume H, Shinozaki K, Tokuhiro S, Capell A, Walter J, Grünberg J, Haass C, Iwatsubo T & Obata K (1997) The presenilin 2 mutation (N141I) linked to familial Alzheimer disease (Volga German families) increases the secretion of amyloid beta protein ending at the 42nd (or 43rd) residue. *Proc. Natl. Acad. Sci. U.S.A.* **94**, 2025–2030.
- 157 Mori C, Spooner ET, Wisniewsk KE, Wisniewski TM, Yamaguchi H, Saido TC, Tolan DR, Selkoe DJ & Lemere CA (2002) Intraneuronal Abeta42 accumulation in Down syndrome brain. *Amyloid* **9**, 88–102.
- 158 Babu MM, van der Lee R, de Groot NS & Gsponer J (2011) Intrinsically disordered proteins: regulation and disease. *Curr. Opin. Struct. Biol.* **21**, 432–440.
- 159 Uversky VN (2009) Intrinsic disorder in proteins associated with neurodegenerative diseases. *Front. Biosci.* **14**, 5188–5238.
- 160 Sachse C, Fändrich M & Grigorieff N (2008) Paired β -sheet structure of an A β (1–40) amyloid fibril revealed by electron microscopy. *Proc. Natl. Acad. Sci. U.S.A.* **105**, 7462–7466.
- 161 Tycko R (2011) Solid-state NMR studies of amyloid fibril structure. *Annu. Rev. Phys. Chem.* **62**, 279–299.
- 162 Schmidt M, Sachse C, Richter W, Xu C, Fändrich M & Grigorieff N (2009) Comparison of Alzheimer Abeta(1–40) and Abeta(1–42) amyloid fibrils reveals similar protofilament structures. *Proc. Natl. Acad. Sci. U.S.A.* **106**, 19813–19818.
- 163 Petkova AT, Leapman RD, Guo Z, Yau W-M, Mattson MP & Tycko R (2005) Self-propagating, molecular-level polymorphism in Alzheimer's beta-amyloid fibrils. *Science* **307**, 262–265.
- 164 Petkova AT, Yau W-M & Tycko R (2006) Experimental constraints on quaternary structure in Alzheimer's beta-amyloid fibrils. *Biochemistry* **45**, 498–512.
- 165 Lührs T, Ritter C, Adrian M, Riek-Loher D, Bohrmann B, Döbeli H, Schubert D & Riek R (2005) 3D structure of Alzheimer's amyloid-beta(1–42) fibrils. *Proc. Natl. Acad. Sci. U.S.A.* **102**, 17342–17347.
- 166 <http://neuropathology-web.org/chapter9/chapter9bAD.html>
- 167 Wu C & Shea J-E (2011) Coarse-grained models for protein aggregation. *Curr. Opin. Struct. Biol.* **21**, 209–220.
- 168 Lomakin A, Teplow DB, Kirschner DA & Benedek GB (1997) Kinetic theory of fibrillogenesis of amyloid beta-protein. *Proc. Natl. Acad. Sci. U.S.A.* **94**, 7942–7947.
- 169 Straub JE & Thirumalai D (2011) Toward a molecular theory of early and late events in monomer to amyloid fibril formation. *Annu. Rev. Phys. Chem.* **62**, 437–463.
- 170 Cerpa W, Dinamarca MC & Inestrosa NC (2008) Structure-function implications in Alzheimer's disease: effect of Abeta oligomers at central synapses. *Curr. Alzheimer Res.* **5**, 233–243.
- 171 Walsh DM & Selkoe DJ (2007) A beta oligomers - a decade of discovery. *J. Neurochem.* **101**, 1172–1184.
- 172 Lambert MP, Barlow AK, Chromy BA, Edwards C, Freed R, Liosatos M, Morgan TE, Rozovsky I, Trommer B, Viola KL, Wals P, Zhang C, Finch CE, Krafft GA & Klein WL (1998) Diffusible, nonfibrillar ligands derived from Abeta1–42 are potent central nervous system neurotoxins. *Proc. Natl. Acad. Sci. U.S.A.* **95**, 6448–6453.
- 173 Gong Y, Chang L, Viola KL, Lacor PN, Lambert MP, Finch CE, Krafft GA & Klein WL (2003) Alzheimer's disease-affected brain: presence of oligomeric A beta ligands (ADDLs) suggests a molecular basis for reversible memory loss. *Proc. Natl. Acad. Sci. U.S.A.* **100**, 10417–10422.
- 174 Dahlgren KN, Manelli AM, Stine WB Jr, Baker LK, Krafft GA & LaDu MJ (2002) Oligomeric and fibrillar species of amyloid-beta peptides differentially affect neuronal viability. *J. Biol. Chem.* **277**, 32046–32053.

- 175 Klein WL, Krafft GA & Finch CE (2001) Targeting small Abeta oligomers: the solution to an Alzheimer's disease conundrum? *Trends Neurosci.* **24**, 219–224.
- 176 Sakono M & Zako T (2010) Amyloid oligomers: formation and toxicity of A β oligomers. *FEBS J.* **277**, 1348–1358.
- 177 Atwood CS, Scarpa RC, Huang X, Moir RD, Jones WD, Fairlie DP, Tanzi RE & Bush AI (2000) Characterization of copper interactions with Alzheimer amyloid beta peptides: identification of an attomolar-affinity copper binding site on amyloid beta1–42. *J. Neurochem.* **75**, 1219–1233.
- 178 Curtain CC, Ali F, Volitakis I, Cherny RA, Norton RS, Beyreuther K, Barrow CJ, Masters CL, Bush AI & Barnham KJ (2001) Alzheimer's disease amyloid-beta binds copper and zinc to generate an allosterically ordered membrane-penetrating structure containing superoxide dismutase-like subunits. *J. Biol. Chem.* **276**, 20466–20473.
- 179 Huang X, Atwood CS, Hartshorn MA, Multhaup G, Goldstein LE, Scarpa RC, Cuajungco MP, Gray DN, Lim J, Moir RD, Tanzi RE & Bush AI (1999) The A beta peptide of Alzheimer's disease directly produces hydrogen peroxide through metal ion reduction. *Biochemistry* **38**, 7609–7616.
- 180 Tabner BJ, Turnbull S, El-Agnaf OMA & Allsop D (2002) Formation of hydrogen peroxide and hydroxyl radicals from A(beta) and alpha-synuclein as a possible mechanism of cell death in Alzheimer's disease and Parkinson's disease. *Free Radic. Biol. Med.* **32**, 1076–1083.
- 181 Smith DG, Cappai R & Barnham KJ (2007) The redox chemistry of the Alzheimer's disease amyloid beta peptide. *Biochim. Biophys. Acta* **1768**, 1976–1990.
- 182 Barnham KJ, Haeflner F, Ciccotosto GD, Curtain CC, Tew D, Mavros C, Beyreuther K, Carrington D, Masters CL, Cherny RA, Cappai R & Bush AI (2004) Tyrosine gated electron transfer is key to the toxic mechanism of Alzheimer's disease beta-amyloid. *FASEB J.* **18**, 1427–1429.
- 183 Shinohara H, Inaguma Y, Goto S, Inagaki T & Kato K (1993) Alpha B crystallin and HSP28 are enhanced in the cerebral cortex of patients with Alzheimer's disease. *J. Neurol. Sci.* **119**, 203–208.
- 184 Iwaki T, Wisniewski T, Iwaki A, Corbin E, Tomokane N, Tateishi J & Goldman JE (1992) Accumulation of alpha B-crystallin in central nervous system glia and neurons in pathologic conditions. *Am. J. Pathol.* **140**, 345–356.
- 185 Renkawek K, Voorter CE, Bosman GJ, van Workum FP & de Jong WW (1994) Expression of alpha B-crystallin in Alzheimer's disease. *Acta Neuropathol.* **87**, 155–160.
- 186 Wilhelmus MMM, Otte - Höller I, Wesseling P, De Waal RMW, Boelens WC & Verbeek MM (2006) Specific association of small heat shock proteins with the pathological hallmarks of Alzheimer's disease brains. *Neuropathology and Applied Neurobiology* **32**, 119–130.
- 187 Goldstein LE, Muffat JA, Cherny RA, Moir RD, Ericsson MH, Huang X, Mavros C, Coccia JA, Faget KY, Fitch KA, Masters CL, Tanzi RE, Chylack LT Jr & Bush AI (2003) Cytosolic beta-amyloid deposition and supranuclear cataracts in lenses from people with Alzheimer's disease. *Lancet* **361**, 1258–1265.
- 188 Shammas SL, Waudby CA, Wang S, Buell AK, Knowles TPJ, Ecroyd H, Welland ME, Carver JA, Dobson CM & Meehan S (2011) Binding of the molecular chaperone α B-crystallin to A β amyloid fibrils inhibits fibril elongation. *Biophys. J.* **101**, 1681–1689.
- 189 Wilhelmus MMM, Boelens WC, Otte-Höller I, Kamps B, de Waal RMW & Verbeek MM (2006) Small heat shock proteins inhibit amyloid- β protein aggregation and cerebrovascular amyloid- β protein toxicity. *Brain Research* **1089**, 67–78.
- 190 Stege GJJ, Renkawek K, Overkamp PSG, Verschuure P, van Rijk AF, Reijnen-Aalbers A, Boelens WC, Bosman GJCGM & de Jong WW (1999) The Molecular Chaperone α B-crystallin Enhances Amyloid β Neurotoxicity. *Biochem. Biophys. Res. Commun.* **262**, 152–156.
- 191 Raman B, Ban T, Sakai M, Pasta SY, Ramakrishna T, Naiki H, Goto Y & Rao CM (2005) AlphaB-crystallin, a small heat-shock protein, prevents the amyloid fibril growth of an amyloid beta-peptide and beta2-microglobulin. *Biochem. J* **392**, 573–581.
- 192 Ecroyd H & Carver JA (2009) Crystallin proteins and amyloid fibrils. *Cell. Mol. Life Sci* **66**, 62–81.
- 193 Levitt M (2001) *Spin Dynamics: Basics of Nuclear Magnetic Resonance*, 1st ed. John Wiley & Sons.
- 194 Duer MJ (2001) *Solid-state NMR spectroscopy: principles and applications* John Wiley & Sons.
- 195 Cavanagh J, Fairbrother WJ, III AGP, Skelton NJ & Rance M (2006) *Protein NMR Spectroscopy, Second Edition: Principles and Practice*, 2nd ed. Academic Press.
- 196 Ernst RR, Bodenhausen G & Wokaun A (1990) *Principles of Nuclear Magnetic Resonance in One and Two Dimensions* Clarendon Press.

References

- 197 Bermel W, Bertini I, Felli IC, Kümmerle R & Pierattelli R (2003) ^{13}C Direct Detection Experiments on the Paramagnetic Oxidized Monomeric Copper, Zinc Superoxide Dismutase. *J. Am. Chem. Soc.* **125**, 16423–16429.
- 198 Bertini I, Luchinat C, Parigi G & Pierattelli R (2008) Perspectives in paramagnetic NMR of metalloproteins. *Dalton Trans.*, 3782.
- 199 Wand AJ, Ehrhardt MR & Flynn PF (1998) High-resolution NMR of encapsulated proteins dissolved in low-viscosity fluids. *Proc. Natl. Acad. Sci. U.S.A.* **95**, 15299–15302.
- 200 Kielec JM, Valentine KG, Babu CR & Wand AJ (2009) Reverse micelles in integral membrane protein structural biology by solution NMR spectroscopy. *Structure* **17**, 345–351.
- 201 LeMaster DM (1990) Deuterium Labelling in NMR Structural Analysis of Larger Proteins. *Q. Rev. Biophys.* **23**, 133–174.
- 202 Gardner KH & Kay LE (1998) The use of ^2H , ^{13}C , ^{15}N multidimensional NMR to study the structure and dynamics of proteins. *Annu. Rev. Biophys. Biomol. Struct.* **27**, 357–406.
- 203 Pervushin K, Riek R, Wider G & Wüthrich K (1997) Attenuated T_2 relaxation by mutual cancellation of dipole-dipole coupling and chemical shift anisotropy indicates an avenue to NMR structures of very large biological macromolecules in solution. *Proc. Natl. Acad. Sci. U.S.A.* **94**, 12366–12371.
- 204 Fiaux J, Bertelsen EB, Horwich AL & Wüthrich K (2002) NMR analysis of a 900K GroEL GroES complex. *Nature* **418**, 207–211.
- 205 Rudiger S, Freund SMV, Veprintsev DB & Fersht AR (2002) CRINEPT-TROSY NMR reveals p53 core domain bound in an unfolded form to the chaperone Hsp90. *Proc. Natl. Acad. Sci. U.S.A.* **99**, 11085–11090.
- 206 Tugarinov V, Hwang PM, Ollerenshaw JE & Kay LE (2003) Cross-correlated relaxation enhanced ^1H [bond] ^{13}C NMR spectroscopy of methyl groups in very high molecular weight proteins and protein complexes. *J. Am. Chem. Soc.* **125**, 10420–10428.
- 207 Sprangers R, Gribun A, Hwang PM, Houry WA & Kay LE (2005) Quantitative NMR spectroscopy of supramolecular complexes: dynamic side pores in ClpP are important for product release. *Proc. Natl. Acad. Sci. U.S.A.* **102**, 16678–16683.
- 208 Christodoulou J, Larsson G, Fucini P, Connell SR, Pertinhez TA, Hanson CL, Redfield C, Nierhaus KH, Robinson CV, Schleucher J & Dobson CM (2004) Heteronuclear NMR investigations of dynamic regions of intact Escherichia coli ribosomes. *Proc. Natl. Acad. Sci. U.S.A.* **101**, 10949–10954.
- 209 Szymczyna BR, Gan L, Johnson JE & Williamson JR (2007) Solution NMR studies of the maturation intermediates of a 13 MDa viral capsid. *J. Am. Chem. Soc.* **129**, 7867–7876.
- 210 Tugarinov V & Kay LE (2003) Ile, Leu, and Val Methyl Assignments of the 723-Residue Malate Synthase G Using a New Labeling Strategy and Novel NMR Methods. *J. Am. Chem. Soc.* **125**, 13868–13878.
- 211 Andrew ER, Bradbury A & Eades RG (1958) Nuclear Magnetic Resonance Spectra from a Crystal rotated at High Speed. *Nature* **182**, 1659.
- 212 Baldus M (2006) Solid - State NMR Spectroscopy: Molecular Structure and Organization at the Atomic Level. *Angew. Chem. Int. Ed. Engl.* **45**, 1186–1188.
- 213 Pines A, Gibby MG & Waugh JS (1973) Proton - enhanced NMR of dilute spins in solids. *J. Chem. Phys.* **59**, 569–590.
- 214 Bennett AE, Griffin RG, Ok JH & Vega S (1992) Chemical shift correlation spectroscopy in rotating solids: Radio frequency - driven dipolar recoupling and longitudinal exchange. *J. Chem. Phys.* **96**, 8624–8627.
- 215 Gullion T & Schaefer J (1989) Rotational-echo double-resonance NMR. *J. Magn. Reson.* **81**, 196–200.
- 216 Raleigh DP, Levitt MH & Griffin RG (1988) Rotational resonance in solid state NMR. *Chem. Phys. Lett.* **146**, 71–76.
- 217 Renault M, Cukkernane A & Baldus M (2010) Solid-state NMR spectroscopy on complex biomolecules. *Angew. Chem. Int. Ed. Engl.* **49**, 8346–8357.
- 218 Morris GA & Freeman R (1979) Enhancement of nuclear magnetic resonance signals by polarization transfer. *J. Am. Chem. Soc.* **101**, 760–762.
- 219 Hartmann SR & Hahn EL (1962) Nuclear Double Resonance in the Rotating Frame. *Phys. Rev.* **128**, 2042–2053.
- 220 Szeverenyi NM, Sullivan MJ & Maciel GE (1982) Observation of spin exchange by two-dimensional fourier transform ^{13}C cross polarization-magic-angle spinning. *J. Magn. Reson.* **47**, 462–475.
- 221 Manolikas T, Herrmann T & Meier BH (2008) Protein structure determination from ^{13}C spin-diffusion solid-state NMR spectroscopy. *J. Am. Chem. Soc.* **130**, 3959–3966.

- 222 Takegoshi K, Nakamura S & Terao T (2001) ^{13}C – ^1H dipolar-assisted rotational resonance in magic-angle spinning NMR. *Chem. Phys. Lett.* **344**, 631–637.
- 223 Verel R, Ernst M & Meier BH (2001) Adiabatic dipolar recoupling in solid-state NMR: the DREAM scheme. *J. Magn. Reson.* **150**, 81–99.
- 224 Lewandowski JR, De Paëpe G & Griffin RG (2007) Proton assisted insensitive nuclei cross polarization. *J. Am. Chem. Soc.* **129**, 728–729.
- 225 Zhou DH, Shah G, Cormos M, Mullen C, Sandoz D & Rienstra CM (2007) Proton-detected solid-state NMR spectroscopy of fully protonated proteins at 40 kHz magic-angle spinning. *J. Am. Chem. Soc.* **129**, 11791–11801.
- 226 Reif B & Griffin RG (2003) ^1H detected ^1H , ^{15}N correlation spectroscopy in rotating solids. *J. Magn. Reson.* **160**, 78–83.
- 227 Zhou DH, Shea JJ, Nieuwkoop AJ, Franks WT, Wylie BJ, Mullen C, Sandoz D & Rienstra CM (2007) Solid-state protein-structure determination with proton-detected triple-resonance 3D magic-angle-spinning NMR spectroscopy. *Angew. Chem. Int. Ed. Engl.* **46**, 8380–8383.
- 228 Chevelkov V, Rehbein K, Diehl A & Reif B (2006) Ultrahigh Resolution in Proton Solid - State NMR Spectroscopy at High Levels of Deuteration. *Angew. Chem. Int. Ed. Engl.* **45**, 3878–3881.
- 229 Akbey U, Lange S, Trent Franks W, Linser R, Rehbein K, Diehl A, van Rossum B-J, Reif B & Oschkinat H (2010) Optimum levels of exchangeable protons in perdeuterated proteins for proton detection in MAS solid-state NMR spectroscopy. *J. Biomol. NMR* **46**, 67–73.
- 230 Linser R, Chevelkov V, Diehl A & Reif B (2007) Sensitivity enhancement using paramagnetic relaxation in MAS solid-state NMR of perdeuterated proteins. *J. Magn. Reson.* **189**, 209–216.
- 231 Linser R, Dasari M, Hiller M, Higman V, Fink U, Lopez Del Amo J-M, Markovic S, Handel L, Kessler B, Schmieder P, Oesterheld D, Oschkinat H & Reif B (2011) Proton-detected solid-state NMR spectroscopy of fibrillar and membrane proteins. *Angew. Chem. Int. Ed. Engl.* **50**, 4508–4512.
- 232 Gasteiger E, Gattiker A, Hoogland C, Ivanyi I, Appel RD & Bairoch A (2003) ExPASy: The proteomics server for in-depth protein knowledge and analysis. *Nucleic Acids Res.* **31**, 3784–3788.
- 233 Sambrook J & Russell DW (2000) *Molecular Cloning: A Laboratory Manual*, 3 Vol., 3rd ed. Cold Spring Harbor Laboratory.
- 234 Laemmli UK (1970) Cleavage of Structural Proteins during the Assembly of the Head of Bacteriophage T4. *Nature* **227**, 680–685.
- 235 Schagger H (2006) Tricine-SDS-PAGE. *Nat. Protocols* **1**, 16–22.
- 236 Jain E, Bairoch A, Duvaud S, Phan I, Redaschi N, Suzek BE, Martin MJ, McGarvey P & Gasteiger E (2009) Infrastructure for the life sciences: design and implementation of the UniProt website. *BMC Bioinformatics* **10**, 136–136.
- 237 Pieper CM & Enderlein J (2011) Fluorescence correlation spectroscopy as a tool for measuring the rotational diffusion of macromolecules. *Chem. Phys. Lett.* **516**, 1–11.
- 238 Wahl M, Gregor I, Patting M & Enderlein J (2003) Fast calculation of fluorescence correlation data with asynchronous time-correlated single-photon counting. *Opt Express* **11**, 3583–3591.
- 239 Segur JB & Oberstar HE (1951) Viscosity of Glycerol and Its Aqueous Solutions. *Ind. Eng. Chem.* **43**, 2117–2120.
- 240 Brunger AT (2007) Version 1.2 of the Crystallography and NMR system. *Nat. Protoc.* **2**, 2728–2733.
- 241 Harding MM (2006) Small revisions to predicted distances around metal sites in proteins. *Acta Crystallogr., Sect. D: Biol. Crystallogr.* **62**, 678–682.
- 242 Linge JP & Nilges M (1999) Influence of non-bonded parameters on the quality of NMR structures: a new force field for NMR structure calculation. *J. Biomol. NMR* **13**, 51–59.
- 243 Kuszewski J, Gronenborn AM & Clore GM (1996) Improving the quality of NMR and crystallographic protein structures by means of a conformational database potential derived from structure databases. *Protein Sci.* **5**, 1067–1080.
- 244 Goddard TD & Kneller DG SPARKY 3, University of California, San Francisco. .
- 245 Garrett DS, Seok Y-J, Peterkofsky A, Clore GM & Gronenborn AM (1997) Identification by NMR of the Binding Surface for the Histidine-Containing Phosphocarrier Protein HPr on the N-Terminal Domain of Enzyme I of the Escherichia coli Phosphotransferase System†. *Biochemistry* **36**, 4393–4398.
- 246 Bermel W, Bertini I, Duma L, Felli IC, Emsley L, Pierattelli R & Vasos PR (2005) Complete assignment of heteronuclear protein resonances by protonless NMR spectroscopy. *Angew. Chem., Int. Ed.* **44**, 3089–3092.

References

- 247 Bermel W, Bertini I, Felli IC, Matzapetakis M, Pierattelli R, Theil EC & Turano P (2007) A method for C(alpha) direct-detection in protonless NMR. *J. Magn. Reson.* **188**, 301–310.
- 248 Bermel W, Bertini I, Felli IC, Kümmerle R & Pierattelli R (2006) Novel ¹³C direct detection experiments, including extension to the third dimension, to perform the complete assignment of proteins. *J. Magn. Reson.* **178**, 56–64.
- 249 Shaka AJ, Keeler J & Freeman R (1983) Evaluation of a new broadband decoupling sequence: WALTZ-16. *J. Magn. Reson.* **53**, 313–340.
- 250 Shaka AJ, Barker PB & Freeman R (1985) Computer-optimized decoupling scheme for wideband applications and low-level operation. *J. Magn. Reson.* **64**, 547–552.
- 251 Wishart DS & Sykes BD (1994) The ¹³C chemical-shift index: a simple method for the identification of protein secondary structure using ¹³C chemical-shift data. *J. Biomol. NMR* **4**, 171–180.
- 252 Vranken WF, Boucher W, Stevens TJ, Fogh RH, Pajon A, Llinas M, Ulrich EL, Markley JL, Ionides J & Laue ED (2005) The CCPN data model for NMR spectroscopy: development of a software pipeline. *Proteins* **59**, 687–696.
- 253 Kay LE, Torchia DA & Bax A (1989) Backbone dynamics of proteins as studied by ¹⁵N inverse detected heteronuclear NMR spectroscopy: application to staphylococcal nuclease. *Biochemistry* **28**, 8972–8979.
- 254 Fushman D, Ohlenschläger O & Rüterjans H (1994) Determination of the backbone mobility of ribonuclease T1 and its 2' GMP complex using molecular dynamics simulations and NMR relaxation data. *J. Biomol. Struct. Dyn.* **11**, 1377–1402.
- 255 García de la Torre J, Huertas ML & Carrasco B (2000) HYDRONMR: prediction of NMR relaxation of globular proteins from atomic-level structures and hydrodynamic calculations. *J. Magn. Reson.* **147**, 138–146.
- 256 Kay LE, Ikura M, Tschudin R & Bax A (1990) Three-dimensional triple-resonance NMR spectroscopy of isotopically enriched proteins. *J. Magn. Reson.* **89**, 496–514.
- 257 Wittekind M & Mueller L (1993) HNCACB, a High-Sensitivity 3D NMR Experiment to Correlate Amide-Proton and Nitrogen Resonances with the Alpha- and Beta-Carbon Resonances in Proteins. *J. Magn. Reson.* **101**, 201–205.
- 258 Weisemann R, Rüterjans H & Bermel W (1993) 3D triple-resonance NMR techniques for the sequential assignment of NH and ¹⁵N resonances in ¹⁵N- and ¹³C-labelled proteins. *J. Biomol. NMR* **3**, 113–120.
- 259 Clore GM & Gronenborn AM (1994) Multidimensional heteronuclear nuclear magnetic resonance of proteins. *Meth. Enzymol.* **239**, 349–363.
- 260 Marsh JA, Singh VK, Jia Z & Forman-Kay JD (2006) Sensitivity of secondary structure propensities to sequence differences between alpha- and gamma-synuclein: implications for fibrillation. *Protein Sci.* **15**, 2795–2804.
- 261 Bax A & Ikura M (1991) An efficient 3D NMR technique for correlating the proton and ¹⁵N backbone amide resonances with the α -carbon of the preceding residue in uniformly ¹⁵N/¹³C enriched proteins. *J. Biomol. NMR* **1**, 99–104.
- 262 Carver JA (1999) Probing the structure and interactions of crystallin proteins by NMR spectroscopy. *Prog. Retin. Eye Res.* **18**, 431–462.
- 263 Treweek TM, Rekas A, Walker MJ & Carver JA (2010) A quantitative NMR spectroscopic examination of the flexibility of the C-terminal extensions of the molecular chaperones, α A- and α B-crystallin. *Exp. Eye Res.* **91**, 691–699.
- 264 Bertini I, Gupta YK, Luchinat C, Parigi G, Schlörb C & Schwalbe H (2005) NMR spectroscopic detection of protein protons and longitudinal relaxation rates between 0.01 and 50 MHz. *Angew. Chem. Int. Ed. Engl* **44**, 2223–2225.
- 265 Bertini I, Fragai M, Luchinat C & Parigi G (2000) ¹H NMRD profiles of diamagnetic proteins: a model - free analysis†. *Magn. Reson. Chem.* **38**, 543–550.
- 266 Zhou DH & Rienstra CM (2008) High-Performance Solvent Suppression for Proton-Detected Solid-State NMR. *J. Magn. Reson.* **192**, 167–172.
- 267 Linser R, Fink U & Reif B (2008) Proton-detected scalar coupling based assignment strategies in MAS solid-state NMR spectroscopy applied to perdeuterated proteins. *J. Magn. Reson* **193**, 89–93.
- 268 Linser R (2011) Side-chain to backbone correlations from solid-state NMR of perdeuterated proteins through combined excitation and long-range magnetization transfers. *J. Biomol. NMR* **51**, 221–226.
- 269 Clark AR, Naylor CE, Bagn  ris C, Keep NH & Slingsby C (2011) Crystal Structure of R120G Disease Mutant of Human α B-Crystallin Domain Dimer Shows Closure of a Groove. *J. Mol. Biol.* **408**, 118–134.

- 270 Pascal SM, Yamazaki T, Singer AU, Kay LE & Forman-Kay JD (1995) Structural and dynamic characterization of the phosphotyrosine binding region of a Src homology 2 domain–phosphopeptide complex by NMR relaxation, proton exchange, and chemical shift approaches. *Biochemistry* **34**, 11353–11362.
- 271 Eigen M, Hammes GG & Kustin K (1960) FAST REACTIONS OF IMIDAZOLE STUDIED WITH RELAXATION SPECTROMETRY. *J. Am. Chem. Soc.* **82**, 3482–3483.
- 272 Ghosh JG, Estrada MR & Clark JI (2005) Interactive domains for chaperone activity in the small heat shock protein, human α B-crystallin. *Biochemistry* **44**, 14854–14869.
- 273 Mainz A, Jehle S, van Rossum BJ, Oschkinat H & Reif B (2009) Large Protein Complexes with Extreme Rotational Correlation Times Investigated in Solution by Magic-Angle-Spinning NMR Spectroscopy. *J. Am. Chem. Soc.* **131**, 15968–15969.
- 274 Bertini I, Luchinat C, Parigi G, Ravera E, Reif B & Turano P (2011) Solid-state NMR of proteins sedimented by ultracentrifugation. *Proc. Natl. Acad. Sci. U.S.A.* **108**, 10396–10399.
- 275 Clubb RT, Thanabal V & Wagner G (1992) A constant-time three-dimensional triple-resonance pulse scheme to correlate intraresidue ^1H N, ^{15}N , and ^{13}C chemical shifts in ^{15}N – ^{13}C -labelled proteins. *J. Magn. Reson.* **97**, 213–217.
- 276 Aquilina JA, Benesch JLP, Ding LL, Yaron O, Horwitz J & Robinson CV (2004) Phosphorylation of α B-crystallin alters chaperone function through loss of dimeric substructure. *J. Biol. Chem.* **279**, 28675–28680.
- 277 Benesch JLP, Ayoub M, Robinson CV & Aquilina JA (2008) Small heat shock protein activity is regulated by variable oligomeric substructure. *J. Biol. Chem.* **283**, 28513–28517.
- 278 Bhattacharyya J, Padmanabha Udupa EG, Wang J & Sharma KK (2006) Mini- α B-crystallin: a functional element of α B-crystallin with chaperone-like activity. *Biochemistry* **45**, 3069–3076.
- 279 Ghosh JG, Estrada MR, Houck SA & Clark JI (2006) The function of the β 3 interactive domain in the small heat shock protein and molecular chaperone, human α B-crystallin. *Cell Stress Chaperones* **11**, 187–197.
- 280 Santhoshkumar P & Sharma KK (2006) Conserved F84 and P86 residues in α B-crystallin are essential to effectively prevent the aggregation of substrate proteins. *Protein Sci.* **15**, 2488–2498.
- 281 Ghosh KS, Pande A & Pande J (2011) Binding of γ -Crystallin Substrate Prevents the Binding of Copper and Zinc Ions to the Molecular Chaperone α -Crystallin. *Biochemistry* **50**, 3279–3281.
- 282 Ghosh JG & Clark JI (2005) Insights into the domains required for dimerization and assembly of human α B-crystallin. *Protein Sci.* **14**, 684–695.
- 283 Mainz A, Bardiaux B, Kuppler F, Multhaup G, Felli IC, Pierattelli R & Reif B (2012) Structural and mechanistic implications of metal binding in the small heat-shock protein α B-crystallin. *J. Biol. Chem.* **287**, 1128–1138.
- 284 Ecroyd H, Meehan S, Horwitz J, Aquilina JA, Benesch JLP, Robinson CV, Macphree CE & Carver JA (2007) Mimicking phosphorylation of α B-crystallin affects its chaperone activity. *Biochem. J.* **401**, 129.
- 285 Koretz JF, Doss EW & LaButti JN (1998) Environmental factors influencing the chaperone-like activity of [α]-crystallin. *Int. J. Biol. Macromol.* **22**, 283–294.
- 286 Truscott RJW (2005) Age-related nuclear cataract–oxidation is the key. *Exp. Eye Res.* **80**, 709–725.
- 287 Lawless MW, O’Byrne KJ & Gray SG (2010) Targeting oxidative stress in cancer. *Expert Opin. Ther. Targets* **14**, 1225–1245.
- 288 Hawse JR, Cumming JR, Oppermann B, Sheets NL, Reddy VN & Kantorow M (2003) Activation of Metallothioneins and α -Crystallin/sHSPs in Human Lens Epithelial Cells by Specific Metals and the Metal Content of Aging Clear Human Lenses. *Invest. Ophthalmol. Vis. Sci.* **44**, 672–679.
- 289 Bertini I, Engelke F, Luchinat C, Parigi G, Ravera E, Rosa C & Turano P (2011) NMR properties of sedimented solutes. *Phys. Chem. Chem. Phys.* **14**, 439–447.
- 290 Knight MJ, Webber AL, Pell AJ, Guerry P, Barbet-Massin E, Bertini I, Felli IC, Gonnelli L, Pierattelli R, Emsley L, Lesage A, Hermann T & Pintacuda G (2011) Fast resonance assignment and fold determination of human superoxide dismutase by high-resolution proton-detected solid-state MAS NMR spectroscopy. *Angew. Chem. Int. Ed. Engl.* **50**, 11697–11701.
- 291 Akbey U, Oschkinat H & van Rossum B-J (2009) Double-nucleus enhanced recoupling for efficient ^{13}C MAS NMR correlation spectroscopy of perdeuterated proteins. *J. Am. Chem. Soc.* **131**, 17054–17055.
- 292 Ramakrishnan V (2009) The ribosome: some hard facts about its structure and hot air about its evolution. *Cold Spring Harb. Symp. Quant. Biol.* **74**, 25–33.

Acknowledgements

This work was carried out at the Department of solid-state NMR spectroscopy at the Leibniz-Institut für molekulare Pharmakologie (FMP), Berlin, Germany, from September 2007 to December 2011 under the supervision of **Prof. Dr. Bernd Reif**. This research was supported by the Leibniz-Gemeinschaft, the Helmholtz-Gesellschaft, the DFG (Re11435, SF449, SFB700, SFB610), the Center for Integrated Protein Science Munich (CIPS-M) and by access to research infrastructures activity in the 7th Framework Program of the EC (project number 261863, Bio-NMR).

The last four years were challenging, exciting, sometimes frustrating and many things more. I have met so many people, that enriched my life and essentially contributed to this work. Hence, these pages of gratitude can not be long enough.

First of all, I would like to express my deepest gratitude to my supervisor **Prof. Dr. Bernd Reif**. He gave me the unique opportunity to follow my scientific interests without any restrictions. This freedom on the one hand, and his commitment to my research on the other hand created a stimulating and inspiring atmosphere. I cannot imagine a better “Doktorvater”. All beginnings are difficult – fortunately, **Dr. Katja Faelber** made them a bit easier for me. Her scientific experience and stamina were of great help and moreover impressive. I am thankful for all the advices in sophisticated research as well as the tips and tricks in everyday labwork. When talking about my “Doktorvater”, it is also necessary to thank my “Doktorschwester” **Verena**. It was a wonderful time to work with her, to share all the problems in daily PhD student life, and to laugh, sometimes without any reason. So finally, I got a sister. Many, many thanks to my “Doktorbrüder” **Tomas, Rasmus** and **Sam** for being the best colleagues I could think of. All their scientific help was crucial for my work, and the spirit in our office was unique at the institute. I’m already missing these good old days. I’m also grateful to **Uwe** and **Kerstin** for the support in the lab and to **Dr. Vipin Agarwal**, who introduced me to the practical aspects of solid-state NMR.

I am particularly indebted to **Stefan Markovic**, who has always been a competent colleague to discuss various aspects of α B. But more importantly, he is one of the most friendly, obliging and good-humored persons I have ever met. I’m really happy to have found a new friend in him.

As is probably the case for all NMR spectroscopists at the FMP, I'm deeply grateful to **Dr. Peter Schmieder**. His comprehensive understanding of NMR theory and practice was always impressive and helpful, as were his didactic skills. His way of organizing the solution-state NMR facility is exemplary. I'm also thankful to **Monika Beerbaum** for her contributions to this exceptional organization. I would like to thank **Dr. Barth van Rossum** for the organization of the solid-state NMR facility and his helpful support at the spectrometers. I really enjoyed his advices and his humor. I am also thankful to **Nadin Jahnke** for her helping hand concerning the ITC instrument and to **Dr. Yvette Roske** for the crystallization trials.

Many of the presented results in this work were made possible by contributions from various collaborators. I am grateful to **Isabella C. Felli** and **Roberta Pierattelli** for my wonderful stay at CERM in Florence and their help with the ^{13}C -detected NMR experiments. I'm also indebted to **Prof. Dr. Hartmut Oschkinat** for his support and contributions to the αB project as well as for providing an impressive NMR facility at the FMP. Furthermore, I would like to express my gratitude to **Prof. Dr. Lewis E. Kay**, **Dr. Tomasz Religa** and **Dr. Remco Sprangers** for providing the proteasome assemblies, and **Prof. Dr. Claudio Luchinat**, **Dr. Giacomo Parigi** as well as **Prof. Dr. Jörg Enderlein** and **Christoph Pieper** for their contributions to the determination of rotational correlation times of protein complexes.

Alongside my colleagues at work, many other people have contributed to this thesis. I am grateful to all my **friends** accepting me the way I am and enduring my permanently filled schedule. I really appreciate your mental support and your patience.

My last words in this thesis are dedicated to my family, which is the actual source of my vigor and my motivation. I am thankful for all the encouragement, the trust and the joyful moments my **parents** and my **brothers** gave me. Sorry Dad, I hope this thesis is somehow compensation for not becoming Boris Becker II. Likewise, my deepest gratitude belongs to my generous **grandparents**, who passed away during the last years of this thesis. At last, it is absolutely impossible to adequately express my gratitude to **Natalie**, who has laughed and suffered with me the last eight years. None of the numerous pages written here would have been possible without her. Our love has strengthened me. You'll be a wonderful mother...

Thank you to all of you...

Publications

A. Mainz, S. Jehle, B. J. van Rossum, H. Oschkinat, B. Reif, “Large Protein Complexes with Extreme Rotational Correlation Times Investigated in Solution by Magic-Angle-Spinning NMR Spectroscopy” (2009) *J. Am. Chem. Soc.* **131**, 15968-15969

(this publication has been further evaluated and selected for the library of the Faculty of 1000 by G. Otting (2011) *Faculty of 1000*, F1000.com/13232957#eval14583055)

A. Mainz, B. Bardiaux, F. Kuppler, G. Multhaup, I. C. Felli, R. Pierattelli, B. Reif, “Structural and Mechanistic Implications of Metal Binding in the Small Heat-Shock Protein α B-Crystallin” (2012) *J. Biol. Chem.* **287**, 1128-1138

A. Mainz, T. Religa, R. Sprangers, C. Pieper, G. Parigi, C. Luchinat, J. Enderlein, L. E. Kay, B. Reif, “NMR Spectroscopy of Soluble Protein Complexes at 1 MDa and Beyond”, *submitted*

Conferences and Workshops

- January 2008: “Particle size determination in the submicron regime by dynamic light scattering”, Advanced training course (Malvern), Kirschau, Germany.
- July 2009: **A. Mainz**, S. Jehle, H. Oschkinat, B. Reif, “The sHSP α B-crystallin: NMR approaches to structural insights to its Cu(II)-dependent chaperone-like activity and its interaction with the Alzheimer’s peptide A β ₁₋₄₀”, Poster presentation, Euromar NMR conference, Göteborg, Sweden.
- March 2010: **A. Mainz**, I. C. Felli, R. Pierattelli, B. Reif, “The small heat-shock protein α B-crystallin: structural insights by versatile NMR approaches”, Oral presentation, Spring Meeting of the Leibniz Graduate School of Molecular Biophysics, Hinterzarten, Germany.
- July 2010: **A. Mainz**, T. Religa, I. C. Felli, R. Pierattelli, L. E. Kay, B. Reif, “The bigger the better: large protein complexes investigated in solution by magic-angle-spinning (MAS) NMR spectroscopy”, Oral & poster presentation, Winner of the ISMAR young investigator award, Euromar & ISMAR Joint Conference, Florence, Italy.
- September 2010: **A. Mainz**, T. Religa, I. C. Felli, R. Pierattelli, L. E. Kay, B. Reif, “The small heat-shock protein α B-crystallin: structural insights by versatile NMR approaches”, Oral presentation, Greifswald University, Germany.
- April 2011: **A. Mainz**, T. Religa, G. Parigi, R. Sprangers, C. Pieper, J. Enderlein, C. Luchinat, L. E. Kay, B. Reif, “FROSTY MAS NMR: A new tool for the investigation of large protein complexes in solution”, Poster presentation, Experimental NMR conference (ENC), Asilomar, California, USA.

Eidesstattliche Erklärung

Hiermit versichere ich an Eides Statt, dass ich die hier vorliegende Dissertation eigenständig angefertigt und keine anderen als die gemäß §6, Absatz 3 der Promotionsordnung vom 01.09.2005 angegebenen Hilfen und Hilfsmittel verwendet habe.

Ich versichere außerdem, dass ich mich weder um einen Doktorgrad anderwärts beworben habe noch einen entsprechenden Doktorgrad besitze.

Des Weiteren bestätige ich hiermit meine Kenntnis über die dem angestrebten Promotionsverfahren zugrunde liegende Promotionsordnung vom 01.09.2005.

Berlin, den

.....

(Andi Mainz)

